Georgia State University
ScholarWorks @ Georgia State University

Physics and Astronomy Dissertations | Department of Physics and Astronomy

4-22-2008

Growth and Characterization of Indium Nitride Layers Grown by High-Pressure Chemical Vapor Deposition

Mustafa Alevli

Follow this and additional works at: https://scholarworks.gsu.edu/phy_astr_diss

Recommended Citation
Alevli, Mustafa, "Growth and Characterization of Indium Nitride Layers Grown by High-Pressure Chemical Vapor Deposition." Dissertation, Georgia State University, 2008.
https://scholarworks.gsu.edu/phy_astr_diss/24

This Dissertation is brought to you for free and open access by the Department of Physics and Astronomy at ScholarWorks @ Georgia State University. It has been accepted for inclusion in Physics and Astronomy Dissertations by an authorized administrator of ScholarWorks @ Georgia State University. For more information, please contact scholarworks@gsu.edu.

GROWTH AND CHARACTERIZATION OF INDIUM NITRIDE LAYERS GROWN BY HIGH-PRESSURE CHEMICAL VAPOR DEPOSITION

by

MUSTAFA ALEVLI

Under the Direction of Nikolaus Dietz

ABSTRACT

In this research the growth of InN epilayers by high-pressure chemical vapor deposition (HPCVD) and structural, optical properties of HPCVD grown InN layers has been studied. We demonstrated that the HPCVD approach suppresses the thermal decomposition of InN, and therefore extends the processing parameters towards the higher growth temperatures (up to 1100K for reactor pressures of 15 bar, molar ammonia and TMI ratios around 800, and a carrier gas flow of 12 slm). Structural and surface morphology studies of InN thin layers have been performed by X-ray diffraction, low energy electron diffraction (LEED), auger electron spectroscopy (AES), high-resolution electron energy loss spectroscopy (HREELS) and atomic force microscopy (AFM). Raman spectroscopy, infrared reflection, transmission,

photoluminescence spectroscopy studies have been carried out to investigate the structural and optical properties of InN films grown on sapphire and GaN/sapphire templates.

InN layers grown on a GaN (0002) epilayer exhibit single-phase InN (0002) X-ray diffraction peaks with a full width at half maximum (FWHM) around 200 arcsec. Auger electron spectroscopy confirmed the cleanliness of the surface, and low energy electron diffraction yielded a 1×1 hexagonal pattern indicating a well-ordered surface. The plasmon excitations are shifted to lower energies in HREEL spectra due to the higher carrier concentration at the surface than in the bulk, suggesting a surface electron accumulation. The surface roughness of samples grown on GaN templates is found to be smoother (roughness of 9 nm) compared to the samples grown on sapphire. We found that the deposition sometimes led to the growth of 3 dimensional hexagonal InN pyramids.

Results obtained from Raman and IR reflectance measurements are used to estimate the free carrier concentrations, which were found in the range from mid 10^{18} cm^{-3} to low 10^{20} cm^{-3}. The optical absorption edge energy calculated from the transmission spectra is 1.2 eV for samples of lower electron concentration. The Raman analysis revealed a high-quality crystalline layer with a FWHM for the E_2(high) peak around 6.9 cm^{-1}. The results presented in our study suggest that the optimum molar ratio might be below 800, which is due to the efficient cracking of the ammonia precursor at the high reactor pressure and high growth temperature.

INDEX WORDS: Indium Nitride, In-rich group III Nitrides, III-V semiconductors, High-Pressure, Chemical Vapor Deposition, V/III molar ratio.

GROWTH AND CHARACTERIZATION OF INDIUM NITRIDE LAYERS GROWN BY HIGH-PRESSURE CHEMICAL VAPOR DEPOSITION

by

MUSTAFA ALEVLI

A Dissertation Submitted in Partial Fulfillment of the Requirements for the Degree of

Doctor of Philosophy

in the College of Arts and Sciences

Georgia State University

2008

Copyright by

Mustafa Alevli

2008

GROWTH AND CHARACTERIZATION OF INDIUM NITRIDE LAYERS GROWN BY HIGH-PRESSURE CHEMICAL VAPOR DEPOSITION

by

MUSTAFA ALEVLI

Committee Chair: Nikolaus Dietz

Committee: Brian D. Thoms
A. G. Unil Perera
Xiaochun He
Douglas Gies

Electronic Version Approved:

Office of Graduate Studies
College of Arts and Sciences
Georgia State University
May 2008

Dedicated to my lovely wife Sema and our infant son Yusuf Eren

Acknowledgements

I would like to express my deepest gratitude to my advisor Dr. Nikolaus Dietz. I was extremely fortunate to have privilege to work in such a work group with Dr. Dietz. He provided me with the motivation, guidance, and support I needed to complete my Ph. D. studies. I would like to especially thank him for giving me the chance to work in the semiconductor growth I wanted to study. His constant interest during my Ph. D. studies makes me working on a challenging problem like indium nitride growth.

I would like to thank Dr. A.G.Unil Perera, Dr. Brian Thoms, Dr. Douglas Gies, and Dr. Xiaochun He for agreeing to serve on my committee by sparing their valuable time and for providing helpful comments and suggestions. I would like extend my special thanks to Dr. Ian Ferguson from Georgia Tech for providing GaN/sapphire substrates and facilities, and Axel Hoffmann from Berlin Technical University for providing photoluminescence and micro Raman studies on InN samples during my Ph. D. studies.

I was really lucky to have perfect team-mates related to the characterization of InN. I would like to thank Goksel Durkaya, Dr. Rhudra Bhatta, Dr. Vincent Woods, Dr. Aruna Weesekara, Ronny Kirste, Ramazan Atalay, William Fenwick, Dr. Gamini Ariyawansa, and Dr. Jayantha Senawiratne with whom I had several stimulating and enjoyable conversations about research, life and everything else. I would like to thank my dear friends Goksel Durkaya, Derya Yildirim, Arif Sen, Cengiz and Dmitry Esaev for getting me and my mind out of Georgia State NSC room #126 every once in a while.

I would like to thank Professor Zikri Altun and in the name of Dr. Altun Turkish Petrol Foundation for their support in every way.

I would like to thank my parents and my wife's parents for everything they have done to help me succeed throughout my life. I am sincerely grateful to my parents Sebahat and Kazim, my wife's parents Omer and Ayse, my sister Nuray, my brother Birol and all of the rest of my family for all of their sacrifices and their unconditional love and support.

Last, but not least, I would like to thank my lovely wife ,Sema, for all her love and companionship. It would have been so much more difficult to complete this dissertation without her presence. Being the person closest to me, she had to suffer through ups and downs of Ph. D. studies, but she never stopped bringing my life joy and happiness, which I needed the most. My wife Sema and my little son Yusuf Eren receive my deepest gratitude and love all the time for their invaluable dedication and sacrifice in every part of my life.

TABLE OF CONTENTS

DEDICATION	iv
ACKNOWLEDGEMENTS	v
LIST OF TABLES	xi
LIST OF FIGURES	xiii
CHAPTERS	
1.1 Motivation	1
1.2 Review of indium nitride research history	2
1.3 InN: A member of the group III-Nitride System	5
1.3.1 Importance of InN	6
1.3.1.1 InN physical properties	6
1.3.1.2 Status of current InN, In-rich group-III Nitrides and competing alternatives	10
1.3.2 Application areas	14
1.3.2.1 Optical applications	14
1.3.2.2 LED applications	15
1.3.2.3 Laser applications	17
1.3.2.4 Electronic applications	18
1.4 State of the art for InN based THz applications	19
1.5 Objectives of this research	23
2.1 InN material system	25
2.1.1 InN crystal structure	25
2.1.2 Fluctuation in the structural properties obtained	28

2.2 Current growth methods used for growth of InN and In rich group III- Nitride 30

2.2.1 Molecular beam epitaxy 31

2.2.2 Organo metallic chemical vapor deposition 33

2.2.3 Hydride vapor phase epitaxy 36

2.2.4 Sputtering 38

2.3 Challenges in growing InN and In-rich group III-Nitrides 39

3. Description of high pressure chemical vapor deposition reactor and real time characterization and ex-situ characterization 41

3.1 Introduction 41

3.2 High pressure chemical vapor deposition approach 43

3.3 Modeling of high pressure CVD processes 46

3.4 High pressure chemical vapor deposition reactor system 52

3.5 High pressure chemical vapor deposition reactor characteristics 55

3.6 Real time optical characterization of gas flow dynamics 55

3.6.1 Laser light scattering 55

3.6.2 Principle angle reflectance spectroscopy 56

3.6.3 Ultraviolet absorption spectroscopy 58

3.7 Growth procedure 61

3.8 Real time characterization of InN growth: nucleation and steady state growth 63

3.9 Substrate choice 68

3.9.1 Sapphire substrate 68

3.9.2 Si substrate 69

3.9.3 GaN and AlN templates 70

3.9.4 Other potential substrates 70

3.10 Ex-Situ characterization 71

3.10.1 X-Ray diffraction 71

3.10.2 Auger electron spectroscopy 72

3.10.3 Low energy electron diffraction 73

3.10.4 High resolution electron energy loss spectroscopy 75

3.10.5 Atomic force microscopy 76

3.10.6 Infrared reflection spectroscopy 78

3.10.7 Raman spectroscopy 80

3.10.8 Transmission spectroscopy 82

3.10.9 Photoluminescence 85

4. Growth of High Quality Single Phase InN crystals by High Pressure CVD 86

4.1 Introduction 86

4.2 Growth of InN by HPCVD 87

4.3 Characterization of InN 88

4.4 Conclusion 95

5. Structural and surface morphological analysis of InN layers grown by high pressure CVD 97

5.1 Introduction 98

5.2 X-ray diffraction 98

5.2.1 Structural characterization of single phase InN thin layers 98

5.2.2 Effect of V/III Ratio 99

5.3 Surface structure, composition of InN Layers 105

5.3.1 Surface electron accumulation in InN thin layers 107

5.3.2 Desorption of hydrogen InN(0001) surface 110

5.4 Atomic force microscopy: surface morphology of InN layers 114

5.4.1 Effect of substrate 115

5.4.2 Formation of hexagonal InN pyramids by HPCVD 123

5.5 Conclusion 124

6. Optical properties of InN thin films 128

6.1 Optical transmission measurement of InN films 128

6.2 Infrared reflection measurements of InN films 138

6.3 Raman spectra of InN film in backscattering geometry 146

6.3.1 Electronic oscillations-phonon interaction in HPCVD grown InN by Raman spectroscopy 148

6.3.2 Micro-Raman analysis: strain relaxation at edge of holes 152

6.4 Photoluminescence 157

6.5 Conclusion 161

7. The effect of the growth surface polarity on physical properties of InN 163

7.1 Introduction 163

7.2 Experimental details 164

7.3 Results 165

7.4 Conclusions 175

8. Conclusion and future work 179

8.1 Introduction 179

8.2 Surface morphology and structural properties 179

8.3 Optical properties 182

8.4 Open questions and future Work 184

List of tables

1.1 Material properties of III-V wide band gap and conventional semiconductors. Errors are within the bracket. 8

2.1 Growth parameters, lattice constants, and crystalline quality of different InN samples grown by different method. 28

3.1 Summary of the selected heterogeneous reactions. Symbol _S in reactions represent the adsorbed species. 49

3.2 Raman selection rules for hexagonal group III-nitrides. 81

5.1 Growth parameters, structural and optical data for InN films grown on GaN template and sapphire substrate. 101

5.2 Growth parameters, FWHM of InN (0002) rocking curves, crystallinity and surface roughness of InN samples. 122

6.1 The optical transmission spectroscopy fitting parameters for InN samples. InN layer thickness (d), the optical absorption edge (**E_0**), high frequency dielectric constant (ε_∞), S_{ab} lorentzian oscillator strength, E_{ab1} energetic position of absorption center, Γ_{ab} damping constant. 134

6.2 The growth parameters of InN samples. R_p reactor pressure was at 15 bar and total gas flow rate was 12 slm. 135

6.3 Model fitting parameters for IR Reflection spectroscopy. Evidence for the existence of two separate InN layers was found by the IR spectra fitting. Layer thickness (d), high frequency dielectric constant (ε_∞), plasma frequency (ω_p), damping constant (Γ), and estimated free concentration are given for each layer. 141

The layer next to GaN or sapphire is the 2nd layer and the layer above is the 1st layer.

6.4 Model parameters for modeling the A_1(LO) line shape. 154

7.1 The optical and structural data for InN samples grown on Ga- polar and N-polar GaN samples. 173

List Figures

1.1 Phase relations of InN shown by a decomposition curve separating InN and In+N_2 phase fields. Tetragons represent experimental conditions where metallic indium is observed. Shaded circles indicate that InN was stable. 3

1.2 Apparent band gap of InN films as a function of carrier concentration. The solid curve represents the theoretical Moss-Burstein effects proposed by Walukewicz *et al.* There is a considerable spread of data for material nominally referred to as InN. 12

1.3 Apparent absorption edge of InN films grown by HPCVD at GSU as a function carrier concentration. 13

1.4 Band gap energy vs. lattice constant for binary group III-Nitrides material systems. 16

1.5 Calculated steady-state drift velocity as function of electric field in group III-Nitride materials and GaAs. In all cases, O'Leary *et al.* assumed a doping concentration of 10^{17} cm^{-3} and a crystal temperature of 300 K. 19

1.6 Free carrier absorption is calculated for different carrier concentration in a 1 μm n-type InN layer grown on sapphire. The calculated absorption coefficient of InN with a doping of 1×10^{18} cm^{-3} is shown in the inset. The free carrier concentration stays constant below 3 THz. 22

2.1 Atomic arrangement in wurtzite InN crystals. 26

2.2	Cubic zincblende structure of InN. Red spheres represent indium atoms and gray unfilled spheres represent nitrogen atoms.	27
2.3	The epitaxial relationship between the sapphire substrate, the zincblende and the wurtzite.	27
2.4	Relationship between the FWHM of X-ray of InN (0002) grown with different techniques and optical band gap energy.	29
2.5	Dependence of the lattice constants a and c on the optical band gap energy.	30
2.6	The equilibrium partial pressures over a) GaN b) InN and c) AlN as functions of input ratios.	35
2.7	Growth temperature dependence of carrier concentration for InN film grown at different pressures.	36
2.8	Growth rate of InN films as a function of growth temperature.	38
3.1	Thermal decomposition pressure vs. reciprocal temperature for AlN, GaN and InN.	45
3.2	Scheme for the selection of a reduced gas-phase chemical reaction model.	46
3.3	Final mass fractions obtained for the steady state and time evolution model using a reduced set of chemical equations. The initial molar ratios and conditions are: N_2:NH_3:$In(CH_3)_3$= 0.99504:0.00493:0.00003, temperature=1300 K, pressure= 12.5 atm.	48
3.4	InN growth rate in μm per hour. The arrow shows the direction of the	51

flow. a) Path one; b) Path Two; c) Path Three; d) Path Four

3.5 Comparisons between experimental and simulated average InN growth rate in μm per hour. The central bar corresponds to the experimental value, the left bar to the simulation at lower substrate heating, and the right bar to the simulation of higher substrate heating. 52

3.6 a) Schematic perspective outline of half of the reactor flow channel assembly showing the flow direction and containing the optical access ports provide an access to the growth surface. 53

b) Cross sectional view of the machined and assembled flow channel assembly with inserted sapphire substrates.

3.7 Schematics of the HPCVD flow control panel for precursor compression and pulsed precursor gas injection. 54

3.8 Schematic cross section of the reactor containing the optical access ports and the center of the substrates. Two optical ports provide access to the flow channel and three ports in each of the two half sections of the reactor provide access to the growth surface. 54

3.9 Transition from laminar to turbulent flow conditions as determined by LLS intensity measurements. The inset depicts LLS in forward geometry to analyze the onset of turbulence. 57

3.10 Angle dependency of reflectance for p- and s- polarized light at the sapphire-ambient interface, depicted are the characteristic angles: principle angle φ_p and total reflection angle φ_T. 58

3.11 a) Change of the ammonia absorption peak maximum as function of 60

temperature.

b) Decomposition of TMI at 10 bar reactor pressure, monitored during pulsed TMI injection as function of temperature.

3.12 Schematic representation of a precursor cycle sequence used for the growth of InN via the precursors TMI and ammonia. 63

3.13 Real time optical monitoring of InN growth by PARS and LLS. 64

3.14 Monitoring of InN nucleation by PARS and UV transmission traces. A precursor cycle sequence of 6 sec with 0.8 sec TMI and 1 sec ammonia pulses, separated by 1.4 sec were used. 66

3.15 PARS and UV transmission traces during steady-state InN growth at 1090 K. The rector pressure was 15 bar with a total flow of 12slm. The overall decrease in the PARS signal corresponds to InN growth. 67

3.16 Diagram of the experimental geometry for X-ray diffraction. 72

3.17 Auger Electron Process. 74

3.18 Schematic representations of the LEED apparatus. 75

3.19 Diagram of an atomic force microscopy set up. 77

3.20 Propagation of an Electromagnetic wave through a double film. 83

3.21 Schematic of possible optical transitions that can be observed via photoluminescence. 85

4.1 XRD spectra for InN layers grown on sapphire (#71 U) and on a virtual GaN/Sapphire substrate (#76U). 89

4.2 Uniformity of an InN layer grown on a virtual GaN/Sapphire substrate. (#76U). The inset shows a photograph of wafer area analyzed. 90

4.3 Raman Spectra for InN layers grown on sapphire (# 71U) and on a GaN epilayer (#76U). 91

4.4 IR reflectance spectrum and best fit for an InN layer deposited on a virtual GaN / Sapphire substrate (#76U). 93

4.5 Transmission spectra for InN grown on sapphire (#71U) and on virtual GaN-sapphire substrate (#76U). 95

5.1 XRD spectra for InN layers on sapphire substrate (#71U and #135U). 102

5.2 XRD spectra for InN layers on a GaN/sapphire template (#76U and #125 L). 103

5.3 X ray diffraction patterns for the InN films grown with different NH_3/TMI ratios. 104

5.4 The XRD peak analysis indicates an asymmetric lower shoulder which might be due to the either native point defects or impurity incorporation. 105

5.5 a) LEED of AHC cleaned InN sample (#65U) at incident electron energy 40 eV. 107

b) LEED of AHC cleaned InN sample (#125) at incident electron energy 40 eV.

5.6 HREELS from an atomic hydrogen cleaned InN sample. Spectra were acquired in the specular direction with incident electron energies of a) 7 eV, b) 15 eV, c) 25 eV, and d) 35 eV. 109

5.7 HREEL spectra from sample #125L after preparation by atomic hydrogen cleaning (AHC) and after heating for 900 s to 375, 400, and 111

425 °C. The surface was restored to the same initial state with AHC prior to each heat treatment.

5.8 AFM image of Sample #74 U (5μm x 5μm, 256 x 256 pixels, Contact mode). 116

5.9 AFM image of Sample #148L (5μm x 5μm, 256 x 256 pixels, Non-Contact mode). 117

5.10 Slightly disoriented hexagonal InN films grown on Sapphire (sample #148L). 118

5.11 AFM image of Sample # 76U (1μm x 1μm, 256 x 256 pixels, Contact mode). 119

5.12 AFM image of Sample # 192L (1μm x 1μm, 256 x 256 pixels, Contact mode). 119

5.13 Real time optical monitoring of an InN film (#125 U) surface by LLS where etching starts to dominate the growth. AFM image of Sample # 125L (5μm x 5μm, 256 x 256 pixels, NC mode is presented in inset). 121

5.14 AFM images of the sample surface containing InN pyramids (50×50 μm, NC mode). 124

5.15 FWHM of XRD rocking curves taken at the (0002) reflex measured on HPCVD grown InN as a function of the surface roughness. 127

6.1 The experimental transmission spectra and their best fit curves of samples #143U and #142U with different V/III molar ratios. Arrows indicate the calculated optical band gap. 131

6.2 The experimental Transmission spectra and their best-fit curves of InN 132

samples grown on GaN templates with different V/III molar ratio. Arrows indicate the calculated optical band gap.

6.3 Optical absorption edge dependence of absorption centers obtained from the analysis of optical transmission spectra of thin InN films. The solid lines represent the linear fitting results. 136

6.4 Comparison of optical absorption edge energy, FWHM of InN (0002) as a function of InN thickness. 137

6.5 The experimental IR spectra and their best fit curves of samples #76U, and #135U. The fitting parameters are given in Table 6.2. All experiments were performed at room temperature 139

6.6 Infrared reflection curve of three InN samples with different free carrier concentrations and two different doping regimes. The crosses are theoretical fits using a complex dielectric function model. 140

6.7 Dependence of optical absorption edge on carrier concentration as obtained from a modified model dielectric function in combination with experimental data. 144

6.8 Surface roughness of InN samples with different carrier mobilities obtained from the fitting of the experimental Infrared reflection spectra. 145

6.9 Room temperature Raman scattering of wurtzite-InN grown on GaN/sapphire and Sapphire substrates. Raman modes are identified using Lorentzian fitting. 147

6.10 The experimental Raman spectra and the simulated A_1(LO) line shapes. The line shape is calculated using the DP+EO scattering mechanism, 151

which provided the best fit of the experimental results.

6.11 Optical absorption edge vs. carrier concentration. 153

6.12 (a) Raman spectra of InN recorded at lateral positions. (b) Spectra were obtained at four different spots. (c) Raman shift of E_2(high) regarding to lateral position. (d) FWHM of E_2(high) against the distance from the InN/Sapphire interface. 156

6.13 Experimental PL spectra of InN samples with an electron concentrations of 6×10^{19} cm^{-3} (from IR reflection data analysis). The inset shows the absorption coefficient calculated by using the film thickness from the fitting of experimental transmission spectra. 159

6.14 Experimental PL spectra of InN samples with electron concentrations of 1×10^{20} cm^{-3} (from IR reflection data analysis). The inset shows the absorption coefficient calculated by using the film thickness from the fitting of experimental transmission spectra. 160

7.1 ω-2θ scan XRD curve for a InN sample grown on a Ga-polar template. 166

7.2 The InN peak deconvolution indicates an asymmetric lower shoulder, which might be due to impurities. 167

7.3 High resolution X-ray rocking curves of InN film grown on OMCVD-GaN with Ga-polarity, InN (002) reflection, (103) reflection and (302) reflection. 168

7.4 Raman spectra of InN layers #207L and #209L grown on N-polar and Ga-polar GaN/sapphire templates, respectively. 171

7.5 Analysis of E_2(high) and A_1(LO) modes in the Raman spectrum for InN 172

layer #209L grown on a Ga-polar GaN/ sapphire template.

7.6 Transmission spectra and their best fits for InN layers deposited on N-polar GaN and Ga-polar GaN substrates. 175

7.7 PL Spectra of sample #209L at 10K. 177

7.8 The value of α versus photon energy at room temperature in a wider energy range for sample #209L. At higher energies the curve shows a monotonic increase and then stays constant. 178

Chapter 1

1.1 Motivation

The unique properties of group III-nitride compound semiconductors, i.e. AlN, GaN, InN and their alloys, have inspired many advanced device designs/structures, integrating electrical, optical, and magnetic functionalities[1-3]. A key challenge in the realization of such true multifunctional devices lays in the integration of InN and indium-rich group III-nitride heterostructures (x > 0.2) in existing Ga1-xAlxN device structures. The integration of In-rich alloys in group III-Nitride heterostructures requires the existence of overlapping processing parameters as well as the precise control of the thermal decomposition pressures of indium-rich alloys at the optimum processing temperatures. A further challenge to be met is the growth of high-quality InN itself and understanding the fundamental physical properties, which presently vary depending on the growth techniques utilized[4-6]. The large thermal decomposition pressures of InN and indium-rich group III-nitrides limits the growth temperatures for low-pressure deposition techniques[3]. Although recent results of InN layers grown by plasma assisted molecular beam epitaxy (MBE) demonstrated that high-quality InN layers can be achieved with low-pressure deposition techniques[7,8], the integration of such layers in $Ga_{1-x}Al_xN$ structures remains challenging problem.

Surface stabilization data have shown that highly volatile compounds such as InN and related alloys can be grown at much higher temperatures if stabilized by elevated

nitrogen over-pressures, evoking the development of a novel ***high-pressure chemical vapor deposition (HPCVD)*** system at Georgia State University (GSU)[9-12]. This work focuses on studying the growth of InN at an intermediate pressure regime of approximately 15 bar, under which laminar flow conditions can be maintained.[13] Optical diagnostic techniques are utilized to monitor in real-time gas phase kinetics as well as growth surface chemistry[9,14]. The following sections provide an overview of the past and current status of InN growth and its properties and the advancements that are required for higher quality InN materials and In rich group III-nitride heterostructures.

1.2 Review of indium nitride research history

Research on InN initiated in 1938 [15] when synthesized powder samples were analyzed by X-ray diffraction in order to determine the crystallographic properties of this material. Juza and Hahn[15] obtained InN from decomposition of $InF_6(NH_4)_3$ at 600 ^oC. Juza and Hahn reported the crystal structure of InN to be wurtzite having lattice parameters a= 3.5377 Å, c= 5.7037 Å. These measured lattice constants are in excellent agreement with the present reported values. Research onto InN was sporadic between 1938 and 1990.

In the 1970's, McChesney *et al*[16] reported the disassociation pressure of InN as extremely high and stated that the formation of InN may require interaction of indium metal with atomic or other excited nitrogen species at high temperature that may require high pressures. They showed that the phase relation of InN results in a $P\text{-}T^{-1}$ relation as depicted Figure 1 according to

$$\Delta H_F = -\frac{1}{2} R \frac{d \ln P_{N_2}}{d(1/T)} \tag{1.1}$$

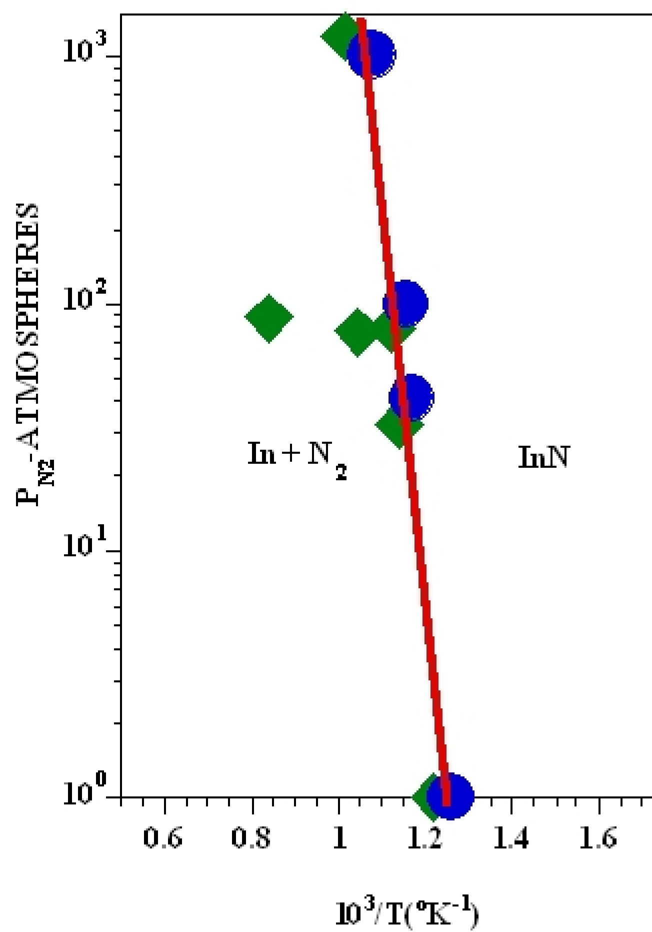

Figure 1. 1 Phase relations of InN shown by a decomposition curve separating InN and In+N_2 phase fields. Tetragons represent experimental conditions where metallic indium is observed. Shaded circles indicate that InN was stable. (From ref. 2)

in which the dissociation pressure rises very steeply toward higher nitrogen pressure. Another report by Trainor and Rose[17] in 1974 argued the partial pressure of atomic nitrogen rather than diatomic nitrogen is a more fundamental parameter describing thermal equilibrium. The thermal stability studies of InN indicate that InN samples decompose in a few minutes leave an indium residue in N_2 (at standard pressure) at 500 ^oC during the annealing process. However, if the InN samples were heated to 500 ^oC in nitrogen pressure (10^{-3} torr), the InN samples did not decompose. The stability of InN films can be achieved by thermal disassociation of N_2. Trainor and Rose found the fundamental band edge for InN films to be 1.7 eV and their absorption study suggested that InN is a direct band gap semiconductor due to the similarity in the shape of fundamental absorption edge to that of GaN. InN samples grown on sapphire by reactive evaporation had a Hall effect mobility of 20 cm^2/Vs and carrier concentration in the 10^{20} cm^{-3} range. Trainor and Rose also suggested that higher quality films could be achieved by growing the films at higher temperatures (~600 ^oC) and lower growth rates. Hovel and Cuomo[18] produced polycrystalline InN films grown on sapphire and silicon substrates with some reasonably good electrical properties (Hall mobility μ=250 ± 50 cm^2/Vs, and n-type carrier concentration 5.8×10^{18} cm^{-3}) by reactive radio frequency (RF) sputtering. The InN films appeared dark red and possessed a resistivity in the range of (3-5) 10^{-3} Ω-cm. Marasina et al[19] utilized chemical vapor deposition to produce InN epitaxial layers with an electron concentration of $2\cdot10^{20}$-$8\cdot10^{21}cm^{-3}$ and a mobility of 50-30 cm^2/Vs. They reported that the disassociation of InN rapidly occurred at 600 ^oC, and there was no deposition of InN layers above 670 ^oC.

In the 1980`s the properties of InN films grown via metallic Indium in a nitrogen environment were mainly studied by Tansley and Folley, who reported an electron mobility as high as 5000 cm^2/Vs[20] and a low background carrier concentration in the InN film ($5\times10^{16}cm^{-3}$) . Those results were early indicators of the potential of InN for high mobility FET devices. However, the optical absorption data of InN samples prepared by reactive RF sputtering indicate an optical absorption edge at 1.89 eV.

Recently epitaxial single-phase InN films have been grown on (0001) sapphire in the temperature range of 400-600^oC by microwave-excited metal organic vapor phase epitaxy (MOVPE)[21] using $(CH_3)_3In$ and pure atomic nitrogen or excited nitrogen species supplied by microwave discharge of N_2. It was shown that (0002) InN layers could be grown on (0001) sapphire at temperatures around 500 ^oC.

More recent publications, mostly describing molecular beam epitaxy (MBE) InN layers, indicate a lower energy band gap, initially reported at around 1.1 eV [5] (Mg-doped InN samples), but later at progressively lower values of 0.9 eV[22], then 0.8-0.7 eV[6,23]. Recently, a band gap value 0.65 of eV[24] has been proposed. These studies include growth by MOVPE and MBE on different substrates and underlying layers over a wide range of growth conditions. The highest mobility and lowest background concentration are 2000 cm^2/Vs and $3.6X10^{17}cm^{-3}$[(25)] for thick InN layers (~1.2 μm) grown by MBE[26]. The first growth of InN at high pressures was made by Dietz *et al* [10] in a High Pressure Chemical Vapor Deposition (HPCVD) system developed at Georgia State University.

1.3 InN: A member of the group III-Nitride system

Relevant questions that should be answered in choosing any particular material system over another are:

- What are the advantages of a new material system compared to existing material systems?
- What are potential new application areas?
- What are the costs and expected market value?

The answers to these particular questions will be examined in the following sections.

1.3.1 Importance of InN

The importance of InN can be examined by comparing their basic material properties with conventional semi conducting material systems such as Si, GaAs, and other wide band gap materials such as GaN, AlN and SiC. Furthermore, important potential applications for InN based devices can be investigated as compared to currently available devices.

1.3.1.1 InN physical properties

The history of InN is closely related to that of GaN. It has been over a decade since the first blue/UV light emitting diodes (LED) composed of GaN came in to the market. GaN is now the second most important semiconductor material after Silicon. The value of the worldwide GaN device market, which is at present $3.5 billion, is estimated to be $7.2 billion by the year 2009[27]. III-V materials are now being investigated for their applicability in high power, high frequency applications which currently rely on vacuum tube technology. Group III-Nitride materials show great promise for the development of device structures for short wavelength light emission, which can be used in full color displays, high density optical information storage media and blue laser diode structures[28]. In addition, high-frequency transistors operating at high powers and temperatures for turbine engine sensors, automotive technology and chemical sensing in corrosive

environments can be realized with group III-Nitride material systems. Generally to achieve high currents and high frequency operation, high charge carrier mobility (μ) and high saturation velocity (ν_{sat}) are desirable. InN is predicted to have the lowest effective electron mass among all the nitride semiconductors[29]. The value is about half that of GaN (See Table 1.1). This would result in a high mobility and high saturation velocity for the electrons[1].

InN exhibits favorable electron transport characteristics compared to other III-Nitrides and III-V groups over a wide temperature range from 150 to 500 K based on the theoretical calculations by O'Leary *et al.*[30]. These authors predict that the peak drift velocity at room temperature in InN is 6×10^{7} cm s^{-1} for an applied electric field strength of 22.5 kV/cm. A more recent comprehensive report by O'Leary *et al*[31] studied how the transient electron transport that occurs in InN based devices has an extremely high speed with a cut off frequency of 2.5 THz for 0.1μm thick sample. This study indicates that InN based HFET (High Field Effect Transistors) can operate at higher microwave frequencies. For all cases a crystal temperature of 300 K and a doping concentration of 10^{17} cm^{-3} have been assumed. Meanwhile, Polyakov *et al.*[32] calculated a maximum low-field electron mobility of 14000 cm^{2}/Vs for low doped, uncompensated, dislocation free InN material at room temperature. These results suggest that InN has distinct advantages in high frequency centimeter and millimeter wave devices.

Table 1.1 Material properties of III-V wide band gap and conventional semiconductors Errors are within the bracket. a[1], b[2], c[6], d[22], e[23], f[24],g[29], h[33], i[34],j[35], k[36],l, m[30], n[37],o[38],p[39],r[8].

Parameters	InN	GaN	AlN	SiC	GaAs
Lattice Constant, a_0(Å)	3.5377 (±0.006)	3.189[(g)]	3.11	3.07	
Lattice constant, c_0 (Å)	5.7037 (±0.01) [(b)]	5.185[(g)]	4.98	10.053	5.65325
Effective mass (m_0)	0.09(±0.02)[(h)]	0.2[(i)]	0.48[(i)]	0.68	0.063
Mobility (cm^2/Vs)					
Theoretical	4400[(i)]	1000 [(i)]	300[(i)]		
Experimental	3500[(j)]	900[(k)]	NA	700	8500
Peak drift velocity (cm/s)	5×10^{7} [(l)]	3.1×10^{7} [(l)]	1.7×10^{7} [a]	2.0×10^{7}	1.0×10^{7}
Dielectric Constant (High frequency)	8.4[(a)] 5.8 [(n)] 6.7 [(r)]	5.3	4.77[(g)]	6.7	10.89
Band Gap (eV)	1.89[(o)] 0.9 [(d)] 0.8 [(e)] 0.7[(c)] 0.65[(f)]	3.47[(p)]	6.2	3.26	1.43

Until 2002 the most commonly quoted[38] band gap value for InN at room temperature was 1.89 eV. However, most of the fundamental properties related to InN are poorly understood, and, a sample of the material still contains a large concentration of defects and dislocations, which limit its application for optical devices. LED's, laser diodes, and transistors typically involve InGaN with low In fractions. However, there will be great advantages if a large fraction of Indium can be incorporated in a ternary InGaN compound. One such advantage would be the ability to emit red light from such devices. If the InGaN heterostructures can be grown with every fraction of indium, red, green, and blue LED's could be created with variations of the same material, making them practical to manufacture. Eventually it may be possible to arrange such LEDs into the pixels of full color displays that are brighter, more efficient, and better looking than today's flat-panel LCD displays. In addition, use of InN-based materials could lead to photonic devices in the red light regime and much faster electronic devices, due to the before-mentioned higher mobility and peak velocity than those of other III-Nitride materials. InN-based optoelectronic devices offer an environmental-friendly emitter with no toxic element, which may replace GaAs-based devices.

The direct band gap of $(Ga_{1-y-x}Al_yIn_x)N$ alloy systems can be continuously tuned from 1.0 eV to 6 eV. This single ternary alloy system will introduce the possibility of single or Multi-Junction (MJ) solar cells for space based applications. It was shown that $In_{1-x}Ga_xN$ retains its optoelectronic properties at radiation damage doses at least 2 orders of magnitude higher than the damage thresholds of the materials (GaAs and GaInP) currently used in high efficiency MJ solar cells[7]. This information indicates that $In_{1-x}Ga_xN$ might be well suited for future ultra-radiation hardened optoelectronics.

Quian *et al*[40]. recently showed that InN thin films are suitable for the application of plasma filters with different carrier concentration, mobility and film thickness. The plasma filters are one of the most effective ways to increase the efficiency in Thermo Photo Voltaic (TPV) systems. InN shows good performance as a plasma filter material for widely employed GaSb or GaInAsSb photovoltaic cells.

1.3.1.2 Status of current InN, In-rich group III-Nitrides and competing alternatives

The material properties of InN change dramatically with the growth techniques employed and the understanding of this novel semiconductor is still very poor. During the last decade there have been several conflicting reports on the band gap of InN; values have varied between 0.6 and 2 eV in different papers[2,33]. Bagayoko and Franklin[41] presented an overview of two groups of experiments that provided different values of the band gap of *w*-InN. Experiments in group I, mostly before 2000, reported band gap values of 1.9–2.0 eV, while the ones in group II found band gap values of 0.7–1.0 eV, depending on the free carrier concentrations. Samples studied by group II, mostly grown by molecular beam epitaxy, were believed to be of much higher quality than those of group I that mostly investigated polycrystalline films. Inushima *et al.*[5] determined the band gap of InN grown on sapphire by MBE was between 0.89 and 1.46 eV at respective electron concentrations of 5×10^{19} cm^{-3} and 2×10^{20} cm^{-3}. Abdulkadir *et al.*[42] studied samples of InN grown by metal-organic vapor phase epitaxy (MOVPE), and they reported that the band gap E_g for the InN samples is ~ 0.7 eV. Recently, the Hydride Vapor Phase Epitaxy (HVPE) growth technique has received attention because it is a useful method for growing thick layers of group III-Nitrides [43-45]. Cathodoluminescence (CL) spectrum measurements of single crystalline (0002) InN grown by HVPE exhibits a

strong peak at 0.75 eV[46]. In conclusion, InN films grown by Molecular Beam Epitaxy[22,47] (MBE), HVPE and MOVPE[48] revealed the band gap energy of InN is about ~0.7 eV.

Until recently, the band gap energy of ~0.7 eV was considered the fundamental narrow band gap due to measurements by infrared photoluminescence (PL) and optical absorption of InN grown by MBE, MOCVD, and HVPE. However, the growth of high quality InN layers and related indium rich III-N alloys remains difficult due to InN stoichiometric instabilities, limited carrier concentration and low disassociation temperatures, leading to inconsistent and process dependent material properties[9]. Nevertheless, Butcher *et al.*[49] has shown that In:N stoichiometry effects the apparent band gap of the InN film very strongly, and evaluation of stoichiometry variations in InN films (MBE grown and Remote Plasma Assisted Chemical vapor deposition (RPECVD)) suggests these films should not to be treated as homogenous materials. For instance, the electron carrier concentration dependence of the optical absorption edge for epitaxial material does not follow the Moss-Burstein effect[12,50] for InN samples grown by different techniques. Figure 1.2 shows the apparent change in the band gap of InN materials grown by different techniques. The solid curve shown in Figure 1.3 is proposed by Walukiewicz *et al.*[7] to describe the differences in the measured band gap with an alternate model. It is clearly shown in Figure 1.2 that the Moss-Burstein model cannot explain those data points below 10^{19} cm^{-3}, which have high optical absorption edge values above 1.5 eV. Figure 1.3 shows variation of the apparent absorption edge for single crystalline InN films grown by HPCVD.

The growth of GaN (0001) and AlN (0001) is quite well established and those samples exhibit both high crystalline quality and smooth surfaces.

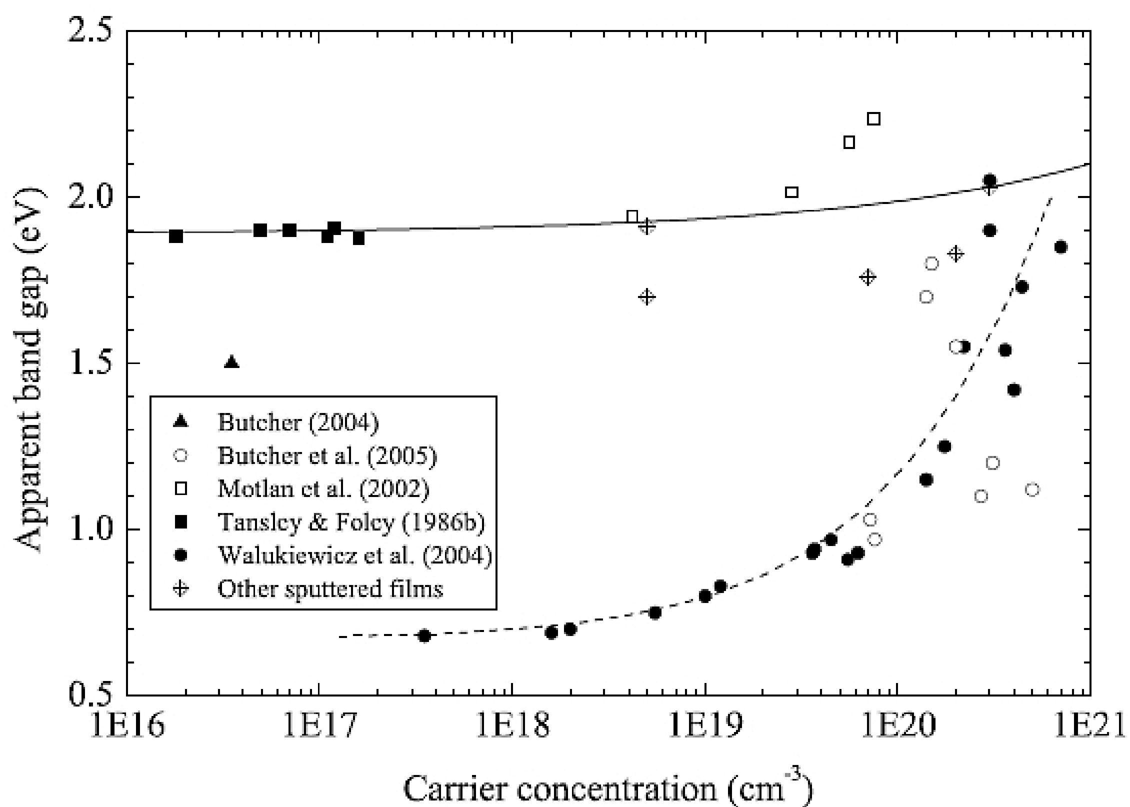

Figure 1. 2. Apparent band gap of InN films as a function carrier of concentration. The solid curve represents the theoretical Moss-Burstein effects proposed by Walukewicz *et al*[7]. There is a considerable spread of data for material nominally referred to as InN (From ref. 50).

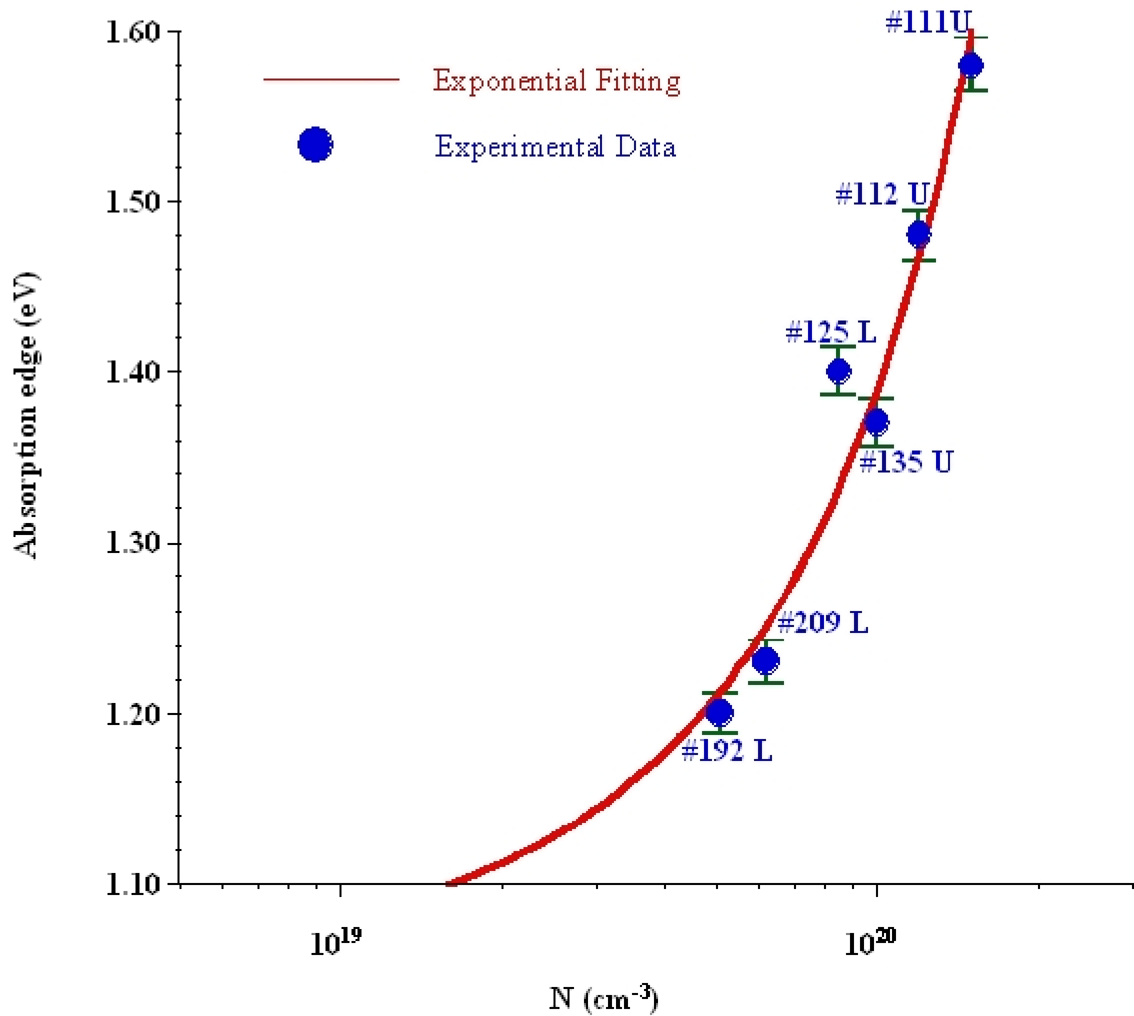

Figure 1. 3 Apparent absorption edge of InN films grown by HPCVD at GSU as a function carrier concentration.

However, it is not easy to adopt this growth mode for InN (0001), which disassociates at temperatures lower than those required for desorption of In[51] and high vapor pressure of nitrogen. The growth of group III-Nitrides via MBE or CVD is limited to the low processing temperatures (usually ≤ 600 °C). Low growth temperature requires the application of extremely high V-III ratios in order to avoid the formation of In metal droplets[9]. Growth of corresponding high-quality N-face $In_xGa_{1-x}N$ alloys with high In (0.5≤x≤0.89) content has been demonstrated by several groups[52,53]. One goal of the

recent study is to identify the nature of radiative recombination in $In_xGa_{1-x}N$ with high In content[52]. Naoi *et al.* conclude that band-to-band recombination processes are responsible for PL emission not the localized state emission. However those samples[54] were grown between 480 and 600 °C with free electron densities of 3×10^{19} cm^{-3} to 1×10^{18} cm^{-3}. Nevertheless, experimental growth parameters such as temperature conflicts with low dissociation temperature of InN (550 °C, 630 °C[4]). In order to realize InN-based photonic devices and overcome the difficulty of the high thermal decomposition pressure of InN, a break through idea is necessary for reducing defect density and improving the quality of InN based III-Nitride alloys[1,3]. In order to grow InN at higher temperatures and higher pressures a High-Pressure Chemical Vapor Deposition was implemented at GSU[9,10,12].

1.3.2 Application areas

The unique properties of group III-nitride compound semiconductors, e.g. AlN, GaN, InN and their alloys, inspired many advanced device designs/structures, integrating electrical, optical, and magnetic functionalities. Ultimately, the usefulness of indium nitride and group III-Nitride alloys depends on the determination of the band gap. A higher band gap preferred for microwave transistor devices, a smaller band gap is preferable for a full solar spectrum cell based on InGaN applications.

1.3.2.1 Optical applications

Electronic lightning technology become important with the invention[55] of first light emitting diode LEDs in 1962. Following the achievement of LED technology, light amplification by stimulated emission (LASER) was demonstrated[56,57] in a semiconductor by 4 groups. Development of semiconductors allowed the production of bright light emitters that are used in optical fiber networks, data storage (Compact-Disc Technology),

and document printing (Laser printers). But LEDs based on GaAs operate only in the red to yellow portion of the spectrum. SiC has been used for the fabrication of blue LEDs. However SiC or II-VI based LEDs were not emitting with enough intensity due to their indirect band gap. The first blue LEDs based on the III-V nitrides were made commercially available by Nichia in early 1994. Much research has been done on III-Nitrides comprising the Al-Ga-In-N alloys and show great promise for meeting the next generation optical applications.

1.3.2.2 LED applications

InN is important as a component of group III-Nitrides $(Ga_{1-y-x}Al_y In_x)N$ enabling the fabrication of high-efficient light emitting diodes in a wide spectral region, depending on the composition at room temperature. As shown in Figure 1.4, $(Ga_{1-y-x}Al_y In_x)N$ alloys system span a wide range of band gap energies from 1 eV to 6.2 eV which correspond to wavelengths ranging from near infrared to deep ultraviolet. In addition, the band gap of the Group III-N system is direct, leading to high quantum efficiency and faster switching speeds. Nakamura and his colleagues demonstrated the first blue/green light emitting diode based on InGaN. The structure consisted of a 3 nm layer $In_{0.2}Ga_{0.8}N$ sandwiched between p-type AlGaN and n-type GaN, all grown on sapphire substrate[58]. Achieving a red light emitting diode based on InGaN structures depends on indium rich InGaN heterostructures. White LEDs have been developed recently by coating GaN LED with phosphorus[59] which produces light that appears white. However this structure is not as efficient as the commercial fluorescent light sources. Combining red light emitting diodes with blue/green ones having the same power and brightness can produce full color displays and efficient white lamps.

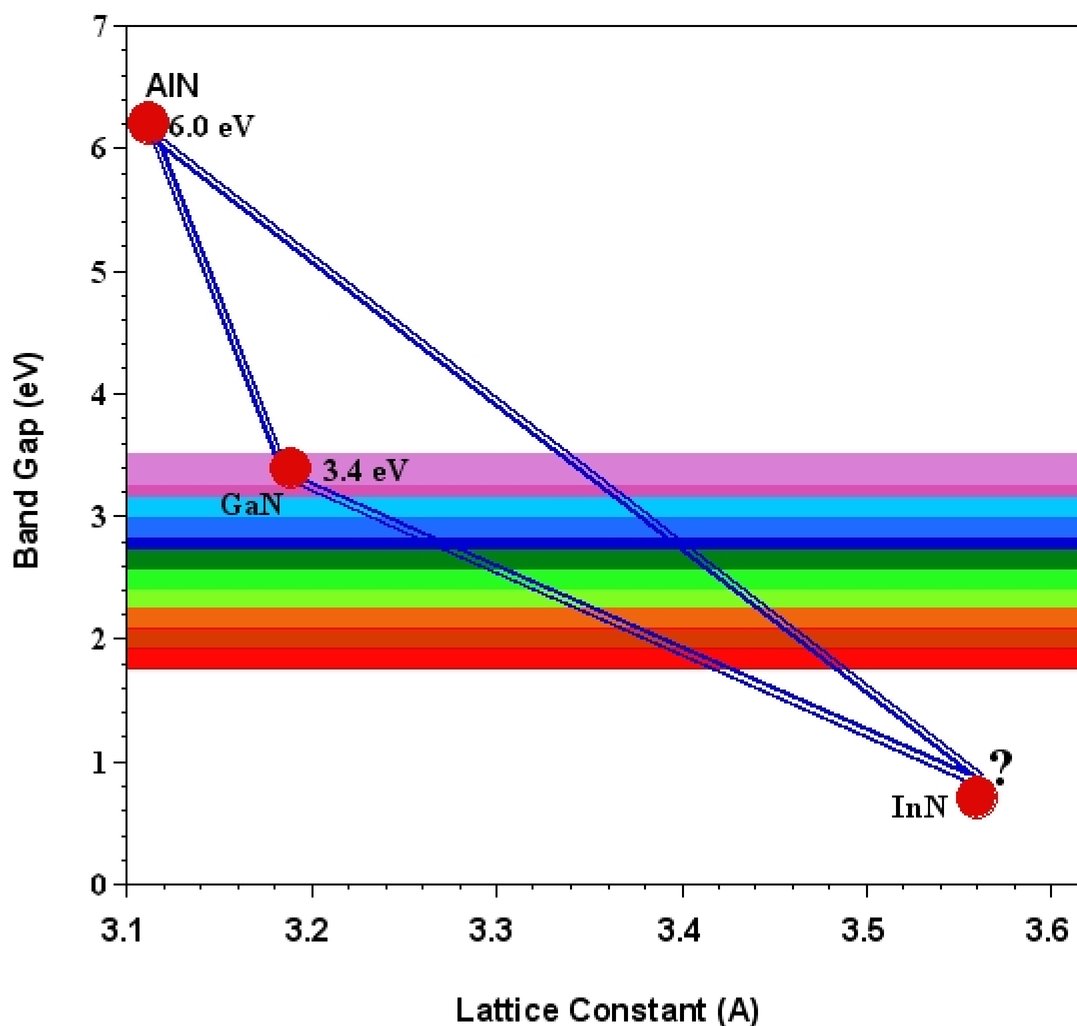

Figure 1. 4 Band gap energy vs. lattice constant for binary group III-Nitrides material systems.

Researchers at IBM[60] demonstrated an InN nanowire LED, which emits infrared light. The nanowires emit infrared light, which makes them ideal for optical communications between devices on microchips that would speed up the computers drastically. If the mechanism in InN nanowires can be tuned to emit red, green and blue light, all nanowire LEDs could be manufactured on the same substrate. That could make LEDS even cheaper and lead to the devices with improved performance.

1.3.2.3 Laser applications

Fabrication of high quality of LEDs enables the fabrication of semiconductor lasers that operate at light wavelengths from ultraviolet to the green. The advantage of blue GaN/InGaN lasers with shorter wavelength (405 nm) than a red laser (605 nm) allows five times more storage capacity (25 GB) over traditional DVDs. Blu-ray disc technology was recently adopted by a group of world leading consumer electronics (including Apple, Dell, HP, JVC, LG, Mitsubishi, Samsung, Sharp, Philips, Pioneer and Sony Corp.) which enable recording and rewriting[61]. The impressive accomplishments taking place and opening a variety of potential markets such as blu-ray are only the beginning of the application of this technology. The performance issues that are related to the crystal growth itself limit further development. It is possible to mix the Al, Ga, and In ratios to make ternary and quaternary alloys such as $(Ga_{1-y-x}Al_y In_x)$ N. It is therefore possible, in principle, to make semiconductor lasers that emit light from the deep ultraviolet with a photon energy of 6 eV, to the infrared with photon energy of 1 eV. However, only a much narrower range of operation from the near ultraviolet (3.5 eV) to the green (2.4 eV) has been demonstrated.

InN one dimensional (1D) nanostructures, such as nanowires, nanorods, nanotubes and nanobelts are currently the most attractive structures due to the easier growth in single crystal forms without defects, and lasing in the crystals could be expected[62]. Hu *et al.*[62] reported the investigation of infrared lasing in high quality single-crystalline InN nanobelts grown by MOCVD. This can be considered a “major advance “ in the nanophotonics field and will impact imaging in chemistry biology, and optical communications.

1.3.2.4 Electronic applications

Small effective electron mass, large polar optical phonon energy[31], high electron mobilities close to the theoretical calculated mobility values[32] make InN a promising device for electronic applications. Nevertheless, theoretical calculations by O'Leary *et al.*[30,31,63] also suggest that InN has superior electrical properties compared to GaN. As shown in Figure 1.5, InN achieves the highest steady-state peak drift velocity $\sim 5\times10^7$ cms^{-1} which is considerably larger than that of other III-Nitrides and of GaAs. The calculated electron mobility of InN by Chin *et al.* [34] is 4400 cm^2/Vs for room temperature. The highest electron mobility measured at room temperature is 3500 cm^2/Vs[35]. Thus, InN based devices offer great potential for high-speed, high performance heterojunction FETs as compared to GaAs based HFETs for both power and frequency response. Wide band gaps enable the application of high supply voltages and also allow the material to withstand high operating temperatures (300° C and 500° C). AlInN might be a good candidate[64]for high-power/high temperature microwave applications because of its higher breakdown voltage.

The current state of the solar cell with 30% percent efficiency are produced from the following materials: Ge (0.66 eV), GaAs (1.43 eV) and GaInP (1.9 eV)[65,66]. For the specific case of $In_{1-x}Ga_xN$ varying x values ($x\leq 0.63$) produces band gaps between 0.7 and 1.9 eV which will cover the whole solar spectrum from infrared to UV. The possibility of designing and fabricating multi-junction solar cells using a single ternary alloy system is attractive. Since space based systems represent the primary application of MJ solar cells, radiation resistance is crucial. It has been shown that InN and InGaN are 2 times more resistant under extraordinary particle radiation[67].

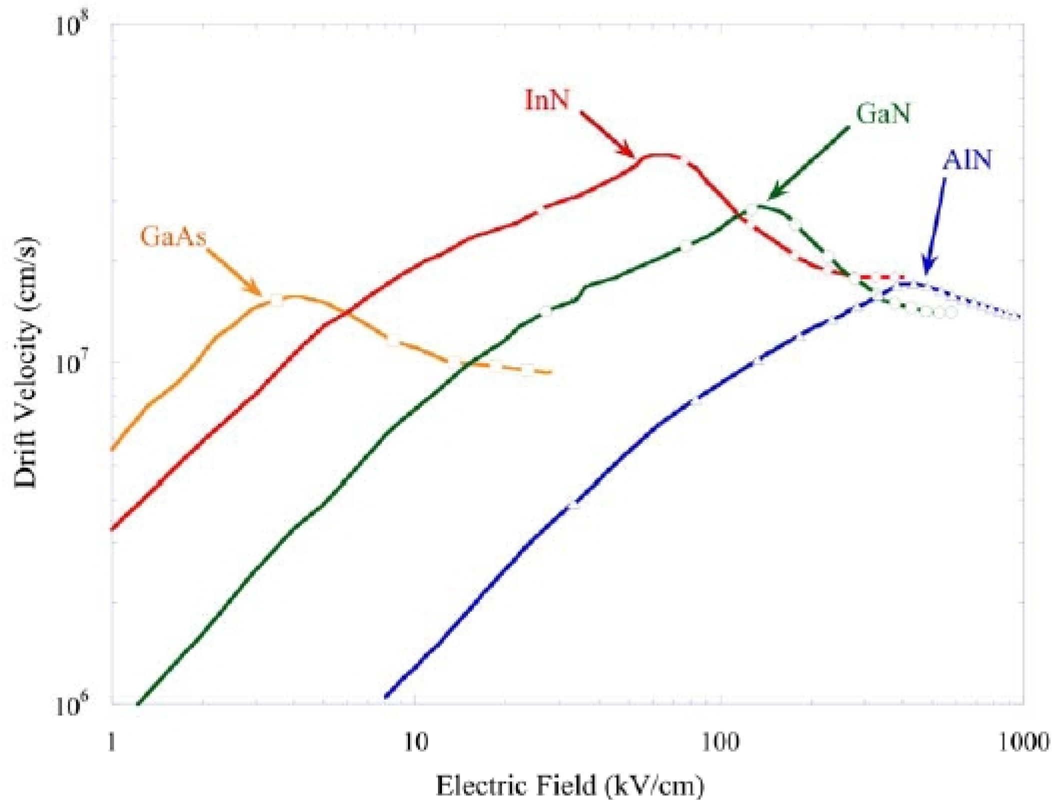

Figure 1. 5 Calculated steady-state drift velocity as function of electric field in group III-Nitride materials and GaAs. In all cases, O'Leary *et al.*[30] assumed a doping concentration of 10^{17} cm^{-3} and crystal temperature of 300 K.

1.4 State of the art for InN based THz applications

The terahertz region of the electromagnetic spectrum lies between 300 GHz and 30 THz, corresponding to the sub-millimeter wavelength range between 1 mm and 10 µm. There are many applications, which require operation in the terahertz region such as:

- Terahertz imaging in medicine and biology could allow monitoring of receptor binding, tumor recognition, recognition of protein structural states, performing label free DNA sequencing, detection of epithelial cancer, and radiation effects on biological samples[68] since THz radiation is not expected to damage tissues and DNA, unlike X-rays. Damage to cells or tissue is limited because of the energy levels are very low (1-12 meV)[68].

- Millimeter/submilimeter wavelength astronomy, which is crucial to understand the formation of the universe by exploring features in the far-IR. In addition, many spectral signatures, namely thermal emission lines from gases that exist in Earth's atmosphere are in the sub-millimeter range between 300- 2500 GHz. Reaction rates of those species contain information about global warming, total radiation balance and air pollution[69]. Furthermore, space applications including asteroid, moon and comet observations require terahertz sensors. [69].
- Terahertz detectors can be used for detecting voids in fabrics and plastics, and can be used in security screening of plastic explosives.

There are two major components technologies for terahertz applications: sensor and sources (emitter, generators etc.). However, the main challenge in terahertz applications is the lack of suitable both terahertz sources and detectors. Detectors that are used in this region are bolometer, pyroelectric detectors, and heterodyne detectors. However, those detectors show slow response, are generally built for low temperatures (~4.2 K) and it is difficult to integrate these detectors into focal plane arrays for imaging. Photon detectors based on semiconductors work in near infrared region ($\lambda \geq 0.8$ μm) to the long wavelength region (30 μm). Detectors based on free carriers are good candidates for far infrared/terahertz detection. Perera *et. al*[70,71]. worked on p-type GaAs /AlGaAs detectors utilizing heterojunction internal workfunction photoemission (HEIWIP) approach. HEIWIP p-type detectors have been demonstrated with the tailoring threshold frequency limit around 3.2 THz (~93 μm) [72]. The Al fraction used for the 3.2 THz threshold detectors is 0.005 and close to the lower limit for MBE growth. The Al Fraction is decreased for lowering the

workfunction further but it may not be possible since the Fermi level will not reach the required level before GaAs becomes metallic as p-doping increases. Therefore, lowering the work function is not possible in p-type HEIWIP GaAs/AlGaAs devices. One potential way to extend terahertz detection beyond the 3.2 THz is to utilize the properties of InN and indium-rich InGaN alloys and heterostructures. These may lead to more advanced THz detector and emitter[73,74] devices, operating at temperatures higher than 77K and having higher sensitivity. The free carrier absorption coefficient and light absorption in n- type doped 1 μm thick InN layer grown on sapphire with carrier concentrations 5×10^{17} cm^{-3}, 1×10^{18} cm^{-3}, and 2×10^{18} cm^{-3} is shown in Fig. 1.7. The inset in Fig. 1.7 shows the optimum calculated absorption coefficient which occurs around 1×10^{18} cm^{-3}. Furthermore, the ferromagnetic behavior of transition metal doped indium rich InGaN may enable unique enhancements of the absorption rates and hence the photo response under an applied magnetic field.

Studies[73-77] on InN show it to be a good material for optically excited THz emission. Monte Carlo simulations of InN, GaN and AlN showed that high frequency power generation in a constant electric field occurs for the whole sub millimeter range (0.25 THz-4 THz) around the liquid nitrogen temperature[75]. The possibility of THz radiation generated from InN films was observed by Ascazubi *et al.*[77]. From this study they concluded that if the carrier concentration of InN films can be reduced by an order of magnitude, InN will surpass InAs as the most efficient semiconductor THz emitter[77]. Chern *et al.*[73] also concluded that power generated from InN films will improve with low carrier concentration. However, the material quality of InN is presently delaying final conclusions about THz generation and sensing in InN films.

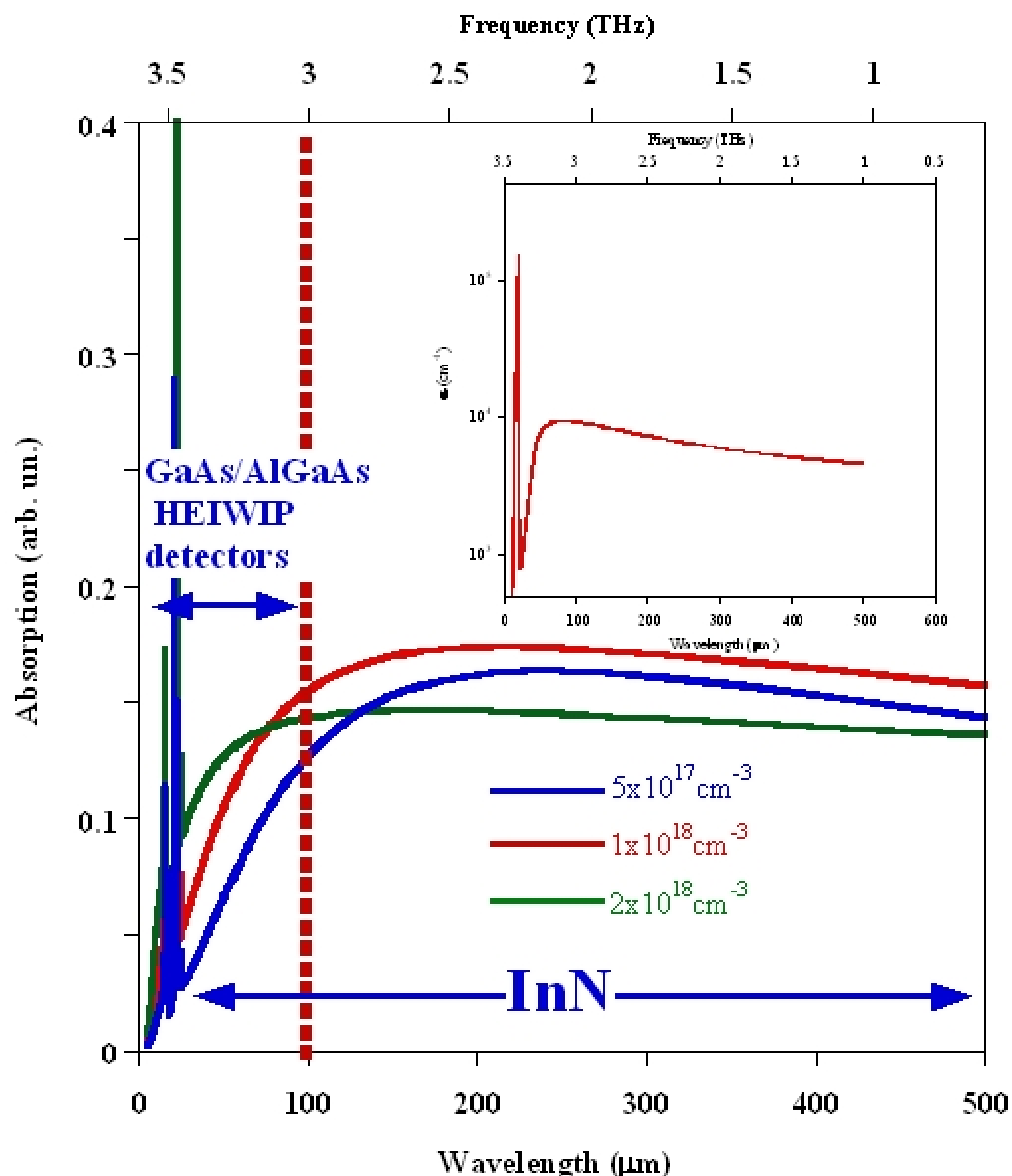

Figure 1. 6 Free carrier absorption is calculated for different carrier concentration in a 1 μm n-type InN layer grown on sapphire. The calculated absorption coefficient of InN with a doping of 1×10^{18} cm^{-3} is shown in the inset. The free carrier concentration stays constant below 3 THz.

1.4 Objectives of this research

The aim of this research is the optimization of the structural, electrical and optical properties of InN utilizing a unique growth process, ***high-pressure chemical vapor deposition (HPCVD).*** During the last 3 years, my research focused on the characterization and optimization of the HPCVD system as well as on the growth of InN epilayers and their characterization. We have demonstrated that the HPCVD approach suppresses the thermal decomposition of InN, enabling the growth of InN at temperatures up to 1100K[12]. The higher growth temperature improves the crystalline quality and brings the growth processing window close to that used for GaInN, which enables the growth of indium-rich group III-Nitrides integrated with GaInN. Our recent results on the structural and optical properties of InN grown by HPCVD revealed good quality single crystal InN epilayers with FWHM 200 arcsec, carrier mobility 400 $cm^2V^{-1}s^{-1}$ and optical band gap is around 1.2 eV[78]. At present the free carrier concentrations are still in the low 10^{18} cm^{-3}, the origin of which is being studied at present. A further reduction in external contamination such as residual oxygen is also investigated. Also, studies are under way in order to find a correlation between the surface morphology and structural properties of InN. For InN samples presented in this study, we have optimized the growth parameter with respect to growth temperature, gas flow velocity, group III:V precursor ratio, and evaluated the optical and structural properties as a function of free carrier concentration and V/III molar ratio.

The most significant results of my research are the demonstration that HPCVD is a viable approach to stabilize high-quality InN layers at growth temperatures around 1100K at reactor pressures around 15 bar. With this, the integration of indium-rich

$In_xGa_{1-x}N$ epilayers into $Ga_{1-x}Al_xN$ device structures will be possible for the future studies of HPCVD growth. However, many process parameters still have to be optimized and the physical properties of InN to be evaluated, before a pathway for truly multifunctional device structures based on AlN-GaN-InN alloys can be established.

Chapter 2

This chapter will begin with a brief overview of the InN material system with a description of its crystal structure following. The effects of various growth techniques on the properties of InN films will be presented, with emphasis on the most popular growth techniques such as Metal Organic Chemical Vapor Deposition (MOCVD), Molecular Beam Epitaxy (MBE), and Hyride Vapor Phase Epitaxy (HVPE). Finally, an explanation of the major challenges present in the growth InN and In-rich group III- Nitride material system will be discussed.

2.1 InN material system

2.1.1 InN crystal structure

Single crystal group III nitrides AlN, GaN and InN crystallize in three structures: wurtzite (hexagonal), zincblende (cubic), and rock salt. The hexagonal wurtzite structure of InN is the thermodynamically stable phase in contrast to cubic III-V semiconductors such as GaAs and InP which possess zincblende structure[79]. The edge length $\boldsymbol{a_0}$ of the basal hexagon, the height $\boldsymbol{c_0}$ of the hexagonal prism and internal parameter anion-cation bond length along the (0001) axis $\boldsymbol{u_0}$ defines the crystal structure of Group III-nitrides[79] as shown in Figure 2.1. The lattice constants for single and poly-crystalline InN films grown on sapphire substrates or GaN epilayers by either MBE or OMCVD technique are found to be in the range of a_0=3.501-3.536 Å and c_0=5.69-5.705 Å[1]. u_0 for hexagonal InN films is found to be 0.377[79] Å.

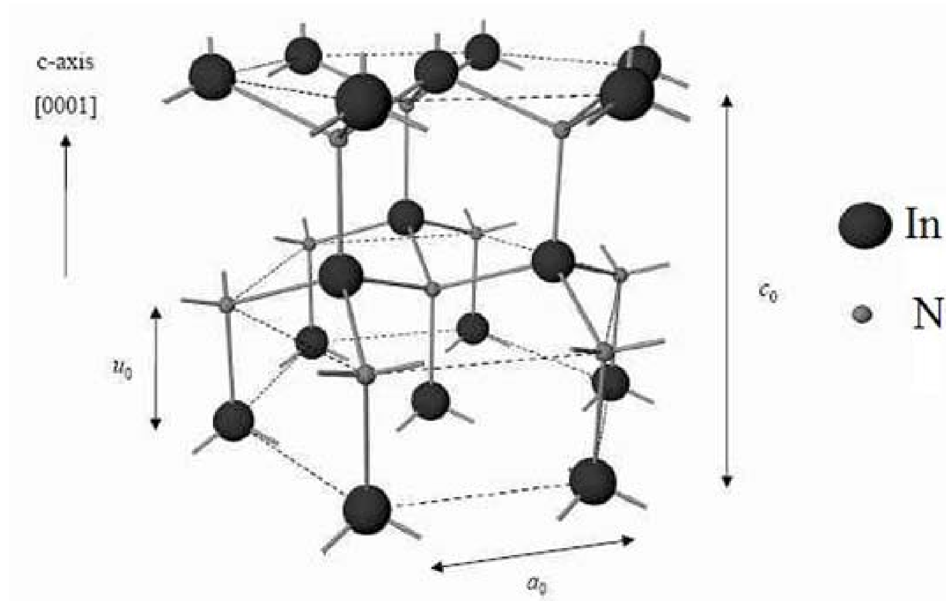

Figure 2. 1: Atomic arrangement in wurtzite InN crystals.

In an ideal wurtzite crystal the c_0 / a_0 ratio equals $\frac{\sqrt{8}}{\sqrt{3}} = 1.633$ and the value for u_0 is 0.375[80]. The possible reason for the variation of the bond lengths and the resultant c_0 / a_0 ratios in crystalline quality is due to the incorporation of external contamination. The most common growth direction of hexagonal InN is normal to the basal plane[81].The InN layers consist of different atoms that have a stacking sequence of bi-layers ABAB consisting of two closely interpenetrating hexagonal close-packed lattices[79].

Two interpenetrating face centered cubic lattices describe the zincblende structure. Zincblende structure has four nearest neighbors all with the same bond length. The lattice constant for cubic InN is a=4.986 Å. Recent studies shows that InN grown directly on r-plane sapphire substrates consists of a predominant zincblende structure along with a fraction in the wurtzite phase[82]. This meta-stable crystal structure is schematically depicted in Figure 2.3

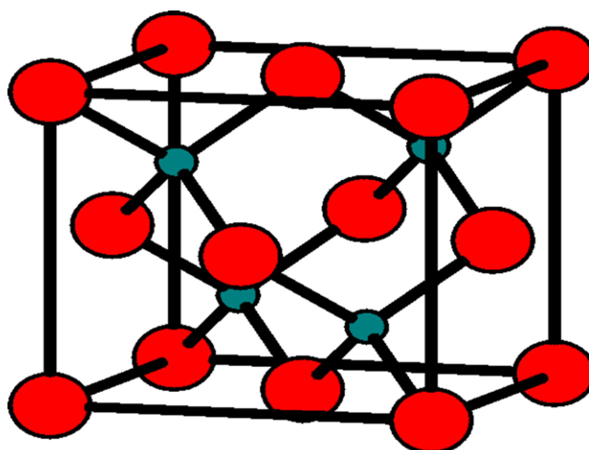

Figure 2. 2 Cubic zincblende structure of InN. Red spheres indium atoms and gray spheres represent nitrogen atoms.

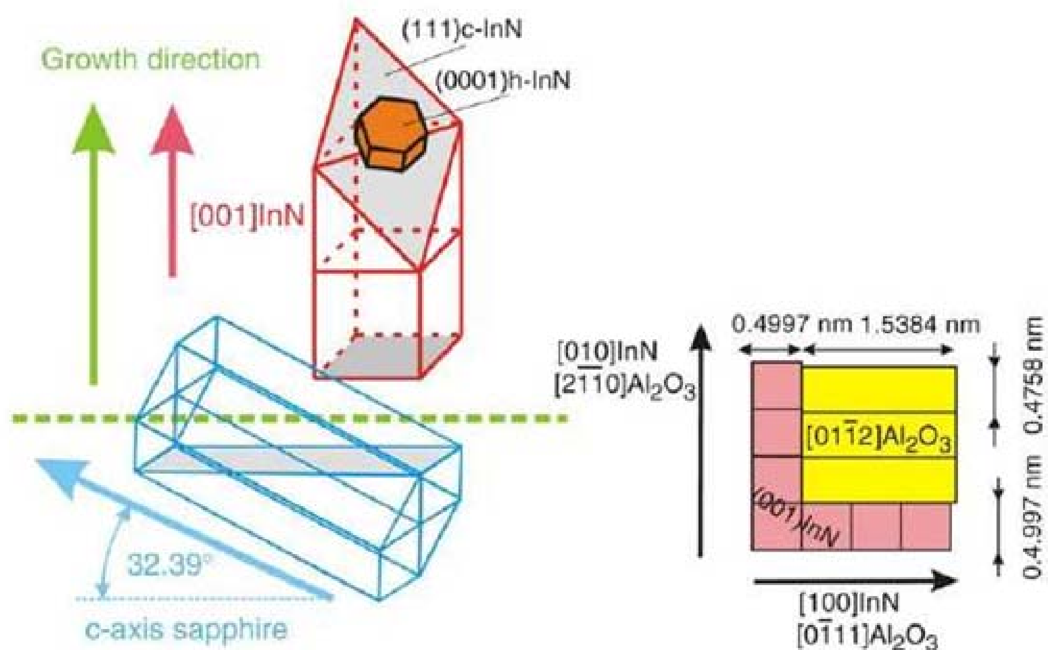

Figure 2. 3 The epitaxial relationship between the sapphire substrate, the zincblende and the wurtzite.

2.1.2 Fluctuation in the structural properties obtained

Materials properties such as crystalline quality, lattice parameters and carrier concentration of InN layers can be affected by the growth technique utilized. InN layers are traditionally grown at reduced processing temperatures due to the low dissociation temperature of InN and high equilibrium N_2 vapor pressure, as shown in Table 2.1. Therefore, the temperature-processing window for the growth of InN is very narrow for MOCVD, MBE and HVPE (450-600ºC) growth techniques. However, these growth techniques do not provide a close match to the optimal processing window of $In_xGa_{1-x}N$ heterostructures. In addition, MOCVD growth of InN is typically performed with elevated V/III ratios, which prevent InN disassociation, but also limit the cracking efficiency of N_2 or NH_3.

Table2. 1: Growth parameters, lattice constants, and crystalline quality of different InN samples grown by different methods.

N (cm^{-3})	T (°C)	E_g(eV)	a (Å)	c (Å)	V/III Molar ratio	Mobility (cm^2/Vs)	FWHM of (0002) arcsec	Growth Method
1×10^{19}	530	.7			18500	200	504	MOVPE[81]
3×10^{19}	500	0.75				890	792	HVPE[46]
1×10^{20}	500	1.44	3.542	5.720		105	400	HVPE[83]
1×10^{20}	550	0.85	3.550	5.700	30000	200	1700	MOVPE[84]
3.5×10^{17}	470	0.69	3.538	5.700		2050	250	MBE[7]
6×10^{18}	475	0.7	3.530	5.700		1900	300	PAMBE-MOMBE[22]
5×10^{18}	450	0.75	3.530				240	RF-MBE[23]
5×10^{19}	806	1.2	3.560	5.700	800	225	290	HPCVD[12]
7×10^{18}	600	0.75	3.540	5.700	10000		540	OMCVD[85]
1.8×10^{18}	480	0.64	3.530	5.700		1250		PAMBE[86]

The material quality of OMCVD, HPCVD and HVPE grown InN films is close to that for MBE grown InN samples as shown in Figure 2.4 (observed in terms of narrower

Full Width at Half Maximum (FWHM) of the X-ray diffraction rocking curve). InN films have a perfect crystalline structure with narrower rocking curve width. Both InN films grown by different techniques are single-phase films. Figure 2.5 shows a collection of band gap (E_g) data, and the data for lattice constant *c* and *a* axis. The *c* values obtained for different InN films grown with different techniques are relatively close, whereas the *a* values obtained from various literature sources are slightly scattered.

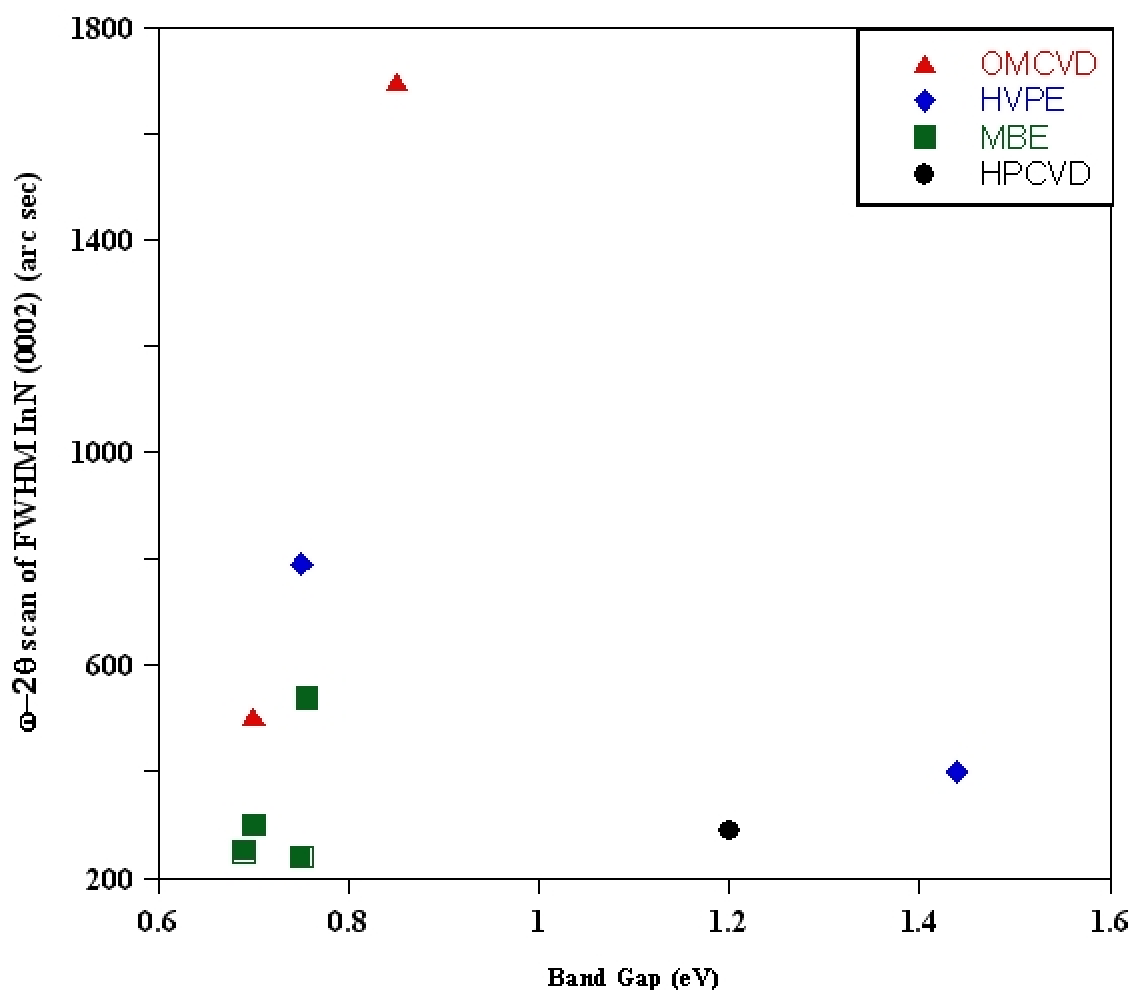

Figure 2. 4 Relationship between the FWHM of X-ray of InN (0002) grown with different techniques and the optical band gap energy.

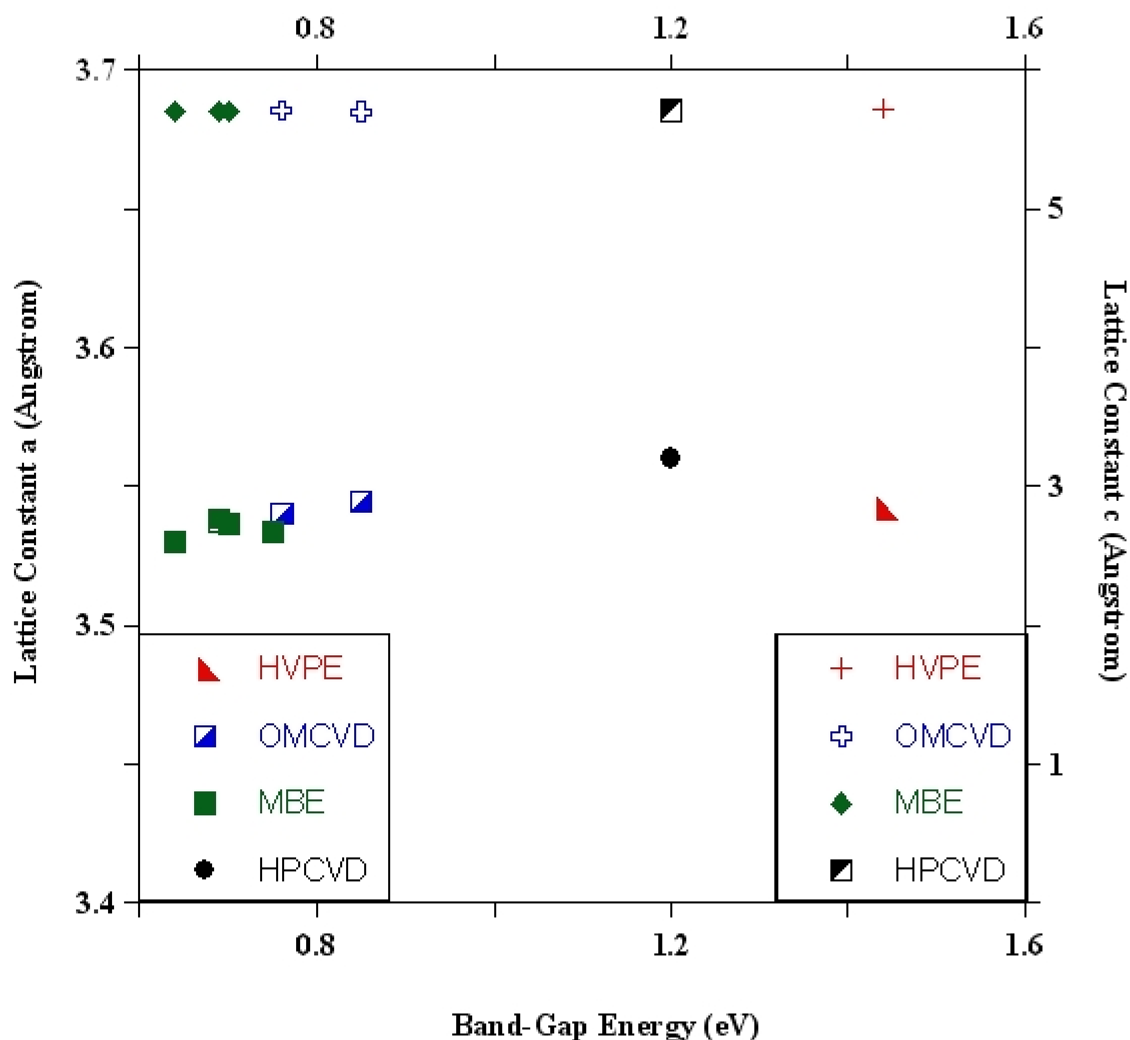

Figure 2. 5 Dependence of the lattice constants *a* and *c* on the optical band gap energy.

2.2 Current growth methods used for growth of InN and In rich group III-nitrides

As outlined in previous chapter, InN layers are grown at reduced temperatures due to the low InN disassociation temperature and high equilibrium N_2 vapor pressure over the InN film. Therefore, the current growth methods for InN and indium rich group III-Nitride materials have been dominated by low temperature growth techniques such as MBE, MOCVD, and HVPE. The following presents the current state of technology

aimed towards the growth of InN and In-rich group III-nitrides, along with appropriate substrates for the epitaxial growth of high quality material systems.

2.2.1 Molecular beam epitaxy (MBE)

The development of MBE systems has been slow due to difficulties associated with Ultra High Vacuum (UHV) Systems, low growth rate, low growth temperature, and a common source of ammonia for nitrides. Because of the low temperatures, the thermal cracking efficiency for NH_3 is greatly reduced. NH_3 and N_2 are used as nitrogen sources during the MBE growth of nitrides. Cracking efficiency and incorporation of ammonia in the GaN layers grown with MBE were investigated at different temperatures[28]. It was found that incorporation of ammonia begins at 450 °C and the incorporation efficiency increases up to 700 °C. The actual efficiency of cracking of ammonia starts at ~ 800 °C. In the case of atomic nitrogen source, the disassociation energy of N_2 is about 9.5 eV, Therefore, the supply of N_2 gas to the substrate surface with the group-III elemental beams cannot induce any growth of nitrides. N_2 molecules are disassociated into atomic reactive nitrogen by radio-frequency (rf) emission or electron cyclotron resonance (ECR). In RF plasma, effective generation of reactive nitrogen requires a small aperture size. In the case of an ECR plasma source, the generation rate of reactive atomic nitrogen increases with increasing input microwave power. However, nitrogen ions with energy higher than ~ 60 eV may induce defects in the epitaxial layer.

Thermodynamic analysis of the MBE growth of III-Nitrides including InN has been reported by Koukitu and Seki[87]. The chemical reaction during the epitaxial growth of InN, which connects the gas phase NH_3 to the species at the substrate surface is given by,

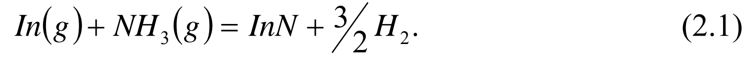

$$In(g) + NH_3(g) = InN + \frac{3}{2} H_2. \qquad (2.1)$$

In the NH_3 case, it is convenient to introduce α, the molar fraction of decomposed NH_3, as follows:

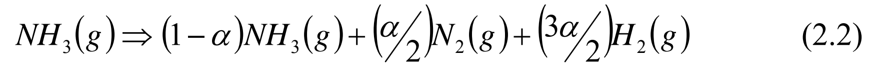

$$NH_3(g) \Rightarrow (1-\alpha)NH_3(g) + \left(\frac{\alpha}{2}\right)N_2(g) + \left(\frac{3\alpha}{2}\right)H_2(g) \qquad (2.2)$$

However, the exact value of α is not known and has been estimated for InN. Koukitu and Seki calculated the phase diagram during deposition to find the suitable growth conditions for the MBE growth of III-Nitrides. They reported that the temperature suitable for the InN MBE growth is from 600 to 700 ºC with V/III ≥1. However, the growth of InN is achieved for the temperature range 450 to 600 °C. As described above, there is 200°C difference between the optimal processing conditions of InN and In-rich InGaN heterostructures.

Growth of good quality InN layers began not long ago, in 2002, Single crystalline hexagonal InN samples were grown and presented by Davydov *et al*[22]. and these samples had a band gap value less than 1.1 eV. Undoped InN layers were grown on the *c* plane sapphire substrates by ECR-plasma assisted MBE[88]. Following this study, *Lu et al*.[89] have grown InN layers using rf - MBE that also provide the band gap energy of InN film below 1 eV. Both of the groups have performed the growth of InN with a turbo molecular pumped MBE chamber with an ultimate background pressure $\sim 10^{-10}$ Torr. Metallic indium was supplied from an effusion cell at different temperatures. An ECR plasma source or EPI unibulk rf plasma source was used for generating atomic reactive nitrogen with different flow rates (0.7 to 5 sccm (standard cubic centimeters per minute)). The nitrogen flux causes a nitrogen partial pressure in the MBE chamber of 1.8×10^{-5} Torr

during growth. To overcome the substrate match problem, various growth initiation techniques were used as introduced in the following;

I. A 2 nm AlN nucleation layer was deposited at 950 °C and the substrate was cooled down slowly to desired InN growth temperature in rf-MBE growth[89].

II. A low temperature (LT) or high temperature (HT) InN buffer layer was first grown, followed by a temperature change to maximize the growth of InN

III. Sapphire wafers were nitrided by nitrogen at higher temperatures (1100 °C) for 3 or 30 minutes for thermal cleaning for both MBE techniques.

IV. A single GaN or LT-InN/ GaN, or AlN/GaN double buffer layers were formed on the substrate.

Application of these steps increases the quality of the InN epilayer, and the surface morphology of the epilayer improves significantly (smoothness of order of 1 nm rms). However, further process optimization needs to be done for high quality InN film production.

2.2.2 Organometallic Chemical Vapor Deposition (OMCVD)

The current market requirements for growing III-Nitride layers are restricting the MBE technique as an industrial growth tool. Today there are organometallic vapor deposition machines (also referred to as metal-organic chemical vapor deposition, vapor phase epitaxy or metal organic vapor phase epitaxy) with high throughput, better uniformity of the layer, and larger wafer areas. The precursors used for the group III component while growing group III nitrides are mainly TMGa (trimethyl Gallium), TEGa (Triethyl Gallium), TMAl, and TMIn. NH_3 is used as group V precursor, which requires a higher growth temperature for group-III Nitrides. However, InN growth is going to be

restricted due to the low growth temperature resulting in a low decomposition rate of NH_3, so a high V/III ratio is needed. The carrier gases N_2 and H_2 crucially determine the group III incorporation efficiency with respect to the role of carrier gas during the growth. Figure 2.6 shows the equilibrium partial pressures over group III-nitrides as functions of the input V/III ratios carried out by Koikutu *et al.* The equilibrium vapor pressure of nitrogen over the InN is several orders higher than that AlN and GaN as shown in Figure 2.6. Therefore, the growth temperature of InN is low due to the low disassociation temperature of InN and high equilibrium N_2 vapor pressure over the InN film. According to Figure 2.6 (b), there are 3-deposition modes for InN growth due to the V/III input ratio. Etching can occur for a low V/III input ratio, and In droplets may appear at the surface for V/III > 50. Therefore, high V/III ratios over 10000 are required for the deposition of InN. However, there is a specific growth regime which allows the deposition of InN between V/III= $10^5 - 2.6\times10^6$. A V/III ratio greater than 2.6×10^6 will create large amounts of H_2 that are produced from the prolysis of NH_3, thus, preventing InN deposition[90]. Good quality InN films have not been achieved using MOCVD technique due to the high quantity of defects. One reason for the defect densities is attributed to the lack of a lattice-matched substrate material. Sapphire is available and is the preferred substrate choice, with relatively low cost and high quality for the epitaxial growth of group III-nitrides. A GaN buffer layer is another option, which reduces the lattice-mismatch from 22% to 10%. In order to overcome these limitations, various techniques have been applied including atomic layer epitaxy, two-step growth techniques and double-zone MOCVD. The suitable growth temperature region for deposition of InN is 450- 600 °C.

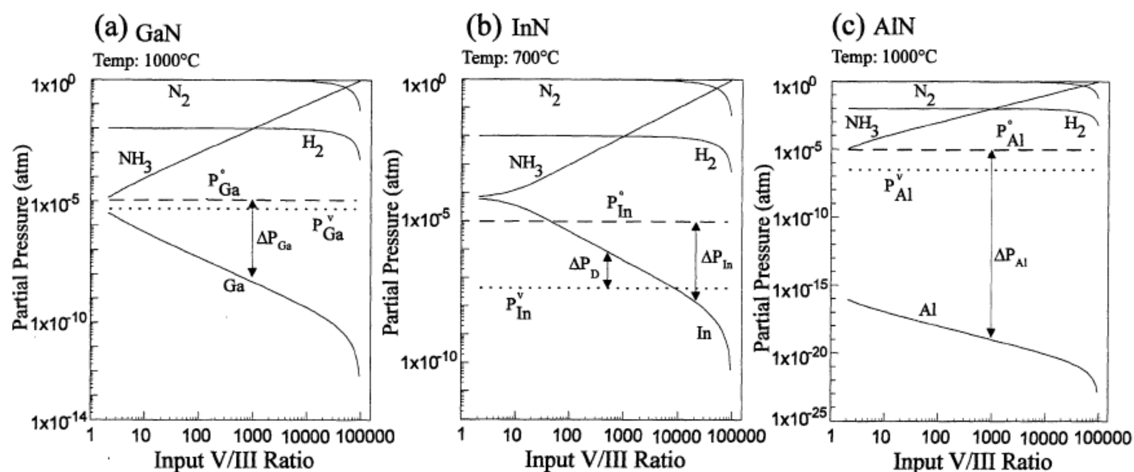

Figure 2. 6 The equilibrium partial pressures over a) GaN b) InN and c) AlN as functions of input ratios[91].

The growth temperature in the MOCVD growth of InN is one of the most crucial parameters to control the film quality. When the growth temperature decreases below 400°C, the resultant InN films contain high levels of oxygen. Figure 2.9 shows the carrier concentration of InN grown at different temperatures under 76 or 760 Torr. The increasing growth temperature decreases the carrier concentration[48]. In the history of MOCVD, high quality GaN and related materials were grown, by implementing different reactor designs. Yamamato *et al*. studied the influence of reactor design by comparing two different horizontal reactors in which the reactant-gas flow spacing between the substrate and ceiling of the quartz chamber were changed. They found that the reactor with smaller spacing made InN films with larger grain size and the 2D growth of InN was enhanced. Enhancement in 2D growth resulted in good crystalline quality. In conclusion, the growth of InN is relatively poor at present compared to MBE grown InN samples with a carrier concentration of 4.7×10^{18} cm^{-3} and Hall mobility of 1100 cm^2/Vs[48]. The growth of InN via traditional MOCVD techniques has proved difficult and has not yielded high quality InN.

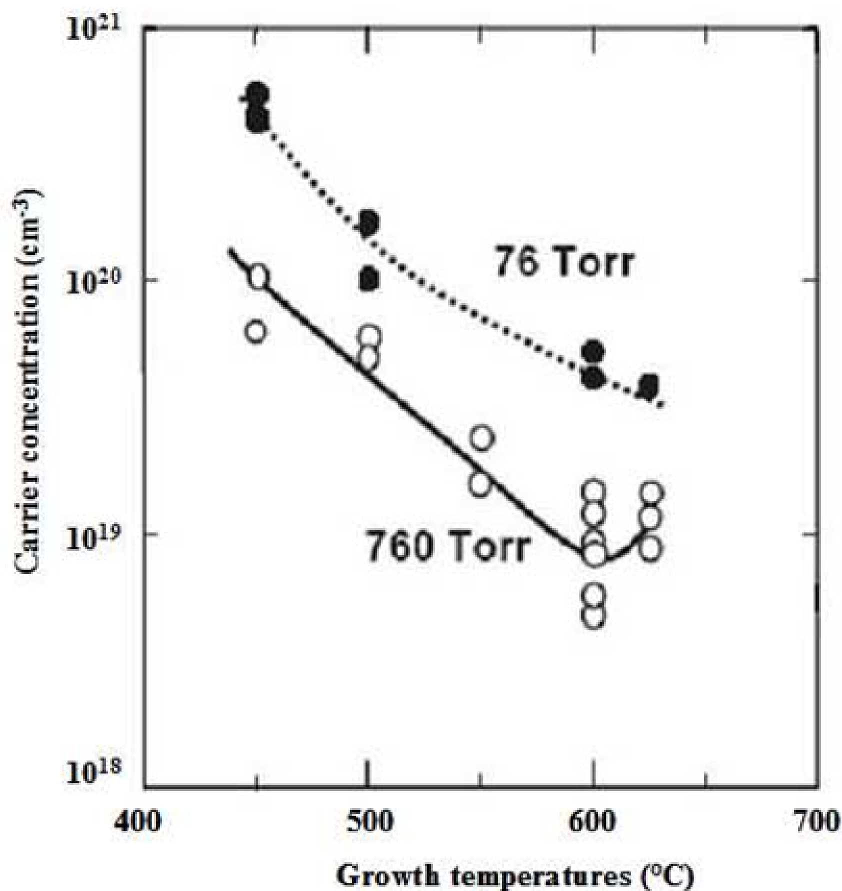

Figure 2. 7 Growth temperature dependence of carrier concentration for InN film grown at different pressures.

2.2.3 Hydride Vapor Phase Epitaxy (HVPE)

Rapid progress in epitaxial technology of MOCVD grown GaN based materials and its capability to produce GaAlN/ InGaN quantum well structures made this growth method an industrial choice for the fabrication of GaN based device structures. However, GaN based structures grown by MOCVD or MBE must utilize foreign substrates such as sapphire, SiC or GaAs due to the absence of native group III-Nitride substrates. Differences in the thermal expansion coefficient and the lattice mismatch between the substrate and group III-Nitrides lead to defects in the epitaxial layer, cracking of layers

during the post growth cooling and residual strains in the epitaxial layers. Those defects contribute to high background electron concentrations and degrade the electrical and optical properties of materials. Slow progress and overwhelming technical difficulties in growing bulk layers via MOCVD and MBE, placed the HVPE method in a pathway to produce substrate materials of group III nitride semiconductor materials. Free standing GaN wafers with an electron mobility of 1320 cm^2/V sec and a donor concentration of 7.8×10^{15} cm^{-3} have been grown via this method [92,93]. It has been shown that the dislocation density in GaN layers decreases with an increase in layer thickness[93]. As a result, HVPE is an attractive technique for the growth of quasibulk materials, which can provide lattice matched growth surfaces and thick, strain relieved buffer layers.

HVPE technology has been used for over 3 decades to deposit single crystal layers of both GaN and AlN for more than 3 decades. The first single crystal InN samples were grown by *Igarashi*[94] using an In-Br_2-NH_3-N_2. Growth of InN epitaxial layers by HVPE were reported using InCl, $InCl_3$ and NH_3 sources[95,96]. A higher growth rate was observed using the $InCl_3$-NH_3 material source system as compared to the InCl-NH_3 material source system. Epitaxial growth of InN has been attempted on a GaN buffer layer using the $InCl_3$-NH_3 source system at growth temperatures as high as 750°C[96]. The growth rate decreases with increasing growth temperature as shown in Figure 2.10, and research showed that a high input partial pressure of $InCl_3$ was necessary for the growth of InN at high temperature.

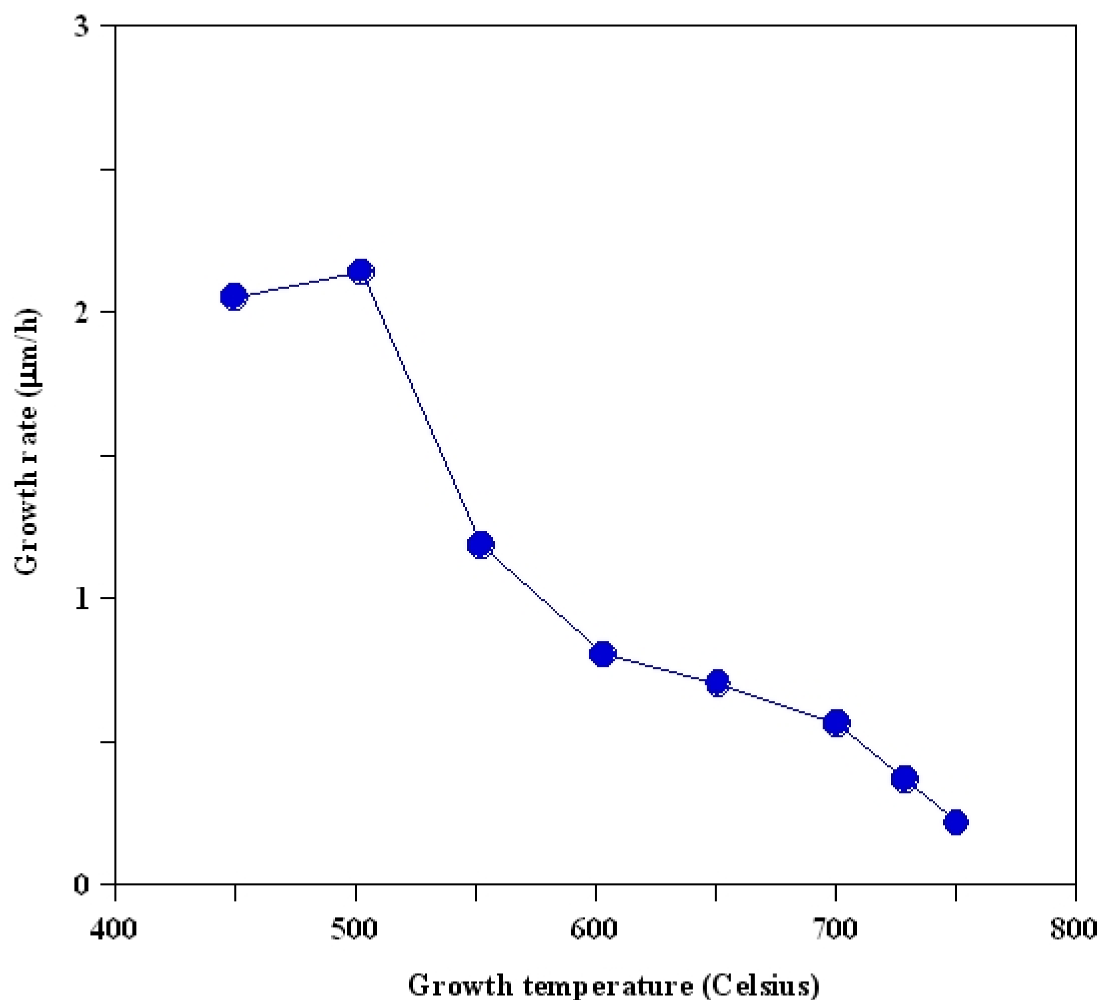

Figure 2. 8 Growth rate of InN films as a function of growth temperature.

It was observed that, depending on the growth conditions, InN materials may be grown as nano-size structures (nano-rods, nano-wires) with typical diameters of 60-500 nm[83].

2.2.4 Sputtering

Plasma-assisted reactive deposition is a suitable method for growing group-III Nitride materials with high melting points, and this method is successful due to the low growth temperature, which enables the deposition of In- containing alloys and interfusion at interfaces of multilayer structures. However, the disadvantage of sputtering is that the

In, Ga, and Al targets are easily oxidized. The first group III nitride grown by plasma assisted deposition was InN powder in 1910[79]. Fischer and Schröter reacted indium metal with nitrogen in a cathodic discharge to produce InN powder. The sputtering system employed a pair of magnetrons sputtering. The substrate assembly is rotatable and substrates were sputtered from a high purity In target which was nitrided under high purity nitrogen. Tansley and Foley reported on InN films grown by RF sputtering with the lowest electron concentration and highest mobility ever reported for nitride semiconductors. However these results have proved un-reproducible. The structural properties of InN grown by sputtering processes at low temperatures are polycrystalline or columnar which limits applications. While single crystalline InN films have been grown[40], films qualities are very poor with high carrier concentration and low electron mobility.

2.3 Challenges in growing InN and In- rich group III nitride material

Thermal instability of InN makes the growth of high quality $Ga_{1-x}In_xN$ films with high In content difficult. This is due partly to the lattice mismatch and mismatch of thermal expansion rates between the epitaxial film and substrate. GaN LED emission efficiency increases even with small additions of In, as outlined in the previous chapter. Several fundamental questions regarding the basic material properties of the InN such as the band gap energy, limited mobility, and limited electron concentration remain unsolved. There exists considerable uncertainty about the band gap of InN, the influence of point defect chemistry on the structural, optical and electrical properties, deep defect levels, and metallic clusters formed within the band gap. CVD growth of InN is a challenging task due to the extremely high equilibrium vapor pressure of nitrogen

required to balance the low decomposition temperature of InN. This low growth temperature requires the application of high V-III ratios in order to prevent the formation of metal droplets on the growth surface. Studies of the decomposition of InN layers have shown that oxygen is incorporated into the InN crystal under thermal treatments and might be one of the reasons for variation in the band gap energy of InN. In order to realize InN-based photonic devices and overcome the difficulty of high thermal decomposition pressure of InN, a disruptive technology is necessary for reducing defect density and improving the quality of InN based III-Nitride alloys.

Chapter 3

Description of High Pressure Chemical Vapor Deposition Reactor and real time characterization tools

3.1 Introduction

Any scientific research requires an understanding of the associated scientific equipment and their working principles. Therefore, it is very crucial that one completely understands the limitations and capabilities of the scientific set up and according to the limitations finding new revolutionary approaches. While success in the hetero-epitaxial growth of single crystal, high quality InN has been achieved utilizing low-pressure techniques, a number of fundamental difficulties still exist:

I. The low disassociation temperature of InN (500°C, 550°C, and 630 °C[4]), which is determined by the relatively low In-N bonding energy,

II. High equilibrium N_2 vapor pressure over the InN film,

III. The low pyrolitic efficiency of NH_3 at low growth temperatures.

The difficulties associated with forming solid alloys of InN with AlN and GaN, along with the well-known difficulties in p-type doping of all III-nitrides plays an important role in the fabrication of electronic and optoelectronic devices. At present, nitride based semiconductors are characterized by low mobility p-type carriers, and obtained p-type materials with low hole concentration. Therefore, doping of group III-nitrides is very important for basic research and applications. A commonly used acceptor impurity for p-

type doping is Magnesium, which leads to creation of Mg-H complexes in MOCVD process in the presence of NH_3. Mg can be activated at temperatures of approximately 800 °C.

Traditionally, InN films require growth temperatures below 600 °C and sub atmospheric pressures. The growth temperature is the most critical parameter to control film quality as the surface mobility of atoms decreases at low temperatures and growth temperature directly influence the fabrication of $Ga_xIn_{1-x}N$ heterostructures. However, growth pressure is also a basic parameter affecting electrical properties of InN films[97]. As outlined in the previous chapter, InN films can be grown in temperature ranges between 820 K-920 K with either atmospheric pressure or sub-atmospheric pressure (76 torr) in a conventional MOCVD system. Under these conditions, it is necessary to reduce the growth temperature in order to prevent the InN decomposition with a corresponding decrease in reactor gas flow rates to enhance TMI decomposition. However, conditions for laminar flow require a low Reynolds number, and Grashof number (G_r), which must be much smaller than the square of the Reynolds number (R_e), as defined by following equations:

$$G_r = \frac{h^3 g \rho^2 \beta_T \Delta T}{\mu^2} \tag{3.1}$$

$$R_e = \frac{\rho u h}{AP\mu} \tag{3.2}$$

where g is the gravity factor, ρ the density of the fluid, β_T the volume coefficient of expansion, u the standard flow, P standard pressure. G_r/R_e^2 ratio is proportional to $g(P/u)^2$, therefore high pressure CVD growth must be carried out at sufficiently high flow velocity to maintain a small G_r/R_e^2 ratio. Furthermore, higher N_2 pressures can suppress

the nitrogen evaporation from the grown InN film. In order to establish the growth at higher pressures, a high-pressure flow channel reactor was implemented at Georgia State University.

3.2 High pressure chemical vapor deposition approach

Low-pressure deposition processes are limited to regimes where the partial pressures of the constituents do not differ vastly and the decomposition process can be countered by off-equilibrium process conditions. This becomes a challenge for InN and related indium rich III-N alloys due to their stoichiometric instabilities and low dissociation temperatures, leading to inconsistent, process dependent materials properties. At present, two of the most severe problems are related to the surface termination of indium-rich InGaN layers and secondly, the large thermal decomposition pressures in InN. This thermal decomposition limits the growth temperatures for low-pressure deposition techniques at and below 500°C, which is at least 200°C lower as compared to GaN growth. Even though recent results of InN layers grown by plasma assisted MBE demonstrated that high-quality InN layers could be achieved with low-pressure deposition techniques, the integration of such layers into wide band gap group III-nitrides heterostructures is a challenging task. Thermodynamic estimates suggest that the surface for highly volatile compounds such as InN and related alloys can be stabilized at much higher temperatures if stabilized at high pressures of the volatile gas species[9,98].

Recent studies in the indium - nitrogen system[13] show much uncertainty in the p - T - x relations due to the missing experimental validation, but studies of the nitrogen pressure are needed to prevent thermal decomposition of bulk InN according to

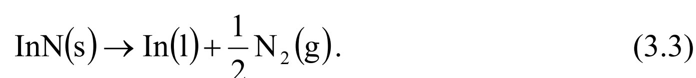

$$\mathrm{InN(s)} \rightarrow \mathrm{In(l)} + \frac{1}{2}\mathrm{N_2(g)}. \tag{3.3}$$

Since McChesney et al.[16] were not able to show reversibility of expected equilibrium: InN is not formed from direct reaction of indium metal and nitrogen. The interpretation of the linear relation between p and T is given in following;

$$p(N_2) \rightarrow p_0\left[\frac{\Delta H_r}{R}\left(\frac{1}{T}-\frac{1}{T_0}\right)\right] \qquad (3.4)$$

which was obtained by integration of Van't Hoff equation. ΔH_r represents the heat of formation, R the universal gas constant and T equilibrium temperature. Results are shown as a plot of P-T^{-1} in Figure 3.1. The relation indicates that in the pressure range $p_{N_2} \leq 10^2$ bar and for substrate temperatures ≤ 900 K the surface decomposition of InN will be effectively suppressed. In view of the higher melting temperature of InN (~1200 °C) as compared to InP (1062 °C) this appears to be a minimum requirement for the growth of high quality epitaxial InN heterostructures.

The HPCVD approach presented here is aimed towards the growth of group III-nitrides at elevated pressures using InN as a model system to demonstrate the capabilities of High-Pressure CVD. Moving towards High-Pressure Chemical Vapor Deposition (HPCVD) for the growth of group III-nitrides, requires a completely new reactor system design, with additional considerations of flow kinetics, gas phase reactions, diffusion through the boundary layer as well as altered surface chemistry. Modeling and simulation of the gas phase and surface reaction kinetics for InN growth at high pressures are presented in the following sections.

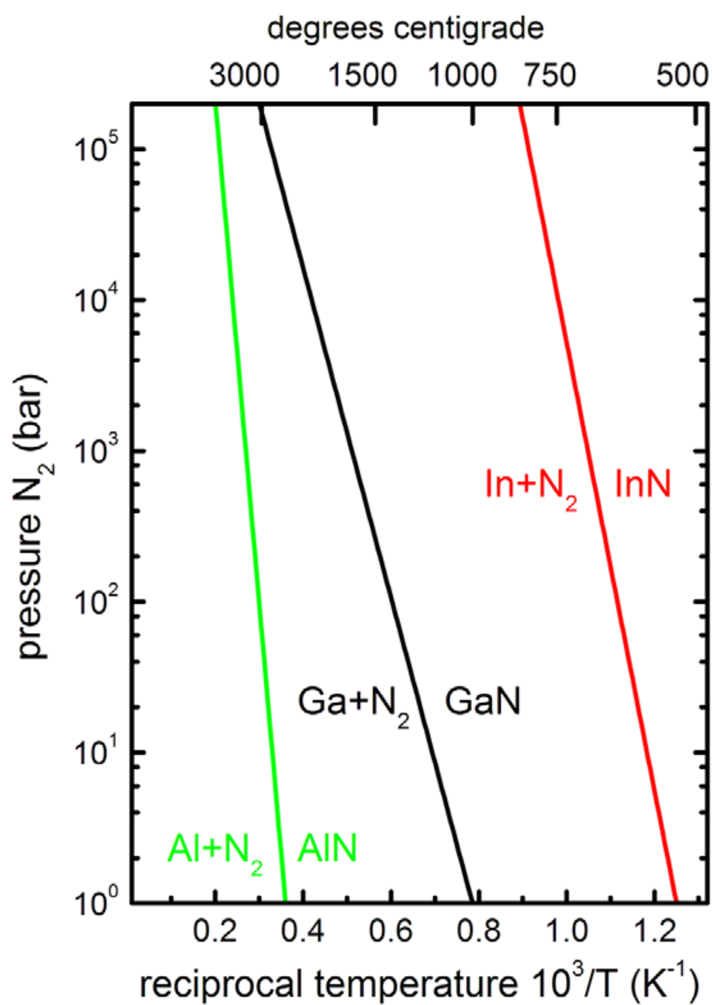

Figure 3. 1 Thermal decomposition pressure vs. reciprocal temperature for AlN, GaN and InN.

3.3 Modeling of high pressure CVD processes

In order to gain an understanding of the growth process of InN, a numerical model was developed based on simulations of fluid dynamics coupled to chemical kinetics within a three dimensional grid that simulates vapor deposition inside the High-Pressure CVD reactor[99]. The HPCVD reactor simulations are based on two different computational approaches due to the complexity of the chemistry:

- A time evolution model based on chemical kinetic equations represented the reactor as a single volume that was kept at a constant temperature and pressure.
- A steady-state model represented the reactor with a three dimensional grid of 97,000 hexagonal cell at different temperatures, with varied flow velocities, and constant pressure.

The steady-state model is computationally intensive and substantially increases with the number of chemical reactions. However, the time evolution model was used mainly to generate a reduced set of reactions to model the disassociation of $In(CH_3)_3$-NH_3 precursors under specific conditions of temperature, pressure, and molar ratios. First of all, the time evolution model calculation was performed using the full set of 79 gas phase reactions, which includes 47 species, by selecting specific initial conditions of molar ratios, temperature and pressure. Furthermore, the time evolution model was performed for the comparison of a reduced chemical set with the full set until the results of full set and reduced set were similar. Finally, the reduced set of chemical reactions generated by the time evolution model was used to perform the steady state calculation and compare the results with the time evolution model. This modeling explained above is depicted in Figure 3.2.

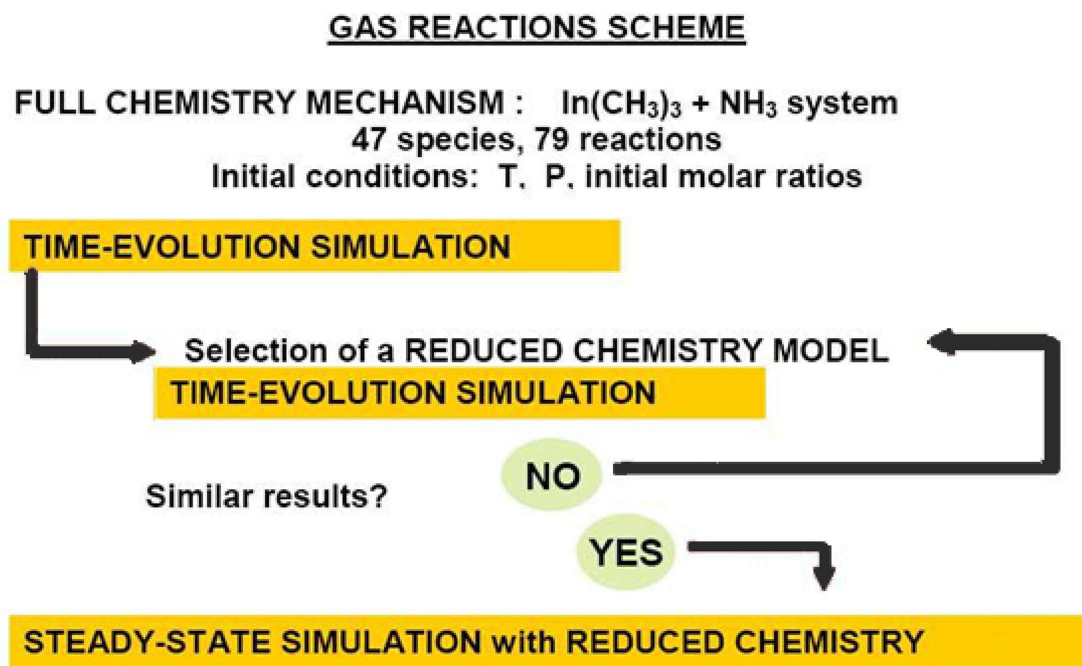

Figure 3. 2 Scheme for the selection of a reduced gas-phase chemical reaction model.

Both models predict the same species, however the resulting largest molar ratios for two models are different. For instance, NH_2 and In are the most abundant species for the steady-state model, but NH_3 and $InCH_3$ are the most abundant species for the time evolution model. These differences in calculated mass fraction values of abundant species indicate that the flow dynamics affects the distribution.

One of the possible surface reaction mechanisms for the growth of InN has been modeled using four paths. As shown in Figure 3.3, atomic indium and of $InCH_3$ were the most abundant group III species in the gas phase for a reactor pressure of 12.5 atmospheres and specific conditions of molar ratios, temperature. Therefore, those two species were selected to model the surface reactions for Path one and Path two, respectively.

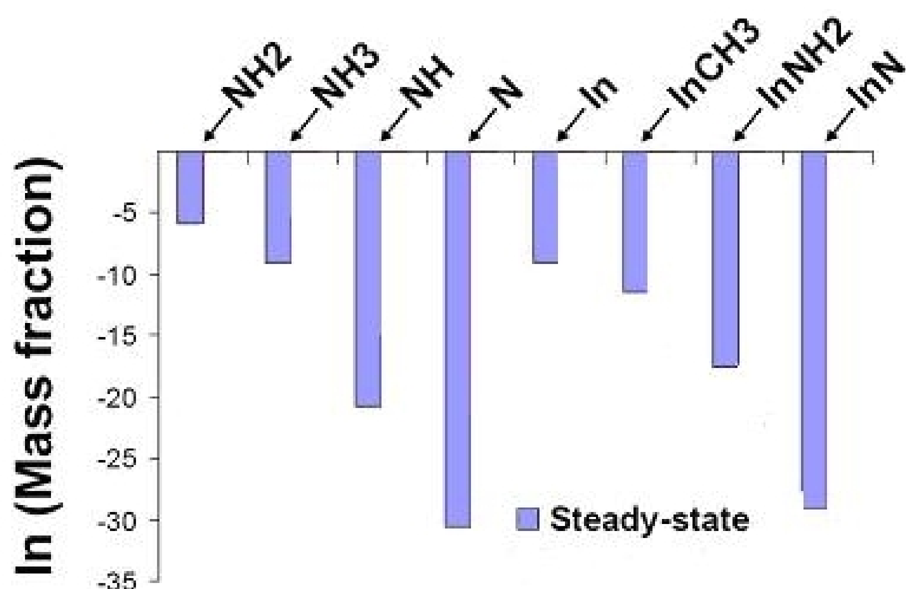

Figure 3. 3 Final mass fractions obtained for the steady state model using a reduced set of chemical equations. The initial molar ratios and conditions are: N_2:NH_3:$In(CH_3)_3$= 0.99504:0.00493:0.00003, temperature=1300 K, pressure=12.5 atm.

The surface reaction paths are summarized in Table 3.1. The first path corresponded to the adsorption of atomic In, the capture of NH_2 to form adsorbed $InNH_2$ and the disassociation of adsorbed $InNH_2$ in to adsorbed InN and H_2. Path two corresponded to the adsorption of $InCH_3$ and the capture NH by adsorbed $InCH_3$ to form adsorbed $InCH_3NH$. Following this, the adsorbed $InCH_3NH$ disassociates into adsorbed InN and methane (CH_4). Path three corresponded to the direct adsorption of InN. Path four corresponded to the direct adsorption of $InNH_2$ and its disassociation into adsorbed InN and H_2. The decomposition or etching of InN film results from the reaction

$$\text{InN_S} \leftrightarrow \text{InN_S} + \text{N} \quad (3.5)$$

and was included in each of the four paths.

Table 3. 1 Summary of the selected heterogeneous reactions. Symbol _S in reactions represent the adsorbed species.

Path One	Path Two	Path Three	Path Four
$In \leftrightarrow In_S$	$InCH_3 \leftrightarrow InCH_3_S$	$InN \leftrightarrow InN_S$	$InNH_2 \leftrightarrow InNH_2_S$
$In_S + NH_2 \leftrightarrow InNH_2_S$	$InCH_3_S + NH \leftrightarrow In(CH_3)NH_S$	$InN_S \leftrightarrow InN_S +$	$InNH_2_S \leftrightarrow InN_S + H$
$InNH_2_S \leftrightarrow InN_S + H_2$	$InN(CH_3)NH_S \leftrightarrow InN_S + CH_4$		$InN_S \leftrightarrow InN_S + N$
$InN_S \leftrightarrow InN_S + N$	$InN_S \leftrightarrow InN_S + N$		

Reaction rate constants were calculated at fixed pressure for the steady state model. The deposition rate constants (first row in Table 3.1) were calculated using the kinetic theory of gases by Cardelino *et al*[99]. The surface reactions (second row in Table 3.1) were calculated from the reverse hemolytic dissociations by Cardelino *et al.*[99]The contribution of the four paths leading to InN formation were simulated using initial conditions N_2:NH_3:$In(CH_3)_3$ with mass ratios of 0.73:0.04:0.23. The basic simulation used an inlet velocity of 0.01 m s^{-1}, a total pressure of 10 atm, and 2.5 MW m^{-2} of substrate heating. These input values for simulation have been used in actual experiments[9].

This simulation resulted in a maximum substrate temperature of 1163 K, an average substrate temperature of 957 K, and a maximum InN growth rate of 190 nm per hour and average growth rate of 40 nm per hour. Figure 3.4 depicts the contribution to the growth rate resulting from four paths. Note that the growth rate for path two becomes negative where the substrate has higher temperatures. This is the due to the decrease in the available gaseous $InCH_3$ at the higher temperatures.

A set of initial conditions for experimental values were chosen by our group[11,12] to verify the result of a steady-state calculation. In that experiment, the $N_2:NH_3:In(CH_3)_3$ experimental ratios were 5.4 slm (standard liter per minute): 500 sccm: 300 sccm. The $N_2:NH_3:In(CH_3)_3$ mass ratios 0.73:0.04:0.23 and inlet flow of 0.17 m s^{-1} were chosen to validate the model chosen here for steady-state simulation. The experimental reactor pressure was 10.2 bar, and pressure was 10 atm for the simulation. The experimental reactor temperature ranged from 800 to 1150 K and the source materials were introduced through a 6s pulsing sequence. The simulation was performed at two different temperatures 1050 K and 1290 K. The calculated average InN growth rate is 0.027 μm per hour and 0.094 μm per hour for the lower and higher temperatures, respectively. The average experimental InN growth rate was 0.081 μm per hour. The simulation results compare very well with the experimental results, as seen in Figure 3.5.

In conclusion, a simple set of heterogeneous reactions is analyzed and organized into four paths. The main path for the formation of InN film was the deposition of atomic In and $InCH_3$ and their reaction with group V species. A reduced set of chemical reactions could be used to represent realistically the complete set of possible chemical equations for the decomposition of NH_3 and $In(CH_3)_3$. Based on the simulation results, a high-pressure chemical vapor deposition reactor model was designed that could realistically simulate experimental results for the deposition of InN from the disassociation of NH_3 and $In(CH_3)_3$. In the following sections, a brief introduction to the design of the HPCVD reactor system is provided together with its real-time optical capabilities in order to characterize flow, gas phase and surface reactions.

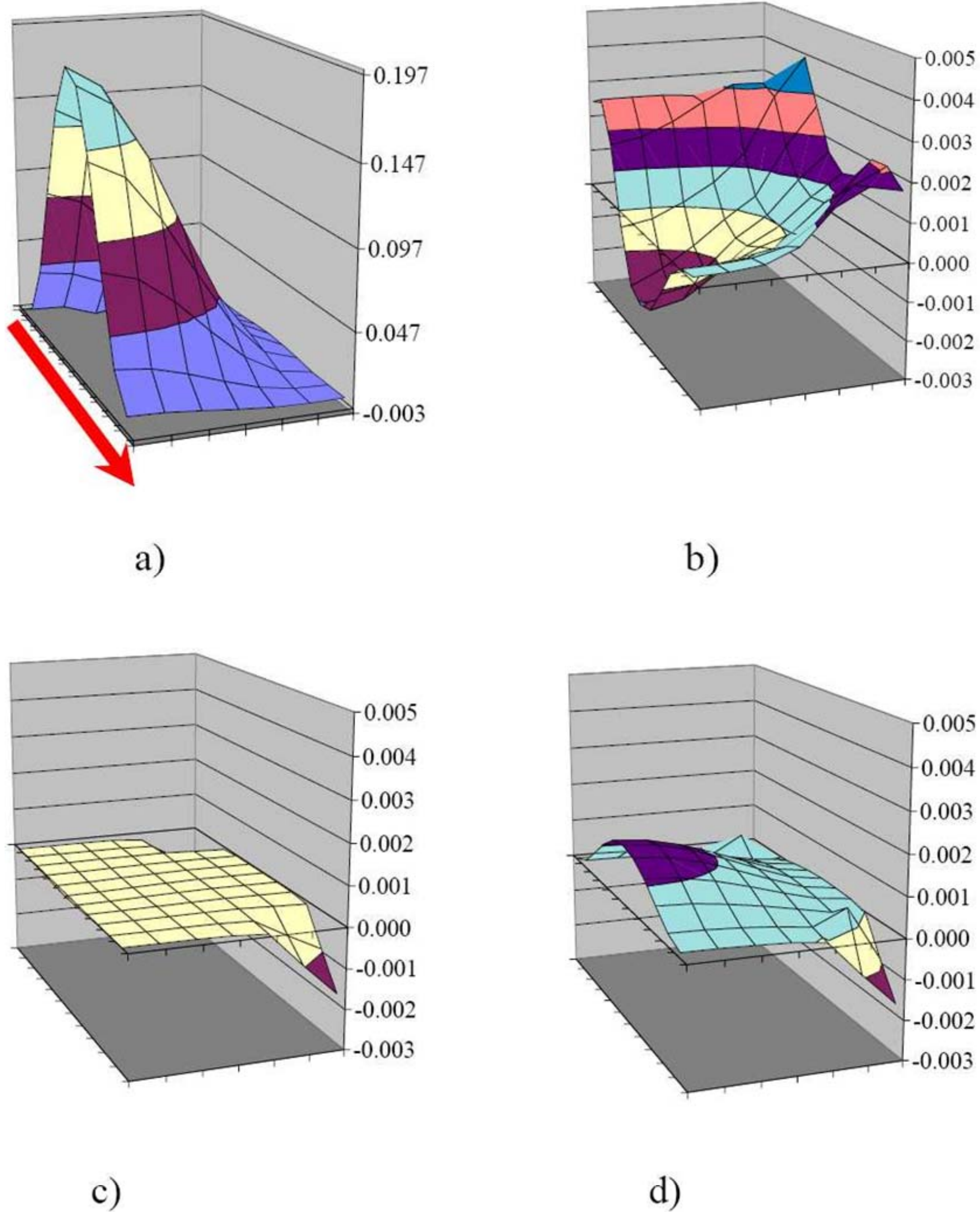

Figure 3. 4 InN growth rate in μm per hour. The arrow shows the direction of the flow. a) Path one; b) Path Two; c) Path Three; d) Path Four.

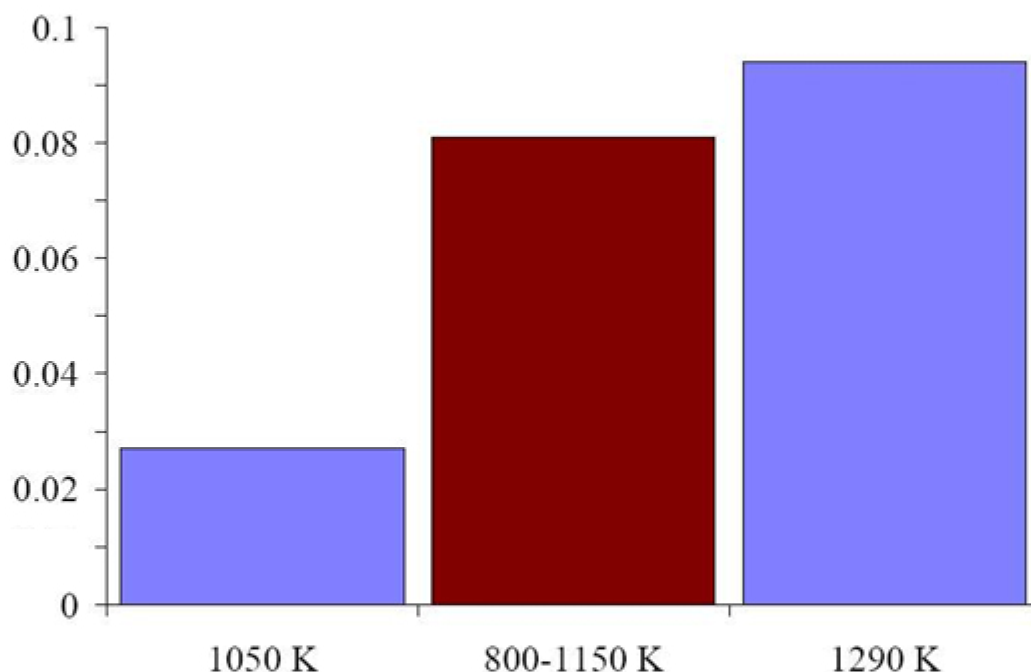

Figure 3. 5 Comparisons between experimental and simulated average InN growth rate in μm per hour. The central bar corresponds to the experimental value, the left bar to the simulation at lower substrate heating, and the right bar to the simulation of higher substrate heating.

3.4 High pressure chemical vapor deposition reactor system

The HPCVD flow channel reactor design shown in Figure 3.6 was based on the result of the flow simulations[100,101]. The inner reactor cylinder consists of two symmetric halves, where each half has a substrate holder embedded in a ceramic plate heated through the backside. Utilizing such an arrangement prevents material deposition on the opposite reactor wall and heat induced turbulence above the substrate surface can be reduced. The reactor channel height is 1 mm, accounting for reduced precursor diffusion length at elevated pressures and optimized use of the gases. In order to minimize the flow-induced turbulence in the reactor, a constant cross section is maintained from gas inlet (circular cross section), throughout the reactor (squared cross section: 24 mm × 24 mm), and the reactor exit (circular cross section).

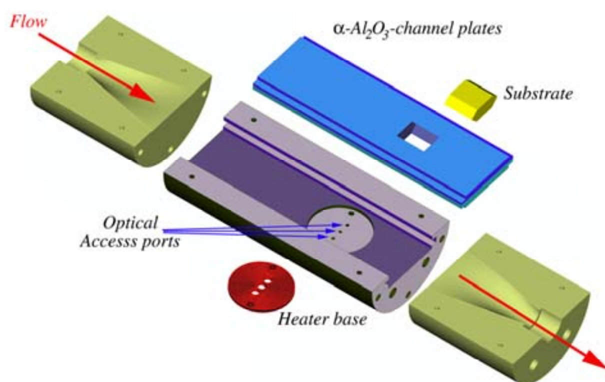

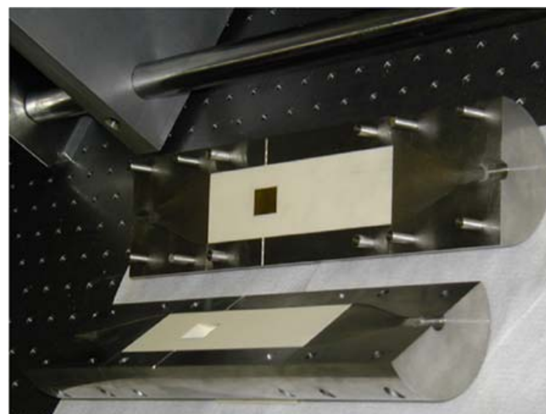

Figure 3. 6 a) Schematic perspective outline of half of the reactor flow channel assembly showing the flow direction and the optical access ports that provide an access to the growth surface.

Figure 3.6 b) Cross sectional view of the machined and assembled flow channel assembly with inserted sapphire substrates.

The inner reactor slides in a second outer cylinder (dia. 6", length = 12") that can be pressurized up to 100 bar.

A schematic of HPCVD flow system is presented in Figure 3.7. In order to *minimize* gas phase reactions, extract sufficient organometallic (OM) nutrients from the bubbler, and embed the precursor flow in the reactor main stream, the design employs pulsed precursor injection schemes, which is advantage of:

- The mixing of the gas sources and dilution of the gases in nitrogen carrier gas,
- The pulsed of injection of all gas sources, and
- Analyzing the gas-phase and surface decomposition dynamics in real-time.

The flow channel reactor is interfaced to the gas injection panel. The gas injection sequences are tested and optimized in timing and flows in order to avoid pressure fluctuations during the switching sequences for real-time gas flow dynamics studies as well as the analysis of the gas-phase decomposition kinetics during the film growth

process. Optical ports are integrated into the flow channel reactor as schematically shown in Figure 3.8.

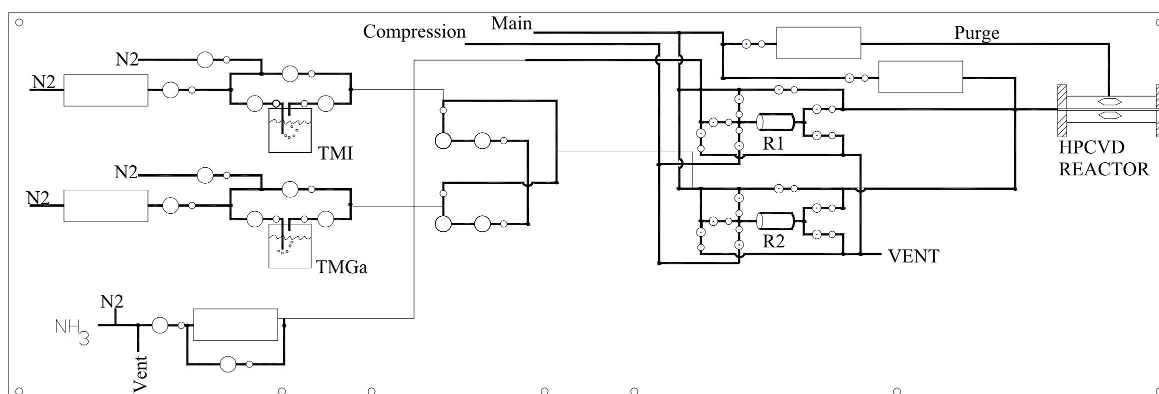

Figure 3. 7 Schematics of the HPCVD flow control panel for precursor compression and pulsed precursor gas injection.

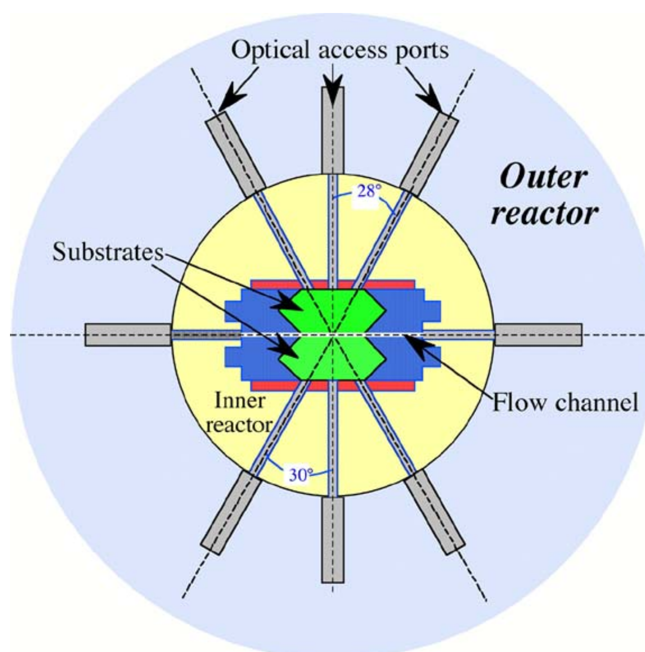

Figure 3. 8 Schematic cross section of the reactor containing the optical access ports and the center of the substrates. Two optical ports provide access to the flow channel and three ports in each of the two half sections of the reactor provide access to the growth surface.

The optical ports along the centerlines of the substrates allow the probing of the gas phase dynamics and chemistry, while three ports entering through the back side of the substrate allow the monitoring of growth surface, film growth, and scattering process from the gas phase.

3.5 High pressure chemical vapor deposition reactor characteristics

Gaining a detailed insight into the growth kinetics at elevated pressure requires analysis of each step critical to the growth process. Gas flow dynamics are characterized by LLS (Laser Light Scattering). Gas phase reactions are monitored using Ultra-violet absorption spectroscopy (UVAS). The InN nucleation and growth process are monitored by Principle Angle Reflectance Spectroscopy (PARS) and LLS.

3.6 Real time optical characterization of gas flow dynamics

In the following sections real time optical characterization techniques integrated to high pressure CVD reactor are going to be presented.

3.6.1 Laser Light Scattering (LLS)

One crucial requirement is the maintenance of the laminar flow conditions in order to provide a consistent supply of precursor constituents above the growth surface. This allows the correlation of gas phase constituent concentrations to the diffusion processes and surface chemistry processes that drive the thin film growth process. The laser light scattering (LLS) in forward scattering geometry was used to analyze the flow characteristics in the HPCVD reactor. This is schematically illustrated in the inset of Figure 3.9. The onset of increased LLS scattering analysis for pure nitrogen flow is summarized in Figure 3.9, indicating the flow and pressure regime at which laminar flow can be maintained. The associated Reynolds number can be calculated via

$$\mathrm{Re} = \frac{\rho u l}{\eta}, \tag{3.6}$$

where $\rho = 1.12\ [\mathrm{kg \cdot m^{-3}}]$ is the density of the gas, "u" the flow velocity, "l" a flow reactor characteristic length parameter, and $\eta = 1.8 \cdot 10^{-5}\ [\mathrm{kg \cdot m^{-1} \cdot s^{-1}}]$ the dynamic viscosity. For ideal gases, a direct proportionality exists between the density of the gas and the pressure. The average of the calculated Reynolds number is approximately 1480 with no significant pressure dependency observed, which is consistent with typical flow channel reactor designs[13]. The LLS analysis indicates that for the high-pressure flow channel reactor laminar process conditions can be maintained for flows up to 20 slm and pressures up to 20 bar.

InN growth surface was monitored through the backside of the sapphire substrate, utilizing laser light scattering (LLS) as shown in Figure 3.8. LLS was applied employing p-polarized light beam (λ=6328Å) and a Glan-Thompson prism during thin film growth. The intensity of the scattered signal was monitored simultaneously by a photo multiplier tube (PMT) located perpendicular to the plane of incidence. The LLS signal recorded during the InN growth will be presented in the following section.

3.6.2 Principle Angle Reflectance Spectroscopy (PARS)

PARS is based on the same principle as p-polarized reflectance spectroscopy. However, as schematically shown in Figure 3.10, PARS utilizes p-polarized light impinging the substrate-ambient interface near the principal angle φ_P corresponding to the pseudo-Brewster angle φ_B for p-polarized light impinging the ambient-substrate interface. Depending on the substrate temperature and monitoring wavelength, the principal angle φ_P varies from 27.5 deg to 30 deg for the sapphire-ambient interface[13]. The angle of total reflection, φ_T, is approximately 5 deg above φ_P.

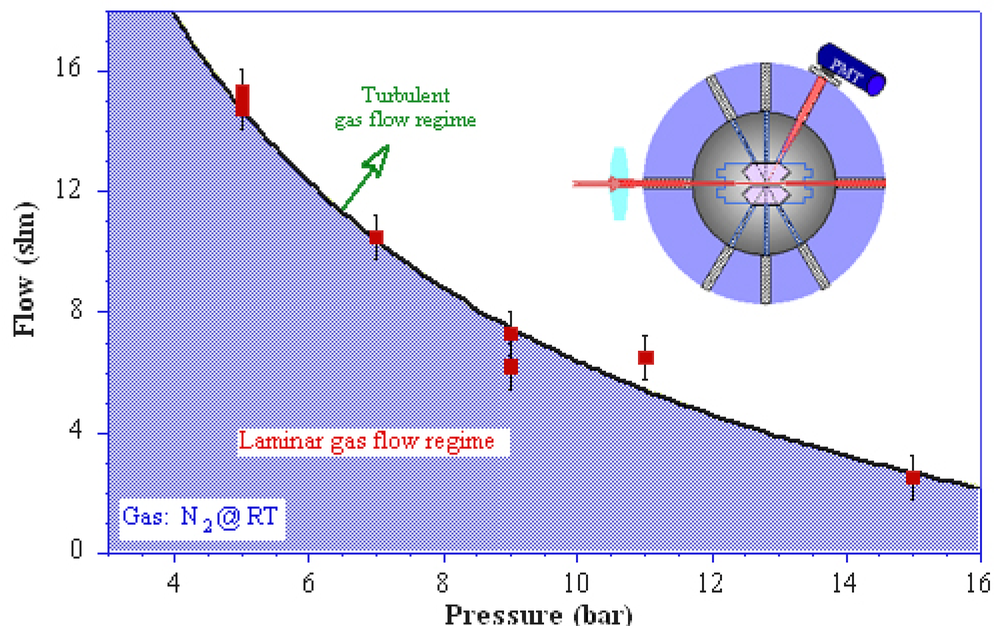

Figure 3. 9 Transition from laminar to turbulent flow conditions as determined by LLS intensity measurements. The inset depicts LLS in forward geometry to analyze the onset of turbulence.

Both inner half parts are identical with the exception of the angle of incidence for (PARS), which are 28 deg and 30 deg for the upper and lower part, respectively, as schematically depicted in Figure 3.8. The monitoring of InN nucleation and growth were monitored using a single wavelength principal angle reflectance (PARS) with a p-polarized light beam (λ=6328Å) and a Glan-Thomson prism. The beams impinge on the substrates at an angle of incidence φ=30° and φ=28° for the upper and lower part, respectively. The reflected beams are detected by Si photodiodes.

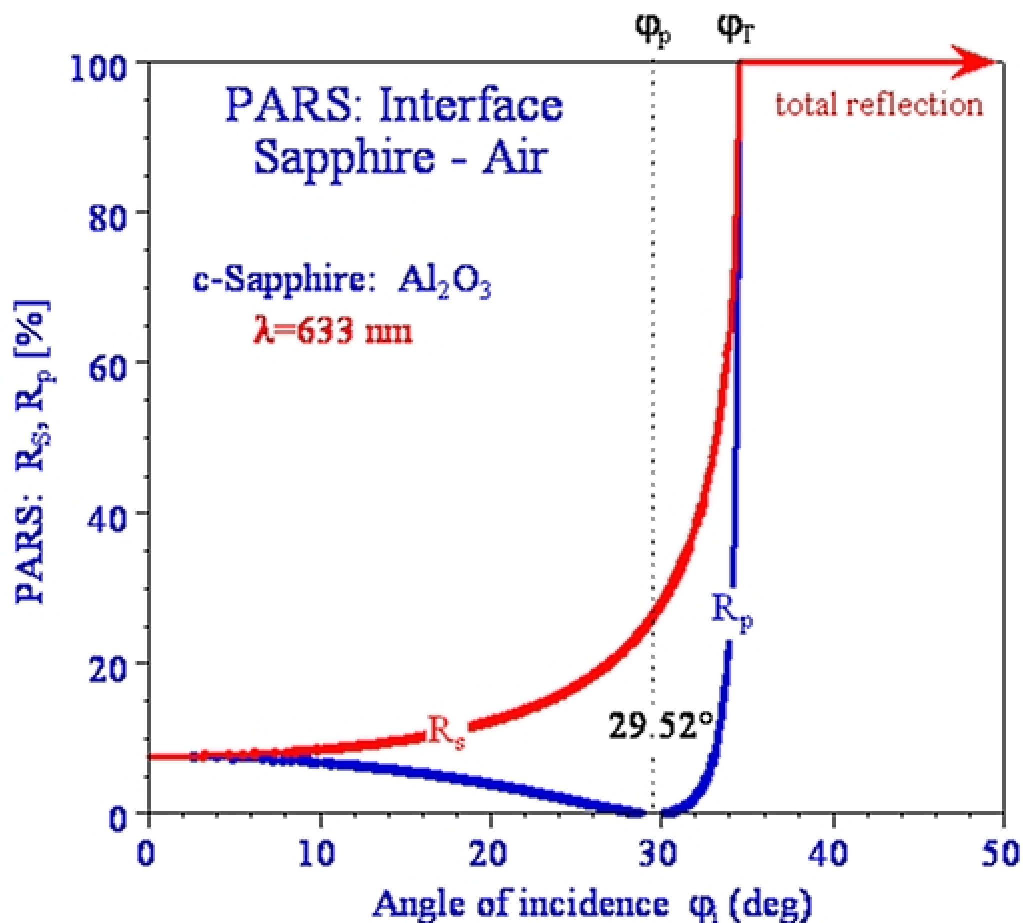

Figure 3. 10 Angle dependency of reflectance for p- and s- polarized light at the sapphire-ambient interface, depicted are the characteristic angles: principle angle φ_p and total reflection angle φ_T.

3.6.3 Ultra violet absorption spectroscopy (UVAS)

The analysis of the decomposition dynamics of ammonia and TMI were analyzed utilizing UVAS for a reactor pressure of 10 bar at different temperatures [102,103]. The reason the UVAS technique has been chosen is that the heater radiation limits the sensitivity of many optical probe techniques in the visible and Infrared (IR) regime, even if modulation techniques are applied. The radiation intensity for a 1000K black body emitter below 350 nm vanishes very quickly with negligible contributions below 300 nm.

A continuous precursor decomposition analysis is no longer possible at higher reactor pressures. In order to grow InN at elevated pressures, a two-step process has been chosen for the injection of the precursors in the HPCVD reactor. The decomposition dynamics of the precursors have been analyzed in the temperature regime of 300 K and 1200 K for single peak absorption maxima. Figure 11a shows the temperature dependant ammonia [NH_3] absorption monitored at 210.7 nm for a reactor pressure of 10 bar. The decomposition at 10 bar pressure starts around 850 K, which is significantly reduced compared to the decomposition temperature at atmospheric pressure, where the onset of ammonia decomposition is observed around 990 K[10]. The decomposition dynamics for TMI is depicted in Fig. 11(b), showing that the onset in the gas phase occurs around 800 K, slightly higher than those reported under low-pressure OMCVD conditions[104,105] for the growth of group V compounds[106,107]. The observed decrease in the ammonia decomposition temperature with increase of reactor pressure is very crucial for InN growth optimization and the control of the point defect chemistry in this material system. It also allows more efficient use of the ammonia precursor, enabling a lower TMI:ammonia flow ratio.

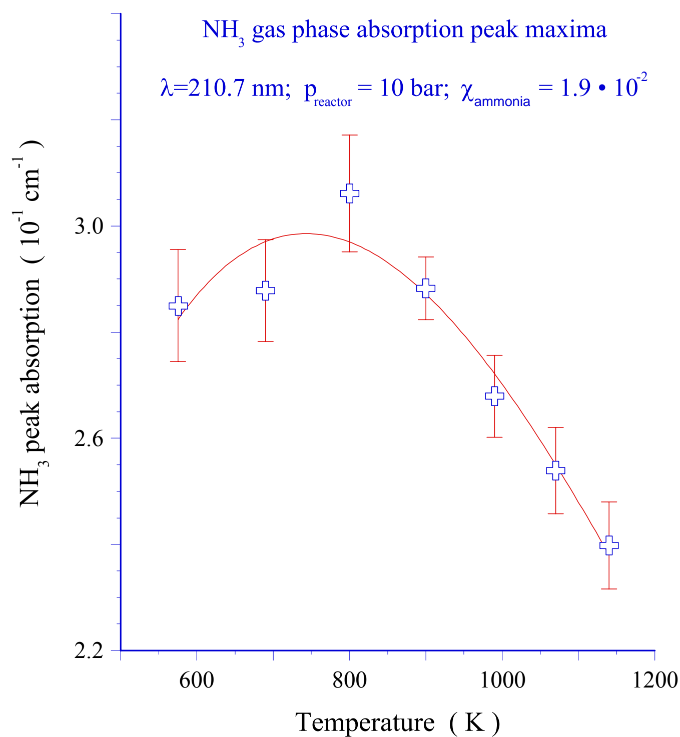

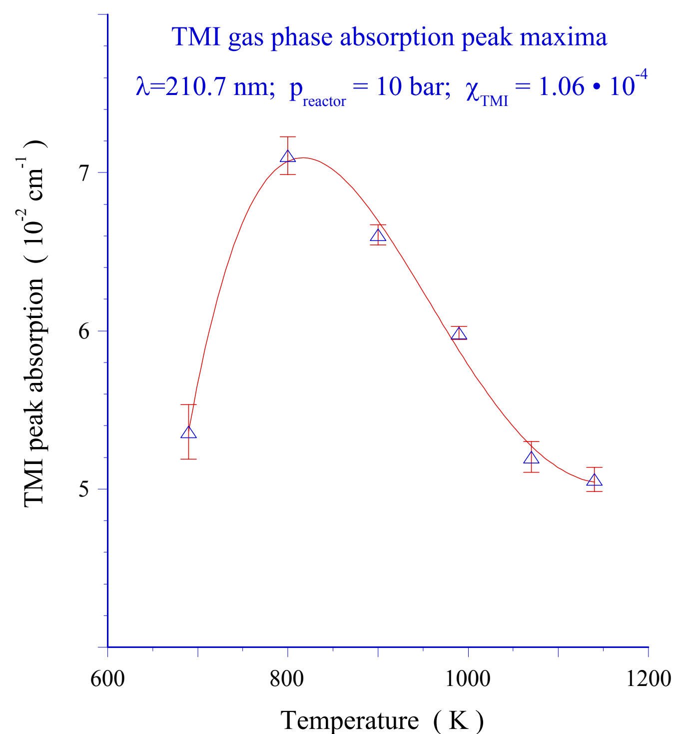

Figure 3. 11 a) Change of the ammonia absorption peak maximum as function of temperature b) Decomposition of TMI at a 10 bar reactor pressure, monitored during pulsed TMI injection as function of temperature.

3.7 Growth procedure

The growth of InN films by HPCVD is achieved by following two different growth procedures. The first growth procedure includes the growth of InN by exposing the substrate surface to pulses of ammonia (NH_3) at typically 1100 K-1115 K. The symmetrically embedded sapphire substrate with a (0001) direction or GaN/sapphire substrates growth surface was heated to 1115 K and exposed to ammonia for typically 30 min. After the nitridation of the sapphire or GaN surface and growth of nucleation layer, the temperature was lowered to the growth temperature. In the following the InN growth was initiated.

The second growth procedure was performed in 3 main steps. First, thermal annealing of the substrate under nitrogen gas for 20 minutes, and nitridation of the substrate (mostly those substrates are GaN/ Sapphire) for 2 minutes at 1080 K. Second, growth of a nucleation layer. Third, the epitaxial growth of InN was performed. Epilayers were grown at a higher or same temperature compared to nucleation and nitridation. Samples with good crystalline quality and surface morphology were obtained in both growth procedures.

The decomposition studies for ammonia in the previous section suggest temperatures above 800K for sufficient cracking of the ammonia precursor for the growth of InN at elevated pressures. However, literature data for InN growth by MOCVD indicate a growth temperature of 675K to 750K[13], 775K[108], 810-840K[109]. Under HPCVD conditions, we can expect to be able to increase the growth temperature about 200K–250K higher than is possible at low-pressure MOCVD conditions. Since the decomposition temperature of ammonia decreases with increasing reactor pressure, the

high temperature and pressure conditions make HPCVD a promising technique for growing InN and In rich group III-Nitride.

A unique pulsed injection scheme was used to temporally separate the precursors trimethylindium (TMI) and ammonia (NH_3) that are embedded into a high pressure nitrogen carrier stream as shown schematically in Figure 3.12. This approach allow us to control the gas phase chemistry and to trace the surface chemistry processes. Those processes were being monitored in real-time using UV absorption spectroscopy and principal angle reflectance spectroscopy (PARS). The precursors were embedded in a high-pressure carrier stream, consisting of ultra-pure nitrogen. At all times during the growth process, the total gas flow through the reactor was kept constant. For the InN layers presented here, the total cycle sequence time was 6 sec, with TMI and ammonia pulse widths of 0.8 sec and 1.0 sec, respectively. The pulse separation was varied from 1 to 1.6 sec. The reactor pressure was 15 bar with a total gas flow of 12 slm. The precursor flow ratio was evaluated for a molar ratio of ammonia to TMI from 600 to 1500 in the growth temperature of 1080 to 1150 °K. The temperature setting refers to the correlation of the analyzed black body radiation as a function of the power setting of the substrate heater and is not corrected for the change in surface emissivity during the growth.

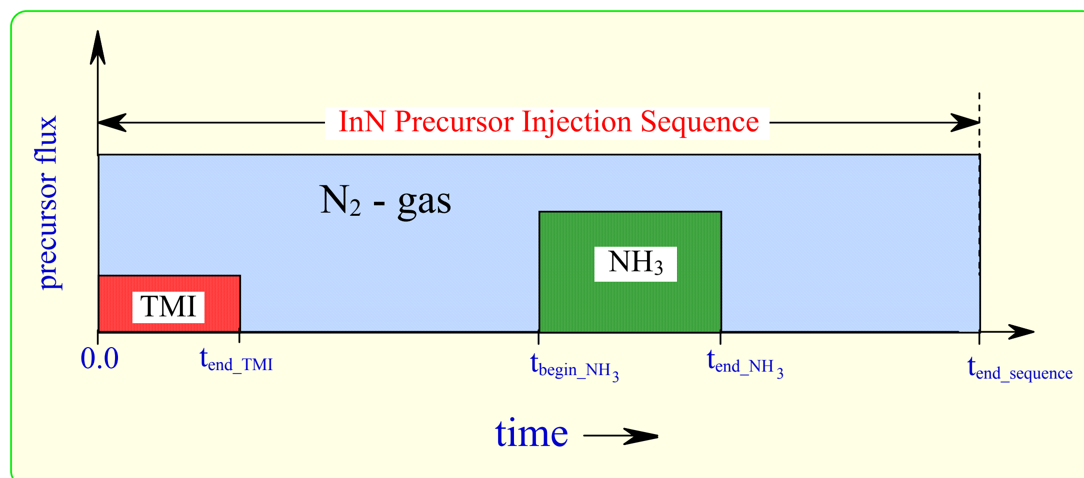

Figure 3. 12 Schematic representation of a precursor cycle sequence used for the growth of InN via the precursors TMI and ammonia.

3.8 Real-time optical characterization of InN growth: nucleation and steady-state growth

A typical set of real-time optical monitoring traces by PARS and LLS is illustrated in Figure 3.13. The temporal evolution of the PARS trace contains crucial information related to the growth surface and information on the overall layer growth. The fine structure superimposed in the interference oscillations is strongly correlated to the time sequence of the supply of precursors. From the analysis of the PAR signal, the average growth rate and the difference between the dielectric functions of film and substrate can be estimated. The monitored LLS trace tracks the evolution of the surface morphology, providing details on the nucleation and overgrowth kinetics as well as the overall surface roughness. As shown in Figure 3.13, the LLS signal increases at the beginning of the growth, but it decreases and becomes smoother during the steady-state growth.

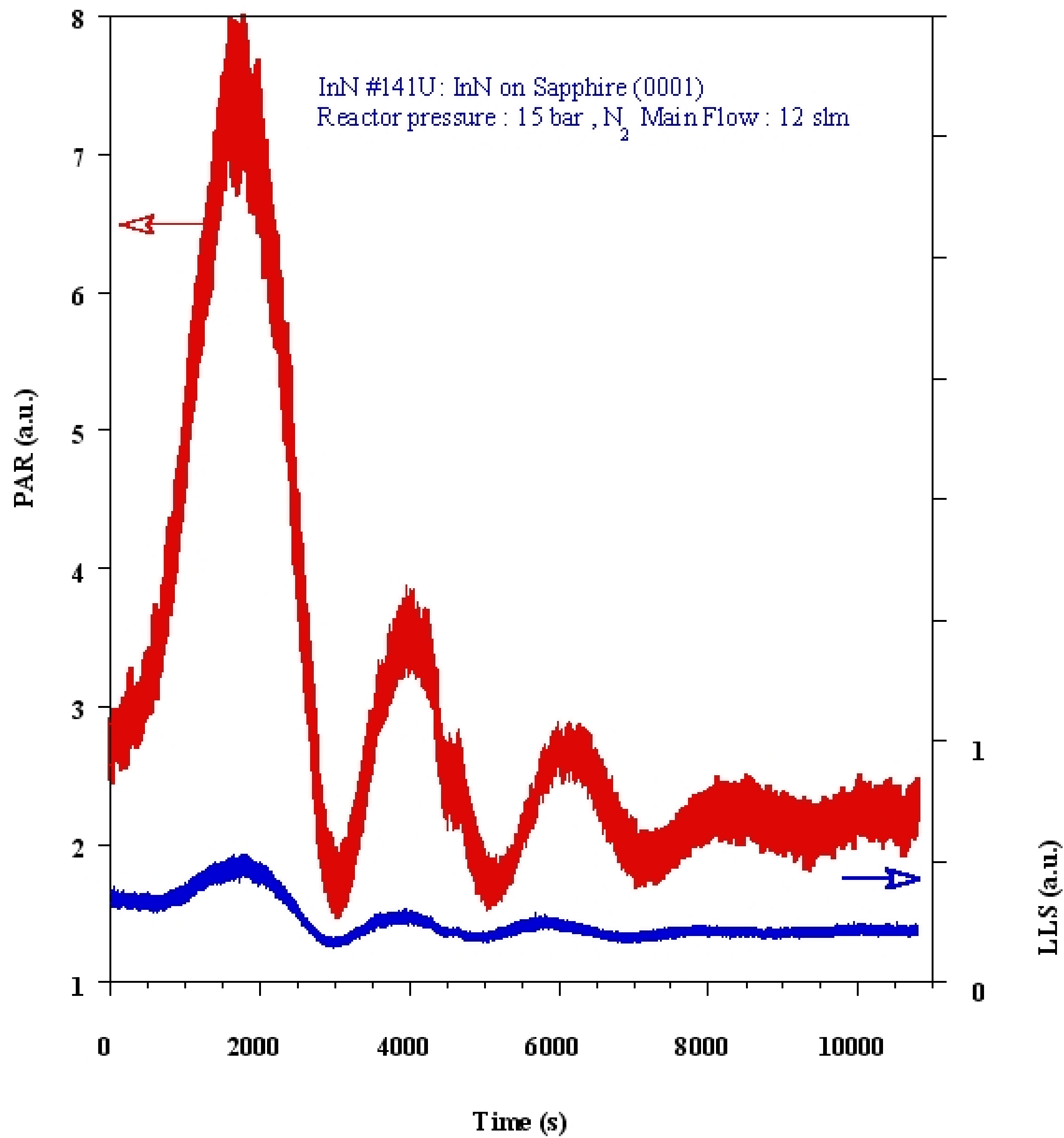

Figure 3. 13 Real time optical monitoring of InN growth by PAR and LLS.

The correlation of the PAR fine structure evolution with the un-decomposed precursors above the growth surface has been studied during the pulsed precursor supply. Figures 3.14 and 3.15 show typical observed PAR and UV transmission traces monitored during nucleation and growth of InN. The lower half shows the UV transmission traces recorded for the wavelength λ=210.8 nm, monitoring the un-decomposed ammonia and TMI species above the growth surface. The PAR trace in the upper half of the figure was recorded for the wavelength λ = 6328 Å, monitoring highly sensitive changes in the dielectric function at the substrate-ambient interface. Also drawn in Figures 3.14 and 15 are the positions of the precursor pulse injection with a total cycle sequence time of 6 sec. Note that the precursor injection time and the response seen in UVAS and PAR signals are temporally shifted according to the average gas velocity in the reactor. As depicted in Figure 3.14, it takes about one to two cycle sequences before the UV absorption feature for TMI clearly can be observed (see arrows). A steady state surface chemistry is typically reached soon thereafter. Figure 3.15 shows the PAR and UVAS responses during steady-state growth conditions. The periodic modulated PAR signal can be directly correlated to the presence of ammonia and TMI fragments on a surface layer. Monitoring the PAR, LLS, and UVAS responses during various growth conditions provides crucial information on the gas decomposition dynamics of the precursor and the subsequent diffusion through the surface boundary layer to the growth surface.

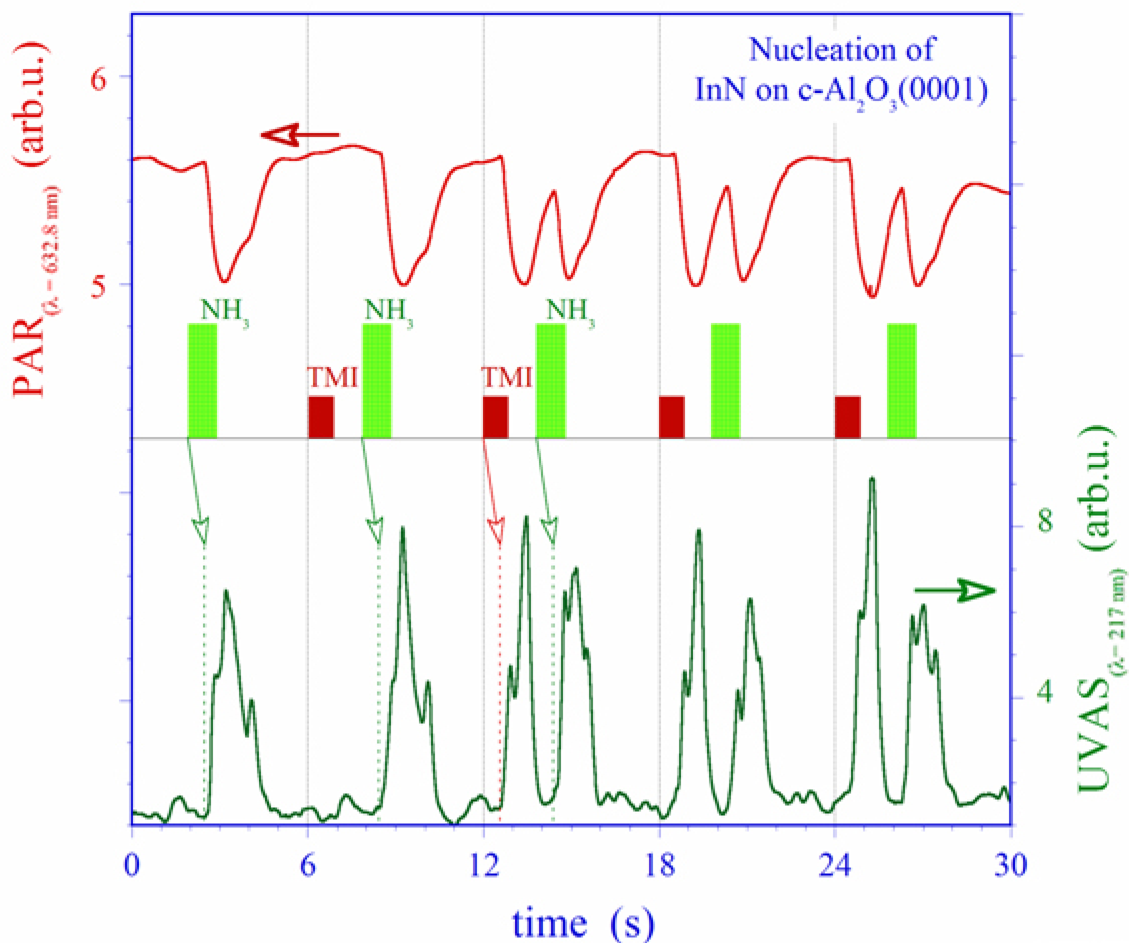

Figure 3. 14 Monitoring of InN nucleation by PARS and UV absorption traces. A precursor cycle sequence of 6 sec with 0.8 sec TMI and 1 sec ammonia pulses, separated by 1.4 sec were used.

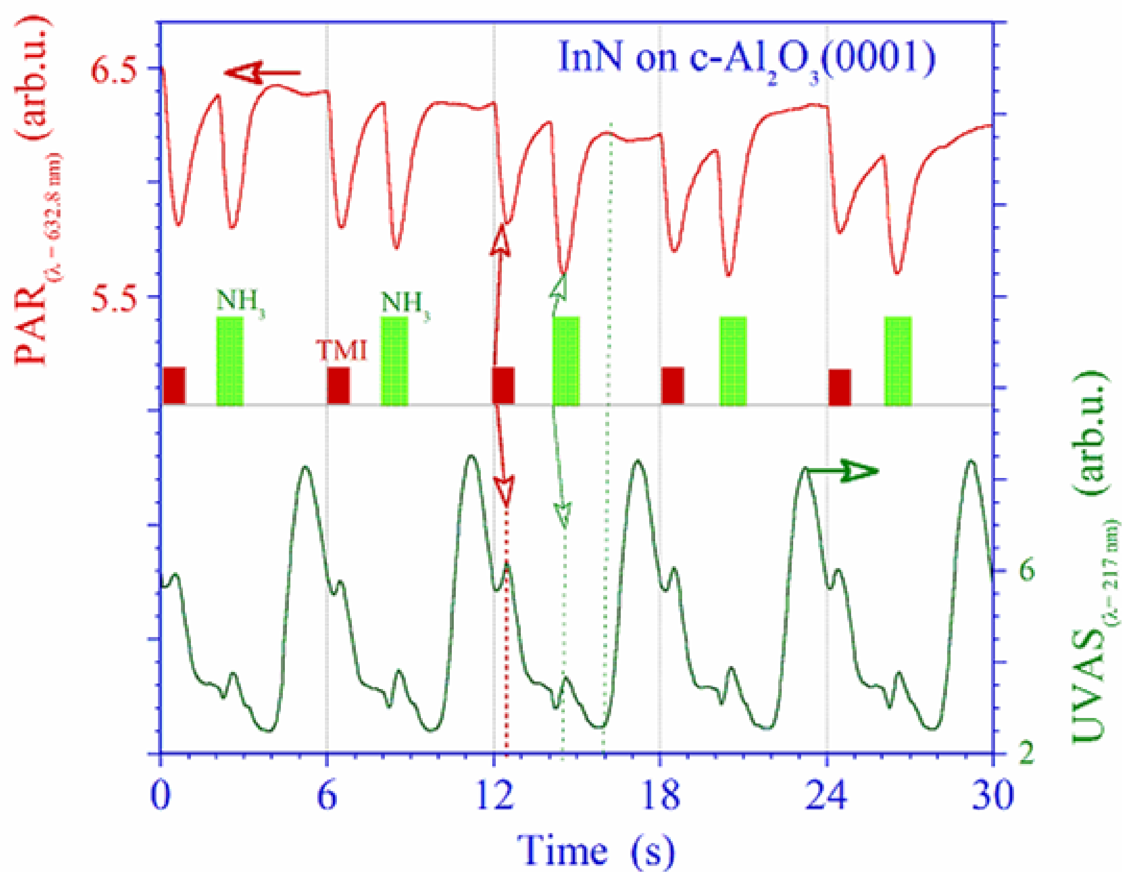

Figure 3.15 PAR and UV absorption traces during steady-state InN growth at 1090 K. The rector pressure was 15 bar with a total flow of 12 slm. The overall decrease in the PARS signal corresponds to InN growth.

3.9 Substrate choice

A primary requirement for the epitaxy of any material system is the availability of the proper substrate. Currently, the growth of group III-N thin films occurs predominately on sapphire substrates and AlN buffer layers. A brief summary of substrates and buffer layers used for growing III-Nitrides layers are going to be presented in the following sections.

3.9.1 Sapphire substrate

Sapphire (Al_2O_3) is the most extensively used substrate material for the growth of the InN, but it has a large lattice mismatch for InN(0001)/α-Al_2O_3(0001). Sapphire is a highly regarded material because it is semi-insulating, it can withstand high growth temperatures (~1000 °C) and good quality sapphire is available at low cost ($30 for a 2 inch wafer). The InN has a large lattice mismatch of ~25% with sapphire, very low thermal expansion coefficient (TEC), and very low thermal conductivity[28]. Those mismatches between sapphire and the InN epilayer can result in an extremely high density of structural defects. However, special growth techniques to alleviate strain and reduce intrinsic defect densities exist, which require substrate surface pretreatment and insertion of an intermediate buffer layer between the substrate and epilayer. Although the importance of a buffer layer was first demonstrated in MOCVD growth, it was also a big step for MBE grown InN layers[92]. Nitridation of the sapphire substrate surface significantly improves the crystalline quality of InN epilayer as a result of AlN layer formation. The AlN layer has the same lattice structure as InN and lattice mismatch is reduced to 13%. Crystal orientations of sapphire and InN (grown on *c* plane [0001] sapphire) are parallel, but two crystallographic orientations $\left([10\bar{1}0]_{InN}/[10\bar{1}0]_{\alpha-Al_2O_3}\right)$ and

$\left([10\bar{1}0]_{InN} / [10\bar{2}0]_{\alpha-Al_2O_3}\right)$ in the (0001) plane of InN crystal (double domain) are observed unlike single domain GaN and AlN. This is because the lattice mismatches of InN are relatively close in the two different orientations. However, only one orientation in the (0001) plane of InN crystal showed the epitaxial relation of $\left([10\bar{1}0]_{InN} / [10\bar{1}0]_{\alpha-Al_2O_3}\right)$[110]. We have reported that the InN film directly grown on sapphire with good crystalline quality is hexagonal and the FWHM of for InN (0002) is around 490 arcsec[12].

3.9.2 Si substrate

In addition to sapphire substrates, much effort has been aimed at the growth of InN on Si substrates[111,112]. Si is a suitable semiconductor substrate material for InN having a smaller lattice mismatch compared with sapphire; 8% for InN (0001)/Si (111). While there is significant lattice mismatch between Si and InN, the potential applications available as a result of implementing such a material system make it quite desirable. To accomplish integration of III-nitride LEDs or LDs with Si electronics, integration of optically active InN and In rich group III-Nitride device structures will have to be grown onto already existing Si based chip technology. The use of ammonia and hydrogen at high temperature will limit the application of Si due to the formation of a SiN_x layer on the substrate surface. The Si substrate surface becomes nitrided during the growth even at low growth temperature (400°C), which causes poor effects on the grown InN film. Recently, heteroepitaxial InN was successfully grown by radio-frequency nitrogen plasma assisted MBE (instead of ammonia) on Si substrates at low temperature by using a double-buffer layer [111]. Ahn *et al.* demonstrated by XRD analysis and scanning electron microscopy that such InN films are high quality and of single crystal form. The carrier concentration of those InN samples is around 6×10^{18} cm^{-3}, but an n-type carrier

concentration lower than 10^{16} cm^{-3} is required for optoelectronic IC devices on Si substrates.

3.9.3 GaN and AlN templates

The difficulties in preparation of high quality InN due to the lattice mismatch and lack of suitable substrate material motivated researchers to seek a new substrate material other than sapphire and Si. One common solution is to insert an intermediate thin buffer layer between α-Al_2O_3 and the subsequent film. In this solution, a thin AlN buffer layer is grown at low temperature (400 °C) after nitridation or deposition of the AlN layer by using a growth technique at high temperature (1050 °C). Using an AlN buffer layer improves the structural (FWHM of XRD InN (0002) ~300 arcsec) and electrical properties of InN (μ_{300K}=2050 $cm^2V^{-1}s^{-1}$). In order to improve the InN quality for realization of optoelectronic device applications, high quality GaN templates are essential for the growth of InN films[1,113]. Growing InN films on GaN/sapphire substrates with a low temperature deposited AlN buffer layer reduces the lattice mismatch to 11%.

One of the important characteristics of III-Nitrides is polarity. Significant effects of the polarities on InN film grown on Ga-Polar and N-Polar GaN templates by different growth techniques were observed[114]. It was found that the quality of InN is strongly affected by the polarity of GaN. High quality and thick InN films can be grown on Ga-Polar GaN templates by High Pressure CVD in contrast to InN samples grown on N-polar GaN by MBE[78,114].

3.9.4 Other potential substrates and templates

Several other materials have also been used as a substrate or template such as MgAl2O4, glass, GaP, GaAs, InP and InAs[1]. From the point of lattice and thermal

mismatch with the InN, GaP and GaAs have a smaller lattice mismatch (8% and 11.3% respectively) than that of sapphire. However, for obtaining uniform and high quality InN, *As* species on GaAs surfaces should be eliminated prior to the InN growth. But high temperature NH_3 nitridation of InAs and GaP causes the formation of AsN_x and PN_x on the substrate surface[1].

3.10 Ex-Situ Characterization Tools

A brief overview of the characterization techniques used in this study is provided in the following sections

3.10.1 X- ray diffraction

X-ray diffraction is a powerful, non-contact method used in order to understand the crystalline phases in bulk materials, thin films and powder samples. Additionally, X – ray diffraction can determine the strain state, grain size, epitaxy, phase composition, preferred orientation, and defect structure of individual phases. The principle of this technique involves X-ray waves interacting with atomic planes in materials that will exhibit the phenomenon of diffraction. A schematic of the diffraction process is shown in Figure 3.16. X-rays scattered off the sample will do so at an equal angle. X-rays scattering off of neighboring parallel planes of atoms will interfere destructively at a certain angle of incidence. At other angles, these waves will interfere constructively and result in a large output signal at those angles. These constructive interferences occur when the Bragg condition is met for these X-rays, given by the famous expression:

$$n\lambda = 2d\sin\theta \tag{3.7}$$

where n is an integer, λ is the wavelength of the X-ray source, d is the lattice spacing, and θ is the Bragg angle. The reflected diffraction pattern from the epilayer determines the *a*-

spacing and *c*-spacing lattice constants of a material according to Bragg's law. The line width of a rocking curve measurement (ω scans) i.e., the full width at half maximum (FWHM), determines the crystalline quality. In addition, a rocking curve scan on an *a*-axis or *c*-axis estimates crystalline quality. X-ray diffraction analysis of InN films was performed using a Philips X`pet MRD with a copper X-ray source.

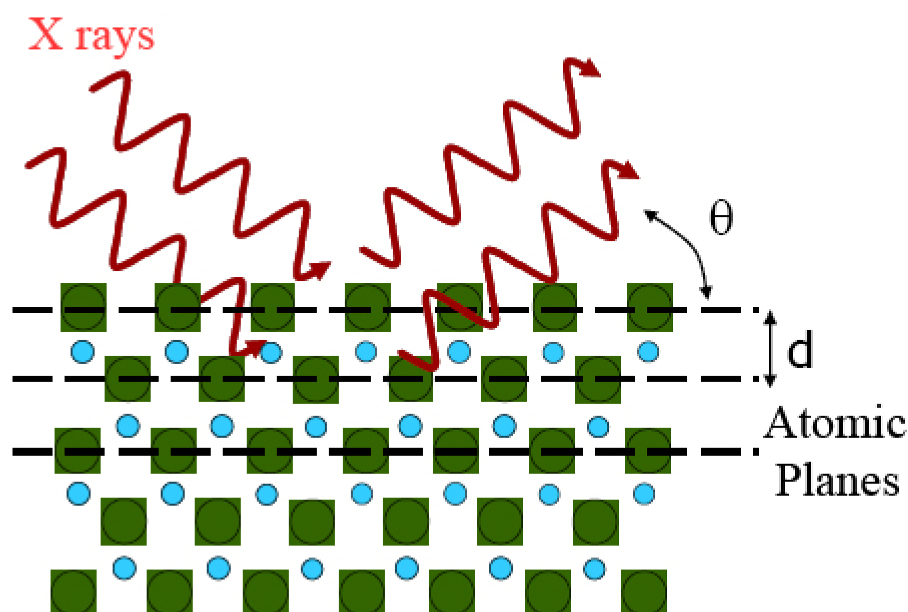

Figure 3. 16 Diagram of the experimental geometry for X-ray diffraction.

3.10.2 Auger electron spectroscopy

Auger Electron Spectroscopy (AES) is a very sensitive technique for monitoring the surface cleanliness and determining surface composition[115]. The sensitivity of AES is ~%1 of a monolayer except for hydrogen and helium, since this technique is a three electron process technique. In an Auger process, the atom is ionized by removal of an electron from the core level by an impinging high-energy electron beam. The atom may decay to a lower energy state by emission of x-rays, by ejecting an electron called an

Auger electron, which leaves the atom in a doubly ionized state. The kinetic energy of the Auger electron is given by

$$E_{kin} = E_1 - E_2 - E_3 \tag{3.8}$$

where E_1, E_2 ,and E_3 are respectively the core level, first outer shell, and the second outer shall electron energies, measured from the vacuum level. Figure 3.17 shows the complete Auger process. The Auger system used for InN sample analysis includes a 4-grid SPECTALEED optics system (retarding field analyzer (RFA)), LEED screen for detection and Lathanum-hexoboride filament for producing the electron beam.

3.10.3 Low Energy Electron Diffraction

LEED is a surface sensitive technique due to its low incident electron energy of approximately around 100 eV. The basic principal underlying the low energy electron diffraction is Bragg's Law. Electrons follow the wave-particle duality. From the De-Broglie relation, the wavelength of the electron having momentum P is given by $\lambda = h / P$ where momentum $P = mv = (2mE_k)^{1/2} = (2meV)^{1/2}$, h = Planck's constant, m = mass of an electron, e = charge of an electron, and V = accelerating voltage. If the incident energy of the electron is in the range of 20-200 eV, then the wavelength varies from 2.7 to 0.87 Å, matching with the

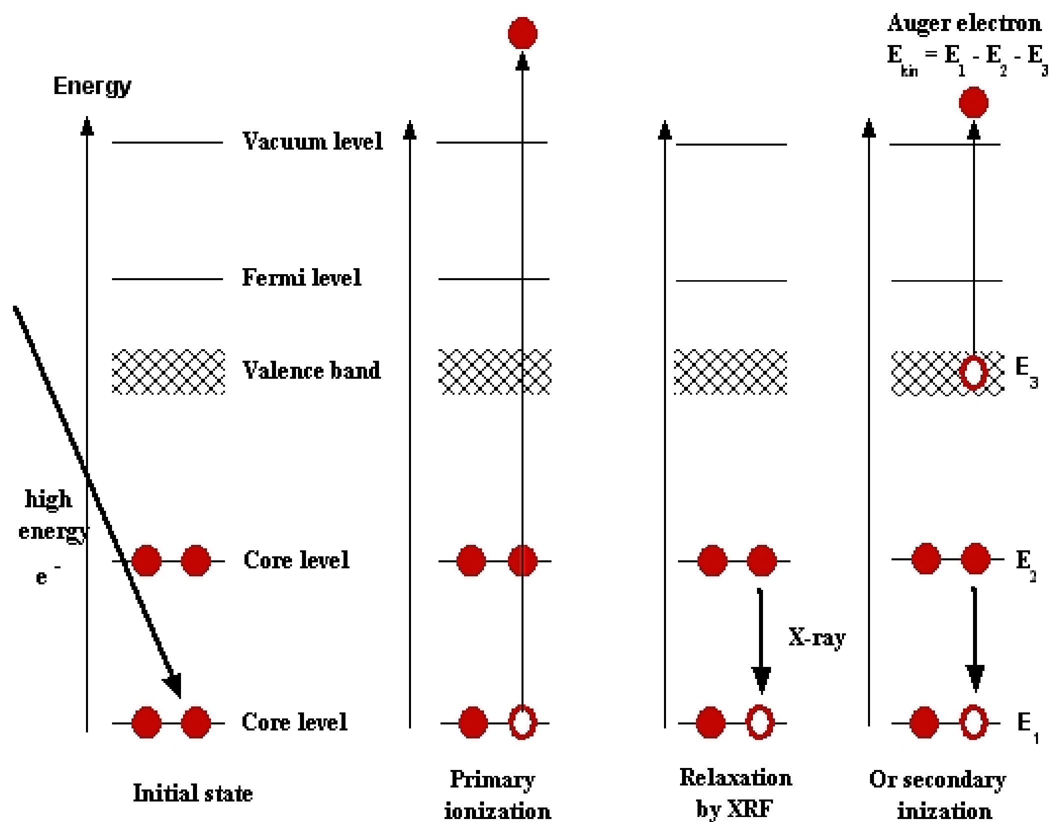

Figure 3. 17 Auger electron process.

lattice spacing which is one of the necessary conditions for diffraction effects associated with atomic structure to be observed.

A schematic diagram of the LEED apparatus[79] is given in the Fig. 3.18. The system consists of an electron gun (which produces the primary electron beam), the sample (mounted perpendicular to the electron gun), four hemispherical grids of high transparency, and a fluorescent screen, which is maintained at a 6 keV positive potential.

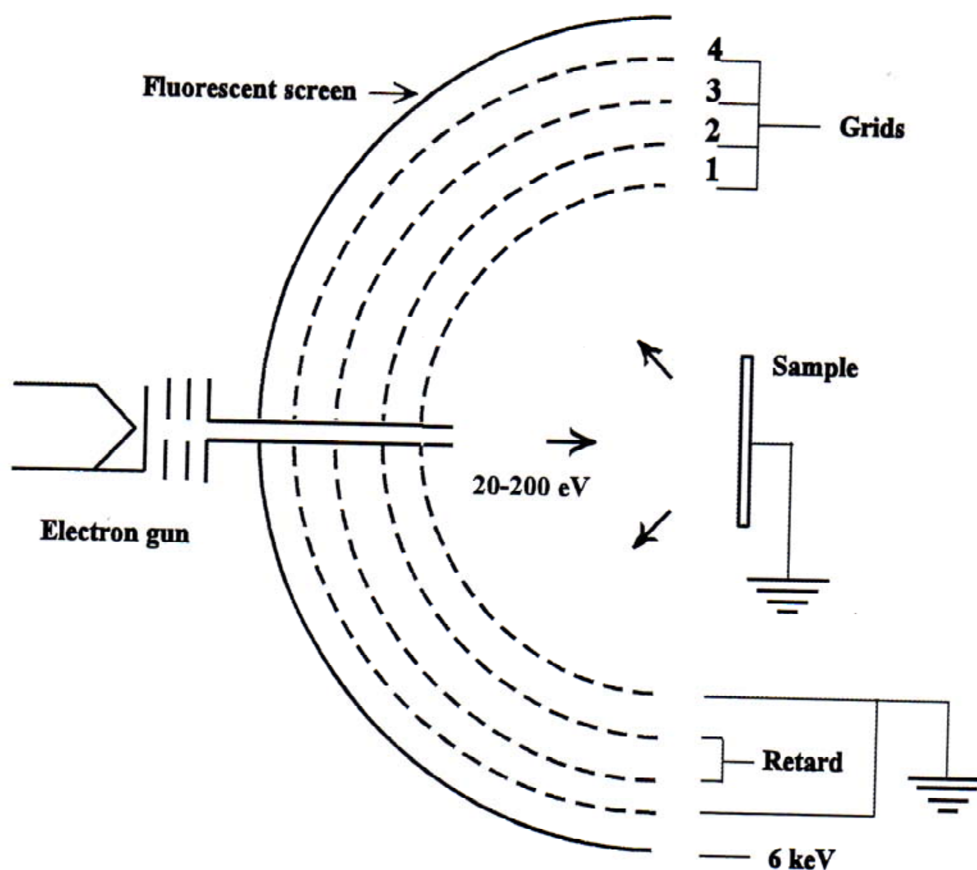

Figure 3. 18 Schematic representations of the LEED apparatus.

3.10.4 High resolution electron energy loss spectroscopy

HREELS is a non-destructive and surface sensitive vibrational spectroscopic technique by which vibrations of adsorbates on the crystal surface and low energy electronic excitations can be studied. The high-sensitivity (< 0.1% of a monolayer) and broad spectral range (0-1000 meV or 0-8000 cm^{-1}) of the method make HREELS an ideal tool for exploring the properties of a wide variety of surfaces. In the HREELS technique, a highly monochromatic beam of electrons is incident on a surface at a particular angle and the electrons are scattered from the surface inelastically. HREELS has several

vibrational excitation mechanisms. In the dipole scattering (long range) mechanism, the electric field of an incident electron interacts with the varying electric field by molecular vibration only perpendicular to the surface. In impact scattering (short range), the incoming electrons impact atoms and molecules at the surface, leading to vibrational excitation. The scattered electrons lose energy by exciting the surface vibrational modes such as surface phonons and the adsorbate vibrational modes of the atoms and molecules on the surface. The energy of the scattered electrons can be given as

$$E_{\text{scattered}} = E_{\text{incident}} - E_{\text{vibration}}. \tag{3.9}$$

The HREELS apparatus used in this study is the ELS3000 manufactured by LK technology.

3.10.5 Atomic Force Microscopy

Atomic force microscopy is a useful technique for deriving atomic-resolution information about the surface morphology and surface roughness in InN samples. Figure 3.19 shows a schematic of the microscopic setup. In this technique, an atomically sharp tip mounted at the end of a cantilever is scanned across the surface of the sample. When the tip moves up and down over its topography, the displacement caused by the features on the surface can be measured to create an image. The AFM measures the Van der Waals force between the tip and the surface; this may be either the short-range repulsive force (in contact-mode) or the longer-range attractive force (in non-contact mode). There are three scanning modes associated with AFM, namely; contact mode, non-contact mode, and tapping mode. Contact mode is the scanning mode in which the tip is in contact with the surface and the image is obtained by repulsive forces between tip and the sample. In tapping mode, the image is obtained by the tip, which just taps the surface for small

periods of time. In non-contact mode, the tip oscillates above the surface, and the image is obtained from the attractive forces between the tip and the sample. The tip is scanned over a surface with feedback mechanisms that enable the piezo-electric scanners to maintain the tip at a constant force (to obtain height information) or height above the sample surface(to obtain force information). As the tip scans the surface of the sample, the focused laser beam is deflected off the attached cantilever into a position sensitive dual photodiode system. Feedback from the dual photodiode system and the control software enables the tip to maintain either a constant force or constant height above the sample. The surface morphology of the InN layers in this thesis was analyzed using a PSIA-XE-100 AFM in both contact and non-contact mode.

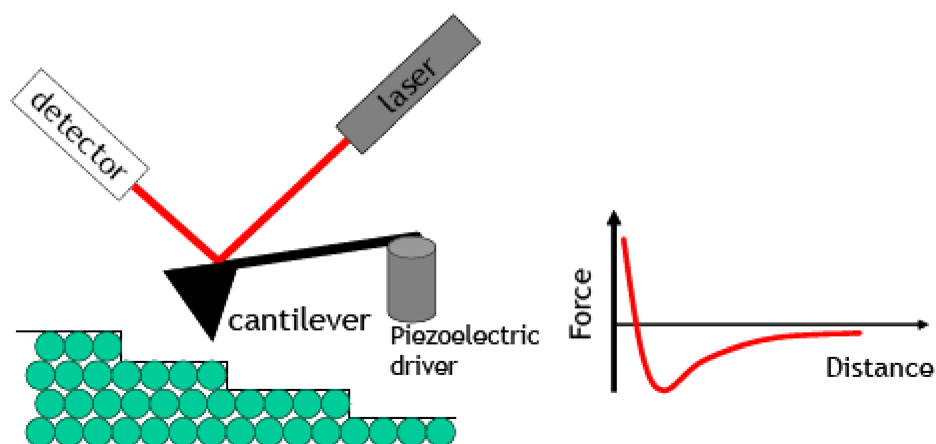

Figure 3. 19 Diagram of an atomic force microscopy set up.

3.10.6 Infrared reflection spectroscopy

Theoretical model

IR reflectance spectroscopy results are analyzed by introducing an IR dielectric function in order to obtain the phonon and plasmon properties, carrier concentrations, carrier mobility, layer thickness, and interface behavior. In order to determine the dielectric function, the interaction of electromagnetic radiation with the matter is established through solution of the equations of motion for atoms. The IR dielectric function can be written as in the following assuming the phonons and free carriers

$$\varepsilon = \varepsilon(\omega) = \varepsilon_\infty + \sum_i \frac{s_i\left(\omega_{TO}^2 - \omega_{LO}^2\right)}{\omega_{TO}^2 - \omega^2 - i\omega\Gamma} - \frac{\varepsilon_\infty \omega_p^2}{\omega^2 + i\omega\gamma_p}, \tag{3.10}$$

where γ_p is the electron damping due to the scattering from randomly distributed stationary impurities, ω_p is the plasmon frequency, Γ is the oscillating broadening constant, $\omega_{TO}, \omega_{LO}, S_i$ are the frequency, oscillator strength, and damping parameter of the *i*th oscillator. ε_∞ is the dielectric response in the high-energy limit for the film.

Light propagation in a multilayer thin film structure is modeled using the Transfer Matrix Method[116,117]. Reflectivity can be calculated by solving the Maxwell equations for plane electromagnetic waves with boundary conditions for the electric/magnetic field component at the air/film and film/substrate interfaces. There are two waves with the electric-field amplitudes E^+ and E^- propagating in opposite directions in each layer. Suppose '0' refers to air, '1' the film, and "2" the substrate, respectively. The resultant matrix M_r is described by the following:

$$M_r = M_{01} M_1 M_{12}. \tag{3.11}$$

Here, the interface matrix between the *jth* and *(j+1)th* layers has the

$$M_{j,j+1} = \frac{1}{2\sqrt{\varepsilon_{j+1}}}\begin{pmatrix} \sqrt{\varepsilon_{j+1}} + \sqrt{\varepsilon_j} & \sqrt{\varepsilon_{j+1}} - \sqrt{\varepsilon_j} \\ \sqrt{\varepsilon_{j+1}} - \sqrt{\varepsilon_j} & \sqrt{\varepsilon_{j+1}} + \sqrt{\varepsilon_j} \end{pmatrix} \quad (3.12)$$

and the propagation matrix for the film with the thickness d is described by

$$M_1 = \begin{pmatrix} \exp\left(i2\pi\sqrt{\varepsilon}d \big/ \lambda \right) & 0 \\ 0 & \exp\left(-i2\pi\sqrt{\varepsilon}d \big/ \lambda \right) \end{pmatrix} \quad (3.13)$$

where λ is the incident wavelength. Thus, the reflectance *R* can be written as

$$R = \left| \frac{M_{r1,0}}{M_{r1,1}} \right|^2 . \quad (3.14)$$

Experimental details

Infrared reflection measurements were carried out using the Perkin Elmer System 2000 Fourier transform infrared spectrometer along with a Graseby reflection accessories set up. A Mercury Cadmium Telluride (MCT) detector was used for the short wavelength (1.5-20 μm) range, and a TGS based pyroelectric detector was used for the long wavelength (<50 μm) range. An aluminum mirror was used to collect background spectra I_0. Then, this mirror was replaced with the InN sample and scanned for the same number of interferograms. After Fourier transformation, this yields I_R, the reflected intensity spectrum. The reflectivity spectrum R of the InN film is then determined by the ratio I_R/I_0.

The best-fit parameters for the InN film and GaN film were obtained using the nonlinear Levenberg-Marquart[118] fitting algorithm.

3.10.7 Raman spectroscopy

Raman spectroscopy is another valuable source of information about the characteristics of the crystal lattice. Raman spectroscopy is used for structure determination, stress analysis, defect analysis, and free carrier determination. The interaction of an external light source (electric field) with the matter leads to a polarization. This induced polarization has two terms; one term represents the elastic scattering and second term represents the inelastic scattering process (Raman Scattering), which consists of Stoke and anti-Stoke terms. These inelastically scattered, anti-Stoke and Stoke light beams appear as weak peaks, several orders of magnitude weaker than the laser line, which must be filtered out in order to observe the Raman signal. According to the symmetry of the crystal and vibrational mode, the intensity of the scattered radiation has a non-zero value only for specific polarizations and scattering geometries. These are known as Raman selection rules, which are essential for determining the crystal symmetry and allowed Raman modes. Hexagonal InN crystallizes into the structure of wurtzite with four atoms in the unit cell and belongs to C^4_{6v} space group. According to group theory analysis at the Γ point, the phonon modes in hexagonal InN are characterized by the following irreducible representations.

$$\Gamma_{ac} + \Gamma_{opt} = \left(A_1 + E_1\right) + \left(A_1 + 2B_1 + E_1 + 2E_2\right). \qquad (3.15)$$

Raman selection rules predict that A_1 and E_1 modes are both Raman and IR active, E_2 is only Raman active and B_1 is called the silent mode. Thus six optical modes may be observed in a first order Raman spectrum[4]: E_2(high), E_2(low), E_1(LO), E_1(TO), A_1(TO),

and A_1(LO). The Raman selection rules for the wurtzite structure of group III-nitrides are given in Table 3.2, of which x(yz)y belongs to 90° scattering geometry, while z(xy)$\underline{z}$, x(zz)$\underline{x}$, x(yy)$\underline{x}$, and x(zy)$\underline{x}$ belong to the backscattering geometry. The allowed modes are highly sensitive to the polarization of the incident light and orientation of the crystal. The Raman spectra reported in accordance with the Porto notation C(BA)D , where C and D the propagation directions of the incident and scattered light and B,A represent their polarizations. Therefore, Porto notation is a convenient method for identifying the direction and polarization of the laser light incident on a crystal. Hexagonal InN thin films are usually grown along the [0001] direction of the substrate, which puts the c-axis of the hexagonal structure perpendicular to the crystal plane. Therefore, under backscattering geometry, the z(xx)$\underline{z}$ and z(xy)$\underline{z}$ configurations are easily observable due to the z-direction being along the [0001] direction.

Table 3. 2 Raman Selection rules for hexagonal group III-nitrides.

Configuration	Allowed Mode
z(xx)$\underline{z}$	A_1(LO), E_2(low), E_2(high)
z(xy)$\underline{z}$	E_2(low) , E_2(high)
x(zz)$\underline{x}$,	A_1(LO)
x(yy)$\underline{x}$,	A_1(LO) ,E_2(low), E_2(high)
x(zy)y,	E_1(TO), E_1(LO)
x(yz)$\underline{x}$,	E_1(TO), E_1(LO)

InN layer Raman measurements were carried out with a custom build Micro Raman spectrometer, which consists of a McPherson 2062 scanning monochromator as the main monochromator, and a McPherson 275 DS double subtractive monochromator

as a variable notch filter with an 2.33 eV excitation source. The signal is collected by a nitrogen cooled CCD.

3.10.8 Transmission spectroscopy

Theoretical model

Photons with sufficient energy can excite electrons from the filled valence band to the empty conduction bands. In the case of samples that are sufficiently thin, the optical transmission spectra lead to the determination of the band gap energy and also defect levels within the band gap of the semiconductor. For photon energies greater than the band gap of the semiconductor, E_g, the absorption is dominated by band-to-band transitions. The spectral region where the material changes from being relatively transparent $(h\upsilon < E_g)$ to strongly absorbing $(h\upsilon > E_g)$ is known as the absorption edge of the material.

The optical properties of InN (ε_{InN}, d_{InN}) were also analyzed by fitting the transmittance spectrum of an “ambient / InN / GaN / Sapphire” stack using the dielectric functions of the group III-nitrides based on the “model dielectric function” (MDF) approach[119]. The MDF model for the InN dielectric function has been modified by adding two additional oscillators at 0.8 eV and 0.4 eV, and by adjusting the band gap oscillator E_0. The modified MDF model dielectric function for InN is given by

$$\tilde{\varepsilon} = \varepsilon'_{InN}(\omega) = \varepsilon_{InN} + \sum_{n=1}^{2} \frac{S_{ab}}{\left[E_{ab}^2 - (h\omega)^2\right] - ih\omega\Gamma_{ab}} \qquad (3.16)$$

where S_{ab} is the oscillator strength, E_{ab} is the energetic position and Γ_{ab} is the damping constant of the added Lorentzian. The transmission coefficient for a double layer system presented below. The system is shown in Figure 3.20 with the Maxwell boundary

conditions at each of the interfaces. The Fresnel equations can also be applied in order to describe changes in the transmittance for multiple heterostructures assuming homogeneous isotropic properties. Fresnel coefficients are the same for both components of polarization for the special case $\varphi_0 = \varphi_t = 0$ and can be rewritten as:

$$r_{k(k+1)p} = r_{k(k+1)s} = r_{k(k+1)} = \frac{\varepsilon_{k+1}\sqrt{\varepsilon_k} - \varepsilon_k\sqrt{\varepsilon_{k+1}}}{\varepsilon_{k+1}\sqrt{\varepsilon_k} + \varepsilon_k\sqrt{\varepsilon_{k+1}}} \tag{3.17}$$

$$t_{k(k+1)p} = t_{k(k+1)s} = t_{k(k+1)} = \frac{2\sqrt{\varepsilon_k}}{\sqrt{\varepsilon_k} + \sqrt{\varepsilon_{k+1}}} \tag{3.18}$$

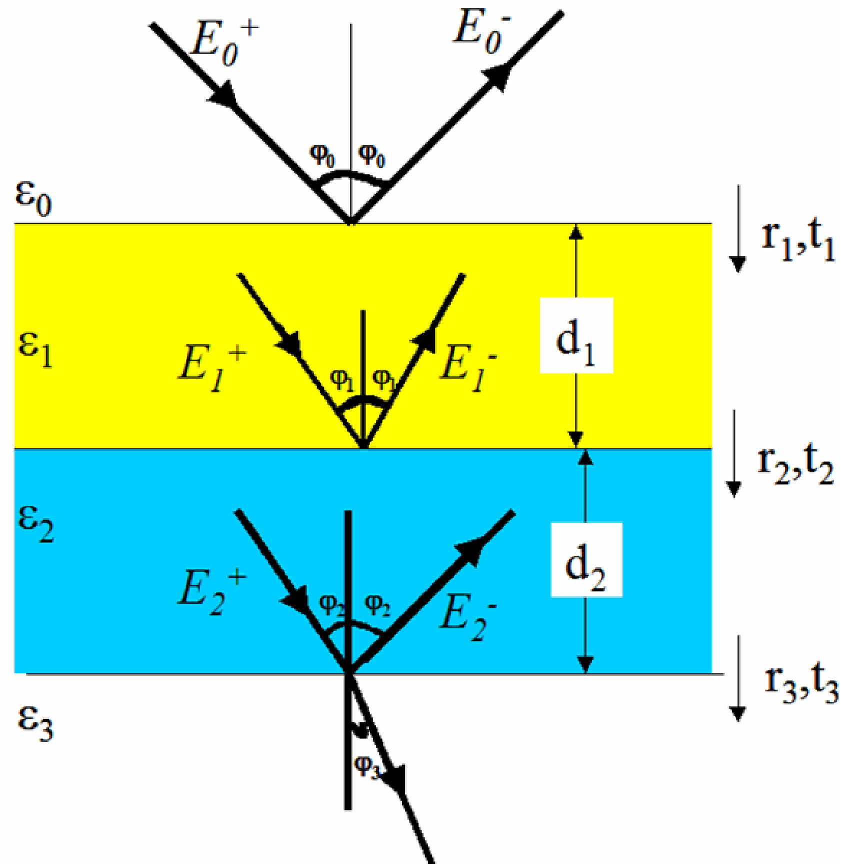

Figure 3. 20 Propagation of an electromagnetic wave through a double film.

The transmitted amplitude *tt* can be calculated from matrix multiplication. The equations can be written in a matrix for the 2 layer stack

$$\begin{pmatrix} E_0^+ \\ E_0^- \end{pmatrix} = \frac{1}{t_1 t_2 t_3} \begin{pmatrix} 1 & r_1 \\ r_1 & 1 \end{pmatrix} \begin{pmatrix} e^{i\delta_1} & r_2 e^{i\delta_1} \\ r_2 e^{-i\delta_1} & e^{-i\delta_1} \end{pmatrix} \begin{pmatrix} e^{i\delta_2} & r_3 e^{i\delta_2} \\ r_3 e^{-i\delta_2} & e^{-i\delta_2} \end{pmatrix} \begin{pmatrix} E_3^+ \\ E_3^- \end{pmatrix} \qquad (3.19)$$

where

$$\delta_k = \frac{2\pi}{\lambda} \sqrt{\varepsilon_k} d_k \cos\varphi_k \,. \qquad (3.20)$$

Labeling starts from "0" for ambient, "1" for the first film, "2" for the second film and "3" for the substrate. The transmitted amplitude for a 2 layer film is given by

$$tt = \frac{E_3^+}{E_0^+} = \frac{t_1 t_2 t_3 e^{-i(\delta_1+\delta_2)} e^{i\frac{2\pi\sqrt{\varepsilon_3} d_2 \cos\varphi_3}{\lambda}}}{e^{i\delta_1} + r_1 r_2 e^{-2i\delta_1} + r_1 r_3 e^{-2i(\delta_1+\delta_2)} + r_2 r_3 e^{-2i\delta_2}} \,. \qquad (3.21)$$

We applied this description to the calculation of transmissions

$$T = tt * tt^* \qquad (3.22)$$

for the Air/InN/GaN/Substrate multilayer heterostructure. The transmitted amplitude for 1 layer is given by

$$tt = \frac{E_2^+}{E_0^+} = \frac{t_1 t_2}{e^{i\delta_1} + r_1 r_2 e^{-i\delta_1}} \,. \qquad (3.23)$$

We used this expression for calculating transmission through the Air/InN/Substrate one layer structure.

Experimental details

Room temperature transmission measurements were performed with a custom built near-infrared-visible-UV spectrometer (scanning spectral range between 300 nm and 2800 nm), which consists of a triple-grating, ½ meter length, monochromator with phase-sensitive signal detection and processing. Emission from a halogen light source

was used to provide the spectral range for the measurements. The transmitted light from the UV to near infrared spectral region was collected using different detectors, including a photo multiplier tube (Hamamatsu R928)(300-900nm), an Indium Gallium Arsenide (InGaAs)(800-1700nm) detector, and a Mercury Cadmium Telluride (HgCdTe or MCT) (1600-2800nm) IR detector.

3.10.9 Photoluminescence

Photoluminescence (PL) refers to the emission of the light resulting from optical stimulation. In the PL technique, a suitable laser that has a photon energy output higher than the band gap of the semiconductor is incident on the surface of the sample, which will generate electron hole pairs. Those electron hole pairs will recombine, often through a radiative transition back to the ground state of the atom. Some of the observed recombination pathways are presented in Figure 3.21. Information about the band structure, donor and acceptor levels, defect types, impurities, crystalline quality, and defect densities in the material system can be extracted by measuring the wavelength of the emitted photon.

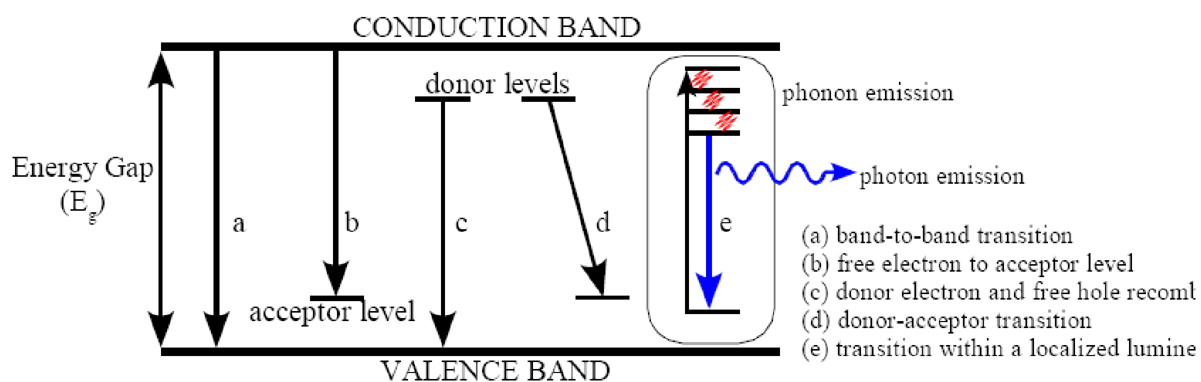

Figure 3. 21 Schematic representation of possible optical transitions that can be observed via photoluminescence.

Chapter 4

Growth of high quality single phase InN crystals by high pressure CVD

Published as: The characterization of InN layers grown by high-pressure chemical vapor deposition. Mustafa Alevli, Goksel Durkaya, William Fenwick, Aruna Weesekara, Vincent Woods, Ian T. Ferguson, A. G. U. Perera and Nikolaus Dietz, Applied Physics Letter, **89,** pp. 112119 (2006)

4.1 Introduction

In recent years, research on InN material optimization has dramatically increased, largely due to the crucial importance of indium-rich group III-nitride alloys in novel devices for solid-state lighting, photovoltaics, spintronics, or terahertz applications, utilizing the large spectral tenability and multi-functionality of group III-nitride alloys. However, the integration of indium-rich group III-nitride layers into $Ga_{1-x}A_{lx}N$ alloys strongly depends on the existence of overlapping processing windows as well as on precise control of thermal decomposition pressures of indium-rich alloys at the optimum processing temperature.

Presently, the most efficient growth of group III-nitride semiconductor devices is by organometallic chemical vapor deposition (MOCVD). However, epitaxial growth of InN at low pressure conditions such as MOCVD or MBE is problematic due to the large thermal decomposition pressure at its optimum growth temperature, creating conflicting

material properties due to the point defect chemistry in InN, which at present is not well understood[2,4]. Surface stabilization data showed that InN can be grown at much higher temperatures in high nitrogen pressures[16], evoking the development of a novel HPCVD system at Georgia State University, in order to control the vast different partial pressures of the constituents involved in the growth of indium-rich group III-nitride alloys[9-11,99,120]. The combination of HPCVD and real time process monitoring control have been demonstrated to be viable to improve the InN materials properties, with InN growth temperatures as high as 1150 K for reactor pressures around 15 bar. This is a major step towards the fabrication of indium rich group III-Nitride heterostructures by providing a close match to the processing windows used for GaN –AlN alloys.

4.2 Growth of InN by HPCVD

InN layers were grown by HPCVD, a high-pressure flow channel reactor with incorporated real time optical characterization capabilities in order to study and optimize InN nucleation and growth. Ammonia (NH3) and trimethylindium (TMI) are employed in a pulsed injection scheme, utilizing pulse width, precursor pulse separation, and cycle sequence time as control parameters to engineer gas phase and surface chemistry kinetics. The precursors are embedded in a high-pressure carrier stream (ultra-pure nitrogen) and injected in the reactor utilizing a temporally controlled gas injection system.

The InN layers investigated here were grown at growth temperatures of 1150 K, a reactor pressure of 15 bar, an ammonia to TMI precursor ratio of 600, and a total gas flow of 12 slm. The gas flow as well as the reactor pressure is kept constant at all times during the growth. The temperature setting refers to the calibrated correlation of the analyzed blackbody radiation as a function of the power setting of the substrate heater

and is not corrected for the change in surface emissivity during the growth. Details of the HPCVD reactor, the growth configuration, as well as real-time optical characterization techniques employed have been published elsewhere[11,13].

4.2 Characterization of InN

XRD measurements were carried out in a theta-two-theta coupled geometry using K_α x-rays to evaluate the presence of secondary phases or polycrystallinity. A one-half degree slit was used on the incident beam optics and a one-quarter degree slit on the diffracted beam optics for XRD. The Raman spectra are observed in backscattering configuration. All spectra are normalized to the peak intensity of the E_2 (high) phonon feature. Room temperature IR reflection measurements have been performed over the frequency range of 200- 8000 cm^{-1} (50-1.25 μm) by using a Perkin-Elmer system 2000, Fast Fourier transform infrared spectrometer (FTIR) and Graesby optical reflection accessory setup. All IR reflection spectra were taken under a near normal (~8 deg) incident light arrangement to minimize anisotropy effects. Room temperature transmission measurements were performed with a custom built NIR-VIS-UV spectrometer, which consists of a triple-grating, ½ meter length monochromator, photomultiplier, InGaAs detector, and HgCdTe photodiodes and phase-sensitive signal detection and processing.

Figure 4.1 shows the variation of XRD patterns in a logarithmic scale for InN layers grown directly on sapphire and on a virtual GaN-Sapphire substrate. The XRD peaks for samples #76 U and #71U are centered at 2-θ= 31.357 and 31.243°, respectively.

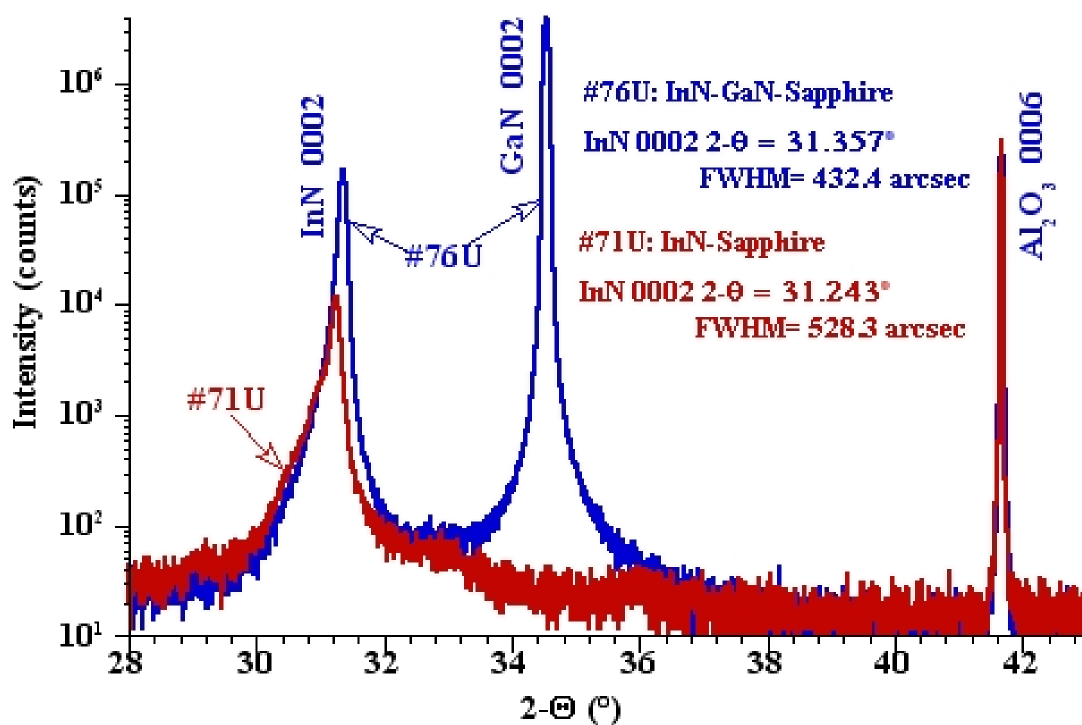

Figure 4. 1 XRD spectra for InN layers grown on sapphire (#71 U) and on a virtual GaN/Sapphire substrate (#76U).

These peaks correspond to the diffraction of the hexagonal phase InN(0002) plane. The " Full width half maximum" (FWHM) of the InN (0002) peaks are 432 arcsec and 528 arcsec for the InN layers deposited on GaN/Sapphire and Sapphire substrate, respectively. The slight asymmetry on the left hand of the InN(0002) peaks may indicate the presence of a second phase in very close proximity, but further studies are needed to clarify its origin. Figure 4.2 shows the uniformity of InN layer grown on GaN/Sapphire substrate. Figure 4.3 shows Raman spectra of InN samples grown on sapphire (#71U) and GaN/Sapphire substrate (#76U), which were analyzed an using excitation energy of 2.33 eV.

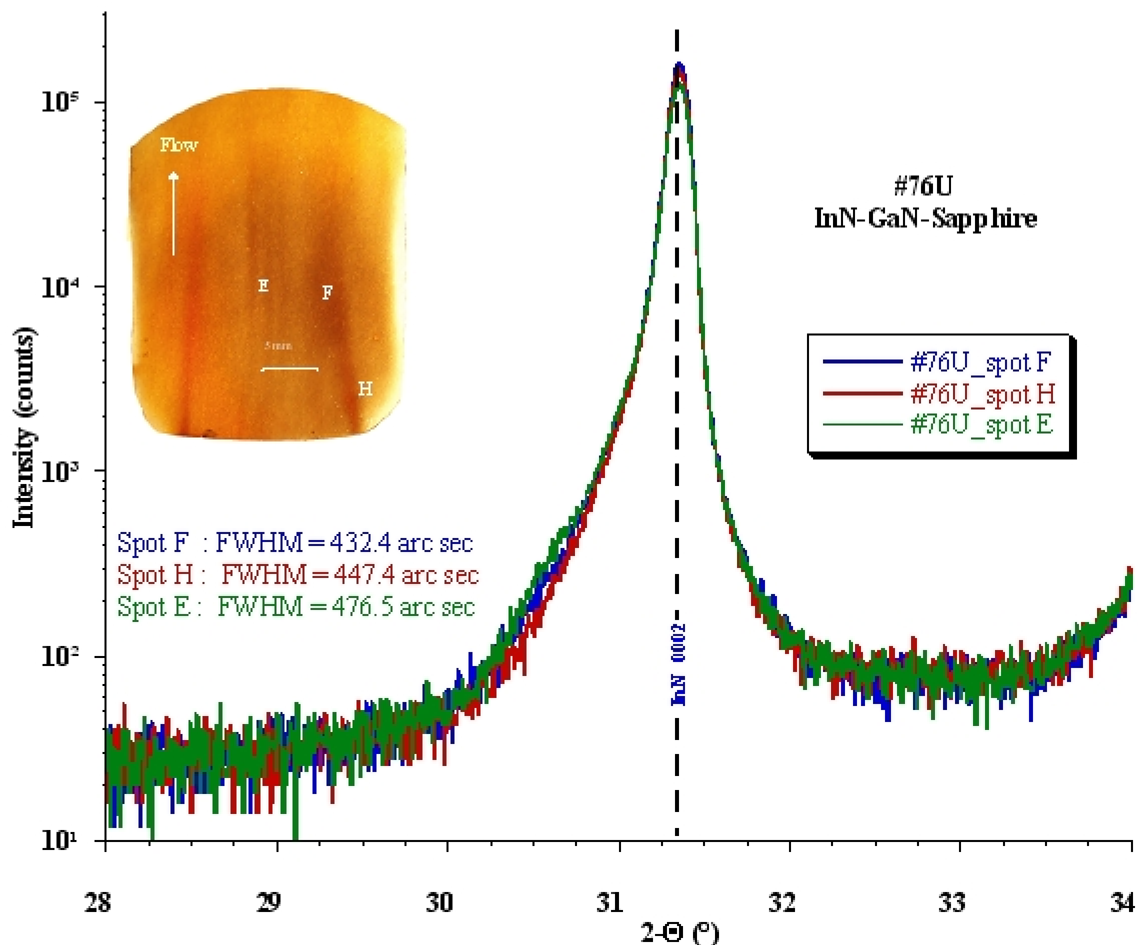

Figure 4. 2 Uniformity of an InN layer grown on a virtual GaN/Sapphire substrate (#76U). The inset shows a photograph of wafer area analyzed.

The three optical phonon modes of hexagonal InN at 300 K analyzed in Raman spectra are E_2 (high), A_1(LO) and B_1(high). The peak centered at wave numbers in the range 489-492 cm^{-1} is attributed to scattering of light from E_2 (high) phonon modes which is most sensitive to strain, whereas, the peak at 587 cm^{-1} is assigned to A_1(LO) phonons in InN. The peak positions are in good agreement with those found in InN layers grown by MBE and OMCVD. Based on the allowed phonon mode peak positions for E_2 (high) and A_1(LO), our experimental peak positions are similar to the calculated values of 483 and 588 cm^{-1} by Davydov and Kloichikhin.[4]

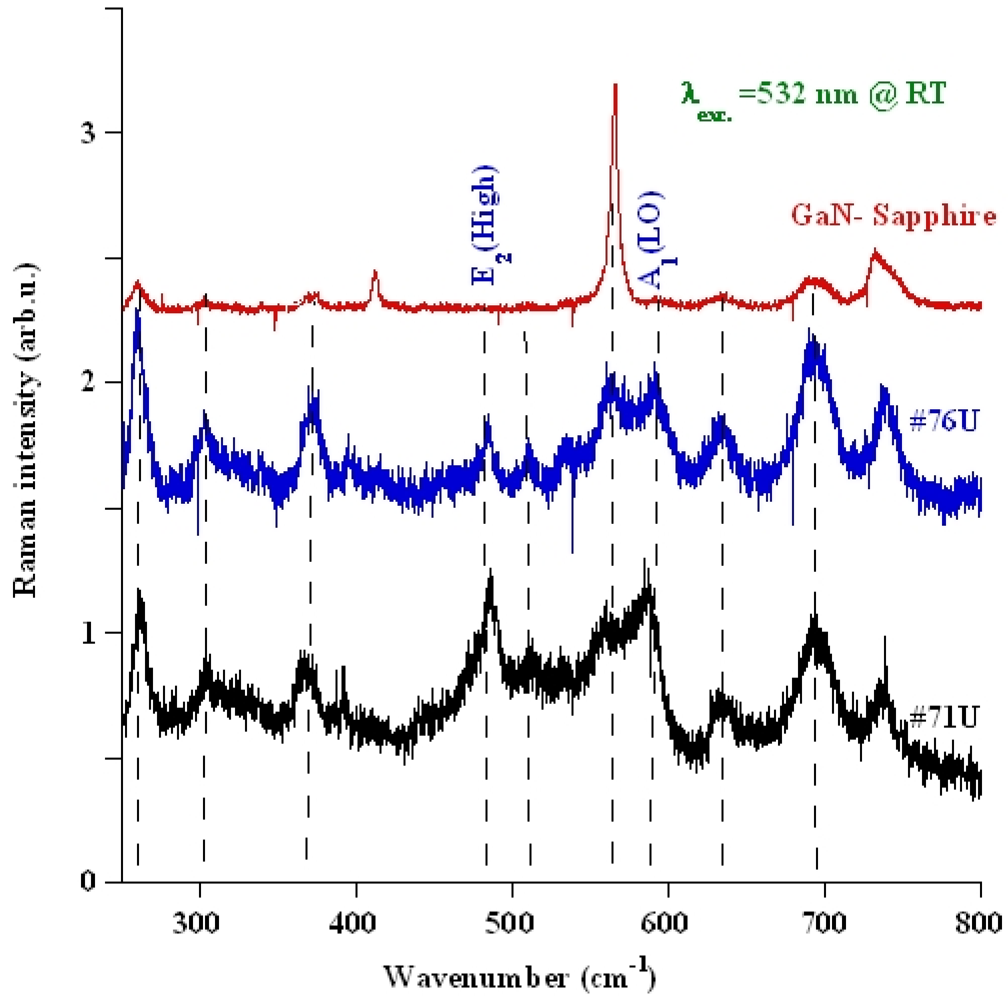

Figure 4. 3 Raman spectra for InN layers grown on sapphire (# 71U) and on a GaN epilayer (#76U).

Figure 4.4 depicts the IR reflectance spectrum for sample #76U and the analysis of optical properties in the IR region. The dielectric functions of the InN and GaN layers are modeled using equation 4.1, assuming two oscillators, one of which is the Lorentz oscillator for phonons and the second the classical Drude oscillator for the plasma frequency,

$$\varepsilon(\omega) = \varepsilon_{\infty}\left[1 + \frac{\omega_{LO}^2 - \omega_{TO}^2}{\omega_{to}^2 - \omega^2 - i\omega\Gamma} + \frac{\omega_p^2}{\omega^2 + i\omega\gamma_p}\right] \tag{4.1}$$

where ε_∞ is the high frequency dielectric constant, ω_{LO} and ω_{TO} are LO and TO frequencies of E_1 phonon mode, ω_p is the plasma frequency, and Γ and γ_p are the damping constants of the two oscillators. Similarly, the dielectric function for GaN epilayer and the sapphire substrate was modeled as described in reference 121. A matrix method[117] is used to calculate the multilayer stack reflection. The optical properties of the GaN layer were measured and analyzed using a three-layer reflection model (Air\GaN\Sapphire) before the InN layer was deposited. The best fit parameters for the GaN film were obtained using the non-linear Levenberg-Marquart fitting algorithm[121]. Thereafter, the IR reflections of InN\GaN\Sapphire structure were measured and the best fit parameters for InN film were obtained by using the same fitting algorithm as above. Frequencies of LO and TO phonon modes were kept constant at 593 and 576 cm^{-1} during the fitting process. The free carrier concentrations were calculated by

$$n_c = \frac{\omega_p^2 \cdot m_{eff} \cdot \varepsilon_\infty \cdot \varepsilon_0}{q^2} \tag{4.2}$$

with ω_p obtained from the fitting process. In Equation (4.2), m_{eff} is the effective mass of electron in InN, ε_0 is permittivity in vacuum and q is the electron charge. The electron effective mass was taken as $0.09m_0$[122], where m_0 is the free electron mass. The average of the values ε_∞ obtained from the fittings is 5.59 and is used in the free carrier calculation.

The best-fit approximation of the experimental data shown in Figure 4.4 revealed a InN layer thickness d=317 nm, a plasma frequency $\omega_p = 3461\,\text{cm}^{-1}$ and a plasma

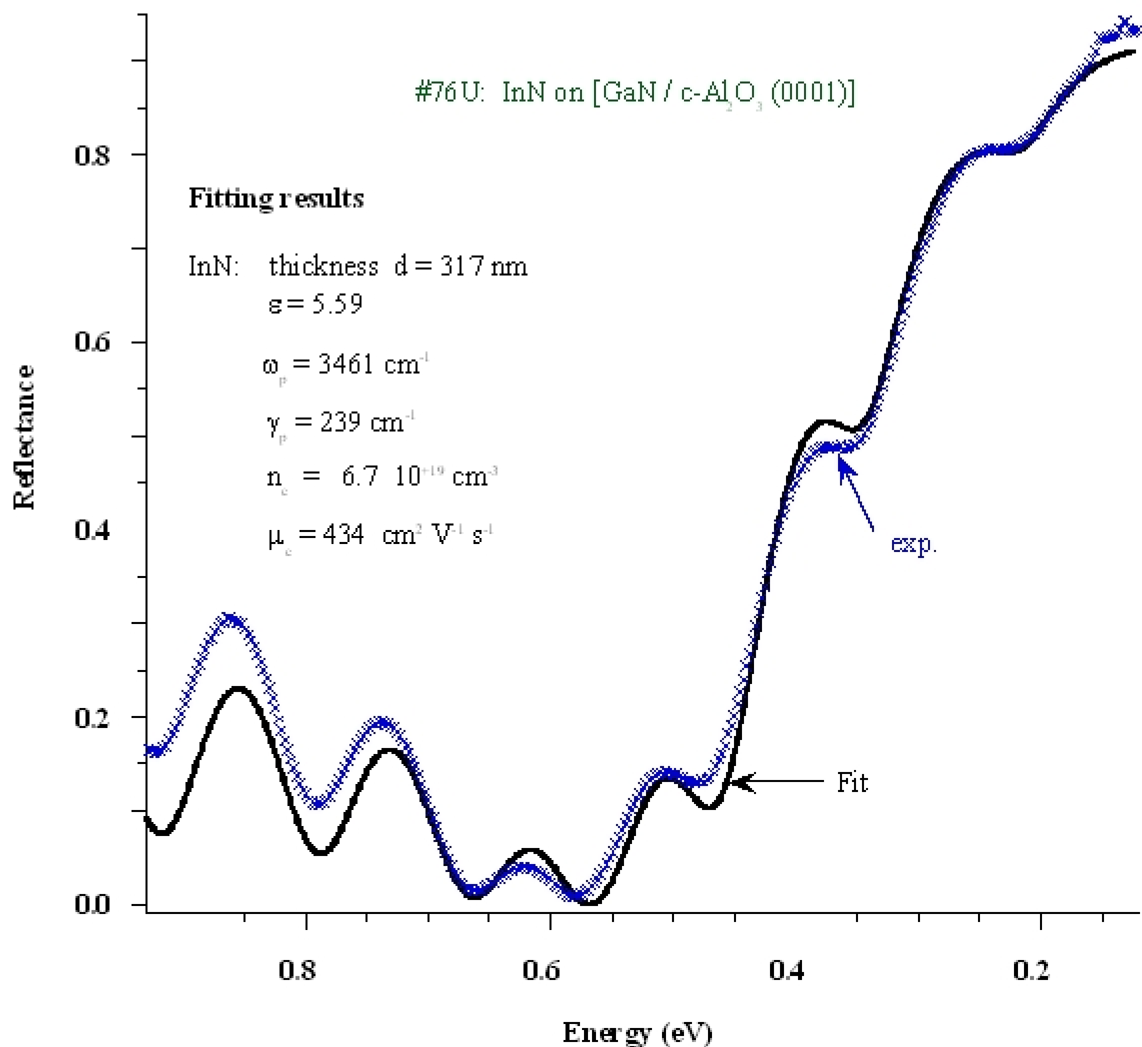

Figure 4. 4 IR reflectance spectrum and best fit for an InN layer deposited on a virtual GaN / Sapphire substrate (#76U).

damping constant $\gamma_p = 239\,\mathrm{cm}^{-1}$. The carrier mobility μ_c is calculated via effective mass and the damping constant γ_p [123]and was found to be $\mu_c = 434\ \ \mathrm{cm}^2 V^{-1} s^{-1}$.

Figure 4.5 show the room-temperature transmission spectra for samples #71U and #76U, taken at the same spots as those for the XRD spectra shown in Figure 4.1. Each spectrum is corrected for the substrate and spectrometer response characteristics. The calculated absorption spectra indicate an absorption edge around 1.5 eV with absorption structures around 1.2 eV and 0.7 eV. The sample 76U characteristic interference fringes

are due to the underlying GaN epilayer of 1789 nm thickness. The optical analysis on InN layers grown under similar conditions but with slight variations in the ammonia: TMI flow ratio (NH_3:TMI=600±30) showed that these small deviations in the InN stoichiometry shift the absorption edge from 1.5 down to 1.1 eV, while the free carrier concentration and mobility values are almost unchanged. The XRD analysis showed single-phase InN (0002) peaks with a slight broadening of the FWHM values for ammonia: TMI flow ratios below 570.

The correlation of absorption edge shift and free carrier concentration as obtained by IR reflectance does not support the proposed Moss-Burstein effect[7] as the leading cause for the shift of the fundamental absorption edge to higher values when the carrier concentration is increased. Additional effects such as stoichiometry deviations[124] and the associated point defect chemistry have to be considered to understand the physical properties of InN.

As shown previously, ammonia: TMI flow ratios below 500 cause an absorption edge shift well below 0.7 eV, while the free carrier concentration remains in the mid 10^{19} cm^{-3}. For ammonia: TMI flow ratios below 500, the XRD analysis has shown also the presence of the InN(101) phase in addition to the InN(0002) phase.

No equivalent changes are found in the Raman spectra that would provide a link between the appearance of the InN(101) peak in the XRD spectra and changes in the E_2(high) and A_1(LO) Raman modes. The analysis of the E_2(high) and A_1(LO) as a function of the ammonia: TMI flow ratio also provided no direct correlation between the free carrier concentration and InN stoichiometry deviation for the InN layers investigated.

Further studies on InN layers grown in an expanded process window are needed to correlate the point defect chemistry, structural and optical properties of InN.

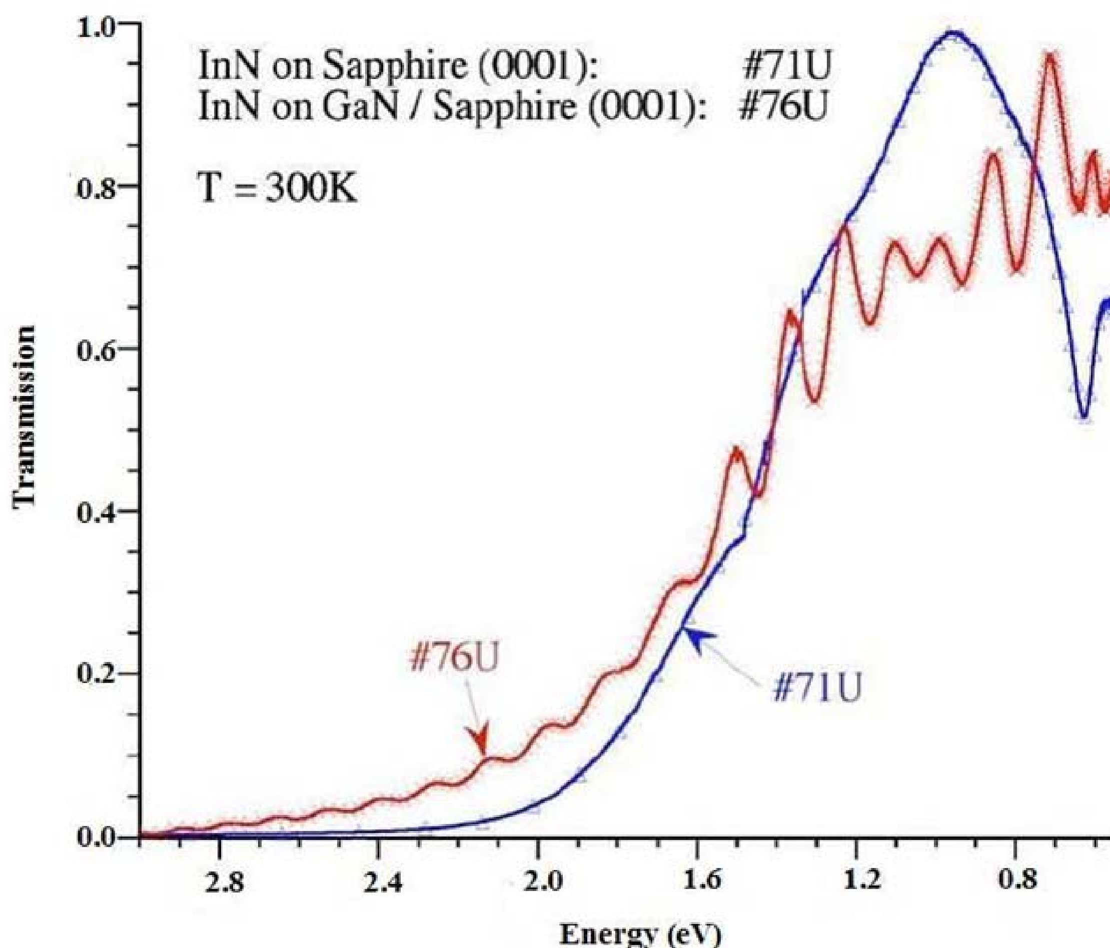

Figure 4. 5 Transmission spectra for InN grown on sapphire (#71U) and on virtual GaN-sapphire substrate (#76U).

4.3 Conclusion

In conclusion we have studied the structural and properties of InN layers grown by HPCVD on quasi lattice-matched virtual GaN substrates and sapphire substrates. The XRD analysis showed high-quality, single-phase InN(0002) peaks with hexagonal symmetry and FWHM around 430 arcsec for InN layers deposited on GaN epilayers. The FWHM increases with lattice-mismatch to about 530 arcsec for InN deposited on

sapphire substrates. Sharp E_2 (high) and A_1(LO) at 488 cm^{-1}, 590 cm^{-1} phonon modes are observed. At present, the free carrier concentrations in these InN layers are in the mid 10^{19} cm^{-3} and carrier mobilities around 430 $cm^2V^{-1}s^{-1}$, values that can be improved by further process optimization. The transmission spectra indicate that the band gap of the InN layers is well above 1 eV, contradicting results reported for plasma- assisted MBE grown InN layers. Our results also indicate that the absorption edge is extreme sensitive to small deviations in the InN stoichiometry, requiring precise control of gas phase and surface chemistry processes.

CHAPTER 5

Structural and surface morphological analysis of InN layers grown by high pressure CVD

5.1 Introduction

In order to understand the physics behind what is occurring in InN material, structural and optical measurements were performed on the grown samples. Therefore, structural characterization and surface morphology techniques were used for determining what sort of InN material has been grown. Structural and surface morphology studies of InN thin film layers have been performed by X-ray diffraction, Low Energy Electron Diffraction (LEED), Auger Electron Spectroscopy (AES), High-Resolution electron energy loss spectroscopy (HREELS) and Atomic Force Microscopy (AFM). In order to obtain high quality In rich group III-nitride heterostructures, it is necessary to grow single phase high quality InN crystals with very low electron concentration and defect densities. Therefore, the analysis of the crystalline quality of InN layers was carried out by X-ray diffraction spectroscopy. Surface structure, surface chemical composition, and surface bonding configuration of InN layers were investigated with AES, LEED and HREELS. Atomic force microscopy was used to derive the information about the growth mechanism of InN and surface roughness of InN layers.

5.2 X ray diffraction

The structural quality of InN epilayer, effects of V/III ratio on the layer quality of InN were studied by means of X ray diffraction and presented in the following sections.

5.2.1 Structural characterization of single phase InN thin film layers

To assess the crystalline quality and crystallographic orientation of the InN films, X-ray diffraction patterns were taken. Structural and compositional characterization was performed using X-ray diffraction with a CuKα (1.54 Å) X-ray source. 2-θ rocking curves with Full Width at Half Maximum (FWHM) of InN samples grown on Sapphire and GaN/ Sapphire are presented in Figures 5.1 and 5.2 in a logarithmic plot, which aids recognition of possible weaker signals from off axis crystal planes. As shown in Figures 5.1 and 5.2, the line width of the 2-θ scans were reduced to ~390 arcsec by optimizing growth conditions and substrates. (The smallest FWHM is 200 arcsec presently; see Chapter 7.). The lowest FWHM for the InN (0002) peaks are 385 arcsec and 495 arcsec for the InN layers deposited on GaN/sapphire and sapphire substrate, respectively. The FWHM of InN (0002) diffraction peak increases for InN layers deposited on sapphire substrates due to the lattice mismatch between the InN and substrate layers. In the XRD spectra presented in the following, the InN (0002) diffraction peak at ~31.3° is observed plus the peak of the (0002) reflection from the GaN buffer layer and (0006) reflection from the α- Al_2O_3 substrate. The InN (0002) diffraction peak is very close to that expected for unstrained InN (31.33° for c=5.7039 Å)[22]. This peak position is a little different for each sample measured. However, due to the uncertainty in the specification of off-angles on the substrate, it is not possible to ascertain θ angles to better less than ±0.5° of the peak position experimentally. The strong intensities of the peaks indicate that

the InN thin films are high purity and that the sample consists of wurtzite material. Refined values of the lattice parameters *c* were extracted from the XRD data, which compared well to the literature values as presented in Table 5.1. The result indicates that the "*c*"-axis of InN with a wurtzite structure is perpendicular to the substrate surface of (0001) α-Al_2O_3. As expected for the film grown on GaN/sapphire at 800 "V/III molar ratios", less distortion is present in InN films. Butcher *et al.*[125] have previously shown that increases in the *c* axis lattice occur when excesses of nitrogen are present in the InN lattice and that such increases are not simply the result of oxygen alloying. All the diffraction peaks in the spectrum are indexed to be hexagonal wurtzite phase. No peak in the vicinity of 33° is observed. This anomalous diffraction peak is attributed to metallic indium, which can be observed in presence of micron sized Indium clusters present in the films[89]. It was concluded that the "anomalous" 33° peak is in fact the $(10\underline{1}1)$ diffraction peak of InN. This peak can also be assigned to diffraction peaks of random InN grains. It is therefore likely that the 33° XRD line observed in some InN films has not been only assigned to metallic Indium[126] but InN itself also. The interpretation of InN diffraction peak positioned at 33° is also presented in the following for different V/III molar ratios.

5.2.2 Effect of V/III ratio

The V/III precursor ratio is one of the most crucial parameters influencing the InN layer quality due to the variable decomposition of NH_3 and TMI. The broadening of the XRD peak is presented in Figure 5.3 as a function of V/III ratio for a series of samples grown at fixed temperature (1080 K) and reactor pressure (15 bar). A weak (101) diffraction peak appears on the lower shoulder of the (0002) diffraction peak, which might be attributed to shifting in the processing window. By further studying the effect of

the V/III molar ratio, we found that its effect was coupled with the effect of growth temperature. It is possible to produce a highly crystalline InN epilayer for up to 1.5-hour growth times (sample #76), but the growth temperature must be lowered while maintaining the same V/III molar ratio. On the other hand, increasing the indium-to-nitrogen flux ratio during epitaxy results in the appearance of the (101) diffraction peak at 33.0°. This observation strengthened the association of diffraction peak at 2θ~33° with surface In layer or the In clusters in the InN samples. We have however verified that by decreasing the growth temperature to 1078 K, and reducing the nucleation temperature, it is possible to grow high quality, single phase, InN at 800 molar ratios (samples #125L, #192L, #207and 209L). Our XRD results strongly indicate that low V/III ratios (between 600 and 800 molar ratios) are required for growing good quality InN layers. The FWHM gradually becomes broader, and the X-ray diffraction intensity approximately same with increasing V/III molar ratio. In addition, peak asymmetry appears on the low angle side of the (0002) peak and asymmetry increases as the V/III molar ratio increases. This asymmetry is due to several peaks underlying in the (0002) structure as shown in Figure 5.4. Although secondary peaks are less prominent as the quality of the layer improves, it is still hard to determine whether those peaks are due to the native point defects or impurity incorporation. However, this secondary peak does not represent a secondary phase.

Table 5. 1 Growth parameters, structural and optical data for InN films grown on GaN template and sapphire substrate.

Sample	V/III molar ratio	Lattice parameter (c) (Angstrom)	FWHM (arcsec)	Sample Thickness (nm)
71U	800	5.7290	528.3	
76U	800	5.7000	432.4	317
110U	800	5.7085	408.1	550
111U	1055	5.7036	439.6	340
112U	1585	5.7021	704.2	320
125L	800	5.6982	385.9	593
135U	800	5.7051	492.7	228

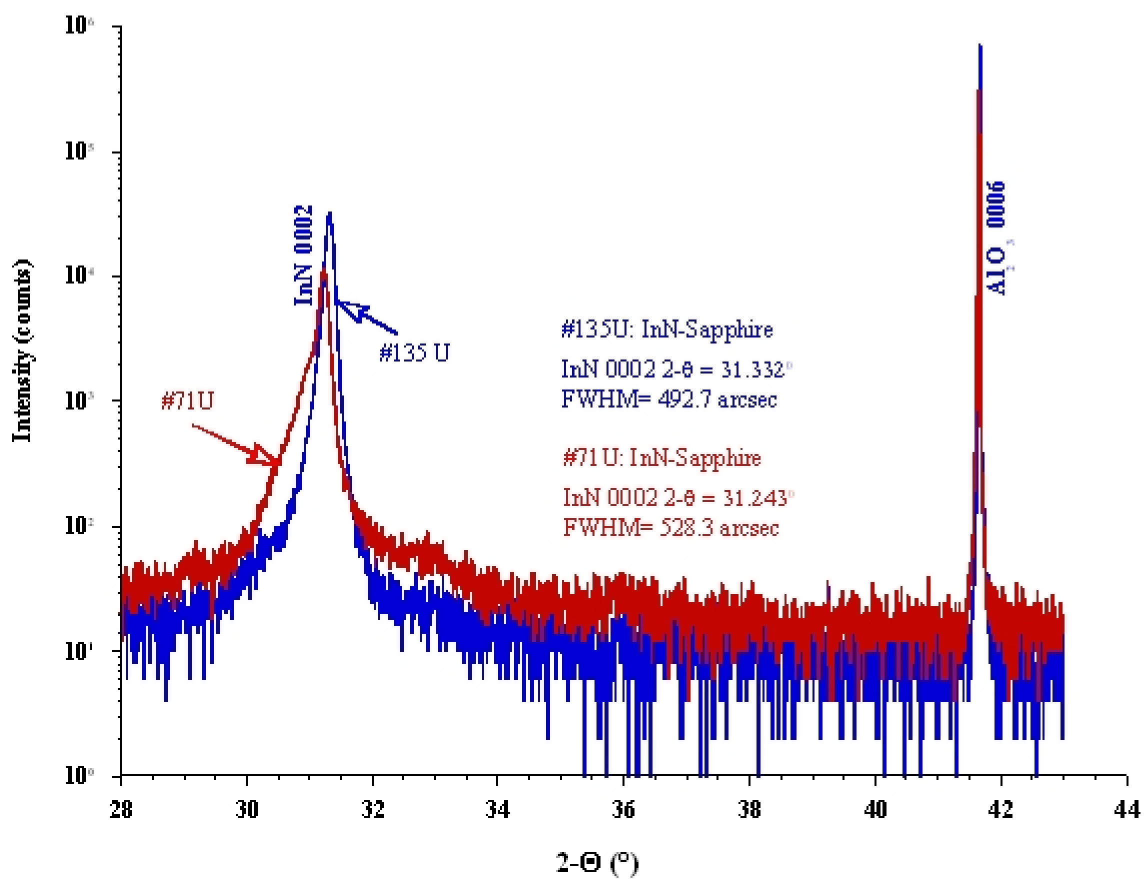

Figure 5. 1 XRD spectra for InN layers on sapphire substrate (#71U and #135U).

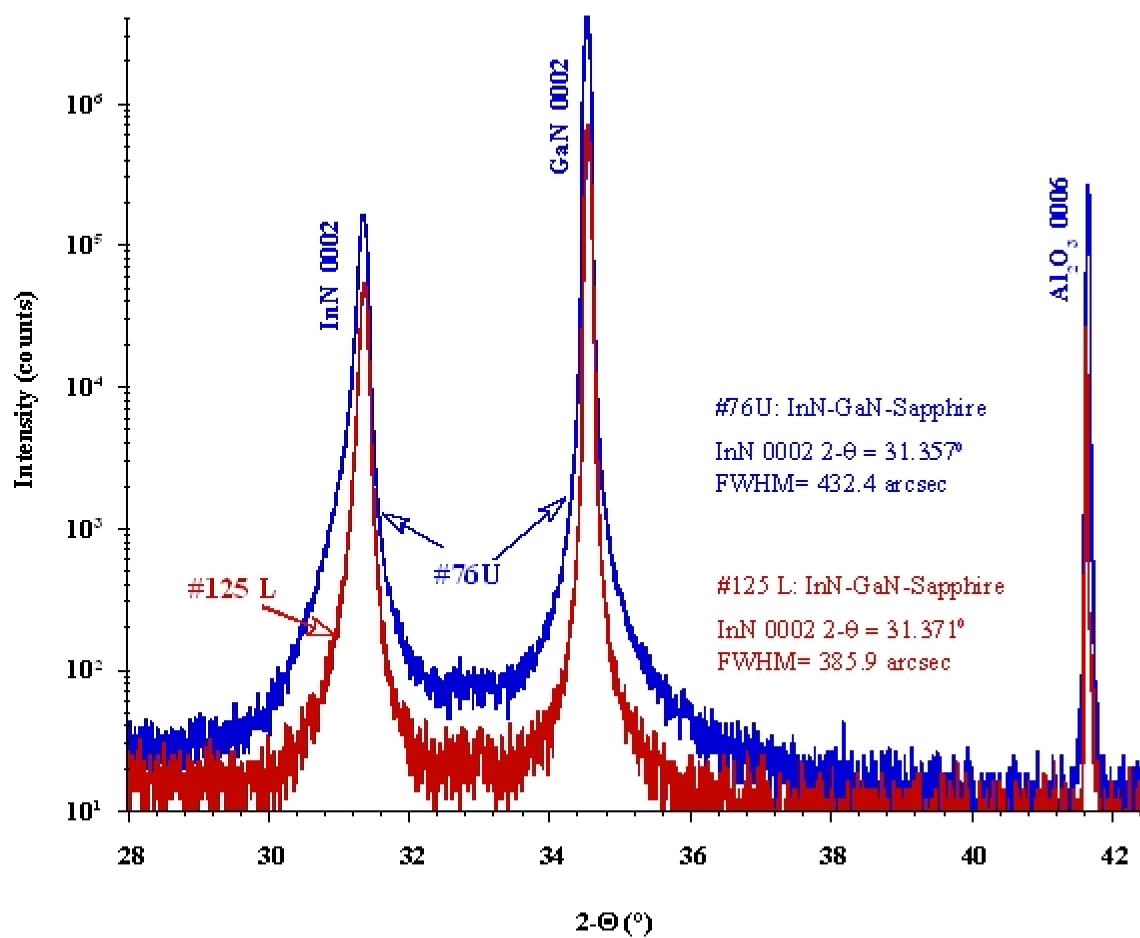

Figure 5. 2 XRD spectra for InN layers on a GaN/Sapphire template (#76 U and #125 L).

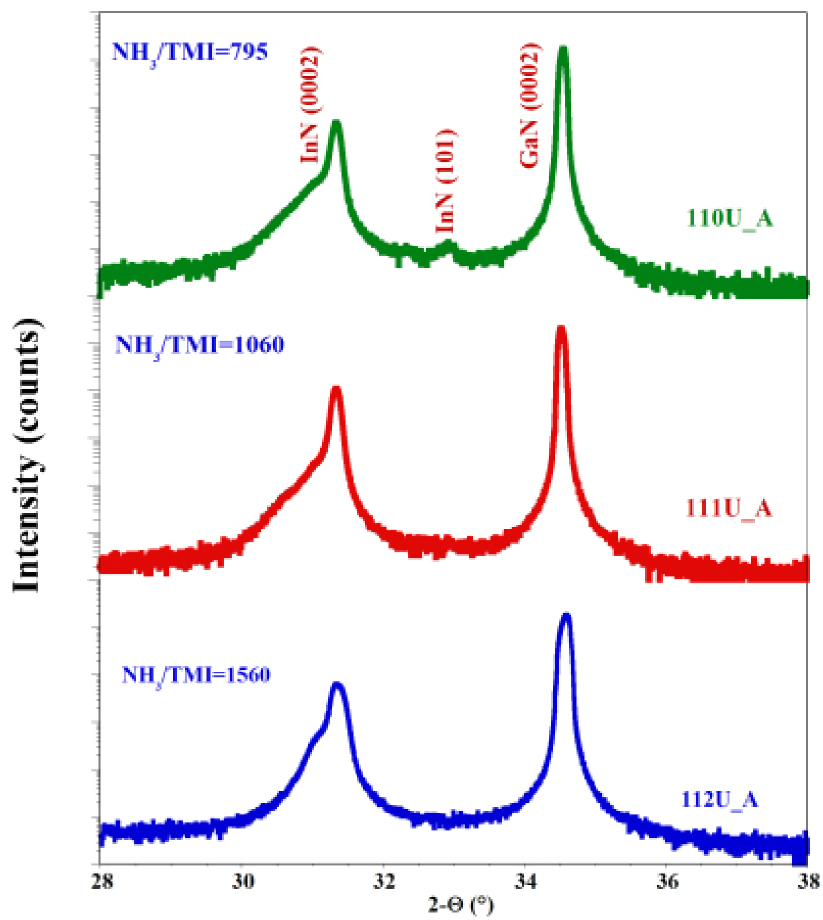

Figure 5. 3 X-ray diffraction patterns for the InN films grown with different NH_3/TMI ratios.

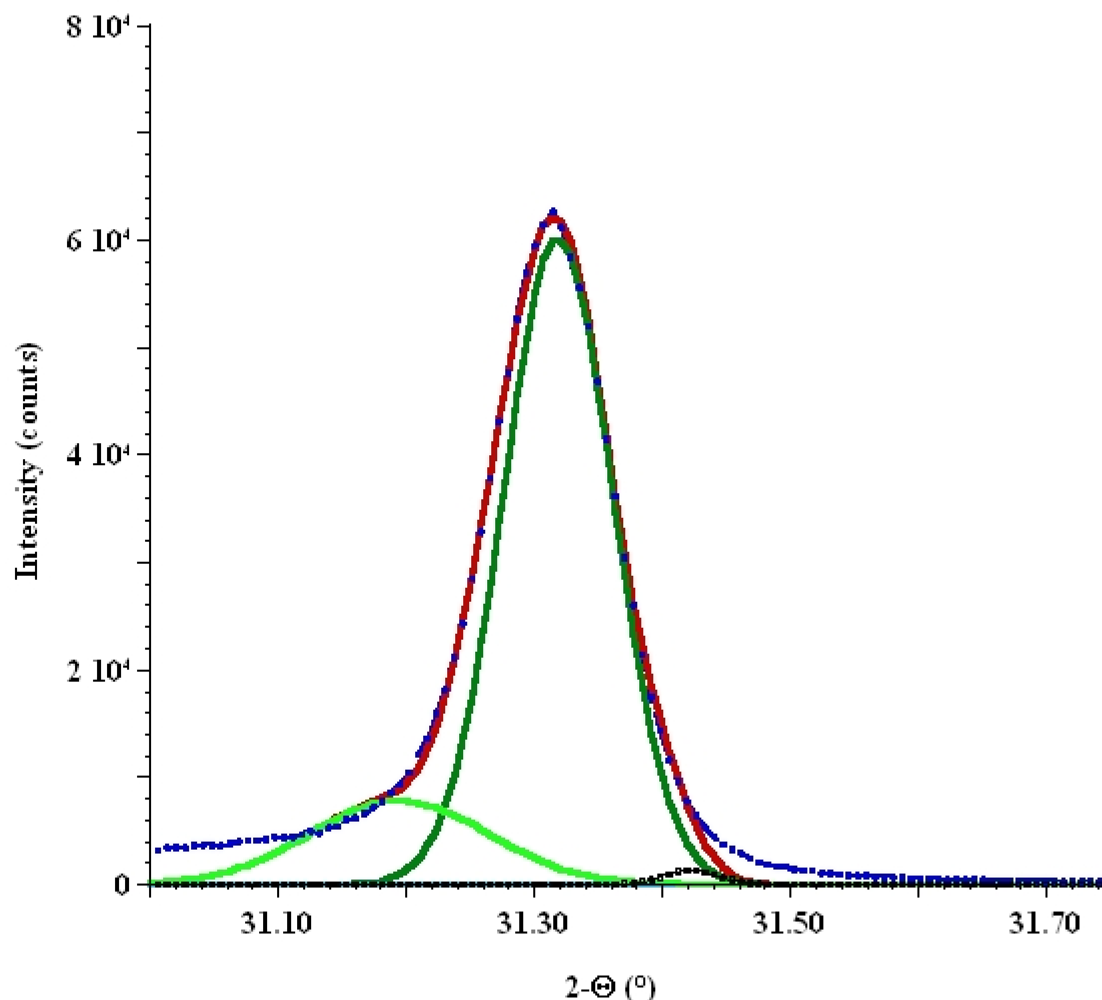

Figure 5. 4 The XRD peak analysis indicates an asymmetric lower shoulder which might be due to the either native point defects or impurity incorporation.

5.3 Surface structure, composition of InN layers.

Studies of the surface structure and reactions are an important aspect in gaining an understanding of growth mechanisms. The surface structure, composition and bonding of InN films were investigated using AES, LEED and HREEL spectroscopic techniques. The InN sample was rinsed with acetone and isopropyl alcohol before insertion into a high vacuum chamber, mounted on a tantalum sample holder and held in place by tantalum clips. Sample heating was done by electron bombardment of the back of the

tantalum sample holder. Auger electron spectroscopy of inserted samples in an UHV chamber revealed that in addition to indium and nitrogen, oxygen and carbon contamination were present due to the exposure of the sample to the atmosphere. Sample cleaning was achieved in two steps. In the first step, the surface carbon of the InN samples was cleaned by bombardment with 0.5 (Sample #125 L)-1 keV (Sample #65 U) Ar ions at a glancing angle of 70˚ from the surface normal. After the sputtering process, AES results revealed that the surface was effectively cleaned with little oxygen remaining. No low energy electron diffraction (LEED) pattern was observed prior to or after the sputtering process. Following the sputtering in the second step, surface preparation for a well-ordered surface was done *in-situ* by Atomic Hydrogen Cleaning (AHC) in order to remove the atmospheric contaminants, particularly oxygen. AHC was performed by backfilling the vacuum chamber with hydrogen to a pressure 8.4×10^{-7} Torr in the presence of a tungsten filament heated to 1850 K to produce atomic hydrogen. The sample was positioned 20 mm from the filament for 20 minutes (giving an exposure of 1000L of H_2). During this time, the sample temperature rose to about 350 K due to the proximity of the heated filament. Following this process, the sample was heated to 600 K while remaining in front of the tungsten filament for an additional 20 minutes (an additional 1000L of H_2). After one cycle of AHC, both AES and HREELS showed that surface carbon and oxygen contaminants had been removed from the surface. Low energy electron diffraction measurements revealed a 1×1 LEED pattern, but after several additional cleaning cycles the hexagonal diffraction pattern became sharper for both samples 125L and 65U (Fig. 5.5 (a) and 5.5 (b)) using various electron energies from 40 to 170 eV. The LEED pattern indicates that the surface is *c*-plane oriented and well

ordered. Veal *et al.*[127,128] reported a similar hexagonal pattern from AHC-cleaned, MBE-grown InN at an incident energy of 164 eV. The intensity of the background indicates the amount of the surface disorder, and bright spots and a dark background reveal that the surface is well ordered.

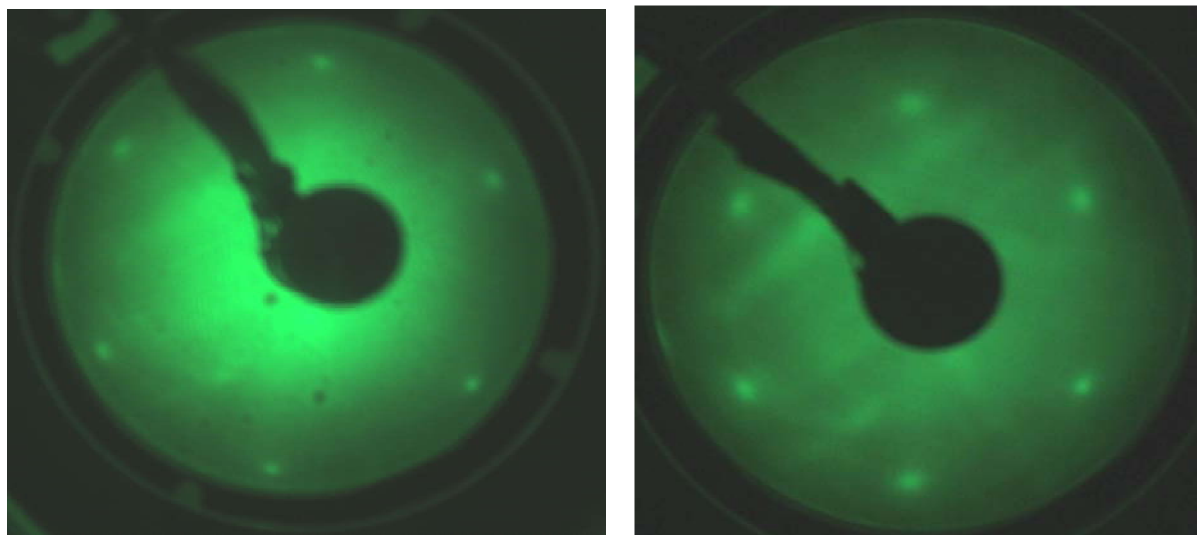

Figure 5.5 (a) LEED of AHC cleaned InN sample (#65U) for an incident electron energy of 40 eV.

Figure 5.5 (b) LEED of AHC cleaned InN sample (#125) for an incident electron energy 40 eV.

5.3.1 Surface electron accumulation in InN layers

InN has a large spontaneous polarization and large piezoelectric coupling with other group III nitrides. Surface and interface properties of InN material will have a crucial influence on the design concept of the low dimensional devices based on InN. It is believed that the high carrier concentration of InN films is due to the surface charge accumulation. Lu *et al.*[129] claimed that the top layer of InN samples possesses a much higher carrier concentration than that in bulk according to I-V and C-V measurements. Since nitride material electron and hole effective masses are much smaller than those in conventional III-V materials, electron and hole confinement may be achieved

simultaneously. Colakerol *et al.*[130] reported quantized energy levels in the surface electron accumulation layer on InN films grown by rf-MBE.

Surface electron accumulation of InN layers grown by High-Pressure CVD were observed with High Resolution Electron Energy Loss Spectroscopy (HREELS) on a surface of known termination with no indium overlayers or droplets. HREELS is a non-contact and nondestructive probing technique that can be used for studying the semiconductor's space-charge region. HREELS is capable of distinguishing between contributions from the accumulation layer and bulk layers. HREELS experiments were performed in a specular scattering geometry with an incident and scattered angle of 60° and incident energy ranging from 7 eV to 35 eV. HREEL spectra recorded from the clean InN (0001) surface are shown in Figure 5.6. The first loss feature in all spectra at ~66 meV (550 cm^{-1}) is assigned to Fuchs-Kliewer surface phonon excitations in agreement with previous reports[54,127,131]. The HREEL spectrum obtained using 7 eV incident electron energy reveals surface adsorbate loss features at 870 and 3260 cm^{-1} due to the bending and stretching vibrations of a surface N-H species[132]. A small peak observed near 1430 cm^{-1} is assigned to a combination loss of the Fuchs-Kliewer phonon and the N-H bending vibration. With increasing incident electron energy, the intensity of the N-H stretch decreased considerably while the N-H bend was almost unchanged. The excitation of the N-H stretch is attributed to dipole scattering while the N-H bend is due to impact scattering. As the incident energy is increased further, all modes due to surface vibrations decrease due to the reduction in surface sensitivity with an increasing penetration depth of the electrons. HREEL spectra of a room temperature, H-dosed surface were unchanged from those shown in Figure 5.6 indicating that no reactive indium exists on this surface.

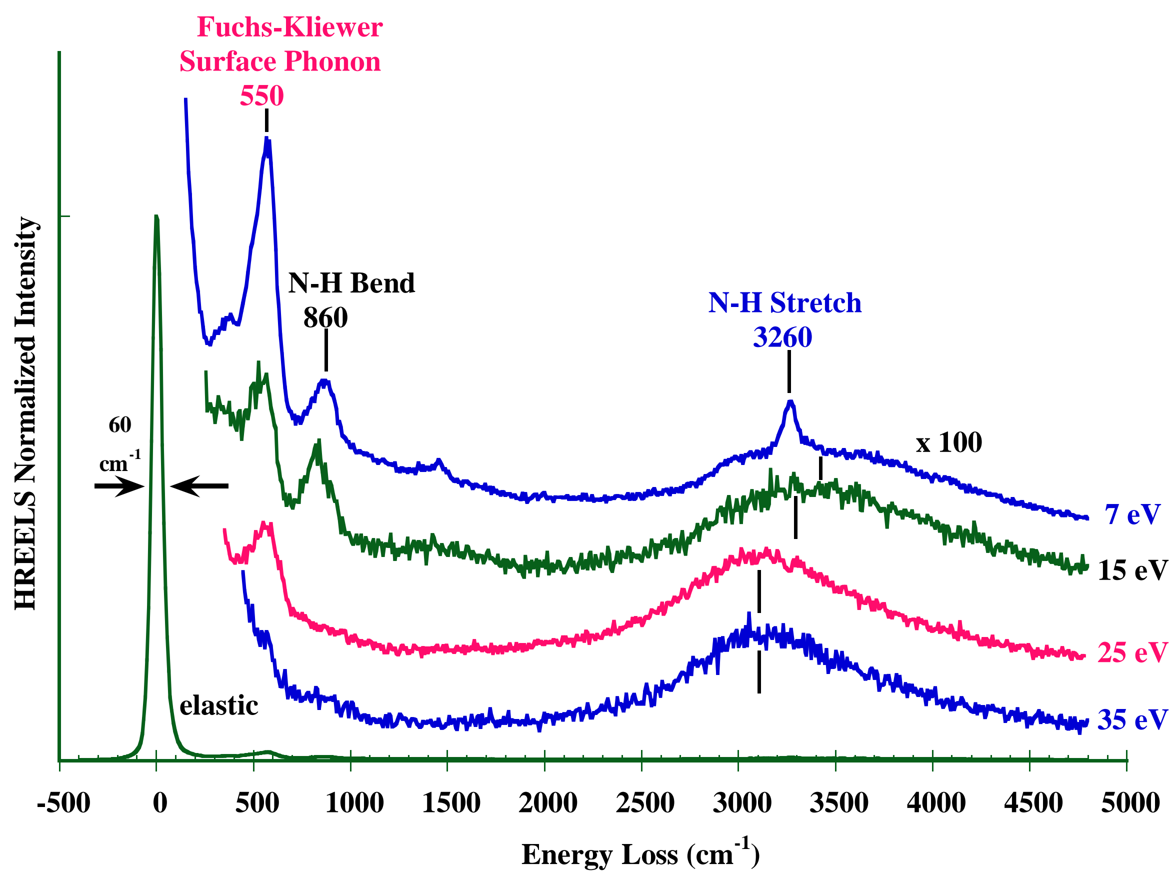

Figure 5. 6 HREELS from an atomic hydrogen cleaned InN sample. Spectra were acquired in the specular direction with incident electron energies of a) 7 eV, b) 15 eV, c) 25 eV, and d) 35 eV.

The presence of N-H and lack of indium-related vibrations demonstrates N-termination of the surface and implies N-polarity of the film.

The shift of the plasmon peak position in the HREEL spectra is attributed to a variation of carrier concentration with depth. The position of the plasmon peak is related to the surface and bulk plasma frequencies[127,133]. The shift of the plasmon feature to lower loss energy as the incident electron energy is increased implies that the plasma frequency is larger for the surface than for the bulk and indicates an accumulation of electrons on the surface. The plasmon peak position shifts most dramatically when the incident electron energy is changed from 15 to 25 eV as shown in Figure 5.6. HREEL spectra reported by Mahboob *et al.* [127] and Veal *et al.* [128] also show that most of the shift occurs as the incident energy is changed from 15 to 30 eV. This feature is reproduced in their simulations using a four or five layer slab model with an electron concentration that is large at the surface and decreasing deeper into the layer. The intensity of the N-H vibrations, and the lack of In-H vibrations even after room temperature atomic hydrogen exposure leads to the following conclusion: the electron accumulation observed here is not caused by indium droplets, indium overlayers, or isolated In-In dimers on the InN surface. This finding is consistent with the pinning of the surface Fermi level in the conduction band and indicates that In-In bonds are not the only source of surface states in the conduction band.

5.3.2 Desorption of hydrogen InN (0001) surface

Surface reactions including hydrogen are crucial steps in the growth mechanism of InN thin films. Surface hydrogen atoms produced by the decomposition of $(In(CH_3)_3$-$NH_3)$ precursors during InN growth are most frequently eliminated by desorption after

reacting with adsorbed methyl groups or other hydrogen atoms. Adsorbed hydrogen reduces the number of available reaction sites for indium and nitrogen precursors. HREELS has been used to determine the kinetic parameters for hydrogen desorption from the N-polar InN surface, and the effects of heating on surface structure and electronic properties are also reported. HREEL spectra from sample #125L, taken after AHC and annealing to various temperatures for 900 s, are shown in Figure 5.7. After annealing to 375 ºC, the intensity of both N-H stretch and bend decrease and disappear completely after heating the sample to 425 ºC for 900 s. The presence of N-H vibrations and the lack of In-H features indicates that the layer is nitrogen terminated which is consistent with N-polar InN$(000\bar{1})$ [131,134]. A broad feature centered at an energy loss of ~3800 cm^{-1} is due to the conduction band plasmon excitation. The peaks at 3260 and 860 cm^{-1} are assigned to N-H stretching and bending vibrational modes, respectively. The reductions in intensity of N-H vibrations are assigned to recombinative desorption of hydrogen. In addition to the N-H vibrational peaks, a small feature appears at 2000 cm^{-1} ,which may be due to a surface N-N vibrational mode. This is possible because N-N stretching vibrational modes have been reported to occur over a wide range of frequencies. De Paola *et al.* [135]reported ν(N-N) on Ru (001) at 2195 cm^{-1} and 2200-2250 cm^{-1}, respectively. Apen and Gland[136] identified the N-N stretching mode on the GaAs surface at 1671 cm^{-1}. At the present time, the broad range of frequencies observed for N-N stretches do not allow an assignment to be definitively made.

The growth temperature regime for MOCVD and MBE suggests that the typical growth temperature of InN is of the same order at which hydrogen desorbs (425 to 500 ºC) from the InN surface. If the growth temperature were lower than the hydrogen

desorption temperature, sites on the InN growth surface could be occupied by hydrogen, which is produced during the precursor decomposition process. This will affect the growth rate.

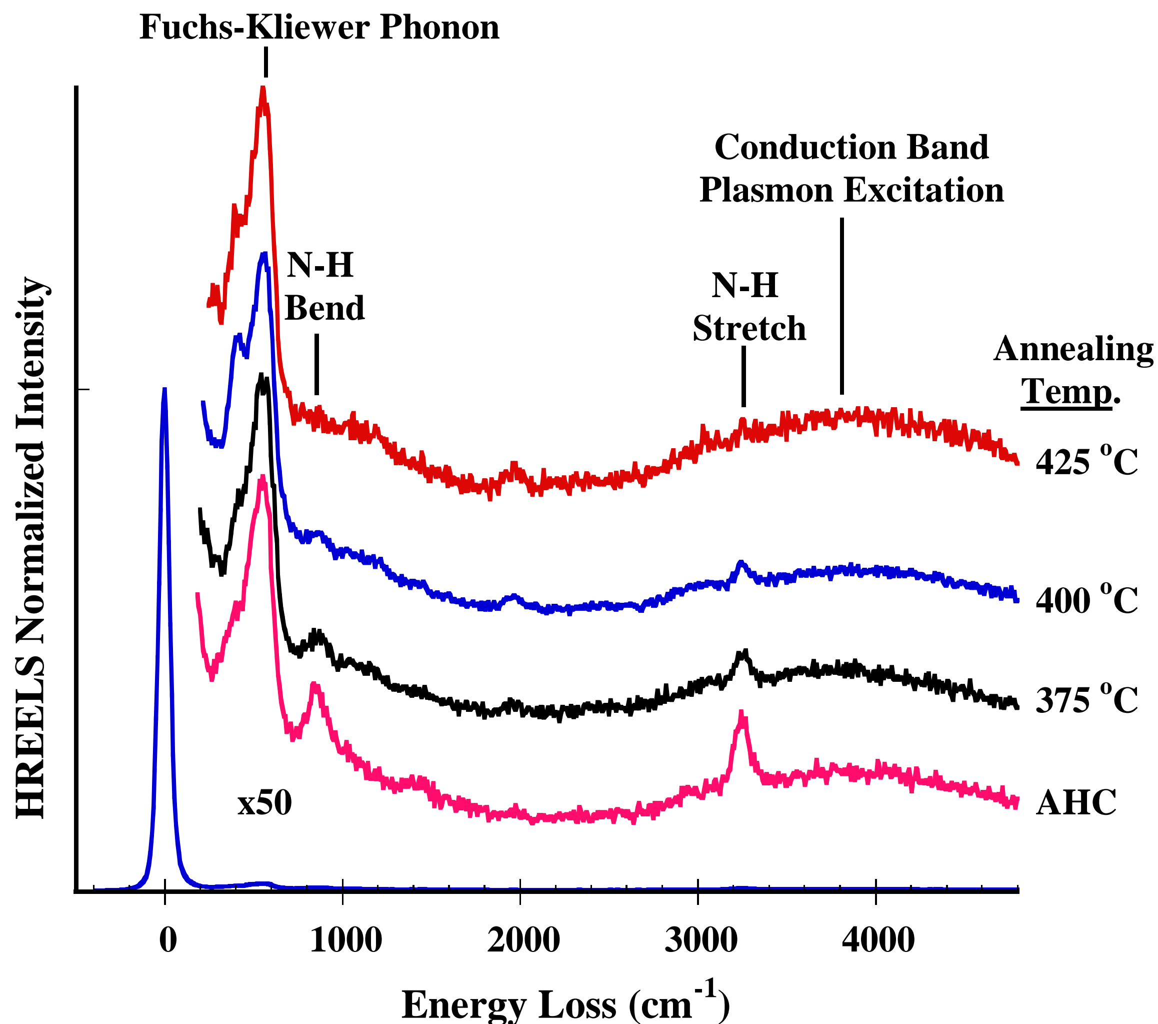

Figure 5. 7 HREEL spectra from sample #125L after preparation by atomic hydrogen cleaning (AHC) and after heating for 900 s to 375, 400, and 425 °C. The surface was restored to the same initial state with AHC prior to each heat treatment.

5.4 Atomic Force Microscopy: Surface morphology of InN layers

In order to improve the growth in a systematic way it is essential to understand the underlying kinetic processes such as adsorption, desorption and diffusion. But a lack of fundamental understanding of deposition of InN has prevented the establishment of a consistent growth strategy. The growth of continuous InN by High-Pressure CVD with low surface roughness and a thickness greater than a few hundred nanometers is challenging. The limitation in thickness of InN thickness is attributed to shifting in the processing window due to the IR absorption of radiation within the growing layer as well as InN etching during the growth. The etching effect on the surface of the InN films will be examined including real time PAR signal traces recorded during the growth. We presented mainly *in situ* characterization of InN growth in the previous chapter, and present herein real-time measurements of the changes in the optical properties of InN layers using Laser Light Scattering (LLS). It was found that the InN deposition was sensitive to V/III molar ratio and growth temperature. Surface morphology has been largely improved by using GaN/sapphire substrate instead of sapphire as substrate. Through 3D (three dimensional) nucleation, and subsequent coalescence, adatom diffusion on growing surfaces is considered to be a key parameter controlling the coalescence, the material quality and surface morphology. The surface morphology of the InN layers was measured by AFM using a PSIA XE 100 in both contact and non-contact mode. Non-contact AFM mode (nc-AFM) is a non-invasive method for sensitive surface studies. Contact mode (C-AFM) is primarily used for power dissipation and friction studies. In the following section, the evolution of surface morphology is examined using AFM images of samples grown on sapphire and GaN templates.

5.4.1 Effect of substrate

The AFM images of InN films (#74U and #148 L) grown on sapphire substrate are presented in Figures 5.8 and 5.9. Analysis of the AFM images reveals that the deposited InN films consist of columnar structures (hexagonal columnars are clearly seen in Figure 5.9.) with diameters ~800 nm (#74U) and ~300 nm (#148L) depending on the growth time and growth temperature (see Table 5.2). This characteristic feature of InN films with columnar structures was reported by Yamamoto *et al.*[137] The hexagonal structure of InN is considered to be seeded from a discrete island. An InN sample (#74U) that was grown at an elevated temperature (1090K) with a V/III ratio of 800 for 1.5 hours exhibited a surface morphology with root mean square (rms) roughness of approximately 52 nm, but with a diameter of structures ~800 nm. On the other hand, an InN sample (#148 L) that was grown at a lower temperature (1078K) with the V/III ratio (800) but for a longer time (~5 hours) exhibits surface morphology with rms roughness near 74 nm. Sample #148L is composed of columnar structures with hexagonal tops separated by deep trenches. This results show that the diameter of the hexagonal tops increases with increasing growth temperature in the range of 1070-1100 K, growth time from 1.5 hours to up to 5 hours and this result is consistent with the literature. Changing the V/III molar ratio, and growth temperature might reduce the hexagonal top size. The coalescence is not complete for both films and large hexagonal domains dominate the surface structure. Increasing the thickness of InN layers grown on sapphire substrate did not accelerate the coalescence process for the InN film. This may be due to insufficient diffusion of the adatoms. However, the average grain area for both samples is about the same at 0.2 μm^2. The InN film consists of disoriented hexagons with respect to each other and the *c* axis of

the substrate as shown in Figure 5.10. This is characteristic of highly mismatched systems with a mismatch x > 10%[138]. The weakness of the InN bond may assist InN columnar growth with different crystal orientations. The magnitude of the tilt angle depends on the magnitude of the mismatch and actual growth conditions[138]. It is found that under the current growth conditions, with InN films grown on sapphire substrates, increasing the film thickness (close to 1 μm) does not lead to an apparent improvement on the surface roughness.

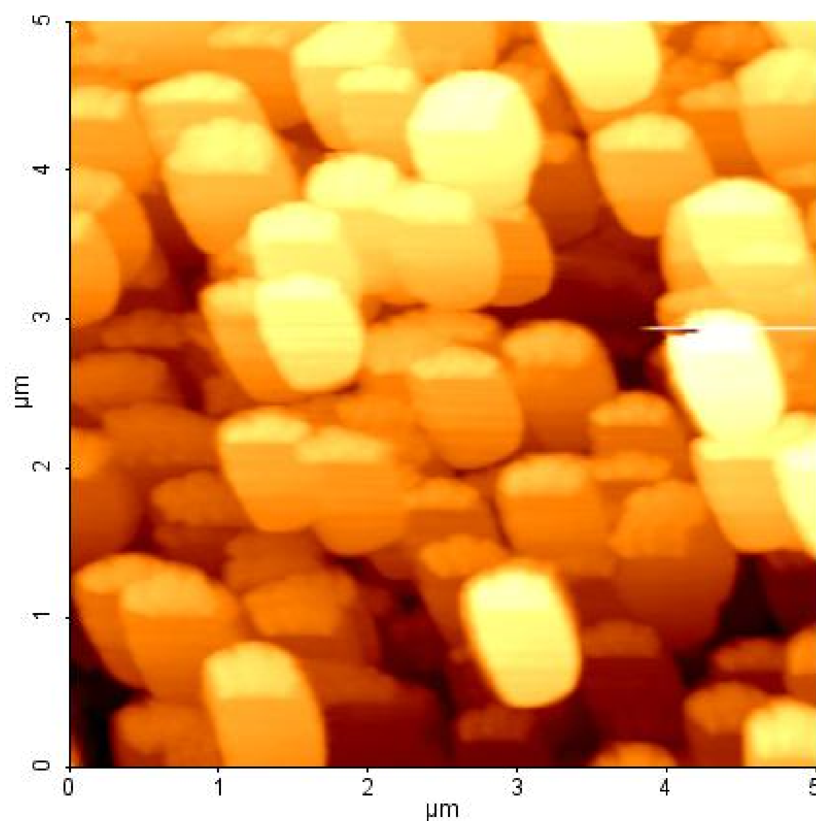

Figure 5. 8 AFM image of Sample #74 U (5μm x 5μm, 256 x 256 pixels, Contact mode).

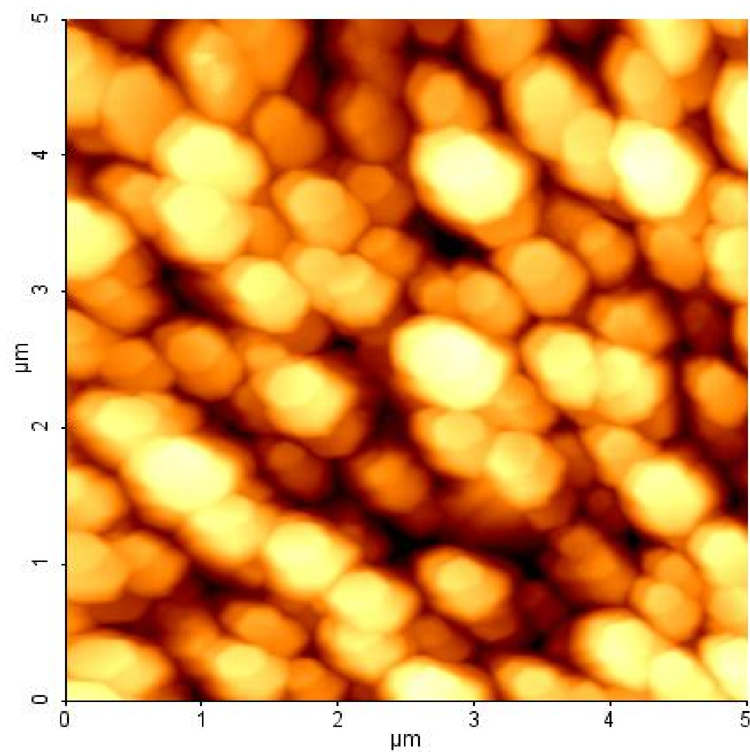

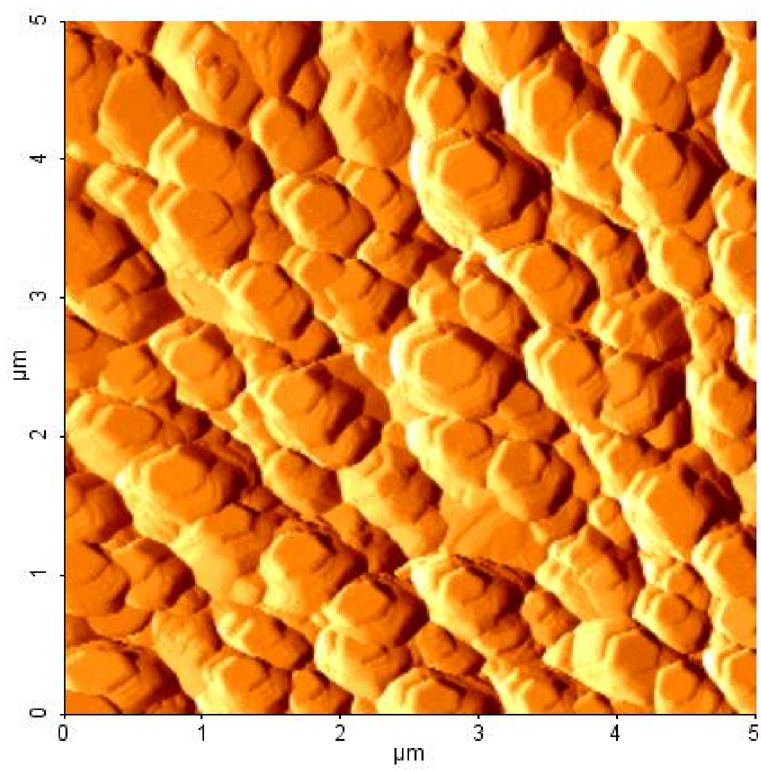

Figure 5. 9 AFM image of Sample #148L (5µm x 5µm, 256 x 256 pixels, Non-Contact mode).

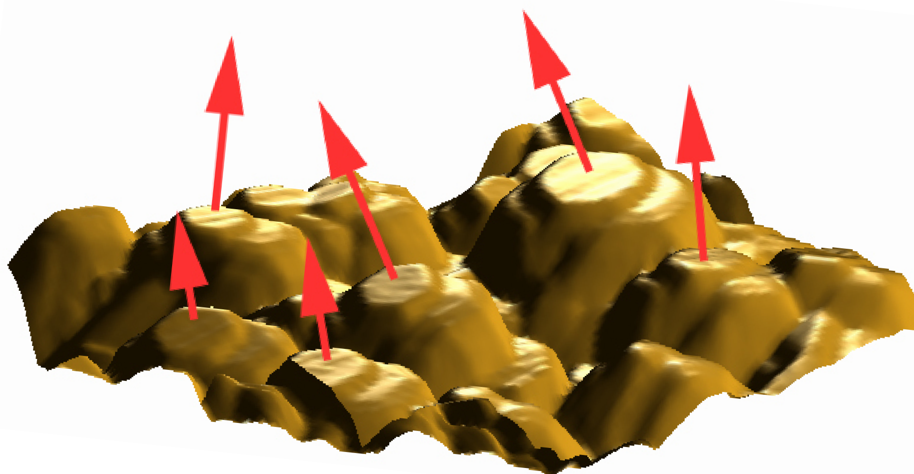

Figure 5. 10 Slightly misoriented hexagonal InN films grown on Sapphire (sample #148L).

The difficulties in the growth of high quality InN due to the lattice mismatch and lack of suitable substrate materials motivated researchers to seek a new technique for improving the material quality as well as the surface quality of the materials. As shown previously, the large lattice mismatch between sapphire and InN leads to a surface roughness ~26 nm (#136U) for the InN samples grown by HPCVD. Therefore, the surface morphology of InN films grown on GaN templates was investigated by means of AFM. In addition to lattice mismatch, the growth temperature utilized for InN is one of the most critical parameters influencing the crystal quality, surface roughness and growth rate of the InN film. For sample #76U, growth was initiated at 1090 K, while for sample #192L, growth was initiated at a lower temperature of 1078 K. The nucleation directly on GaN/sapphire substrates for sample #192L is a relatively long nucleation when compared to #76U sample. As shown in Figures 5.11 and 5.12, some important improvement was obtained for samples #76U and #192 L. The RMS roughness over the entire 1μm^2 is 14.3 nm for sample grown at higher temperature (#76U) and 8.9 nm for the sample grown at lower temperature (#192 L).

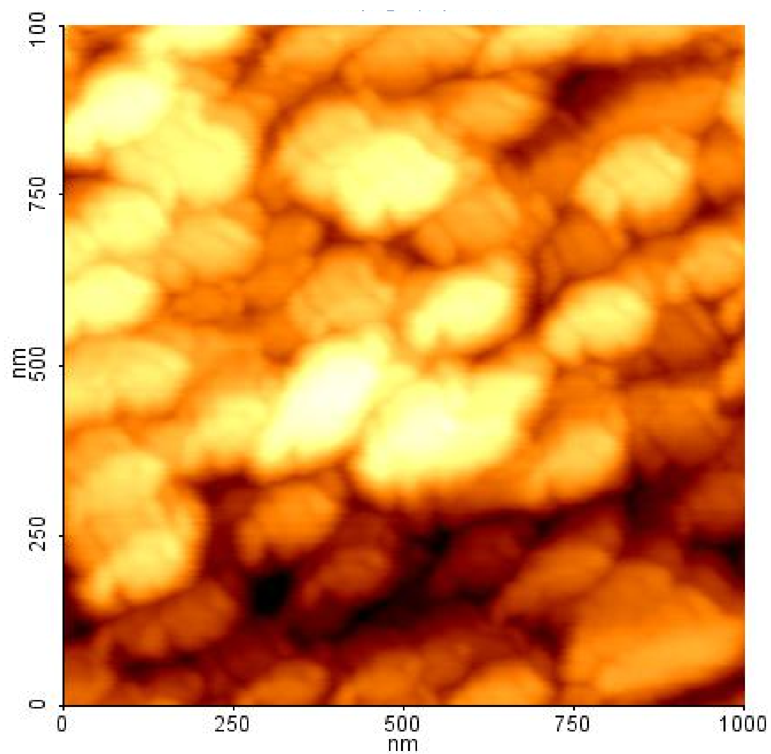

Figure 5. 11 AFM image of Sample # 76U (1µm x 1µm, 256 x 256 pixels, Contact mode).

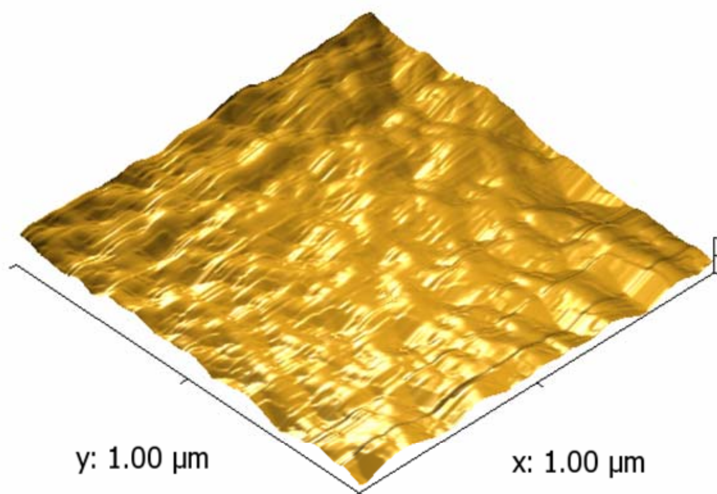

Figure 5. 12 AFM image of Sample # 192L (1µm x 1µm, 256 x 256 pixels, Contact mode).

InN samples were grown with an aim towards the optimized growth temperatures, V/III ratios and total gas flow through the reactor. However, thermal etching sometimes dominates the growth kinetics. Therefore, steady state growth parameters often do not allow InN growth after a certain period of time. Thermal etching generates holes, trenches, and increase roughness on the film surface, which has been correlated to LLS monitoring during film growth. The LLS monitoring was used to measure the surface roughness qualitatively on the GaN/sapphire. The reflected intensity of the LLS signal was recorded and a typical intensity versus time plot obtained during the InN growth is shown in Figure 5.13 during the InN growth. The decrease in laser intensity is believed to be due to absorption of the laser light by the growing InN layer. The increase in the laser intensity starts at approximately 90 min after the beginning of growth when etching dominates the film growth. This experimental observation for the growth/etching transition will allow us fine control on the nucleation and steady state growth. If growth is dominant over etching, InN samples are produced with good quality and smoother surface.

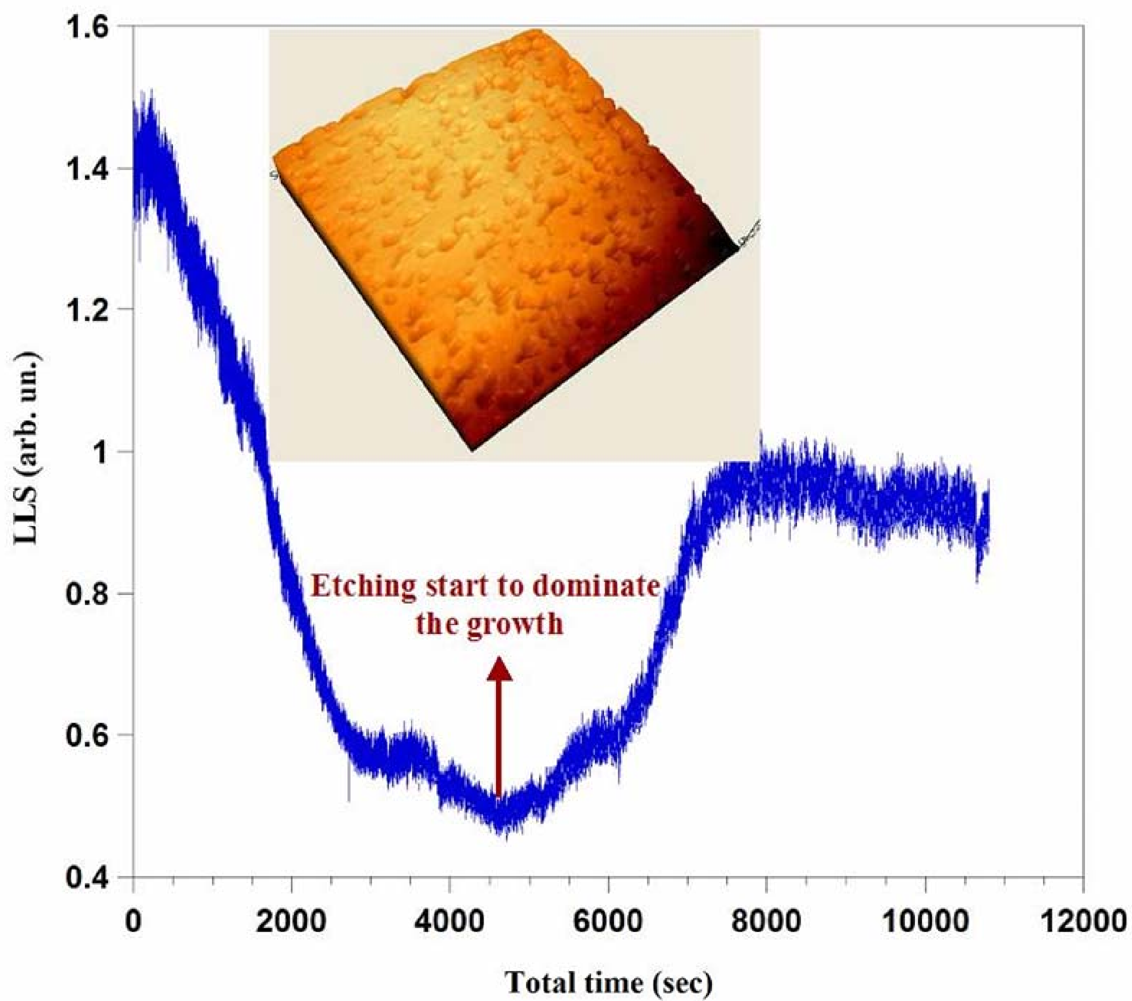

Figure 5. 13 Real time optical monitoring of InN film (#125 U) surface by LLS where etching starts to dominate the growth. AFM image of Sample # 125L (5µm x 5µm, 256 x 256 pixels, NC mode is presented in inset).

Table 5. 2 Growth parameters, FWHM of InN (0002) rocking curves, crystallinity and surface roughness of InN samples

Sample	V/III ratio During nucleation	V/III ratio During growth	Temp. during nucleation (K)	Temp. during growth (K)	Substrate	Growth time (minute)	FWHM (0002) arc sec	Roughness (nm)	Structure
74U	475	950	1100	690	Sapphire	90	NA	52	NA
76 U	400	800	1100	1090	p-GaN/Sapphire	90	432.4	14.2	Single crystal
111U	530	1055	1100	1090/1085	p-GaN/Sapphire	180	439.6	17.2	Single-Crystal
120U	1055	800	1070	1090	p-GaN/Sapphire	180	593.6	32.4	Poly-crystalline
125U	1055	800	1078	1090	p-GaN/Sapphire	180	468	10.5	Poly crystalline
126U	1500	800	1078	1090	p-GaN/Sapphire	180	643.2	44	Poly-crystalline
136U	400	800	1100	1090	Sapphire	180	649.8	26	Single-Crystal
139U	400	800	1100	1090	i-GaN/Sapphire	180	495	13	Poly-crystalline-
148 L	400	800	1100	1078	Sapphire	300	852	74	Single crystal
150L	400	800	1100	1078	GaN/Sapphire	180	1638	79	Single crystal
192L	1055	800	1078	1078	p-GaN/Sapphire	180	443	8.98	Single crystal

5.4.2 Formation of hexagonal InN pyramids by HPCVD

We have demonstrated that 3D InN pyramids can be produced on 2 μm GaN templates using the HPCVD technique. The impact of large InN hexagonal pyramids with different sizes on the crystal quality of InN epilayer was evaluated by means of X-ray diffraction of InN (0002) rocking curves, which yielded a full width at half maximum below 1643 arcsecond. The effects of very small misorientation of the pyramids and different sizes of hexagonal pyramids observed over the InN surface lead to poor crystalline quality of InN. From XRD measurements, we observed that there was no In metal peak and no other InN related peak except the InN (0002) diffraction peak. The size and shape of pyramids under study have been determined by means of AFM analysis. Figure 5.14 presents an example image of hexagonal pyramids. The growth is 2D at the earlier stage of InN growth as observed in Figure 5.14. On the other hand, by the time when InN growth continued, the surface of InN became populated by 3D hexagonal pyramids as depicted in Figure 5.14. Interestingly, it is found that for the growth of InN on a GaN template, there is a transition from the 2D growth mode to the 3D growth mode. From a higher magnification AFM image of the pyramid, we determined a diameter of 24 μm and a height of 500 nm; the shape corresponds to a perfect hexagon in the film plane and to a truncated pyramid in the vertical direction. Nevertheless, further investigations are needed to understand better the factors controlling the nucleation and growth of InN pyramids.

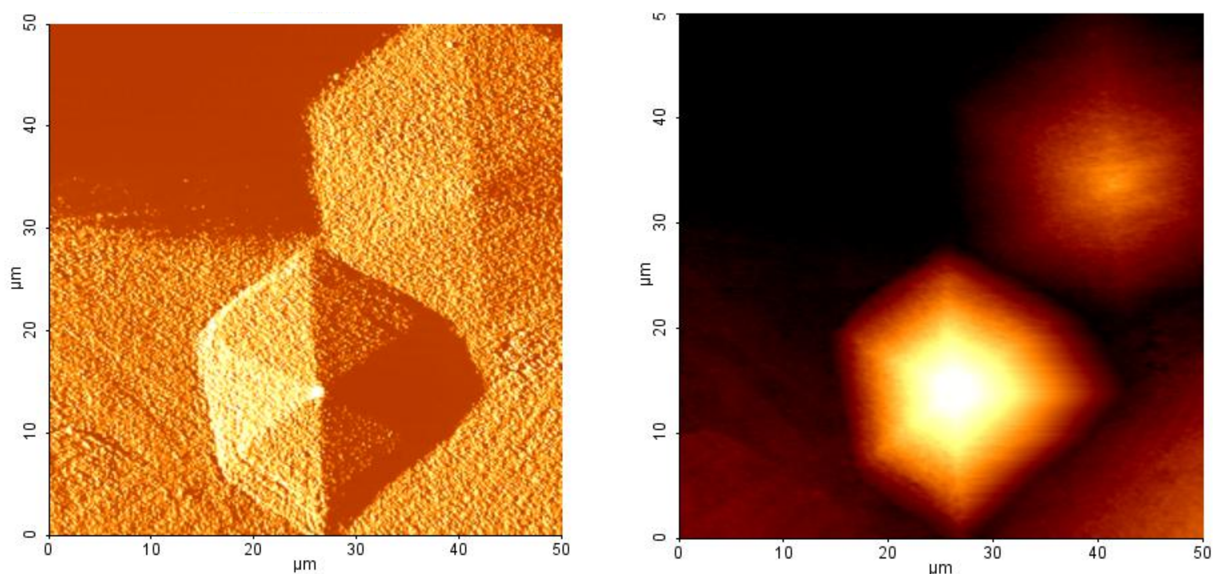

Figure 5. 14 AFM images of the sample surface containing InN pyramids (50×50 μm, NC mode)

5.5 Summary and conclusion

We have studied the structural and surface morphology properties of InN layers grown on GaN (0002) epilayer/sapphire substrates and sapphire substrates. InN layers grown on GaN epilayers exhibit single phase InN (0002) Bragg peaks with FWHM around 200 arc sec. Lattice parameters "*c*" extracted from the XRD data were found to be deviating from the unstrained InN film ±0.0015 Å. The XRD results show that InN grown with a lower ammonia:TMI molar ratio have better crystalline quality. InN films of high crystalline quality have been grown by HPCVD and no Bragg peak in the vicinity of 33° is observed in the XRD spectra good quality InN thin epilayers. The increasing indium-to-nitrogen flux ratio during epitaxial growth results in the appearance of the (101) diffraction peak at 33.0°. This observation strengthened the association of the diffraction peak at 2θ~33° which might be due to the In clusters in the InN samples. A

peak asymmetry appears on the low angle side of (0002) peak and the asymmetry increases as the V/III molar ratio increases due to several peaks underlying in the (0002) structure. Secondary peaks are less prominent as the quality of the layer improves, and it is still hard to determine whether those peaks are due to the native point defects or impurity incorporation. However, this secondary peak does not represent a secondary phase. LEED yielded a 1×1 hexagonal pattern demonstrating a well-ordered *c*-plane surface. HREEL spectra after AHC cleaning exhibit bending and stretching vibrations with no indications of an indium droplet formation. The plasmon excitations shifted about 300 cm^{-1} higher in spectra acquired using 7 eV electrons due to higher plasma frequency and carrier concentration at the surface than in the bulk, which indicates surface electron accumulation. Since HREEL spectra taken with low incident energy show that the surface is N-H terminated, the electron accumulation on InN surfaces is not due to the excess of indium. We have investigated the surface morphology properties of InN films grown by the HPCVD technique on different templates with different growth parameters by using AFM. Some InN films show that columnar structures were grown on sapphire at temperatures of 1078 and 1090 K. Several of InN layers exhibit disoriented hexagonal columnar structures with respect to each other and the *c* axis of the substrate due to the lattice mismatch between the InN film and sapphire substrate. Samples grown on GaN templates are found to be smoother (9 nm) compared to the samples grown on sapphire (~26 nm). The surface roughness of the InN samples has been correlated with the FWHM of InN (0002) rocking curve and this correlation is shown in Figure 5.16. This result suggesting that crystalline quality is improved if the surface topography is smoother. The appearance of second phase InN (101), which is attributed to In metallic

clusters, makes the InN surface is rougher commensurate with its increasing contribution in the XRD spectrum. We have demonstrated growth of 3 dimensional hexagonal InN pyramids, which are a forerunner of InN nanostructures of targeted geometries. The growth was observed to be 2D at the earlier stage of InN growth but as InN growth continued, the surface became populated by 3D hexagonal pyramids. Interestingly, it is found that for the growth of InN on a GaN template, there is a transition from a 2D to a 3D growth mode.

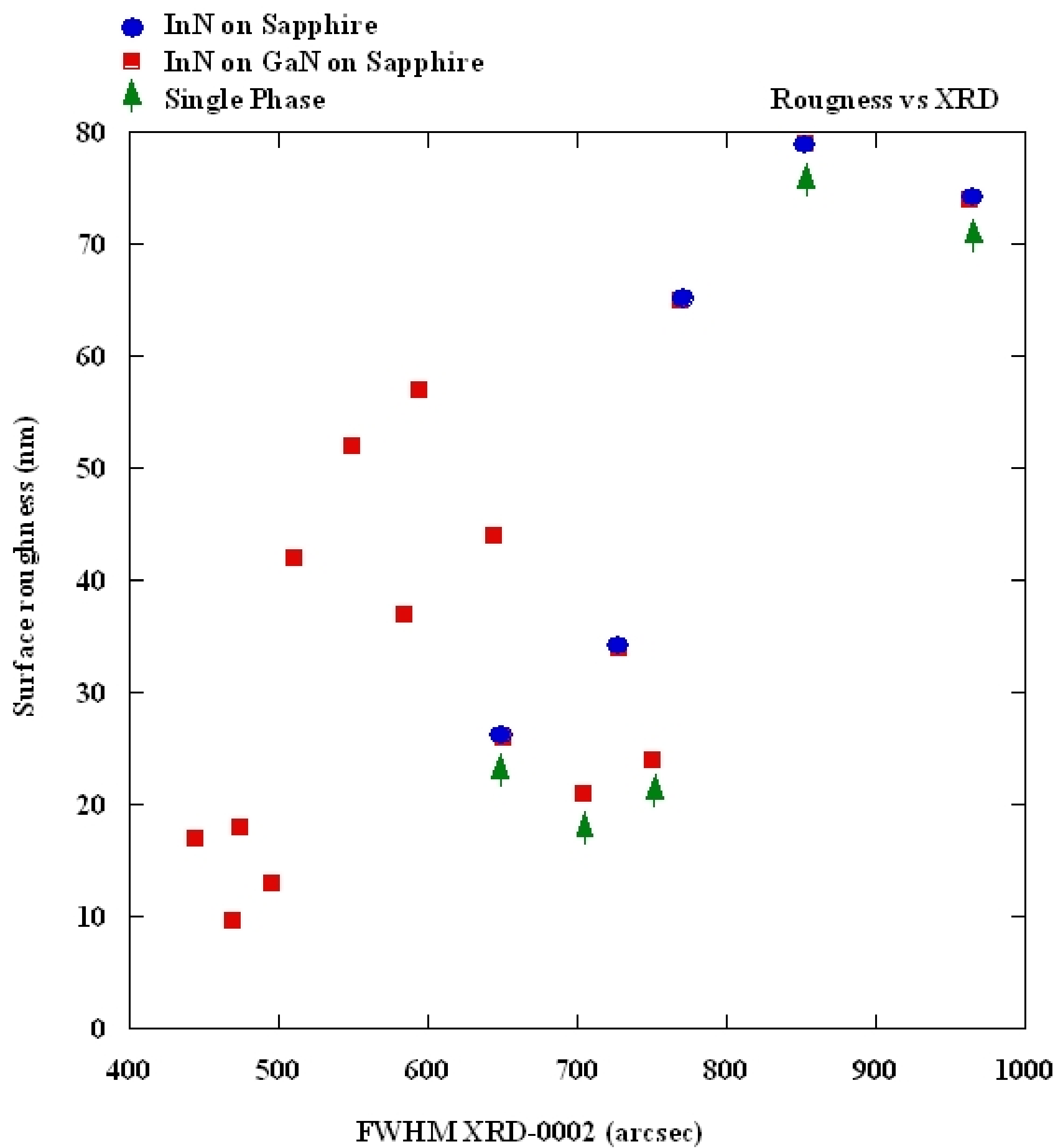

Figure 5. 15 FWHM of XRD rocking curves taken at the (0002) reflection measured on HPCVD grown InN as a function of the surface roughness.

Chapter 6

Optical properties of InN thin films

6.1 Optical transmission measurements of InN films

The electronic structure of single crystalline InN layers was carefully studied by means of optical transmission. In the case of most semiconductor samples, the fundamental energy band gap can be observed by transmission spectroscopy in the range from 0 to 6 eV. Therefore, optical transmission spectra lead to the determination of the band gap energy and also defect levels within the band gap of the semiconductor. When a photon is incident on a semiconductor several interactions with carriers can take place which depend on the energy of the incident photon. These mechanisms are band-to-band (interband) transitions, impurity-to-band transitions excitonic transitions, free carrier (intraband) transitions and phonon transitions. For incident photon energies greater than the band gap of the semiconductor, E_g, the absorption is dominated by band-to-band transitions.

As discussed in previous chapters, the InN band gap was estimated to be 1.85 eV until 2000[38]. Since then, it has been reported by several groups that band gap energy of InN is approximately 0.7 eV[89,139]. We have reported InN layers grown via HPCVD with different III/V precursor rations which exhibit absorption edge energies of 0.75 –1.6 eV[14]. In addition, we have reported that the optical absorption shifts below 1.1 eV as carrier concentration decreases[140]. The variation of the optical absorption edge can be

attributed to the following causes. High carrier densities (~10^{20} cm^{-3}) introduce a large concentration of donors, charge dislocation lines[141], grain boundaries (in polycrystalline films) and surface charge defects[127]. It is generally believed that the smaller band gap values are due to the higher quality films while those showing large band gap values possess carrier densities in the range of ~ 10^{20} cm^{-3} and contain a large number of defects. However, Shubina *et al.* recently reported Mie resonances observed in low band gap InN films that are a result of metallic In clusters in the films, which can cause strong photo-emission around 0.7 eV. This emission is attributed to the surface states at metal-InN interfaces. Our results revealed for hexagonal InN an optical absorption edge of about 1 eV, which is much smaller than 1.85 eV, the value established for many years.

Normal incidence optical transmission measurements of a series of InN thin film layers grown by HPCVD on sapphire substrates and GaN templates were performed. Optical transmission measurements at room temperature were carried out in the 300 nm – 2800 nm wavelength range (4 eV-0.4 eV) as outlined in Chapter 3. The sample identification numbers, sample growth conditions and substrate are given in Table 6.2.

Acquired transmission spectra for InN films on sapphire and GaN templates are presented in Figures 6.1 and 6.2 with varying NH_3/TMI ratio. Each spectrum represents transmission through the entire stack. Transmission spectra of Samples #142 U, #143 U that were grown on sapphire, as shown in Figure 6.1, were modeled using a three phase model (air/InN/Sapphire) as discussed in Chapter 3. On the other hand, the spectra of samples 110U, 111U, 112U that were grown on GaN/Sapphire templates as shown in Figure 6.2 were modeled using a four-phase model (air/InN/GaN/sapphire). The experimental spectra and the best-fit spectra of these samples are shown in Figures 6.1

and 6.2. Samples grown on GaN/Sapphire exhibit characteristic interference fringes due to the underlying GaN epilayer with a thickness of approximately 2 μm. The optical analysis of InN layers grown under similar condition but with slight variations in the ammonia:TMI molar ratios showed a shift in the absorption edge from 1.65 down to 1.48 eV. Optical absorption edges calculated from the fitting of transmission spectra indicate a down turn with increasing ammonia:TMI molar ratio. This behavior is valid for both InN samples grown on both sapphire and GaN/sapphire substrates. It was found from the best-fit algorithm that there are absorption structures centered around ~1.1 eV, ~0.8 eV and ~0.5 eV. The development of the absorption structures for these samples suggest that the observed absorption edge shift to lower energy values is caused by these absorption structures centered at different energies[14].

Numerical analysis of the optical transmission data is used to examine the absorption edge and the absorption centers present in the InN films. The energetic position of two optical absorption centers present in InN films is shown in Figure 6.3 as a function of InN optical absorption edge. The linear correlation between the optical absorption edge and the two absorption centers indicates a closed relation between the carrier concentration and the absorption centers in the film. However, the strength and broadening of these two absorption centers do not directly correlate to the optical absorption edge. It is observed that there is a shift to lower energies with the shift in absorption edge. The correlation between the optical absorption edge and the carrier concentration will be presented in the following section. Additional effects such as point defect chemistry, defect levels and structural quality must considered in order to understand the optical absorption edge and the absorption centers present in the InN film.

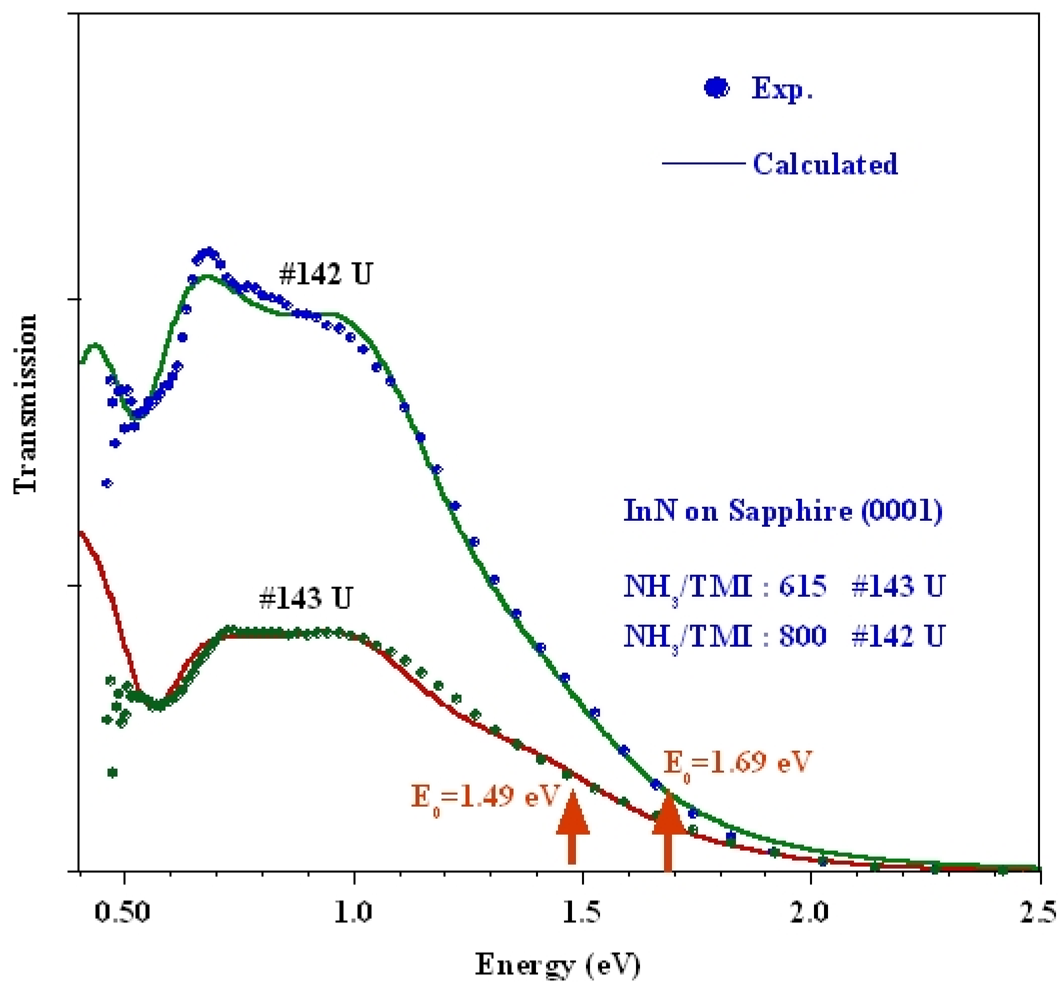

Figure 6. 1 The experimental transmission spectra and their best-fit curves of samples #143U and #142U with different V/III molar ratios. Arrows indicate the calculated optical band gap.

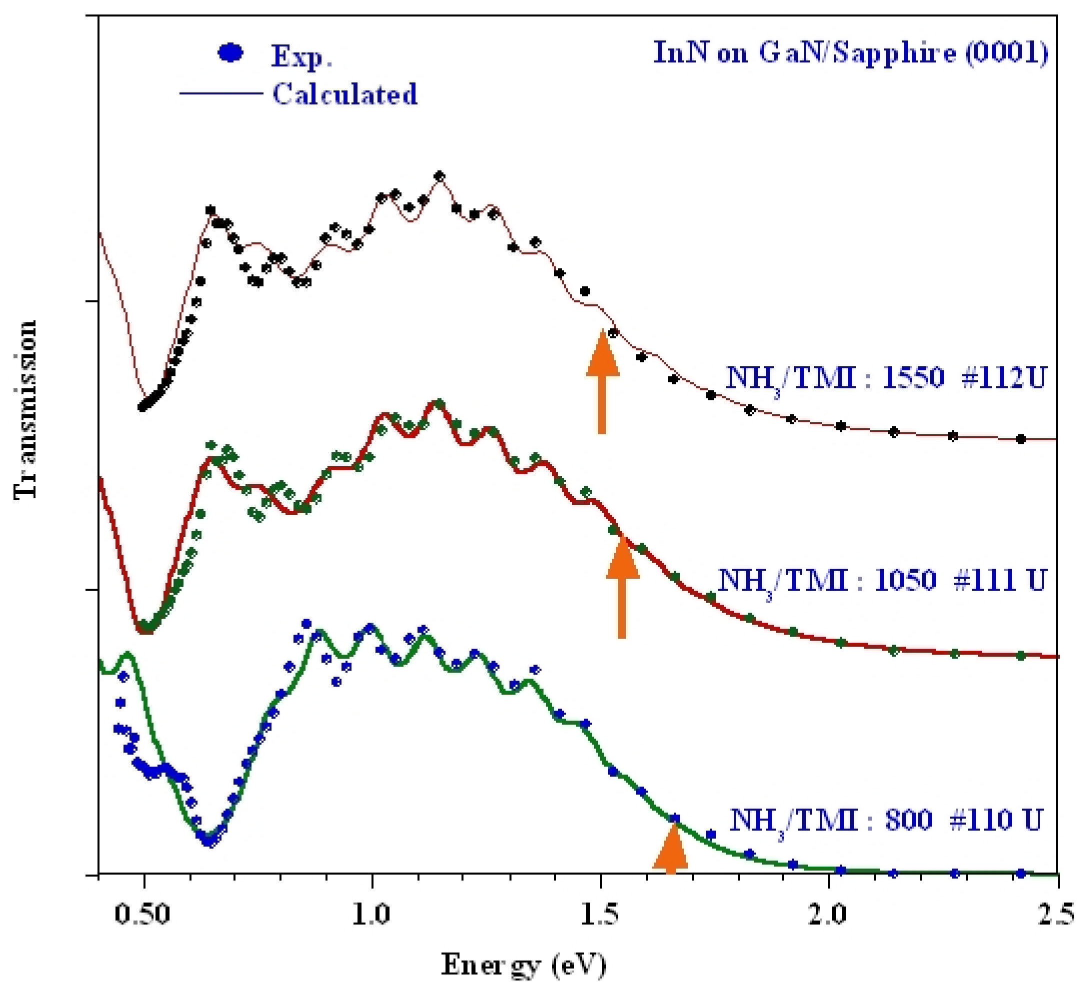

Figure 6. 2 The experimental transmission spectra and their best-fit curves of InN samples grown on GaN templates with different V/III molar ratio. Arrows indicate the calculated optical band gap.

However, the absorption centers that appear at ~0.5 eV might be attributed to the spectra of recombination of degenerate electrons with the holes trapped by deep acceptors states [142]. In other words, the absorption center around 0.5 eV is due to the unidentified deep defect centers. The absorption centers at ~0.75 eV can be attributed to either In clusters formed (Mie resonance) or InN related band to band transitions[143]. It is worth mentioning that the observed variation of the optical absorption energy and the absorption centers is related not only to the variation of carrier concentration but also to the nitride-indium stoichiometry, the degree of impurity incorporation and/or crystalline quality. The optical transmission measurements and numerical analysis of the optical absorption edge has shown that the band gap of this semiconductor is narrow and consistent with the recent observed improvements in InN film technology.

A correlation of analysis the thickness of the InN film with the optical absorption edge and FWHM of InN (0002) X-ray rocking curve has been performed. Figure 6.4 compares the optical absorption edge obtained from the optical transmission fit above, and the crystalline quality (as measured by X-ray diffraction) for various InN film thicknesses. The optical absorption edge decreased from 1.6 eV to 1.2 eV as the film thickness increased from 300 nm to 550 nm. This is most likely due to the reduction in residual compressive strain in the crystal structure.

Table 6. 1 The optical transmission spectroscopy fitting parameters for InN samples. The columns list InN layer thickness (d), the optical absorption edge (E_0), high frequency dielectric constant (ε_∞), S_{ab} Lorentzian oscillator strength, E_{ab1} energetic position of absorption center, and Γ_{ab} damping constant.

Sample	d (nm)	E_0 (eV)	ε_∞	S_{ab1}	E_{ab1}(eV)	Γ_{ab1}	S_{ab2}	E_{ab2}(eV)	Γ_{ab2}
110U	490	1.66	7.6	0.6	0.63	0.17	0.07	1.08	0.3
111U	338	1.63	7.1	0.55	0.5	0.1	0.5	0.8	0.34
112U	290	1.54	7.8	0.52	0.51	0.36	0.52	0.83	0.36
125L	305	1.4	7	0.92	0.44	0.39	0.27	0.82	0.5
192L	400	1.2	8.3	0.29	0.49	0.14	0.45	0.77	0.8
135U	210	1.37	NA	2	0.4	0.6	0.46	0.84	0.45
142U	335	1.49	6.5	0.19	0.53	0.19	-	-	-
143U	380	1.69	5.5	0.2	0.56	0.17	-	-	-
207L	470	1.23	8	1	0.48	2.1	0.5	0.75	0.95
209L	470	1.21	8	0.73	0.45	2	0.53	0.75	0.63

Table 6. 2 The growth parameters of InN samples. R_p reactor pressure was at 15 bar and total gas flow rate was 12 slm.

Sample	V/III ratio Nucleation	V/III ratio Growth	Temp. Nucleation (K)	Temp. Growth (K)	Substrate	Growth time (min.)
76U	400	800	1100	1090	p-GaN/Sapphire	90
110U	400	800	1100	1090/1085	p-GaN/Sapphire	180
111U	530	1055	1100	1090/1085	p-GaN/Sapphire	180
112U	800	1583	1100	1090/1085	p-GaN/Sapphire	180
125L	1055	800	1078	1078	p-GaN/Sapphire	180
192L	1055	800	1078	1078	p-GaN/Sapphire	180
135 L	400	800	1100	1078	Sapphire	180
135U	400	800	1100	1090	Sapphire	180
142U	400	800	1100	1090	Sapphire	180
143U	350	615	1100	1090	Sapphire	180
207L	1055	800	1078	1078	GaN/Sapphire	180
209L	1055	800	1078	1078	GaN/Sapphire	180

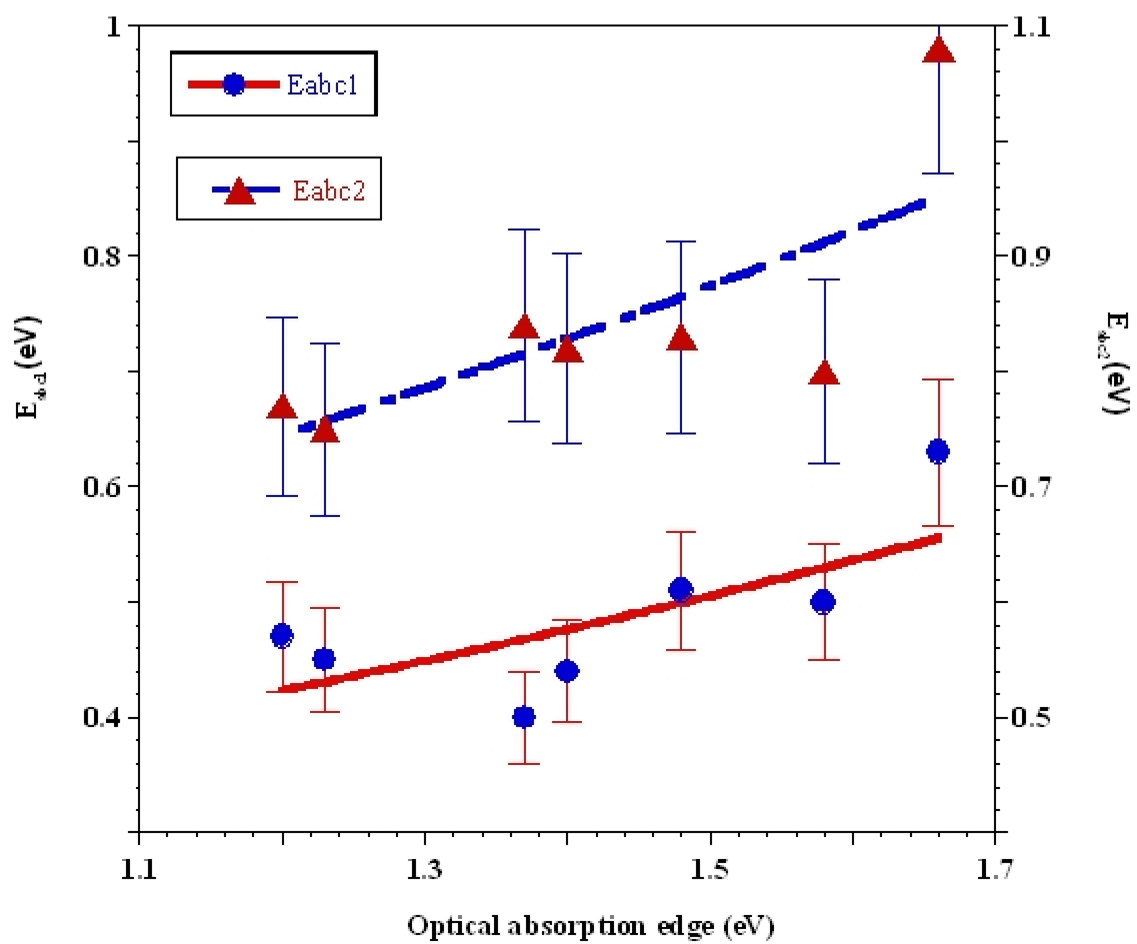

Figure 6. 3 Optical absorption edge dependence of absorption centers obtained from the analysis of optical transmission spectra of thin InN films. The solid lines represent the linear fitting results.

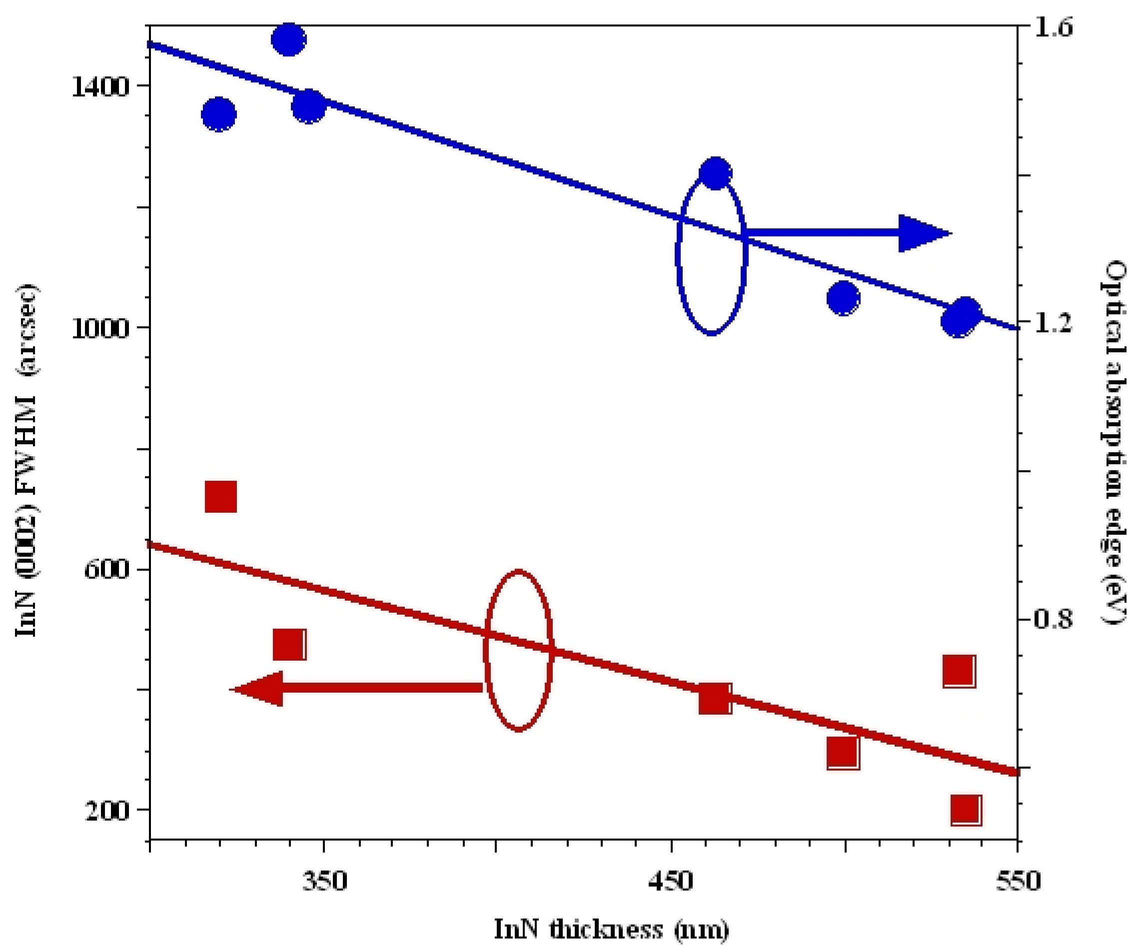

Figure 6. 4 Comparison of optical absorption edge energy and, FWHM of InN (0002) as a function of InN thickness.

6.2 Infrared reflection measurements of InN films

Infrared reflection spectroscopy has been recently proven to be a powerful tool for the determination of free carrier properties and determination of free carrier effective mass[1,6]. Infrared reflection measurements of the InN films were performed at room temperature in the frequency range of 1000 – 8000 cm^{-1} (~1.25 μm - 10 μm) under near-normal incidence geometry (less than 8° incidence angle). The shift of the IR reflection line was caused by plasma oscillations in the range of 4500 to 3000 cm^{-1} with increasing free carrier concentration, as shown in Figures 6.5 and 6.6. Therefore, we can estimate electron concentration in the sample with this shift. Interference fringes were observed for every IR reflection spectrum in the range above the plasma frequency and were used to calibrate the film thickness. IR reflection spectra of samples grown on sapphire were modeled using a three phase (air/InN/Sapphire) while the spectra of samples grown on GaN/sapphire templates were modeled using a four-phase model (air/InN/GaN/sapphire). Based on a multi-oscillator model for optical phonons and a Drude model for free carriers, the theoretical IR reflection spectra can be calculated with a standard multilayer technique. The InN optical phonon frequencies of E_2(high) and A_1(LO) were assumed constant at 479 and 590 cm^{-1}, respectively. It is reasonable to keep the optical phonon frequencies fixed because the reflection spectra are dominated by the plasma frequency. The best-fit parameter values obtained for thickness, high frequency dielectric constant (ε_∞), plasma frequency (ω_p), and damping constant of plasma oscillator (Γ) are listed in Table 6.3.

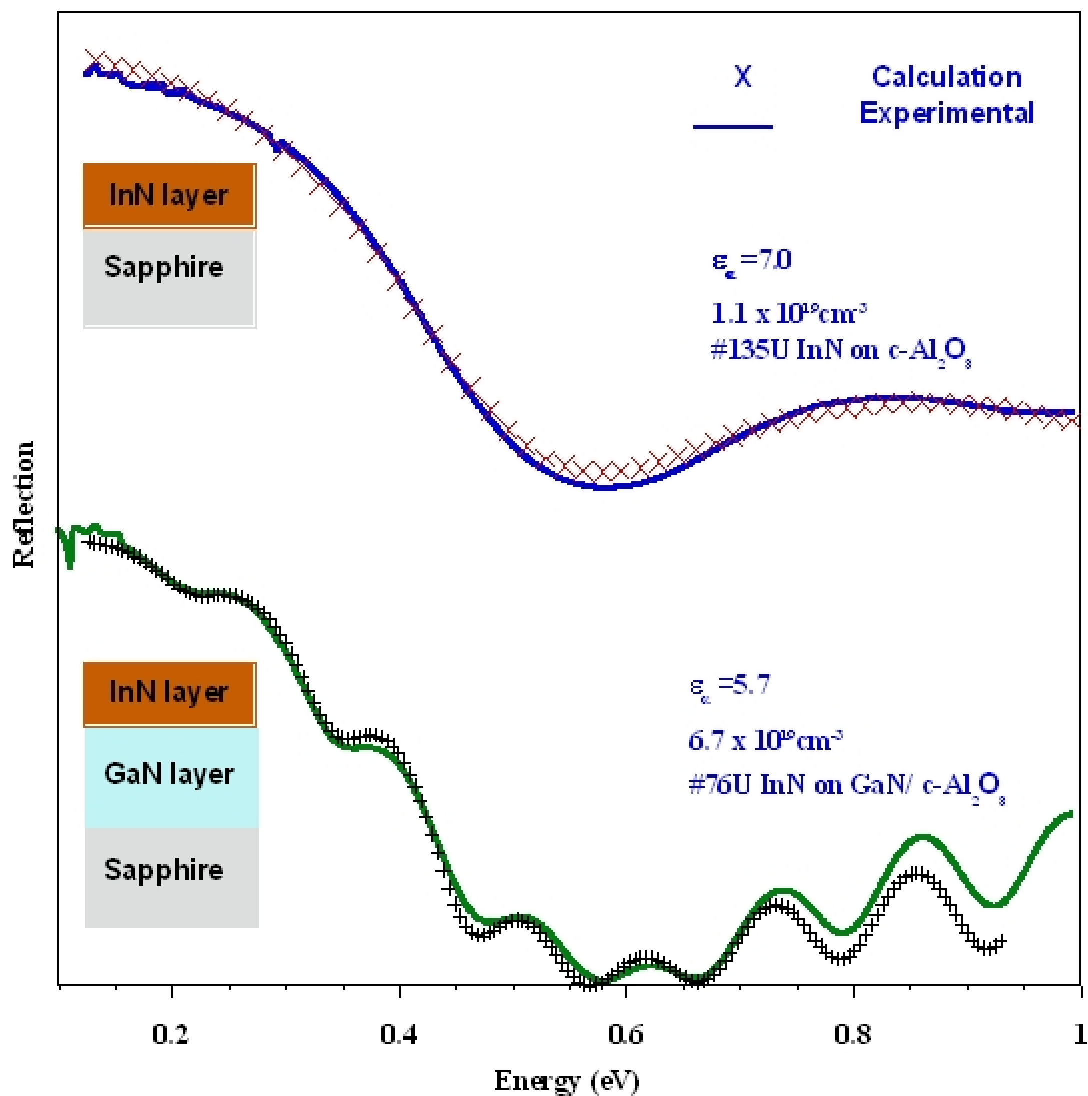

Figure 6. 5 The experimental IR spectra and their best fit curves of samples #76U, and #135U. The fitting parameters are given in Table 6.3. All experiments were performed at room temperature.

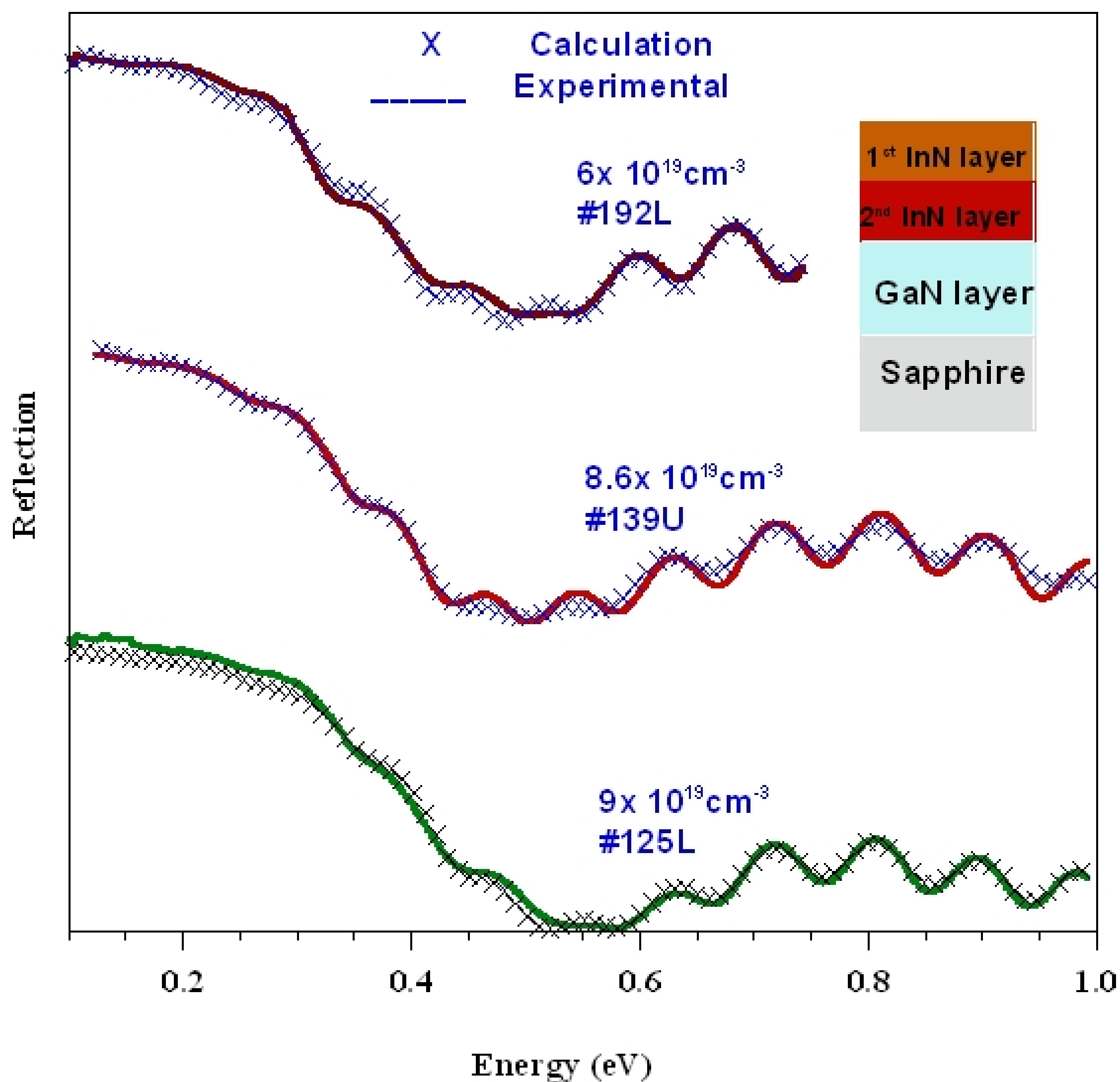

Figure 6. 6 Infrared reflection curve of three InN samples with different free carrier concentrations and two different doping regimes. The crosses are theoretical fits using a complex dielectric function model.

Table 6. 3 Model fitting parameters for IR reflection spectroscopy. Evidence for the existence of two separate InN layers was found by the IR spectra fitting. Layer thickness (d), high frequency dielectric constant (ε_∞), plasma frequency (ω_p), damping constant (Γ), and estimated free concentration are given for each layer. The layer next to GaN or sapphire is the 2nd layer and the layer above is the 1st layer.

Sample	$N \times 10^{19}$ (cm^{-3})		ω_p (cm^{-1})		Γ(cm^{-1})		ε_∞		μ (cm^2/Vs)		d (nm)	
76U	6.7		3471		860		5.7		434		256	
110U	16		4530		820		7.6		126		520	
111U	15		4450		980		7.6		105		340	
112U	12		3990		490		7.6		2111		320	
135U	11		3720		327		7.0		327		228	
	1st	2nd	1st	2nd	1st	2nd	1st	2nd	1st	2nd	1st	2nd
125L	9	<0.05	3494	-	390	-	7.5	7.3	266	-	393	79
139U	8.6	<0.04	3110	<200	423	-	8.8	8.4	245	-	373	64
192L	6	<0.05	3029	-	460	-	6.5	7.5	225		452	81
207L	10	<0.1	3660	-	860	-	7.8	8	120	-	452	41
209L	8.5	<0.1	3250	-	427	-	8	7.5	250	-	415	120

A Levenberg-Marquardt fitting algorithm was used[121], where the model parameters were varied until a close fit between calculated and experimental data was found. The best-fit of the infrared reflection spectra reveals the plasma frequency ω_p and the plasma damping constant γ_p. The plasma parameters ω_p and γ_p are related to the concentration N_e, the effective mass m_e, and the mobility μ_e of the free electrons by the following equations:

$$\omega_p^2 = \frac{N_e q^2}{m_e \varepsilon_0 \varepsilon_\infty} \tag{6.1}$$

$$\gamma_p = \frac{q}{m_e \mu_e}. \tag{6.2}$$

The effective electron mass of InN was set constant to $0.09m_0$[122], neglecting the first order dependency of the electron mass with the free carrier concentration. The experimental spectra and the best-fitted spectra of these samples are shown in Figure 6.5. The calculated results agree well with the experimental data, including the interference fringes. According to the fitting analysis, the high frequency dielectric constant ε_∞ varies from 5.2 to 8.3 with an average value of 7.5. Other reported values for the high frequency dielectric constant ε_∞ are so far controversial; 9.3[144], 8.4[34], 7.5, 6.7[145], and 5.8[146]. The obtained free carrier concentrations from IR reflection spectra fitting of these samples are in the mid 10^{19} or lower 10^{20} cm^{-3} range. The carrier mobilities of these thin films are generally in 100 cm^2/Vs to 400 cm^2/Vs range. The detailed parameters, such as the film thickness d , mobility μ , carrier concentration n, plasma frequency ω_p , damping constant γ_p and high frequency dielectric constant ε_∞, are listed in Table 6.3.

The infrared reflection spectra of samples #192 L, #125L and #139U could only be modeled by assuming two InN layers with different film thickness and doping levels as shown in Figure 6.6. The best-fit parameters of those two layers are also listed in Table 6.3 with the estimated free carrier concentration. In Table 6.3, the top most layer of the structure, which is open to the air, is labeled as the 1st layer and the 2nd layer is under the 1st layer. The plasma frequency of the 1st layer is much higher as is the free carrier concentration. The required 2nd InN layer for samples #125L, #192L and #139U was found to have a low free carrier concentration. This reveals that an InN layer with a low free carrier concentration has been formed during the initial growth of the first few hundreds of nanometers. After that, the free carrier concentration in the InN layer rapidly increased requiring it to be considered as a separate layer for modeling purposes. The average ε_∞ value of these low doped InN layers is around 8 which is close 8.4, the theoretically predicted value[34]. It should be noted that ω_p and Γ were found to be below 200 and 100 cm^{-1}, respectively, but precise values could not be found from these fits. The reason for this difficulty is that ω_p of the top-most layer is much higher than that of the 2nd layer and it is overshadowed by the plasma oscillator of the 2nd layer. Therefore, the fitting algorithm could not find a reasonable minimum.

The correlation of optical absorption edge of the InN films with the free carrier estimates obtained by IR-reflection spectroscopy is shown in Figure 6.7. The sample #192L with lowest carrier concentration has an absorption edge situated near 1.2 eV. The energy of the edge is a little higher than ~1.1 eV[147] expected for the 6×10^{19} cm^{-3} carrier concentration, which takes into account the Burstein-Moss effect and assumes a band-gap of ~0.7 eV. This small difference between our optical absorption edge and the optical

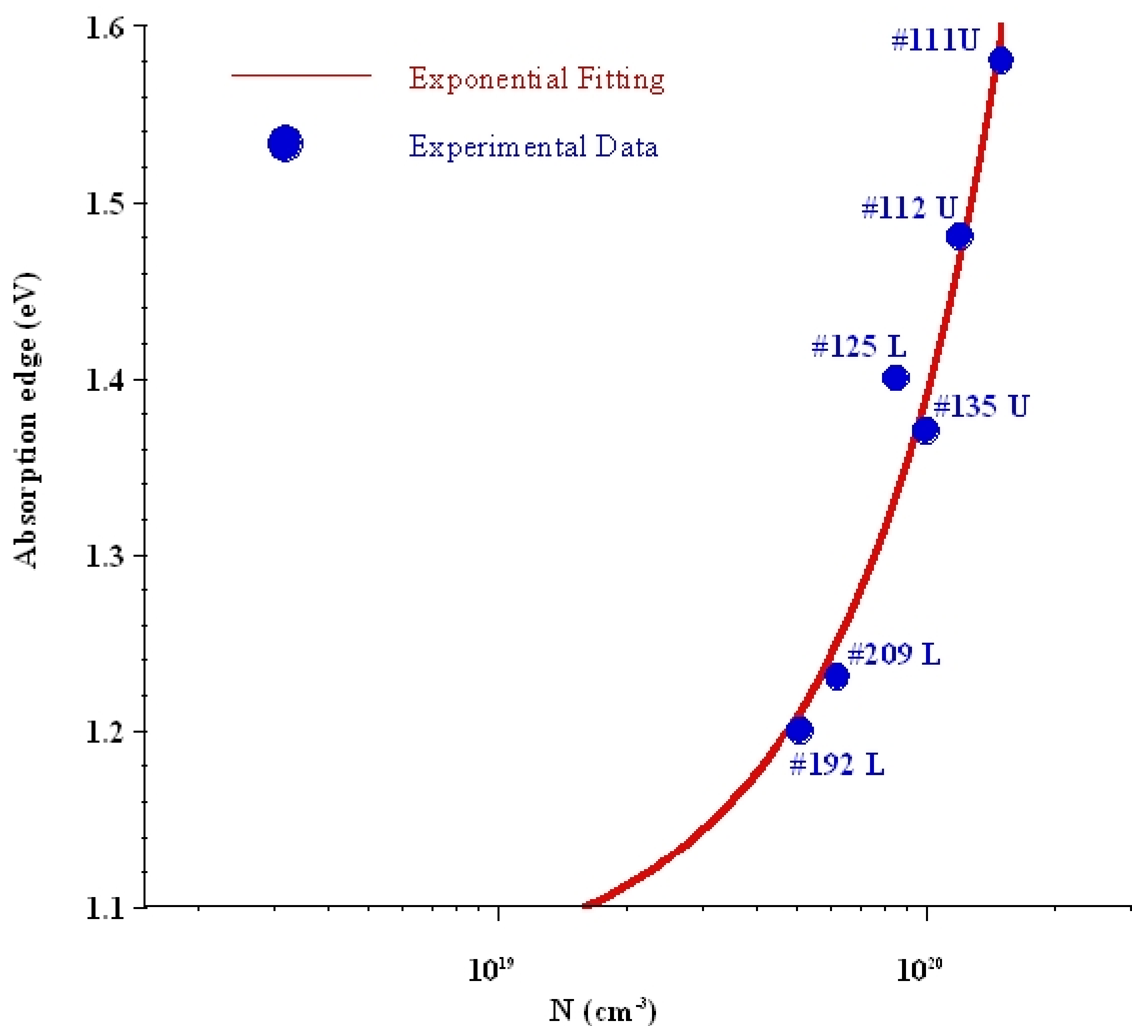

Figure 6. 7 Dependence of optical absorption edge on carrier concentration as obtained from a modified model dielectric function in combination with experimental data.

absorption accounting for Moss-Burstein effect can be due to the non-stoichiometry contribution, residual oxygen causing oxides in InN films and /or voids for both InN samples either grown by HPCVD or MBE.

The surface morphology analysis of the HPCVD grown InN samples and their surface roughness is presented in Chapter 5. Figure 6.8 shows the surface roughness dependence of mobility for InN films. One can see that the samples with relatively smooth surfaces have high mobility (432 cm^2/Vs) in spite of the fact that the difference in

roughness is on a nm scale. Excellent morphology for InN is important to attain a high electron mobility as reported by Yamamoto *et al*[148].

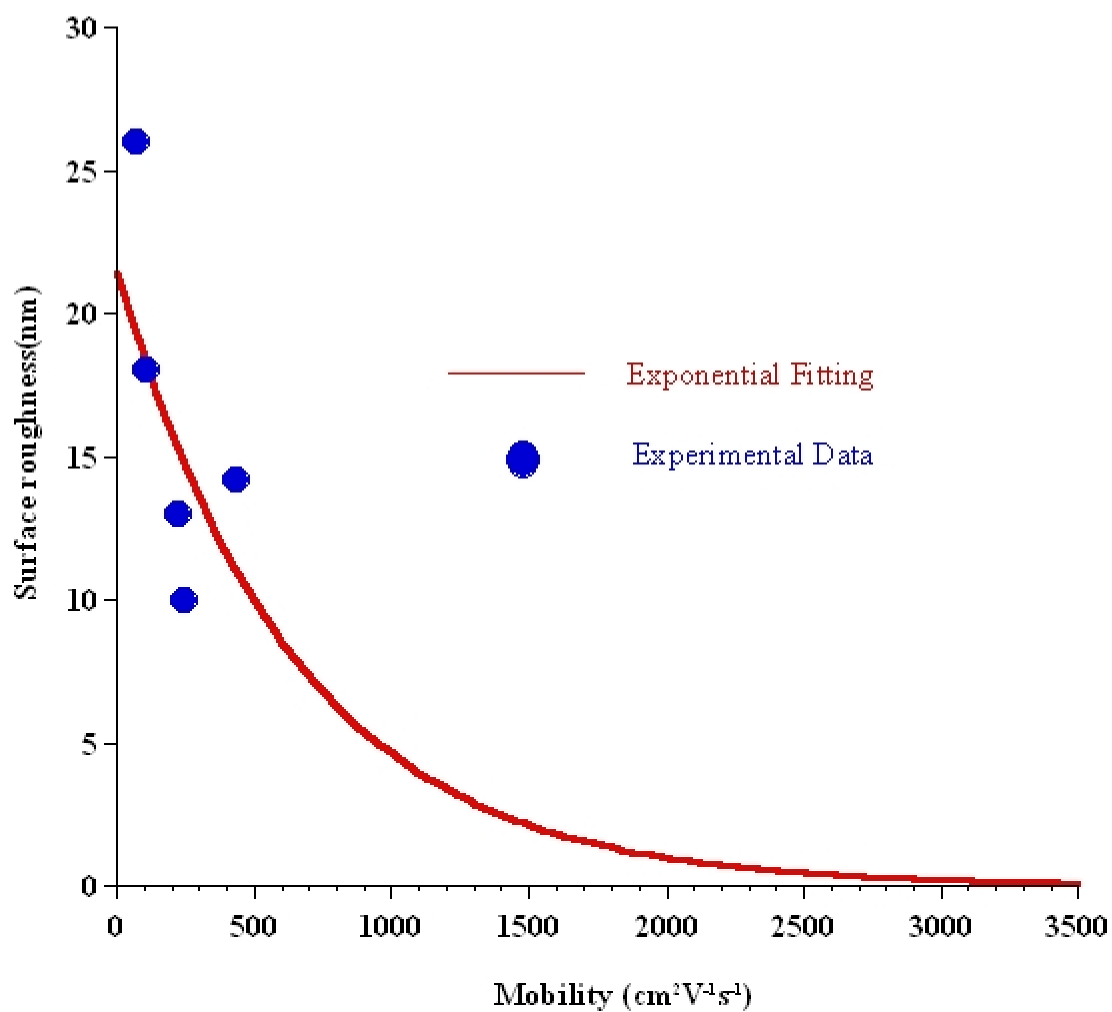

Figure 6. 8 Surface roughness of InN samples with different carrier mobilities obtained from the fitting of the experimental infrared reflection spectra.

6.3 Raman spectra of InN film in backscattering geometry

InN epilayers grown by HPCVD with different carrier concentration were investigated by Raman spectroscopy. Raman spectroscopy is a valuable tool that can probe collective oscillations of free electrons, via their coupling with LO phonons of the wurtzite structure. As photoluminescence experiments do not give a complete description of the electron gas in doped semiconductors, Raman spectroscopy is a crucial step in determining crystalline parameters. In addition, Raman spectroscopy is a nondestructive and fast method to measure strain and structural quality of the InN material[149]. In order to gain insight into the free carrier concentration, the observed line shape of the A_1(LO) mode damped by free electrons is simulated by using Linhard-Mermin approach[149]. DP+EO is considered as the major light scattering mechanism within the interaction. In the DP-EO scattering mechanism, the crystal potential is modulated by the relative displacement in atomic configuration where atomic displacement introduces elastic strain while the effective masses remain unchanged by the induced strain.

The Raman spectra of the InN layers were obtained in back scattering geometry $z(\ldots.)\underline{z}$ using an excitation energy of 2.33 eV at room temperature. Figure 6.9 shows Raman spectra of InN films grown on GaN/Sapphire and sapphire substrates. The spectra are normalized to intensity of the E_2 (high) line. The two allowed optical phonon modes of hexagonal InN are E_2(high) and A_1(LO) for Raman in back-scattering geometry. The peak positions of the observed E_2 (high) and A_1 (LO) are in good agreement with that predicted as ~486 cm^{-1} and ~590 cm^{-1}, respectively, by Davydov *et al*[4].

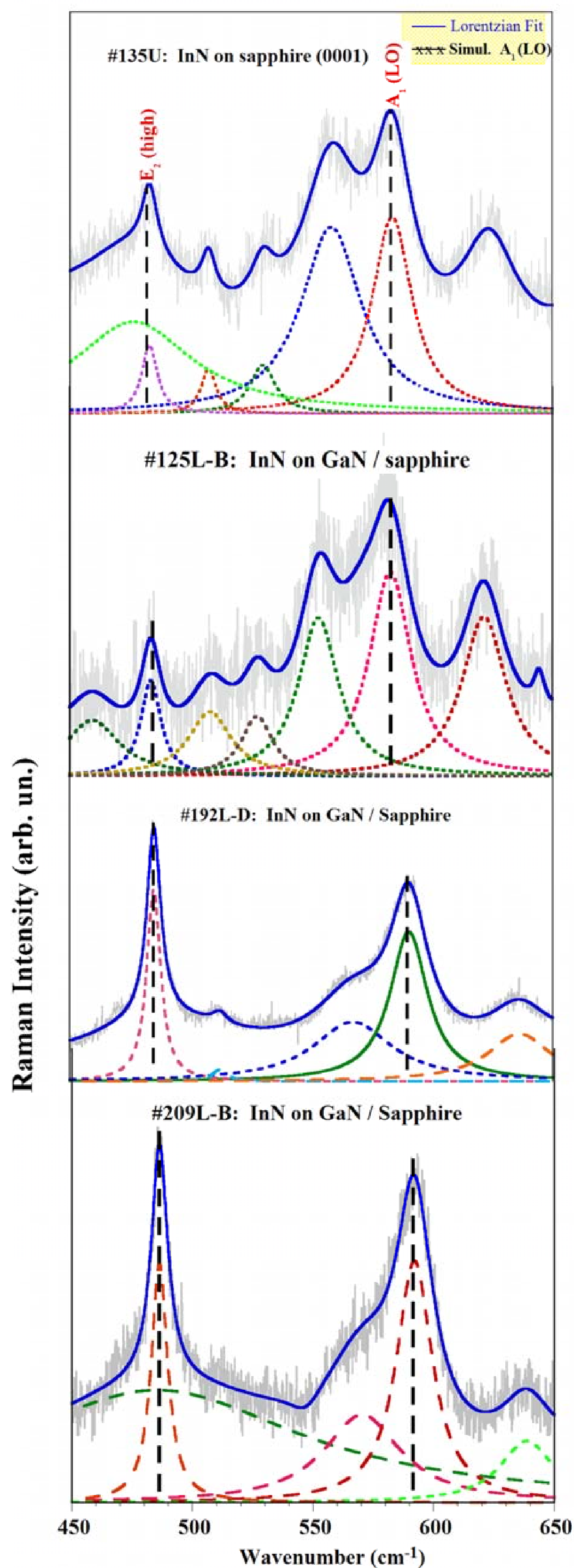

Figure 6. 9 Room temperature Raman scattering of wurtzite-InN grown on GaN/sapphire and Sapphire substrates. Raman modes are identified using Lorentzian fitting.

The line shape of E_2 (high) is related to structural defects and impurities in GaN structures. Wei *et al.*[150] used this relation as a valuation method for expressing crystalline quality, and concluded that the E_2(high) line with FWHM of 4 cm^{-1} indicated a superior crystalline quality material. The FWHM of the E_2(high) line in sample # 192L is 6.9 cm^{-1} and in sample #209L is 8.3 cm^{-1} exhibiting high crystalline quality[4]. Due to the non-polar character of the E_2 (high) mode, there is no interaction of this mode with the conduction-band electrons[151]. The observed Raman bands E_2 (high) and A_1 (LO) become broader for the samples depicted in Figure 6.9 indicating the presence of structural defects. However, the sharper peak structures observed for #192L and #209L indicate improved crystalline quality of the HPCVD grown InN films. The broad Raman mode around 560 cm^{-1} is mainly attributed to the substrates (GaN/Sapphire).

The excitation (2.33 eV) applied in the Raman investigation is above the speculated band gap of InN (0.67 eV)[152]. Therefore, some defect related luminescence contribution to the Raman scattering is unavoidable. We distinguish the overlapped Raman modes by applying Lorentzian curve fittings as shown Figure 6.9. The summary of the Lorentzian curve fittings results is given in Table 6.4.

6.3.1 Electron oscillations –phonon interaction in HPCVD grown InN by Raman spectroscopy

The broadening of A_1(LO) phonon mode, illustrated in Figure 6.10, indicates that changes are induced in InN layers when layers have different free carrier concentration. By monitoring the E_2 (high) phonon mode, we can conclude that no significant structural changes occur with varying carrier concentration. The mechanism responsible for the broadening of LO-phonon modes in InN must therefore be attributed to the change in the

phonon-electron oscillation interaction. The total longitudinal dielectric function of a polar lattice can be written as the sum of background (first term), phonon (second term) and free carrier (third term) contributions

$$\varepsilon(q,\omega) = \varepsilon_\infty + \varepsilon_\infty \frac{\omega_{LO}^2 - \omega_{TO}^2}{\omega_{TO}^2 - \omega^2 - i\omega\Gamma} - \varepsilon_e(q,\omega) \qquad (6.3)$$

where ε_∞ is the background dielectric constant, $\boldsymbol{\omega}$ is the frequency, $\boldsymbol{q}$ is wave vector, Γ is the phonon anharmonic damping parameter, ω_{LO} and ω_{TO} are the longitudinal and transverse phonon frequencies, respectively. The Linhard approach does not include the effect of collisional damping due to the impurities, etc. Mermin incorporated the effect of collisional damping into the Linhard theory within the relaxation time approximation[153]. The dielectric susceptibility of a free electron gas is given by the Linhard-Mermin expression[153]

$$\varepsilon_e(q,\omega) = \frac{(1 + i\Gamma_e/\omega)\chi_e^0(q,\omega + i\Gamma_e)}{1 + (i\Gamma_e/\omega)\{\chi_e^0(q,\omega + i\Gamma_e)/\chi_e^0(q,0)\}} \qquad (6.4)$$

where $\Gamma_e = \tau^{-1} = e/\mu m^*$ is the electron collision frequency, and $\chi_e^0(q,\omega + i\Gamma_e)$ is the temperature-dependent Linhard expression for the dielectric susceptibility[154]. We also assume $m^*=0.14\ m_e$. The Raman scattering intensity of the coupled modes is determined by integrating all scattering processes up to cut-off wavevector q_{max}

$$I(\omega) = \int_0^{q_{mx}} W(q)S(\omega)\,\mathrm{Im}\left[-\frac{1}{\varepsilon(q,\omega)}\right]dq \qquad (6.5)$$

including the Yukawa-type impurity potential weighting function $W(q)$ for $q \neq 0$ processes. The Yukawa-type impurity potential is given by

$$W(q) = \left(\frac{4\pi}{q^2 + q_{TF}^2} \right)^2 \tag{6.6}$$

where q_{TF} is Thomas-Fermi screening wave-vector given by

$$q_{TF}^2 = \frac{6\pi n e^2}{E_F \varepsilon_\infty}. \tag{6.7}$$

The response function $S(\omega)$ in Eq. (6.5) is determined by the predominant scattering mechanism, and in our case DP+EO is considered as the major light scattering mechanism within the interaction. The corresponding scattering factor for the DP+EO mechanism is

$$\begin{aligned} S(\omega) = 1 + 2C \frac{\omega_{TO}^2}{\Delta} \left[\omega^2 \gamma_p \left(\omega_{TO}^2 - \omega^2 \right) + \omega^2 \Gamma \left(\omega_p^2 - \gamma_p^2 - \omega^2 \right) \right] \\ + C^2 \frac{\omega_{TO}^4}{\Delta} \frac{\omega_p^2}{\Omega^2} \left[\gamma_p \Omega^2 + \Gamma \left(\omega_p^2 - 2\omega^2 \right) \right] + \omega^2 \Gamma \left(\omega^2 + \gamma_p^2 \right) \end{aligned} \tag{6.8}$$

where

$$\Delta = \omega_p^2 \gamma_p \left[\left(\omega_{TO}^2 - \omega^2 \right)^2 + \omega^2 \Gamma^2 \right] + \omega^2 \Gamma \left(\omega^2 + \gamma^2 \right) \tag{6.9}$$

$$\Omega^2 = \omega_L^2 - \omega_L^2 \tag{6.10}$$

where C is the first Faust-Henry coefficient.

The intensity of scattered light is calculated by integrating the spectral line shape function up to the maximum wave-vector limit by weight factor due to the Yukawa -type impurity potential. The free electron concentration was used as an input parameter for that routine so that the numerically produced curve and Lorentzian curve, which fitted experimental data, are fitted to each other. The values ω_{TO}=445 cm^{-1} and ω_{LO}=592 cm^{-1} used here were obtained from IR reflection analysis. Figure 6.10 illustrates the simulated Raman line shape of InN films with different free carrier concentrations.

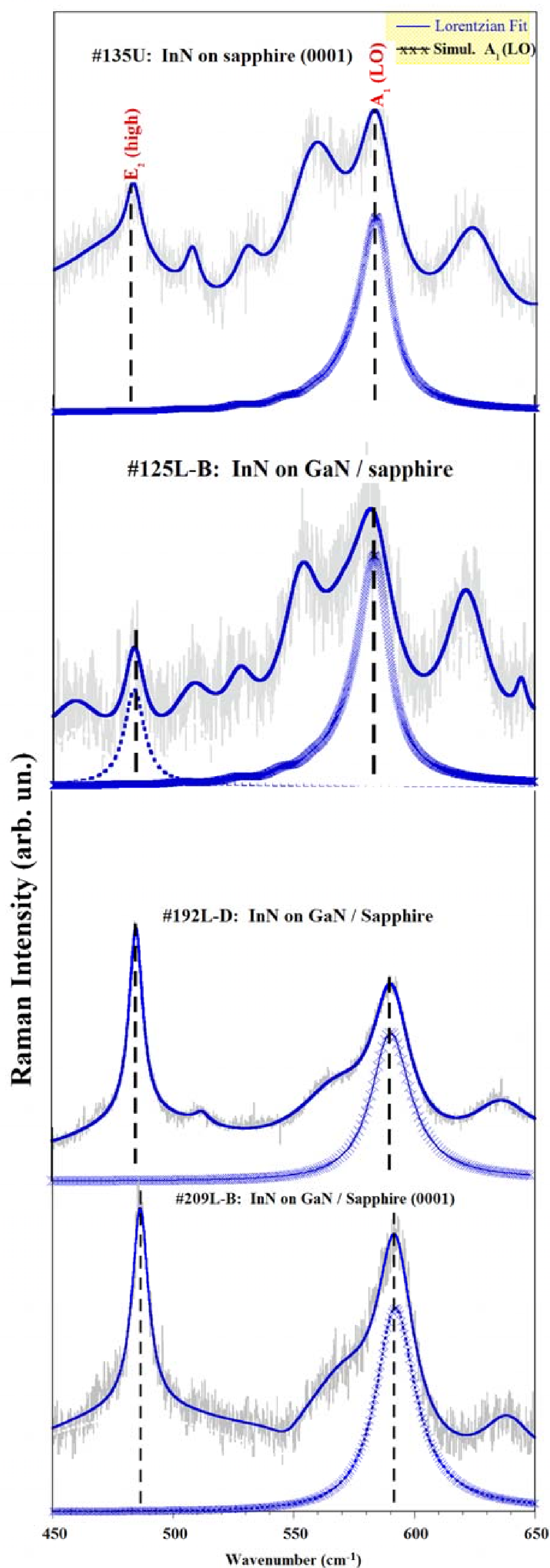

Figure 6. 10 The experimental Raman spectra and the simulated A_1(LO) line shapes. The line shape is calculated using the DP+EO scattering mechanism, which provided the best fit of the experimental results.

The A_1(LO) mode broadens with increasing carrier concentration. The simulated line shape shows a small asymmetry on the low frequency side with respect to the other mechanisms that we have investigated. The free carrier concentrations of the samples were observed in the range $\sim 8\times10^{17}$-$\sim 1.6\times10^{20}$ cm^{-3}. The plasma frequency has been obtained from IR reflection analysis and used in Raman simulations for better compatibility of results with those from IR reflection simulations. Figure 6.11 illustrates the estimated free carrier concentrations obtained from plasmon-phonon coupling as a function of optical absorption edge, which has been calculated from the optical transmission spectra analysis. The optical absorption edge behavior versus the free carrier concentration shows an exponential behavior in free carrier concentration range 10^{+17} cm^{-3} $< n_e < 10^{+20}$ cm^{-3}. The calculated trend of decreasing carrier concentration with decreasing optical absorption edge is consistent with the trend obtained from the IR reflectance data. The estimated band gap energy is slightly higher than the reported ~0.8 eV which is expected for samples of free carrier concentration in the order of $\sim 10^{+18}$ cm^{-3}.

6.3.2 Micro-Raman analysis: strain relaxation at the edges of holes

Micro Raman experiment and analysis of InN thin epilayer was performed by Ronny Kirste at Technical University Berlin. While epitaxial thin film InN samples are currently available, there are currently no bulk InN films in existence. Strain exists in InN films due to the lattice and thermal coefficient mismatches between InN epilayer and substrates such as GaN and sapphire. As this strain greatly influences growth behaviors and optical properties of InN, it is important to know the strain level at GaN/InN or sapphire/InN interfaces.

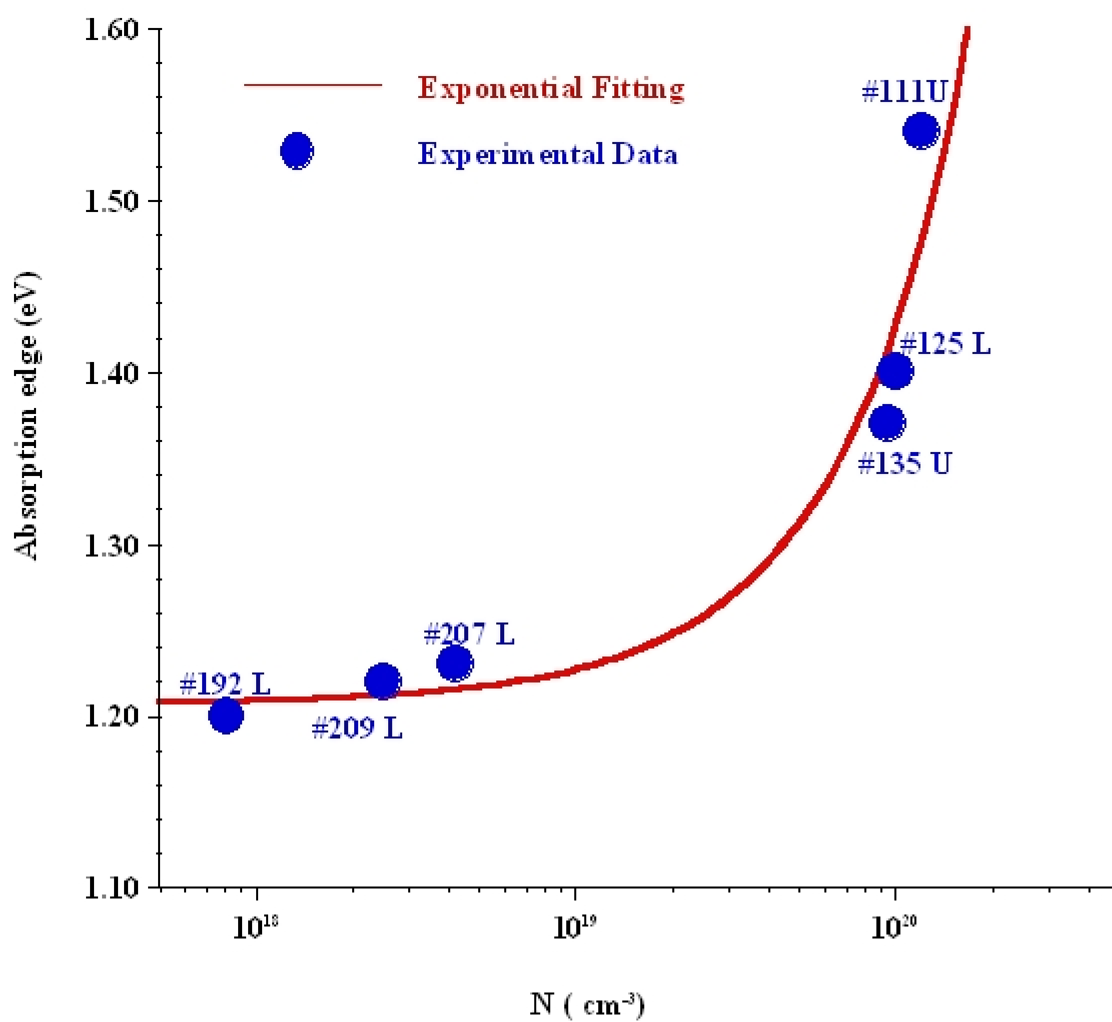

Figure 6. 11 Optical absorption edge vs. carrier concentration.

Table 6. 4 Model parameters for modeling the A_1(LO) line shape

Sample	#192L	#135U	#125L	#111U
N (cm^{-3})×10^{19}	8.1	9.4	10	12
ω_p (cm^{-1})	3029	3930	3441	3736
γ_p (cm^{-1})	129	394	368	421
$q_{TF}\times 10^6$	4.2	5.25	-	7.22
A_1(LO) position (cm^{-1})	591.1	591.1	589.1	590.9
FWHM A_1(LO) (cm^{-1})	18.9	20.1	24.8	20.8
E_2 (High) position (cm^{-1})	486.8	486.8	486.7	486.1
FWHM E_2 (High) (cm^{-1})	6.9	10.6	9.2	10

Raman spectroscopy is a fast method capable of measuring strain in epitaxial films. Micro-Raman spectroscopy was performed at room temperature in back scattering geometry with excitation energy of 488 nm. Raman spectra in the E_2(high) mode frequency regions obtained at different lateral positions from InN (spot 1) to sapphire (spot 4) are depicted in Figure 6.12(a) in order to probe the actual strain conditions. It is noted that the obtained strain-free frequency of 489.9±0.2 cm^{-1} for the E_2(high) mode coincides well with the reported value of 490 cm^{-1} at the spot (1)[155]. High impurity density leads to tensile strain (2) at the transition of the InN-thin film (1) to substrate as shown in Figure 6.12 (c). The frequency of the E_2 (high) mode softens from 490 cm^{-1} to 488 cm^{-1} on transition from spot (2) to (3) and finally the Raman signal from the substrate dominates. Analysis of the shift and FWHM of E_2 (high) regarding the lateral position is

depicted in Figure 6.12(c-d). E_2 (high) is nearly relaxed and constant with a low FWHM at Spot (1), a growing tensile strain with increasing FWHM is established at Spot (2), a relaxation occurs with increasing FWHM at Spot (3), and the amplitude of E_2 (high) decreases and shifts into the sapphire mode at Spot (4). In conclusion, Micro-Raman analysis reveals that high impurity density leads to tensile strain at the InN-sapphire transition indicated by the position of E_2 (high).

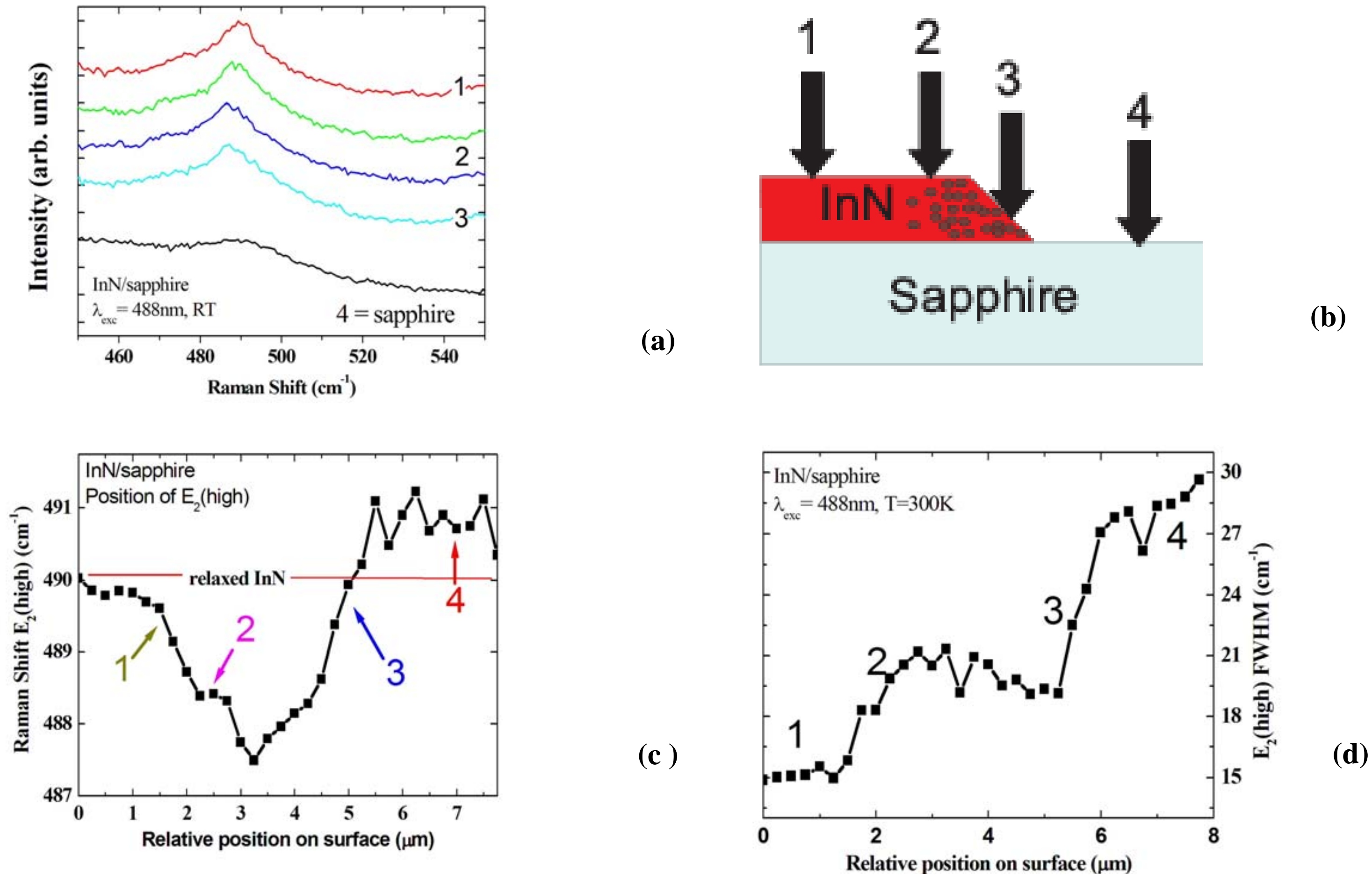

Figure 6. 12 (a) Raman spectra of InN recorded at lateral positions. (b) Spectra were obtained at four different spots. (c) Raman shift of E_2(high) related to lateral position. (d) FWHM of E_2(high) against the distance from the InN/sapphire interface.

6.4 Photoluminescence

It was found that the apparent band gap energy for InN is near ~0.67eV[33,152], which is much smaller than the 1.89 eV[38] value. A few groups measured the photo-luminescence (PL) of InN samples grown by MBE. It has been a mystery until 2000 that no photoluminescence spectrum could be observed for InN. The optical band gap or absorption edge energy has been primarily determined by optical absorption or transmission measurements. Evidence of a narrower band gap for InN was reported in 2001. Davydov *et al.*[22] reported a band gap value of 0.9 eV for high quality MBE grown InN by means of optical absorption, PL, photoluminescence excitation (PLE) spectroscopy, as well as by *ab initio* calculations. Wu *et al.* have shown good consistency of data for the optical absorption edge, PL peak energy, and photo-modulated reflectance for MBE grown epitaxial layers with a carrier concentration of the order of 10^{18} cm^{-3} and a mobility higher than 1000 cm^2/Vs, which resulted in the band gap energy for InN between 0.7 and 0.8 eV.

PL studies were performed in the visible and near infrared spectral range in order to examine the PL peak position of InN samples grown by HPCVD. PL spectra of three InN samples with free electron concentrations 6×10^{19} cm^{-3} (Sample #209) and $1\times10^{20}cm^{-3}$ (Sample #102U) are shown in Figures 6.13 and 6.14. The PL analysis revealed PL emissions as low as 0.75 eV, but no PL was detected below 0.75 eV. It is found that the shape of spectrum with higher concentration becomes slightly asymmetric and shifts towards higher energy. The upper energy tail is probably due to an additional distribution defect or impurity states. The PL spectrum of sample #209L with higher crystal quality is narrow and can be fitted with three Gaussians at 0.8, 0.95 and 1.1 eV. According to the 2

observed PL spectra, the FWHM increases with increasing free carrier concentration. To further justify our determined PL peak position for InN epifilms, we have performed transmission measurements. The inset of Figures 6.13 and 6.14 show the typical absorption curves obtained for those InN samples. Corresponding absorption coefficient curves are calculated from the experimental transmission spectra and thickness extracted from the fitting of transmission spectra. It is seen that there is a good agreement between the photoluminescence and absorption curves. It can be speculated that the optical absorption and luminescence bands of InN crystals clearly have characteristics typical of interband transitions. It is also clear that the optical absorption edge as well as the PL peak position shifts down to 1.1 eV with decreasing carrier concentration. This discrepancy between PL peak positions is probably due to the large layer inhomogeneity for the sample with the highest carrier concentration.

It should be pointed out that there is a possible influence of the surface on the optical data. It was already discussed in Chapter 5 that there are surface donor states degenerate with the conduction band that lock the position of the Fermi level above the valence band maximum, and these should be taken into account in the interpretation of the optical data. The surface accumulation layer caused by these degenerate surface donors itself is absorbing for the exciting photons. Therefore, the surface electron layer should be taken in to account in the evaluation of optical data.

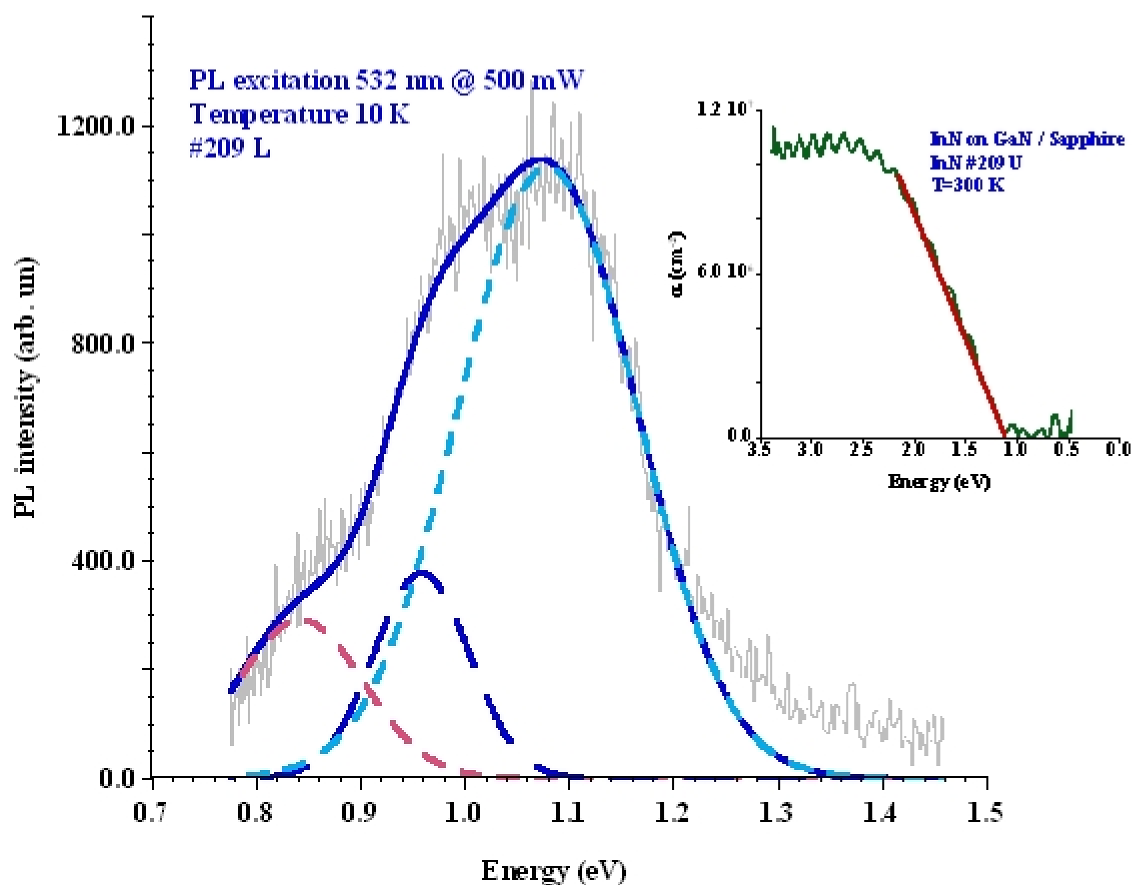

Figure 6. 13 Experimental PL spectra of InN samples with an electron concentration of 6×10^{19} cm^{-3} (from IR reflection data analysis). The inset shows the absorption coefficient calculated by using the film thickness from the fitting of experimental transmission spectra.

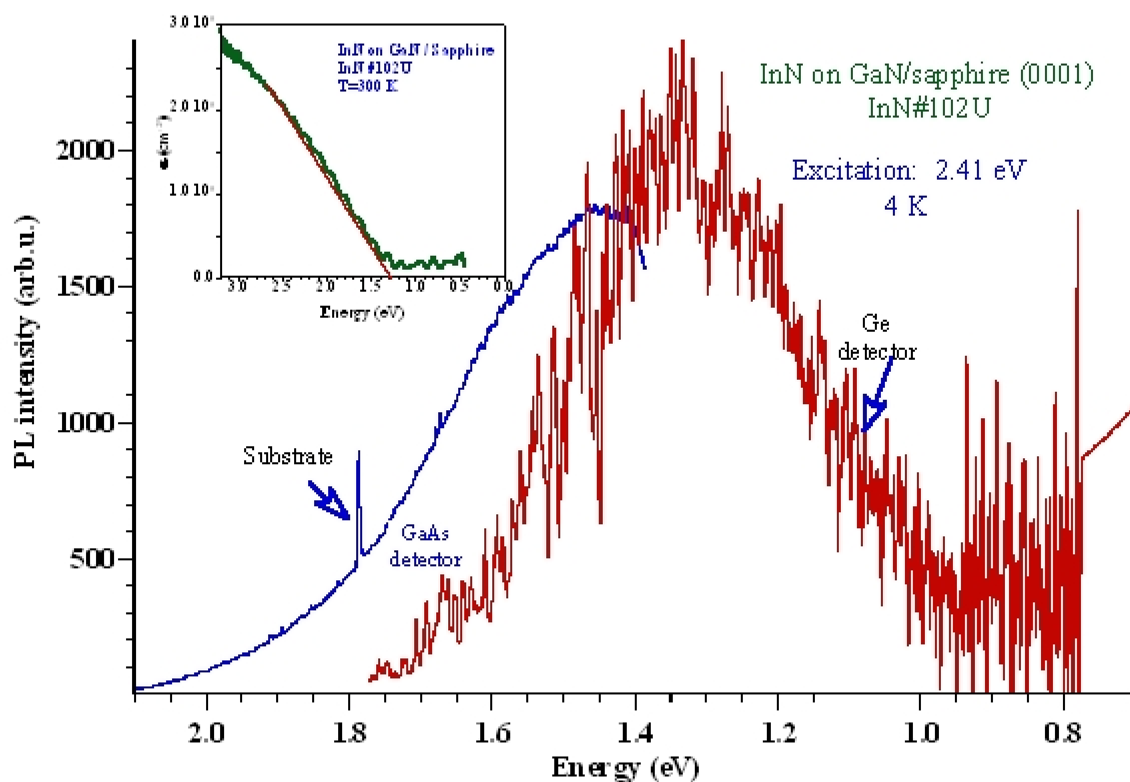

Figure 6. 14 Experimental PL spectra of InN samples with an electron concentration of 1×10^{20} cm^{-3} (from IR reflection data analysis). The inset shows the absorption coefficient calculated by using the film thickness from the fitting of experimental transmission spectra.

6.5 Conclusion

InN layers grown by HPCVD were studied by Raman, infrared reflectance, transmission spectroscopy and photoluminescence spectroscopy. InN materials are typically single crystalline with electron concentration varying from the mid 10^{18} cm^{-3} to the low 10^{20} cm^{-3}. The spectra were analyzed to extract the free electron concentrations and correlated to the optical absorption edge obtained from optical transmission spectra analysis using a *Modified Model Dielectric Function* approach. The numerical analysis of the optical transmission data shows that the optical absorption edge for InN layers shifts below 1.1 eV as the free carrier concentration decreases to low 10^{18} cm^{-3}. An exponential dependence is observed between optical absorption edge and free carrier concentration. It is observed that the absorption centers shift to lower energies with the shift in absorption edge. The observed absorption edge shift to lower energy values may be caused by the appearance of several absorption centers whose origin might be due to the unidentified deep defect centers. Experimental IR reflection and Raman spectra are modeled as alternative approaches to Hall Effect measurements since high surface carrier density and difficulties in having ohmic contacts from the InN surface limit accuracy of the technique. The electron density in the bulk of InN is difficult to measure experimentally, due to the presence of the surface electron accumulation for InN layers and due to gradient defect properties across the film. For this reason, Hall data for the electron concentrations have to be treated with caution, since Hall measurements typically produce some average value of the electron concentration across the sample thickness. IR reflection spectra analysis have been analyzed using, two-layer model, which indicates the existence of the surface layer with a higher free carrier concentration than that of

inner layer. The required second InN layer is estimated to have a free carrier concentration (below 5×10^{17} cm^{-3}). The Raman analysis revealed a high-quality crystalline layer with a FWHM of the E_2(high) around 6.9 cm^{-1}. the A_1(LO) mode analysis reveals that the carrier concentration is in the range 8×10^{20} -.1.6×10^{20} cm^{-3}. A strong correlation between crystal quality and optical properties is observed with a shift of the high energetic PL emission to lower energies and a narrowing of the luminescence spectra as the structural quality improves. The PL spectrum of InN samples with high crystal quality is narrow and was fitted with three Gaussians at 0.8, 0.95 and 1.1 eV. The optical absorption edge agrees very well with the PL peak position positioned at 1.1 eV.

Chapter 7

The effect of the growth surface polarity on physical properties of InN

Part of this chapter has been published in: “The influence of substrate on the structural quality of InN layers by high pressure chemical vapor deposition”, N. Dietz, M. Alevli, R. Atalay, G. Durkaya, R. Collazo, J. Tweedie, S. Mita, and Z. Sitar, Applied Physics Letter, **92**(4), 041911(2008)

7.1 Introduction

An extremely important characteristic of III-nitride semiconductor materials is surface polarity. In GaN semiconductor based materials, it has been shown that Ga-polarity is highly favorable to achieve thin films via metalorganic vapor phase epitaxy (MOVPE) and molecular beam epitaxy[114,156]. However, there is little information reported about the effects of polarity on InN growth[114,156,157]. In this chapter, the effect of thin film polarity on InN growth on Ga-polar and N-polar GaN templates was investigated utilizing High Pressure Chemical Vapor Deposition. It has been found that InN films grown on Ga-polar GaN templates possess a higher crystalline quality than InN films grown on N-polarity GaN. The resulting FWHM of the x-ray rocking curve analysis around the InN (0002) reflections were approximately 200 arcsec for InN samples grown on Ga-polar GaN as opposed to 295 arcsec for InN sample grown on N-Polar GaN. The

FWHM of x-ray rocking curves of InN layer grown in Ga polarity were very close to the those of InN layer grown by MBE, which is 82 arcsec.[158]

7.2 Experimental details

Two substrates with different polarities were used for the growth of InN under HPCVD conditions. InN thin films were deposited on epitaxial GaN layers (thickness ~0.9 µm), which were grown by Low-pressure MOCVD on *c*- plane sapphire substrates. The control of polarity was achieved by substrate pretreatment and subsequent low temperature AlN buffer growth[159]. The conditions for the pretreatment and the buffer growth were specific to each type of polarity. The conditions for the pretreatment and the buffer growth are described in detail elsewhere[159]. The polarity of the GaN film was determined from etching experiments. N-polar GaN is etched in KOH solution while Ga-Polar GaN is inert. The FWHM of the (0002) symmetric reflection and the (302) skew-symmetric reflection for the N-polar GaN were 774 and 1395 arcsec, respectively. The FWHM for the Ga-polar GaN were 410 and 1386 arcsec, respectively. The observed difference between the FWHM of the ω-rocking curves of the two films is attributed to the absence of the low-temperature AlN nucleation layer on the N-polar films. It is important to note that the initial roughness of the template is different, i.e., for the Ga polar template the roughness is 0.2 nm root mean square (RMS), and while for the N-polar template it is greater than 2 nm RMS. The details of the growth and physical properties of GaN layers have been described elsewhere[159]. The InN layers were grown by High Pressure CVD by employing ammonia (NH_3) and trimethylindium (TMI) as precursors. A pulsed injection scheme utilizing pulse width, precursor pulse separation, and cycle sequence time as control parameters was followed in order to control the gas

phase and surface chemistry kinetics. For the layers described below, the reactor pressure was 15 bar, the total gas flow 12 slm (standard liters per minute), the precursor molar ratio 630, and the growth temperature 1100 K. The GaN templates did not receive any further treatment prior to the InN layer growth. No buffer layer was used for the growth of InN on the Ga- and N-polar templates.

With the same precursor molar ratio and same growth temperature we compared the InN film growth on two-polar substrates surfaces. Crystallographic characterization was carried out by acquiring on- and off-axis high-resolution X-ray diffraction ω-rocking curves and 2-θ-ω scans using a Phillips X`Pert MRD with a Cu X-ray source operated at 40 kV and 45 mA. An open slit on the detector side in the double axis configuration was used for the ω-rocking curves, while a triple axis configuration was used for the 2θ-ω scans perpendicular to the sample surface.

7.3 Results

Figure 7.1 shows the XRD pattern on a logarithmic scale for InN layers grown on Ga-polar GaN (#209L) that includes three Bragg peaks corresponding to the InN (0002), GaN (0002) and sapphire (0006) reflections. Figure 7.2 shows the InN (0002) Bragg peak, along with the peaks resulting from deconvolution procedure using Gaussian peaks. The Bragg peak includes 2 peaks, a sharp dominant peak at 31.345° corresponding to InN and a second peak at 31.31° with an area ratio and a height ratio between the main peak and the secondary peak of 1.3 and 3.2, respectively. The rocking curves for the InN symmetric (0002) and skew symmetric (103) and (302) reflections are shown in Figure 7.3.

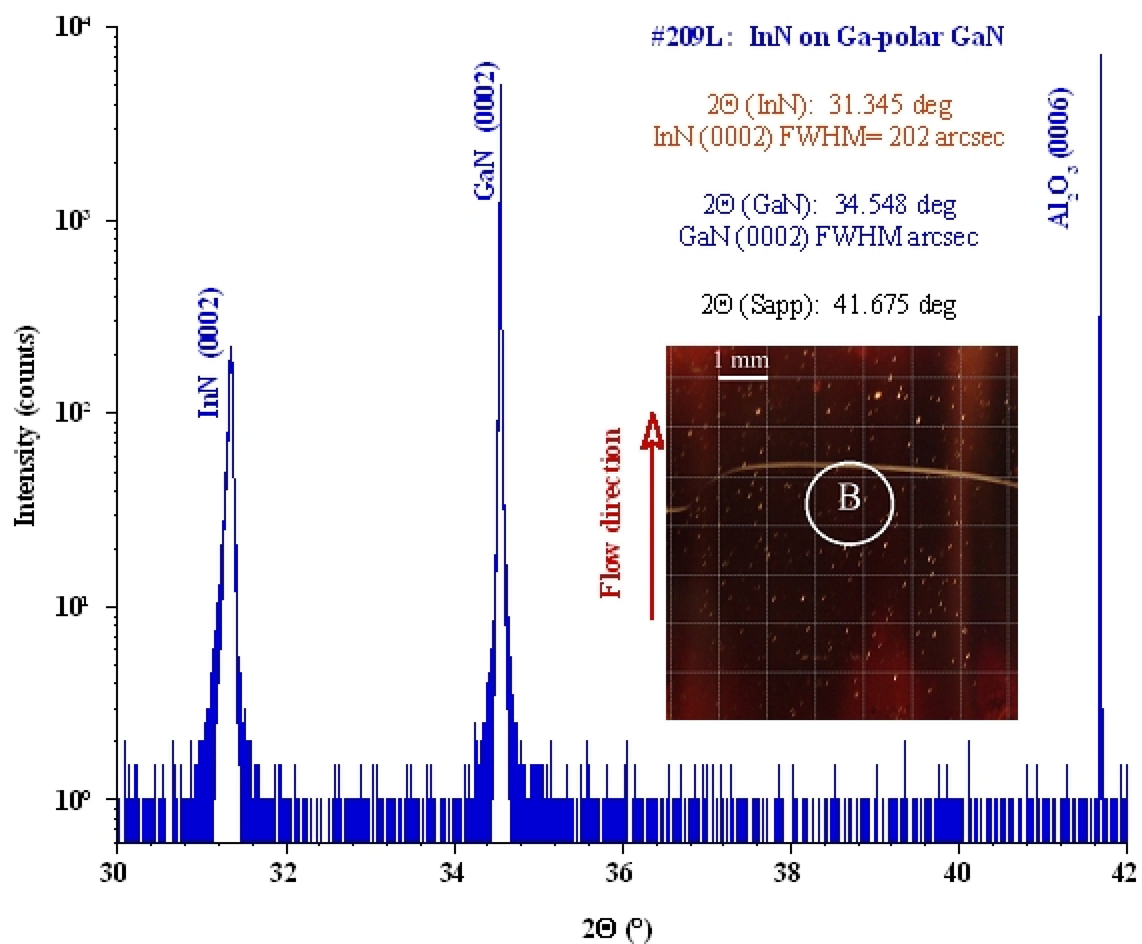

Figure 7. 1 ω-2θ scan XRD curve for a InN sample grown on a Ga-polar template.

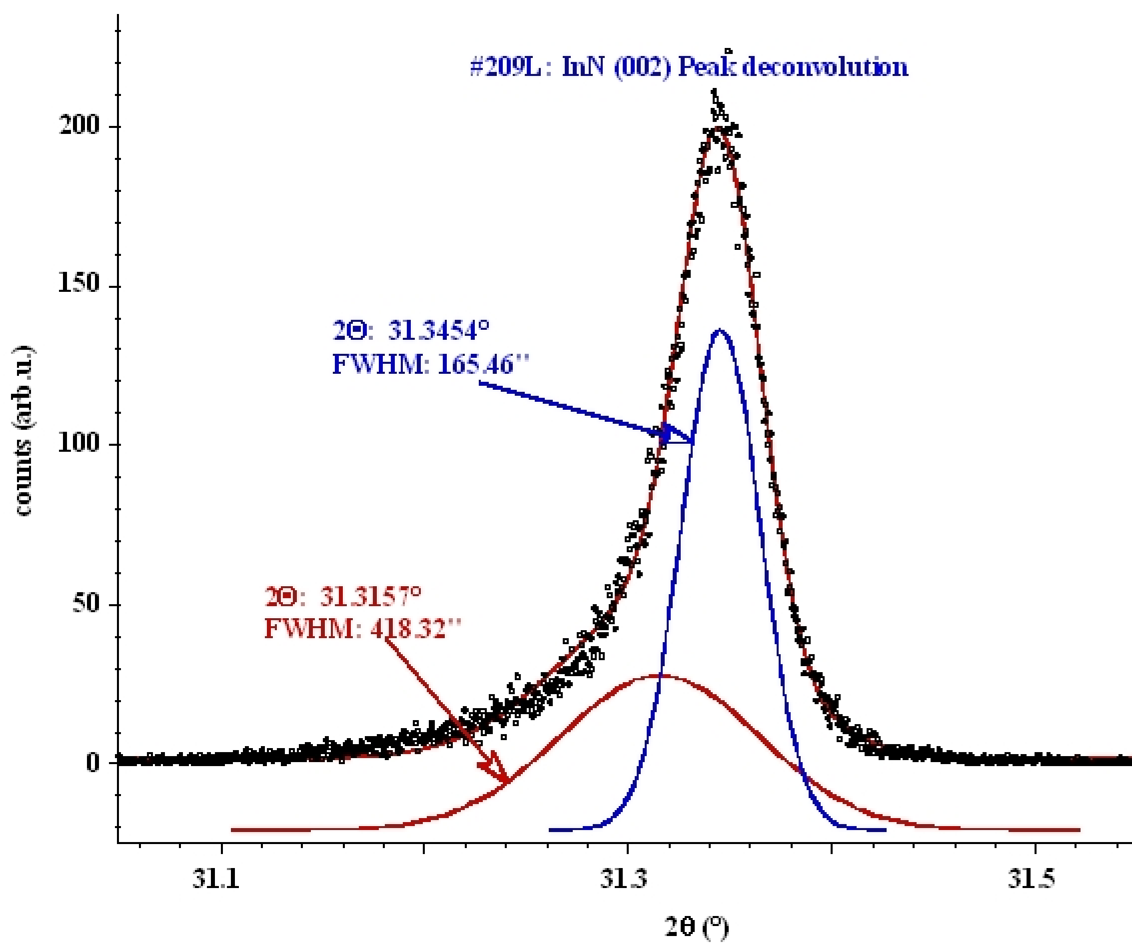

Figure 7. 2 The InN peak deconvolution indicates an asymmetric lower shoulder, which might be due to impurities.

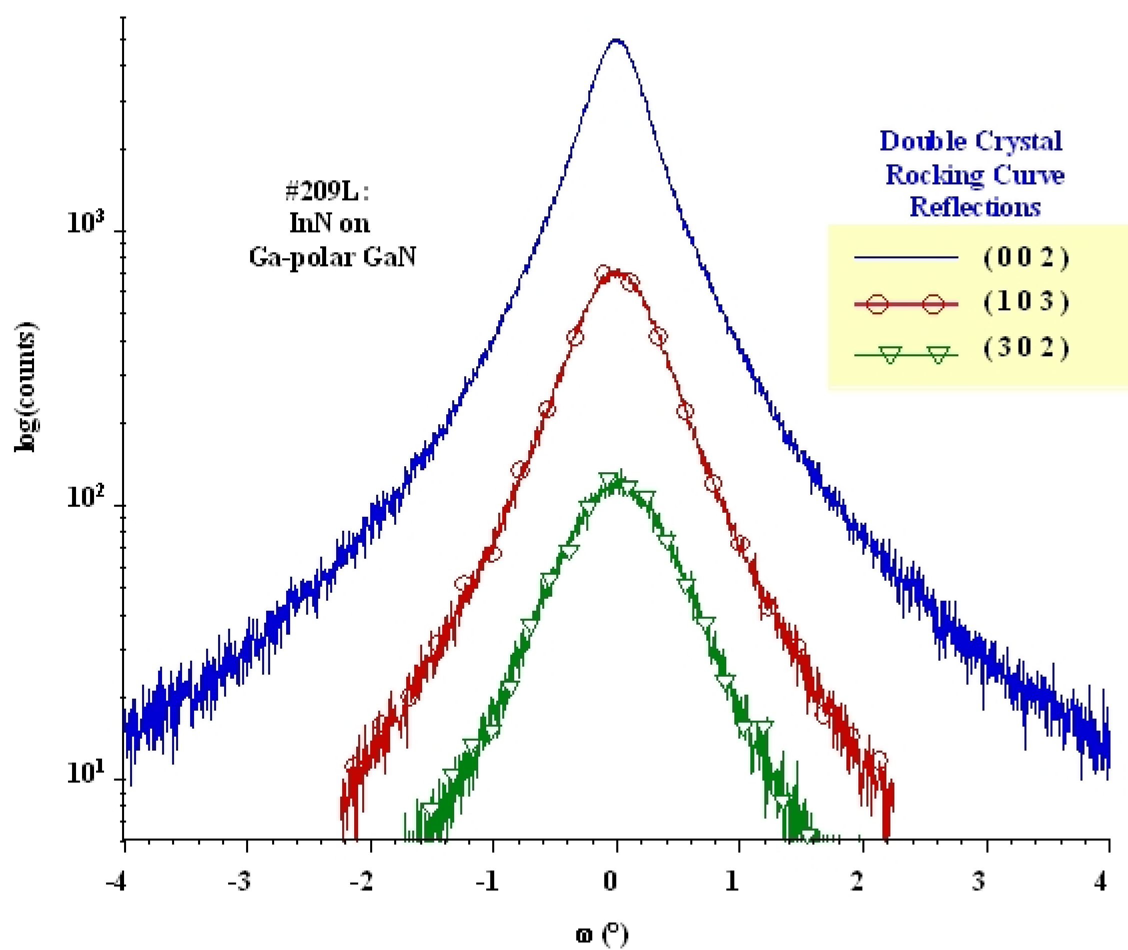

Figure 7. 3 High resolution X-ray rocking curves of InN film grown on OMCVD-GaN with Ga-polarity, InN (002) reflection, (103) reflection and (302) reflection.

The FWHM of these curves are summarized in Table 7.1, along with other crystallographic information. Similar to #209L, the 2θ-ω scan performed on the layer grown on a N-polar template doesn't show any other reflections besides those already listed. However, the FWHM (0002) and (002) of InN layer grown on N-polar GaN template were about 290 arcsec and 4450 arcsec, respectively, much poorer compared to the quality of InN sample grown on N-polar GaN template. The Bragg peak for InN sample grown on N-polar template also consists of two peaks. Although the secondary peak is more prominent in the layer grown on the N-polar template than in the layer grown on the Ga-polar template, its nature is difficult to assess. The secondary peak may represent a strain state due to biaxial stresses, the presence of native point defects, and/or impurity incorporation.

InN layer etching using 3M KOH solutions at 65 °C for 10 min shows no selective etching of the surface, which would suggest an In-polar surface. Further etching with a stronger 10M KOH solution revealed nonselective etching; however, the etched features for the InN layer grown on N-polar GaN were much larger in number and size. This could be due to the either different starting surface morphology or the high defect incorporation.

In addition to the high resolution XRD measurements, the Raman spectra for the InN layers grown on N-polar and Ga-polar GaN templates were carried out in the energy range of 200-900 cm^{-1}. The spectra were taken in back scattering geometry $z(\ldots.)\underline{z}$ using an excitation energy of 2.33 eV at room temperature, and they are depicted in Figure 7.4. The observed E_2(high) and A_1(LO) peak positions are in good agreement with predicted phonon frequencies of 486 cm^{-1} and 591 cm^{-1} respectively, as reported by Davydov *et al.*[4]

The line shape of E_2 (high) is related to structural defects and impurities in GaN structures. Wei *et al.*[150] used this relation as a valuation method for expressing crystalline quality, and they concluded that the E_2(high) line of FWHM of 4 cm^{-1} indicated a superior crystalline quality material. The FWHM of the E_2(high) line in sample # 209L is 8.3 cm^{-1} exhibiting high crystalline quality[4]. Due to the non-polar character of the E_2 (high) mode, there is no interaction of this mode with the conduction-band electrons[151].

On the other hand, the A_1 (LO) mode interacts with free carriers resulting in broadening of the line shape. In order to estimate free carrier concentration, the observed line shape of A_1(LO) mode damped by free electrons is simulated by using Linhard-Mermin approach[149]. DP+EO is considered as the major light scattering mechanism within the interaction. The intensity of scattered light is calculated by integrating the spectral line shape function up to maximum wave-vector limit by weight factor due to a Yukawa-type impurity potential. Figure 7.5 shows experimentally obtained Raman spectra and simulated A_1 (LO) peak for InN layers grown on Ga-polar GaN (sample #209L) and grown on N-polar GaN (sample #207L). The general form of the dielectric function used for numerical calculations is given by[149,160]

$$\varepsilon(q,\omega) = \varepsilon_\infty \left(1 + \frac{\omega_L^2 - \omega_T^2}{\omega_T^2 - \omega^2 - i\omega\gamma_p} + \frac{(1 + i\Gamma_e/\omega)\chi_e^0(q,\omega + i\Gamma_e)}{1 + (i\Gamma_e/\omega)\{\chi_e^0(q,\omega + i\Gamma_e)/\chi_e^0(q,0)\}}\right) \qquad (7.1)$$

where Γ_e corresponds to electron damping constant and $\chi_e^0(q,\omega)$ is the temperature dependent Lindhard susceptibility. The plasma frequency has been obtained from IR reflection analysis and used in Raman simulations for a better compatibility of results with those from IR reflection simulations.

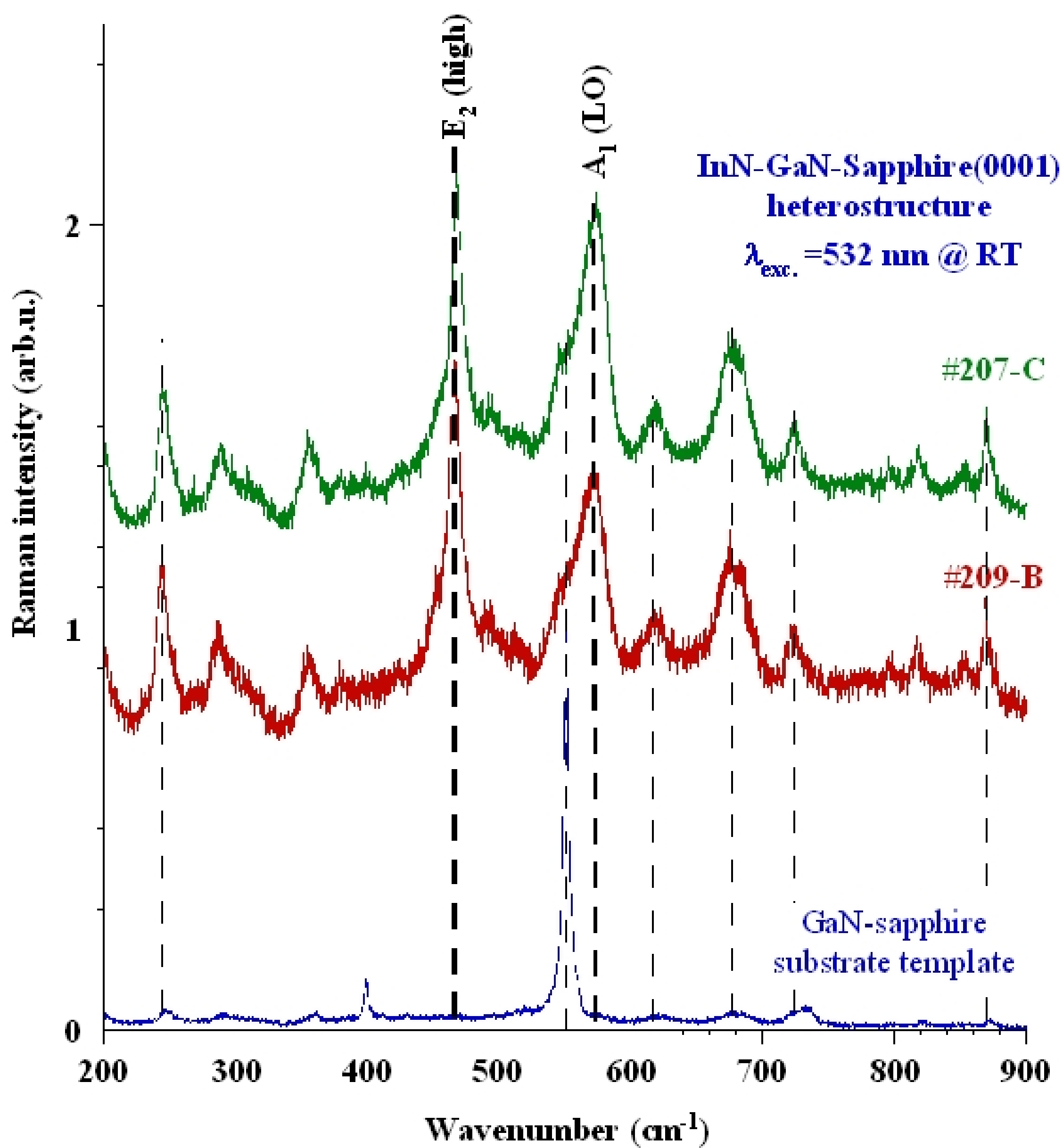

Figure 7. 4 Raman spectra of InN layers #207L and #209L grown on N-polar and Ga-polar GaN/sapphire templates, respectively.

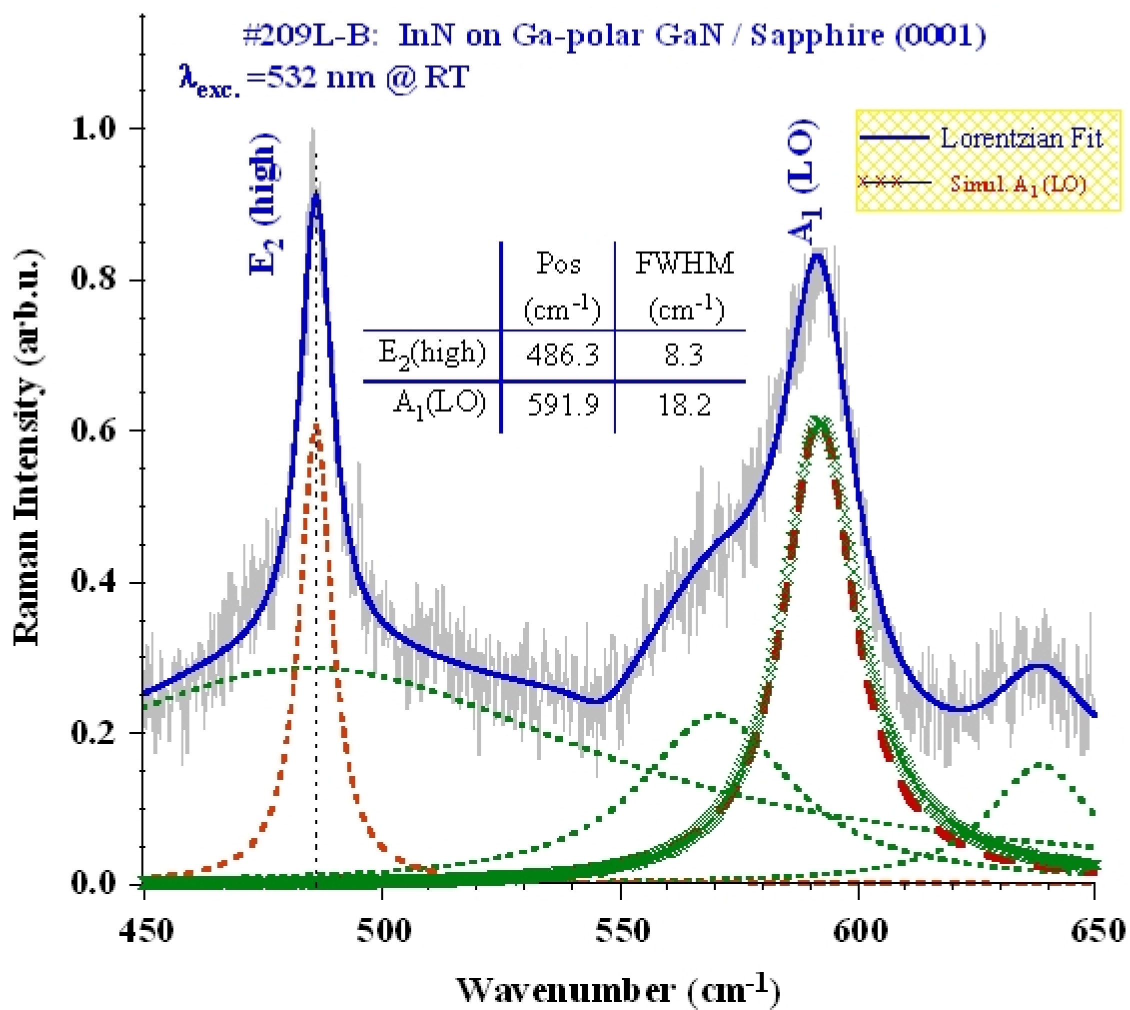

Figure 7. 5 Analysis of E_2(high) and A_1(LO) modes in the Raman spectrum for InN layer #209L grown on a Ga-polar GaN/ sapphire template.

The theoretical background used to describe the behavior of the LO mode is described in detail elsewhere[113,149]. The effective electron mass of InN is set constant to $0.14m_0$, noting that this will slightly underestimate the free carrier concentration.[122]

Figure 7.6 shows the optical transmission spectra of InN samples with the simulated spectra. The transmission spectra have been fitted by applying a modified Model dielectric Function (MDF) discussed Chapter 3 and Chapter 5.[119] The best-fit parameter values provide estimates of the thickness, high frequency dielectric constant, and optical absorption edge (see Table 7.1). From the fitting analysis, the optical absorption edge of the InN layers was found to be 1.23 eV and 1.21 eV for samples #207L and #209L, respectively.

Table 7. 1 The optical and structural data for InN samples grown on Ga- polar and N-polar GaN samples.

	Sample#207L InN on N-polar GaN	Sample#209L InN on Ga-polar GaN
XRD: 2-θInN (002) Pos.	31.311°	31.345°
2-θInN (002) FWHM (arcsec)	295	202
ω-RC(002) FWHM (arcsec)	4243	2082
ω-RC(103) FWHM (arcsec)	5000	2857
ω-RC(302) FWHM (arcsec)	6100	3501
Raman: E_2(High) pos. (cm^{-1})	487.7	486.3
E_2(High) FWHM (cm^{-1})	9.4	8.3
A_1(LO) pos. (cm^{-1})	593.1	591.9
A_1(LO) FWHM (cm^{-1})	20.8	18.2
ε_∞ (via A_1(LO) simulation)	7.9	7.8
N_e (via A_1(LO) simulation) (cm^{-3})	4.3×10^{18}	2.5×10^{18}
d_{InN} (from transmission) (nm)	470	470
Absorption band edge (eV)	1.23	1.21

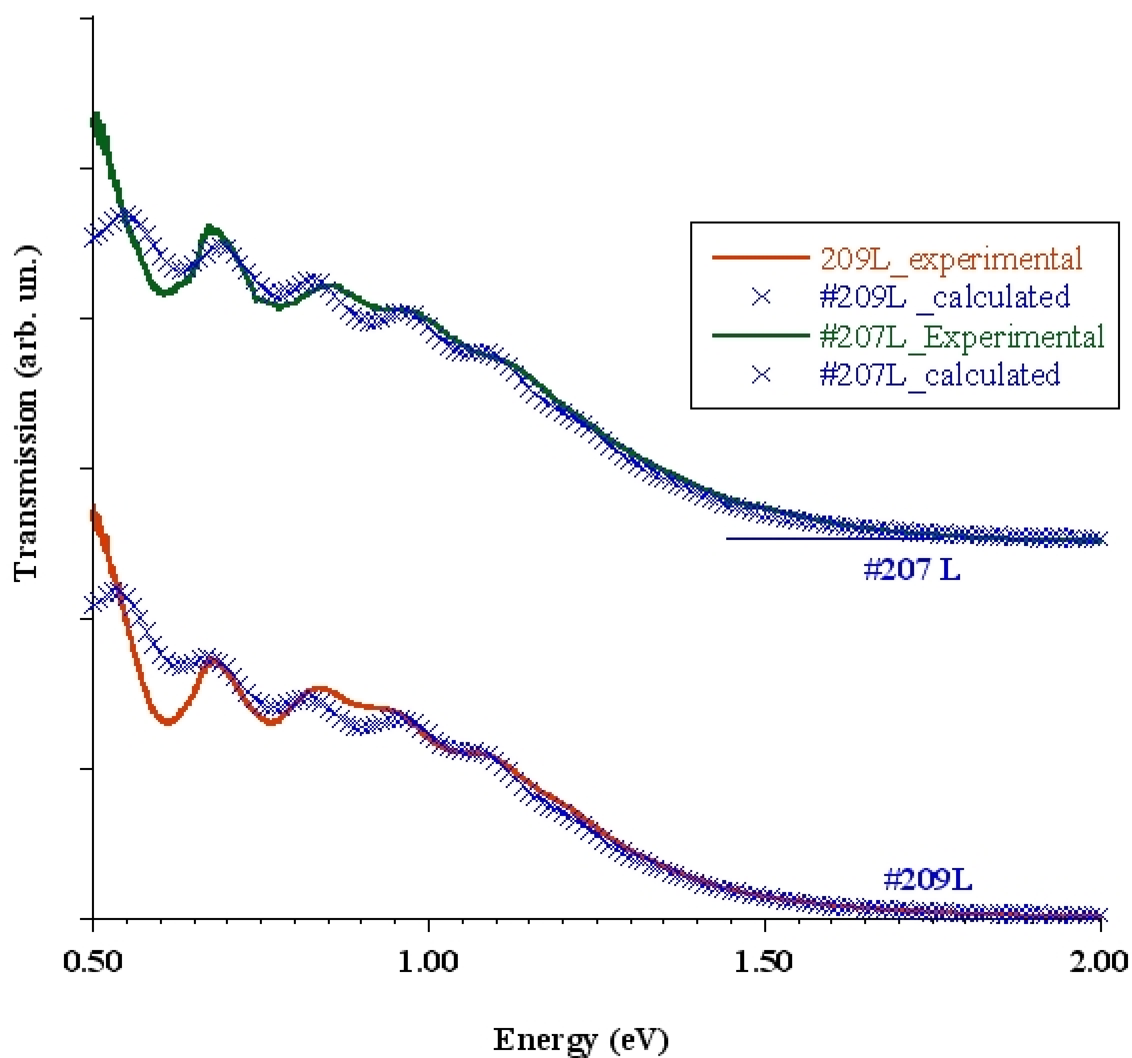

Figure 7. 6 Transmission spectra and their best fits for InN layers deposited on N-polar GaN and Ga-polar GaN substrates.

The PL spectra obtained from ~0.5μm thick InN grown on Ga-polar GaN at 10K is shown in Figure 7.7. Here, a laser at 532 nm was used as the excitation source and a Germanium, GaAs photodetector was used for monitoring the luminescence. A broad spectrum was observed which can be fitted with three Gaussian functions centered at 0.85, 0.95 and 1.1 eV. It should be emphasized that PL corresponding to the 0.85 eV transition could be from the absorption center at 0.75 eV obtained from the experimental transmission spectra fitting. The optical absorption of InN was also studied at room temperature, and the absorption coefficient versus the photon energy suggests that the absorption edge is at 1.1 eV or 1.2 eV (transmission spectrum fitting), which may correspond to the 1.1 eV PL peak position. The optical absorption of InN is presented in Figure 7.8. It should be noted that no PL corresponding to the 1.9 eV transition could be observed from sample #209L.

7.4 Conclusions

In conclusion, we have analyzed the structural properties of InN layers grown by High Pressure CVD on polarity controlled GaN/Sapphire substrate templates. The XRD analysis and Raman analysis revealed that the FWHM of InN (0002) layers with hexagonal symmetry and the E_2(high) phonon mode of Raman scattering were as small as 200 arcsec and 8.3 cm^{-1}, respectively, for layers deposited on Ga-polar GaN epilayers. The FWHM increases for InN layers grown on N-polar GaN templates, using the same growth conditions. The free carrier concentrations in these InN layers were estimated by A_1(LO) line shape analysis and determined to be in the low 10^{18} cm^{-3} range. The luminescence and transmission measurements suggested that the optical band gap energy of InN is approximately ~1.1 eV at 10K. However, a high density of residual carriers in

the middle 10^{18} cm^{-3} range still exists in the film. For the determination of the accurate band gap energy of InN, however, further reduction in residual carrier concentration is needed. Also, there is a surface electron layer, which should be considered in the interpretation of optical PL data, since the surface accumulation layer itself is absorbing the exciting photons. The results suggest that the polarity of the substrate surface affects the defect incorporation during the growth and the subsequent structural and electrical properties of the InN layers. Further work is necessary to verify this understanding.

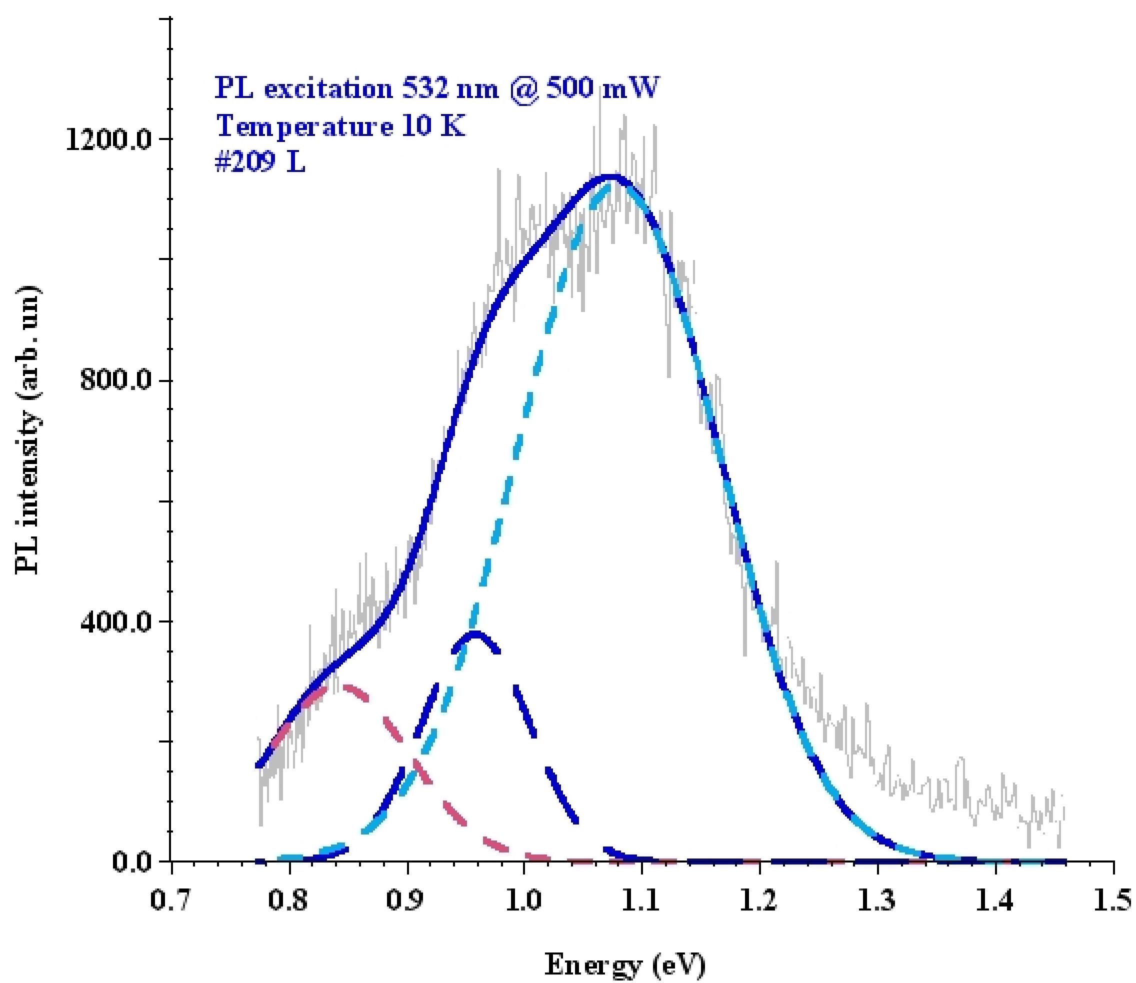

Figure 7. 7 PL spectra of Sample #209L at 10K.

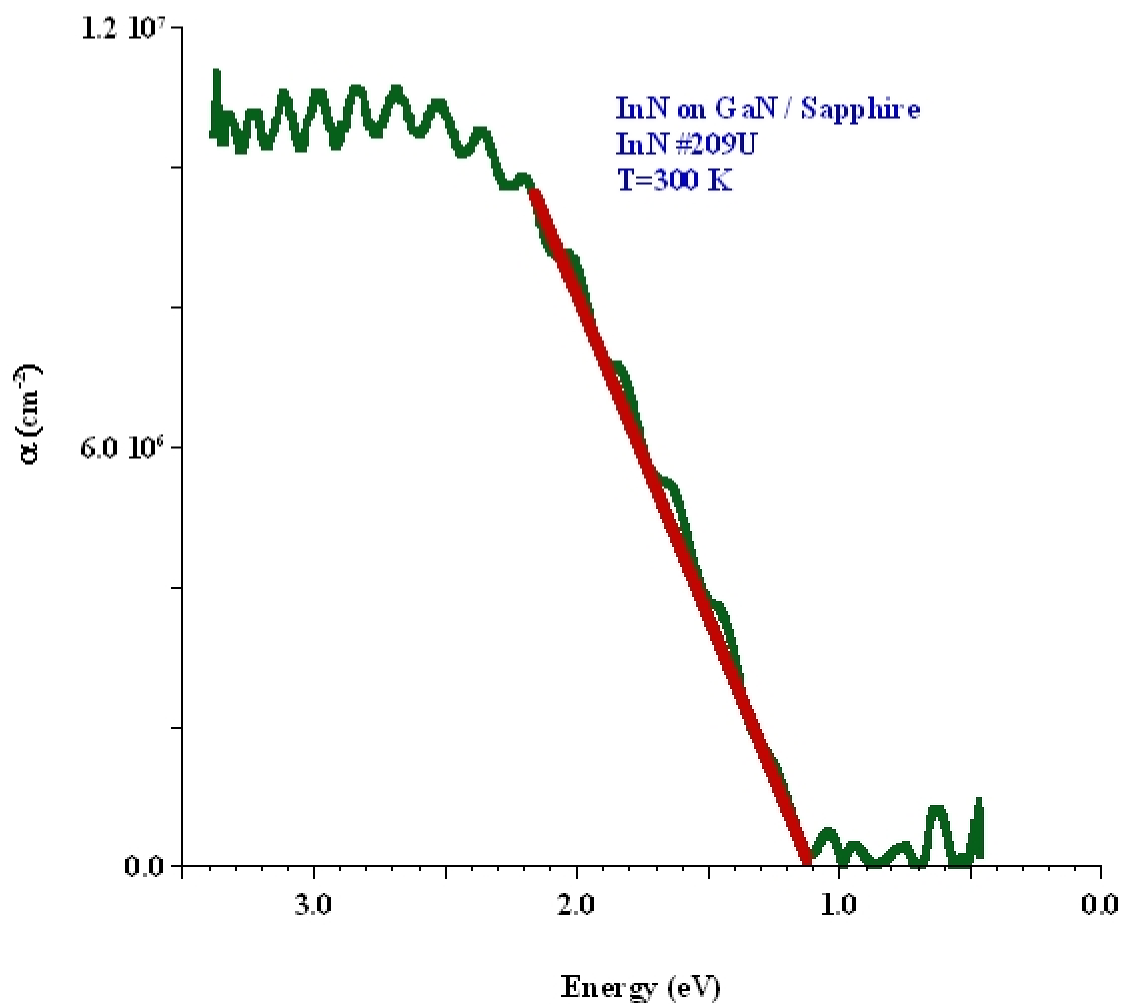

Figure 7. 8 The value of α versus photon energy at room temperature in a wider energy range for sample #209L. At higher energies the curve shows a monotonic increase and then stays constant.

Chapter 8

Conclusion and future Work

8.1 Introduction

The InN growth studies performed during this thesis showed that the HPCVD approach reduces the thermal decomposition of InN, which enabled the growth of InN layers at growth temperatures around 1100 K for reactor pressures of 15 bar. This thesis concentrated on the structural and optical properties of single crystalline InN films that were grown at different growth temperatures, on different substrates, and with varying V/III molar ratios. The relevant discussion is the crystalline quality, the variation in the optical absorption edge of InN, and free carrier concentration of InN film and their relation to the In:N stoichiometry. We correlated the in-situ real-time surface characterization (LLS) to the ex-situ X ray diffraction and AFM results to investigate the role of surface morphology. While excellent progress has been made in the crystalline quality of InN films to date, there is still more work required for defining the defect centers, the origin of the high free carrier concentration, and the origin of the surface electron accumulation layer. In this chapter, a summary of the structural properties, surface morphology, and optical properties are presented, future work is outlined.

8.2 Surface morphology and structural properties

The XRD analysis showed high-quality, single-phase InN based on InN(0002) Bragg peaks with FWHM around 200 arcsec for InN layers deposited on GaN epilayers.

The FWHM increases to about 490 arcsec for InN deposited on sapphire substrates, an affect attributed to due to the increase in lattice-mismatch. The structural characterization using XRD demonstrated that InN film grown under HPCVD have hexagonal wurtzite structure. Refined lattice parameters "*a*" and "*c*" were extracted from the XRD data, which compared well to the values in the literature. However, the *c*-axis lattice constant obtained from the (0002) InN XRD diffraction peak is 5.70 Å, which is close to the commonly accepted value that deviates from the unstrained InN film ±0.0015 Å. Broadening of FWHM of InN (0002) peak is observed with varying V/III ratio for a series of samples grown at fixed temperature and reactor pressure. The XRD results showed that InN films grown with lower ammonia:TMI molar ratio have better crystalline quality. No peak in the vicinity of 33° is observed for high quality InN thin films presented in this thesis study. However, a weak peak appears at 33° due to the increasing indium-to-nitrogen flux ratio. This observation strengthens the assignment of diffraction peak at 2θ~33°, which might be due to microscopic indium clusters, are present in the films. We have analyzed the structural properties of InN layers grown by HPCVD on polarity controlled GaN/sapphire substrate templates. It was found that high quality single crystalline InN films with a FWHM of 2Θ-ω scan of around 200 arcsec could be grown on Ga-polar GaN templates, while the FWHM increases for InN layers grown on N-polar GaN templates.

The surface structure and chemical composition of InN samples were investigated using AES, HREELS and LEED. AES confirms the removal of the contaminants such as carbon and oxygen from the InN surface. LEED patterns taken from clean InN layers showed a clear hexagonal 1x1 pattern demonstrating the surface was well ordered and c-

plane oriented. HREEL spectra taken at low incident electron energy demonstrated that the surface was N-H terminated and free of indium over-layers and droplets and that the film is InN$(000\bar{1})$. HREELS spectra also showed a shift to lower plasma frequency when electrons with larger penetration depths are used due to a higher electron concentration on the surface when compared with bulk InN. This result supports the presence of a surface electron accumulation.

An AFM studies on InN surfaces reveals that some InN layers exhibit columnar hexagonal structures with diameters of ~300 nm to ~800 nm depending on the V/III ratio, growth time and growth temperature. InN films show that columnar structures were grown on sapphire substrates at temperatures of 1078 and 1090 K. Several of InN layers that exhibit hexagonal columnar structures show that disoriented columns with respect to each other and the *c* axis of the substrate. The surface roughness of InN samples grown on GaN templates is found to be lower (9 nm) compared to the samples grown on sapphire (~26 nm). The surface roughness of the InN samples has been correlated with the FWHM of the InN (0002) rocking curve suggesting that crystalline quality is improved if the surface topography is smoother. The appearance of a second phase InN (101) in InN film, which is attributed to In metallic clusters, makes the InN surface rougher commensurate with its increasing contribution in the XRD spectrum. We also observed the growth of three-dimensional hexagonal InN pyramids with up to 24 μm diameter. The appearance of such pyramids lead to the broadening of the XRD (0002) Bragg peak. The growth was observed to be two-dimensional at the earlier stage of InN growth often continues three-dimensional during the later stage of growth leading to hexagonal pyramid structures.

8.3 Optical properties

Normal incidence optical transmission measurements were performed on a series of InN thin layers grown by HPCVD on sapphire substrates and GaN templates were performed. The optical properties of the InN films were modeled by approximating the transmission spectra using a *Modified Model Dielectric Function* approach. From this approach we were able to estimate the optical absorption edge and the absorption centers present in the InN layers. The best-fit algorithm indicated the presence of absorption structures centered around 1.1 eV, 0.8 eV and 0.5 eV. The analysis also showed that optical absorption edge in InN shifts below 1.1 eV as the free carrier concentration decreases in the 10^{18} cm^{-3} free carrier concentration range. The observed optical absorption edge shift to lower energy values might be caused by the absorption centers, whose origins are not clear at present. Our results indicate a direct correlation between the optical absorption edge and the two absorption centers confirms a close relation between the carrier concentration and the absorption centers in the InN layers. The absorption centers that appear at ~0.5 eV might be caused by unidentified deep defect states. The absorption centers at ~0.75 eV might be attributed to the either In clusters (Mie resonances) or the InN-related band to band transitions.

The calculated optical absorption edge of the InN films was correlated with free carrier concentration in the layers extracted via IR-reflection spectra fittings. An exponential dependence is observed between the optical absorption edge and free carrier concentration. A correlation of these results to determine the true band gap energy of InN is at present not possible, since a further reduction in residual carrier concentration is needed. The sample with the lowest carrier concentration has an absorption edge situated

near 1.2 eV. The energy of the edge is a little higher than the ~1.1 eV expected value for the 6 × 10^{19} cm^{-3} carrier concentration, which takes into account the Burstein-Moss effect and assumes a band-gap ~0.7 eV. The average ε_{∞} value of these InN layers is around 8±0.4, which is close to the theoretically predicted value of 8.4. IR reflection spectra analysis have been analyzed using, a two-layer model, which indicates the existence of a surface layer with a higher free carrier concentration than that of the inner layer. The required 2nd InN layer is estimated to have a free carrier concentration (below 5 × 10^{17} cm^{-3}). The surface roughness dependence of mobility and surface morphology suggests that the surface roughness of our InN films has to be significant improved in order to attain a high electron mobility.

Two of the allowed optical phonon modes in InN are the hexagonal InN are E_2 (high) and A_1 (LO), which are analyzed in more detail in the measured Raman spectra taken in back-scattering geometry. The peak positions of the observed E_2 (high) and A_1 (LO) modes are in good agreement with the predicted values of 486 cm^{-1} and 591 cm^{-1}. The FWHM of the E_2 (high) line is 6.9 cm^{-1} indicates a high crystalline quality. The A_1 (LO) mode line shape analysis revealed the carrier concentrations in the range 8×10^{17}-1.6×10^{20} cm^{-3}. The optical absorption edge behavior versus the free carrier concentration shows an exponential behavior in the free carrier concentration range 10^{17} $cm^{-3}$$<n_e<$$10^{20}$ cm^{-3}.

PL spectra of two InN samples with free electron concentrations of 6 ×10^{19} cm^{-3} and 1×10^{20} cm^{-3} were observed. The FWHM of PL spectra increase with increasing free carrier concentration. The PL spectrum of InN with higher crystal quality is narrower and

can be fitted with three Gaussians at 0.8, 0.95 and 1.1 eV. The PL emission is in good agreement with the absorption edge at around ~1.1 eV.

8.4 Open questions and future work

The growth of InN layers under high-pressure CVD reactor system has provided very promising results. However, there is still significant work to be done in order to reduce or eliminate the uncertainties in the fundamental properties of InN. The InN band gap was believed to be 1.85 eV until 2000, but since been revised to approximately 0.7 eV. One of the assumptions is that the band gap shift is related to the reduction of the free carrier concentration in InN. Since the free carrier concentration in the InN layers investigated in this thesis are still well above 10^{18} cm^{-3}, further efforts are needed to reduce the free carrier concentration in the InN layers. Relevant questions that are still open are;

- What is the origin of the high free carrier concentration?
- How can the occurrence of the surface electron accumulation layer be suppressed?
- What is the effect of surface electron accumulation layer on optical properties (PL,IR reflectance…)
- How much improvement on the optical and structural properties of InN can be expected by going at even higher rector pressures?

Further studies of InN layers grown by HPCVD are needed to correlate the point defect chemistry, growth temperature, and reactor pressure with the structural and optical properties of InN. The present integration of a two-stage nitrogen compressor will enable the future growth of InN layers for pressures up to 100 bar. Accessing the higher

pressures regimes might further stabilize the InN at elevated pressures, preventing thermal decomposition and improving the crystalline quality.

REFERENCES

[1] A. G. Bhuiyan, A. Hashimoto, and A. Yamamoto, Journal of Applied Physics,**94**, 5, 2779-2808 (2003).

[2] K. S. A. Butcher and T. L. Tansley, Superlattices and Microstructures **38,** 1 (2005).

[3] V. Y. Davydov and A. A. Klochikhin, Semiconductors **38,** 897-936 (2004).

[4] V. Y. Davydov and A. A. Klochikhin, Semiconductors **38,** 861-898 (2004).

[5] T. Inushima, V. V. Mamutin, V. A. Vekshin, S. V. Ivanov, T. Sakon, M. Motokawa, and S. Ohoya, Journal of Crystal Growth **227-228,** 481-485 (2001).

[6] J. Wu, W. Walukiewicz, W. Shan, K. M. Yu, J. W. A. III, E. E. Haller, H. Lu, and W. J. Schaff, Physical Review B, **96,** 200 (2002).

[7] W. Walukiewicz, S. X. Li, J. Wu, K. M. Yu, J. W. Ager, E. E. Haller, H. Lu, and W. J. Schaff, J. Cryst. Growth **269,** 119 (2004).

[8] C. L. Wu, C. H. Shen, H. W. Lin, H. M. Lee, and S. Gwo, Applied Physics Letters **87,** 241916-3 (2005).

[9] N. Dietz, in *III-Nitrides Semiconductor Materials*, edited by Z. C. Feng (Imperial College Press, 2006), p. 203-255.

[10] N. Dietz, M. Strassburg, and V. Woods, Journal of Vacuum Science & Technology A: Vacuum, Surfaces, and Films, **23,** 1221–1227 (2005).

[11] V. Woods and N. Dietz, Mater. Sci.& Eng., **127,** 239-250 (2006).

[12] M. Alevli, G. Durkaya, W. Fenwick, A. Weerasekara, V. Woods, I. T. Ferguson, A. G. U. Perera, and N. Dietz, Appl. Phys. Lett. **89,** 112119 (2006).

[13] V. Woods, J. Senawiratne, and N. Dietz, J. Vac. Sci. Technol. B **13,** 1790-1794 (2005).

[14] N. Dietz, M. Alevli, V. Woods, M. Strassburg, H. Kang, and I. T. Ferguson, Phys. stat. sol. (b) **242,** 2985-2994 (2006).

[15] R. Juza and H. Hahn, Z. Anorg. Alleg. Chem. **239,** 282 (1938).

[16] J. MacChesney, P. M. Bridenbaugh, and P. B. O'Connor, Mater. Res. Bull. **5,** 783 (1970).

[17] J. W. Trainor and K. Rose, J. Electron. Mater. **3,** 821 (1974).

[18] H. J. Hovel and J. J. Cuomo, Appl. Phys. Lett. **20,** 71 (1972).

[19] L. A. Marasina, I. G. Pichugin, and M. Tlaczala, Krist. Tech. **12,** 541 (1977).

[20] T. L. Tansley and C. P. Foley, Electron. Lett. **20,** 1066 (1984).

[21] A. Wakahara, T. Tsuchiya, and A. Yoshida, J. Cryst. Growth **99,** 385 (1990).

[22] V. Y. Davydov, A. A. Klochikhin, R. P. Seisyan, V. V. Emtsev, S. V. Ivanov, F. Bechstedt, J. Furtmuller, H. Harina, A. V. Mudyri, J. Aderhold, O. Semchinova, and J. Graul, Phys. Status Solidi b **229** (2002).

[23] Y. Nanishi, Y. Saito, and T. Yamaguchi, J. Appl. Phys. **42,** 2549 (2003).

[24] M. Higashiwaki and T. Matsui, J. Cryst. Growth **162,** 269 (2004).

[25] A. A. Klochikhin, V. Y. Davydov, V. V. Emtsev, A. V. Sakharov, V. A. Kapitonov, B. A. Andreev, H. Lu, and W. J. Schaff, Phys. Rev. B. **71,** 195207 (2005).

[26] H. Lu, W. J. Schaff, and L. F. Eastman, in *Mater. Res. Soc. Symp. Proc.*; *Vol. 9* (2002), p. 693.

[27] M. C. J. C. M. Kramer, PhD Thesis, Eindhoven Technische Universiteit, 2006.

[28] S. C. Jain, M. Willander, J. Narayan, and R. V. Overstraeten, J. Appl. Phys. **87,** 965 (2000).
[29] S. N. Mohammad and H. Morkoc, Prog. Quantum Electron. **20,** 361 (1996).
[30] S. K. O'leary, B. E. Foutz, M. S. Shur, U. V. Bhapkar, and L. F. Eastman, J. Appl. Phys. **83,** 826 (1998).
[31] S. K. O'Leary, B. E. Foutz, M. S. Shur, and L. F. Eastman, Appl. Phys. Lett. **88,** 152113 (2006).
[32] V. M. Polyatov and F. Schwierz, Appl. Phys. Lett. **88,** 032101 (2006).
[33] J. Wu and W. Walukiewicz, Superlattices and Microstructures **34,** 63–75 (2003).
[34] V. W. Chin, T. L. Tansley, and T. Osotchan, J. Appl. Phys. **75,** 7365 (1994).
[35] C. H. Swartz, R. P. Tomkins, T. H. Myers, H. Lu, and W. J. Schaff, Phys. stat. sol. (c) **2,** 2250-2253 (2005).
[36] S. C. Binari and H. C. Dietrich, *GaN and Related Materials* (Gordon and Breach, Newyork, 1997).
[37] T. Inushima, T. Shiraishi, and V. Y. Davydov, Solid State Communications **110,** 491–495 (1999).
[38] T. L. Tansley and C. P. Foley, Journal of Applied Physics, **59, 9,** 3241-3244 (1986).
[39] S. N. Mohammad and H. Morkoc, Prog. Qunatum Electron. **20,** 361 (1996).
[40] Z. G. Qian, W. Z. Shena, H. Ogawa, and Q. X. Guo, Journal of Applied Physics **92,** 3683-3687 (2002).
[41] D. Bagayako and L. Franklin, J. Appl. Phys. **97,** 123708 (2005).
[42] A. Kadir, T. Ganguli, M. R. Gokhele, A. P. Shah, S. S. Chandvankar, B. M. Arora, and A. Bhattacharya, journal of Crystal Growth **298,** 403-408 (2007).
[43] A. Nikolaev, I. Nikitina, A. Zubrilov, M. Mynbaeva, Y. Melnik, and V. Dimitriev, Material Res. Soc. Symp. Proceed **595,** W6.5 (2000).
[44] H. Lee and J. J. S. Harris, J. Cryst. Growth **169,** 689 (1996).
[45] Y. Kumagai, T. Yamane, and A.Koukitu, J. Cryst. Growth **281,** 62 (2005).
[46] Y. Kumagai, J. Kikuchi, Y. Nishizawa, H. Murakami, and A.Koukitu, J. Cryst. Growth **300,** 57-61 (2007).
[47] J. Wu, W. Walukiewicz, K. M. Yu, J. W. A. III, E. E. Haller, H. Lu, W. J. Schaff, Y. Saito, and Y. Nanishi, Appl. Phys. Lett. **80,** 3967 (2002).
[48] A. Yamamoto, H. Miwa, Y. Shibata, and A. Hashimoto, Thin Solid Films **491,** 74-78 (2006).
[49] K. Scott, A. Butcher, M. Wintrebert-Fouquet, P. P.-T. Chen, K. E. Prince, H. Timmers, S. K. Shrestha, T. V. Shubina, S. V. Ivanov, R. Wuhrer, M. R. Phillips, and B. Monemar, phys. stat. sol. (c) 2, No. 7, 2263–2266 (2005).
[50] K. S. A. Butcher, A. J. Fernandes, P. P. T. Chen, M. W. Fouquet, H. Timmers, S. K. Shrestha, H. Hirshy, R. M. Perks, and B. Usher, J. Appl. Phys. **101,** 123702 (2007).
[51] T. Ive, O. Brandt, M. Ramsteiner, M. Giehler, H. Kostial, and K. H. Ploog, Appl. Phys. Lett. **84,** 1671 (2004).
[52] G. Franssen, T. Suski, P. Perlin, H.Teisseyre, A. Khachapuridze, L. H. Dmowski, J. A. Plesiewicz, A. Kaminska, M. Korouchi, Y. Nanishi, H. Lu, and W. Schaff, Appl. Phys. Lett. **89,** 121915 (2006).

[53] H. Naoi, M. Korouchi, D. Mato, S.Takado, T. Araki, T. Miyajima, H. Na, and Y. Nanishi, Phys. stat. sol. (a) **203,** 93 (2006).
[54] T. D. Veal, P. H. Jefferson, L. F. J. Piper, C. F. McConville, T. B. Joyce, P. R. Chalker, L. Considine, H. Lu, and W. J. Schaff, Applied Physics Letters **89,** 202110-3 (2006).
[55] J. Black, H. Lowckwood, and S. Mayburg, J. Appl. Phys. **34,** 178-180 (1963).
[56] R. D. Dupuis, IEEE Quant. Electr. **QE-23,** 651-657 (1987).
[57] M. G. Craford, IEEE Circuit Devices **8,** 25-29 (1992).
[58] S. Nakamura and G. Fasol, *The Blue Laser Diode* (Springer, Berlin, 1997).
[59] D. B. Nicol, PhD. Thesis, Georgia Institute of Technology, 2006.
[60] K. Bullis, in *Technology Review Published by MIT* (August 01, 2007).
[61] www.blu-ray.com.
[62] M. S. Hu, G. M. Hsu, K. H. Chen, C. J. Yu, H. C. Hsu, L. C. Chen, J. S. Hwang, L. S. Hong, and Y. F. Chen, Appl. Phys. Lett. **90,** 123109 (2007).
[63] S. K. O'Leary, B. E. Foutz, M. S. Shur, and L. F. Eastman, Applied Physics Letters **87,** 222103-3 (2005).
[64] W. J. Schaff, H. Lu, J. Hwang, and H. Wu, IEEE **IV-8,** 225-231 (2000).
[65] M. Yamaguchi, Solar Energy Materials and Solar Cells **75,** 261 (2003).
[66] K. A. Bertness, S. R. Kurtz, D. J. Friedman, A. E. Kibbler, C. Kramer, and J. M. Olson, Appl. Phys. Lett. **65,** 989 (1994).
[67] J. Wu, W. Walukiewicz, K. M. Yu, W. Shan, J. W. Ager, E. E. Haller, H. Lu, and W. J. Schaff, J. Appl. Phys. **94,** 6477 (2003).
[68] P. H. Siegel, IEEE transactions on microwave theory and techniques **52,** 2438 (2004).
[69] P. H. Siegel, IEEE transactions on microwave theory and techniques **50,** 910 (2002).
[70] M. B. M. Rinzan, A. G. U. Perera, S. G. Matsik, H. C. Liu, Z. R. Wasilewski, and M. Buchanan, Appl. Phys. Lett. **86,** 071112 (2005).
[71] A. G. U. Perera, S. G. Matsik, B. Yaldiz, H. C. Liu, A. Shen, M. Gao, Z. R. Wasilewski, and M. Buchanan, Appl. Phys. Lett. **78,** 2241 (2001).
[72] A. Weerasekara, M. Rinzan, S. Matsik, A. G. U. Perera, M. Buchanan, H. Liu, G. V. Winckel, A. Stintz, and S. Krishna, Optics Letter **32,** 1335 (2007).
[73] G. D. Chern, E. D. Readinger, H. Shen, M. Wraback, C. S. Gallinat, G. Koblmuller, and J. S. Speck, Applied Physics Letters **89,** 141115-3 (2006).
[74] V. Gruzinskis, P. Shiktorov, E. Starikov, L. Reggiani, L. Varani, and J. C. Vaissière, Semiconductor Science and Technology **19,** S173-S175 (2004).
[75] E. Starikov, P. Shiktorov, V. Gruzinskis, L. Reggiani, L. Varani, J. C. Vaissiere, and J. H. Zhao, Physica B **314,** 171-175 (2002).
[76] P. Shiktorov, E. Starikov, V. Gruzinskis, M. Zarcone, D. P. Adorno, G. Ferrante, L. Reggiani, L. Varani, and J. C. Vaissiere, Phys.Stat. Sol. A **1,** 271 (2002).
[77] R. Ascazubi, I. Wilke, K. Denniston, H. Lu, and W. J. Schaff, Appl. Phys. Lett. **84** (2004).
[78] N. Dietz, M. Alevli, R. Atalay, G. Durkaya, R. Collazo, J. Tweedie, S. Mita, and Z. Sitar, Appl. Phys. Lett. **92,** 041911 (2008).
[79] O. Ambacher, J. Phys. D: Appl. Phys **31,** 2653-2710 (1998).

[80] J. I. Pankove and T. D. Moustakas, *Gallium Nitride (GaN)I* (Academic Press, San Diego, 1998).
[81] T. Araki, Y. Saito, T. Yamaguchi, M. Kurouchi, Y. Nanishi, and H. Naoi, J. Vac. Sci. Technol. B **22(4), pp. 2139-2143** (2004).
[82] V. Cimalla, U. Kaiser, I. Cimalla, G. Ecke, J. Pezoldt, L. Spiess, O. Ambacher, H. Lu, and W. Schaff, Superlattices and Microstructures **36,** 487-495 (2004).
[83] D. Y. Song, V. Kuryatkov, M. Basavaraj, D. Rosenbladt, S. A. Nikishin, M. Holtz, A. L. Syrkin, A. S. Usikov, V. A. Ivantsov, and V. A. Dmitriev, J. Appl. Phys. **99,** 116103 (2006).
[84] S. Suihkonen, J. Sormunen, V. T. Rangel-Kouppa, H. Koskenvaara, and M. Sopanen, Journal of Crystal Growth **291,** 8-11 (2006).
[85] K. J. Chang, J. Y. Chang, M. C. Chen, S. M. Lahn, C. J. Kao, Z. Y. Li, U. W. Y., and G. C. Chi, Journal of Vacuum Science & Technology A **25,** 701 (2007).
[86] T. Inushima, M. Higashiwaki, T. Matsui, T. Takenobu, and M. Motokawa, Phys. Rev. B **72,** 085210 (2005).
[87] A. Koukitu and H. Seki, Jpn. J. App. Phys. **36,** L750-L753 (1997).
[88] V. V. Mamutin, V. A. Vekshin, V. Y. Davydov, V. V. Ratnikov, T. V. Shubina, S. V. Ivanov, P. S. Kop'ev, M. Karlsteen, Soderwall. U, and M. Willander, Phys. stat. sol. (a) **176,** 247 (1999).
[89] H. Lu, W. J. Schaff, J. Hwang, H. Wu, W. Yeo, A. Pharkya, and L. F. Eastman, Appl. Phys. Lett. **77,** 2548 (2000).
[90] M. C. Johnson, S. L. Konsek, A. Zettl, and E. D. Bourret-Courchesne, Journal of Crystal Growth **272** (2004).
[91] A. Koukitu, N. Takahashi, and H. Seki, Jpn. J. App. Phys. **36,** L1136-L1138 (1997).
[92] D. C. Look, J. R. Sizelove, J. Jasinski, Z. Liliental-Weber, K. Saarinen, S. S. Park, and J. H. Han, in *Mater. Res. Soc. Symp. Proc.*, (2003), p. 575-590.
[93] Z. C. Feng, *III-Nitride Semiconductor Materials* (Imperial College Press, 2006).
[94] O. Igarashi, Jpn. J. App. Phys. **31,** 2665-2668 (1992).
[95] N. Takahashi, J. Ogasawara, and A. Koukitu, Jpn. J. App. Phys. **172,** 298-302 (1997).
[96] N. Takahashi, R. Matsumoto, A. Koukitu, and H. Seki, Jpn. J. App. Phys. **36,** L743-L745 (1997).
[97] B. H. Cardelino, C. E. Moore, S. McCall, C. A. Cardelino, N. Dietz, and K. J. Bachmann, in *CAITA-2004*, Purdue University, 2004, p. 1-13.
[98] N. Dietz, V. Woods, S. McCall, and K. J. Bachmann, in *Proc. Microgravity Conf.*, 2002, p. 169-181.
[99] B. H. Cardelino, C. E. Moore, C. A. Cardelino, and N. Dietz, in *Proc. SPIE*, 2005, p. 86-99.
[100] N. Dietz, V. Woods, S. McCall, and K. J. Bachmann, in *Proc. Microgravity Conf.*, 2003, p. 169-181.
[101] B. H. Cardelino, C. E. Moore, C. A. Cardelino, S. McCall, D. O. Frazier, and K. J. Bachmann, J. Phys. Chemistry **A107,** 3708-3718 (2003).
[102] G. A. Hebner, K. P. Killeen, and R. M. Biefeld, J. Cryst. Growth **98(3),** 293-301 (1989).

[103] M. C. Johnson, K. Poochinda, N. L. Ricker, J. W. Rogers, and T. P. Pearsall, J. Cryst. Growth **212** (2000).
[104] G. A. Hebner and K. P. Killeen, J. Appl. Phys. **67(3),** 1598-1600 (1990).
[105] J. Haigh and S. O'Brien, J. Cryst. Growth **68,** 550-556 (1984).
[106] N. I. Buchan, C. A. Larsen, and G. B. Stringfellow, J. Cryst. Growth **92,** 591-604 (1988).
[107] R. J. McCaulhey and V. M. Donnelly, J. Vac. Sci. Technol. A **9(6),** 2872-2886 (1991).
[108] N. Dietz, Mater. Sci.& Eng. B **87(1),** 1-22 (2001).
[109] N. Dietz and K. J. Bachmann, in *Mat. Res. Soc. Symp. Proc.*, 1996, p. 341-6.
[110] Q. X. Guo, T. Yamamura, A. Yoshida, and I. Itoh, J. Appl. Phys. **75,** 4927 (1994).
[111] H. Ahn, C. H. Shen, C. L. Wu, and S. Gwo, Thin Solid Films **494,** 69-73 (2006).
[112] T. Yodo, T. Shimada, T. Sumito, and Y. Harada, Journal of Crystal Growth **301-302,** 504-507 (2007).
[113] M. Alevli, G. Durkaya, R. Kirste, A. Weerasekara, W. Fenwick, V. Woods, I. T. Ferguson, A. Hoffmann, A. G. U. Perera, and N. Dietz, in *Mat. Res. Soc. Symp. Proc.*, Boston, 2007, p. 1-6.
[114] K. Xu and A. Yoshikawa, Appl. Phys. Lett. **83,** 251 (2003).
[115] R. Fuchs and K. L. Kliewer, Phys. Rev. B **140 A,** 2076 (1965).
[116] M. V. Klein and T. E. Furtac, *Optics* (Wiley, NY, 1986).
[117] C. C. Katsidis and D. I. Siapkas, Appl. Optics **41,** 3978 (2002).
[118] W. H. Press, W. T. Teukolsky, W. T. Vetterling, and B. P. Flannery, *Numerical Recipes in C: The art of Scientific Computing* (Cambridge University Press, Cambridge, 2003).
[119] T. Kawashima, H. Yoshikawa, S. Adachi, S. Fuke, and K. Ohtsuka, J. Appl. Phys. **82,** 3528-3535 (1997).
[120] N. Dietz, M. Alevli, V. Woods, M. Strassburg, H. Kang, and I. T. Ferguson, Phys. stat. sol. (b) **242,** 2985-2994 (2005).
[121] S. A. Teukolsky, W. T. Vetterling, B. P. Flannery, and W. H. Press, *Numerical Recipes in C: The Art of Scientific Computing* (Cambridge University Press, Cambridge,MA, 1992).
[122] T. Inushima, M. Higashiwaki, and T. Matsui, Phys. Rev. B **68,** 235204 (2003).
[123] A. Kasic, E. Valcheva, B. Monemar, H. Lu, and W. J. Schaff, Phys. Rev. B **70,** 115217 (2004).
[124] P. P. T. Chen, K. S. A. Butcher, M. Wintrebert-Fouquet, R. Wuhrer, M. R. Phillips, K. E. Prince, H. Timmers, S. K. Shrestha, and B. F. Usher, Journal of Crystal Growth **288,** 241-246 (2006).
[125] K. S. A. Butcher, M. Wintrebert-Fouquet, P. P.-T. Chen, T. L. Tansley, H. Dou, S. K. Shrestha, H. Timmers, M. Kuball, K. E. Prince, and J. E. Bradby, J. Appl. Phys. **95** (2004).
[126] T. V. Shubina, S. V. Ivanov, V. N. Jmerik, D. D. Solnyshkov, V. A. Vekshin, P. S. Kop'ev, A. Vasson, J. Leymarie, A. Kavokin, H. Amano, K. Shimono, A. Kasic, and B. Monemar, Physical Review Letters **92,** 117407-1-4 (2004).
[127] I. Mahboob, T. D. Veal, L. F. J. Piper, C. F. McConville, H. Lu, W. J. Schaff, J. Furthmuller, and F. Bechstedt, Physical Review B (Condensed Matter and Materials Physics) **69,** 201307-4 (2004).

[128] T. D. Veal, I. Mahboob, L. F. J. Piper, C. F. McConville, H. Lu, and W. J. Schaff, J. Vac. Sci. Technol. B **22,** -- July 2004 -- Volume 22, Issue 4, pp. 2175-2178 (2004).

[129] H. Lu, W. Schaff, L. F. Eastman, and C. E. Stutz, Appl. Phys. Lett. **82,** 1736 (2003).

[130] L. Colakerol, T. D. Veal, H.-K. Jeong, L. Plucinski, A. DeMasi, T. Learmonth, P.-A. Glans, S. Wang, Y. Zhang, L. F. J. Piper, P. H. Jefferson, A. Fedorov, T.-C. Chen, T. D. Moustakas, C. F. McConville, and K. E. Smith, Physical Review Letters **97,** 237601-4 (2006).

[131] R. P. Bhatta, B. D. Thoms, M. Alevli, and N. Dietz, Surface Science **601,** L120-L123 (2007).

[132] R. P. Bhatta, B. D. Thoms, M. Alevli, V. Woods, and N. Dietz, Applied Physics Letters **88,** 122112-3 (2006).

[133] L. F. J. Piper, T. D. Veal, I. Mahboob, C. F. McConville, H. Lu, and W. J. Schaff, Phys. Rev. B **70,** 115333 (2004).

[134] R. P. Bhatta, B. D. Thoms, A. Weerasekara, A. G. U. Perera, M. Alevli, and N. Dietz, Journal of Vacuum Science & Technology A **25,** 967 (2007).

[135] R. A. De Paola, F. M. Hoffmann, D. Heskett, and E. W. Plummer, Phys. Rev. B **B35,** 4236 (1986).

[136] E. Apen and J. L. Gland, Surface Science **321,** 308 (1994).

[137] A. Yamamoto, Y. Murakami, K. Koide, M. Adachi, and A. Hashimoto, Phys. stat. sol. (b) **228,** 5-8 (2001).

[138] V. Lebedev, K. Tonisch, F. Niebelschutz, V. Cimalla, D. Cengher, I. Cimalla, C. Mauder, S. Hauguth, O. Ambacher, F. M. Morales, J. G. Lozano, and D. Gonzales, Journal of Applied Physics **101,** 054906 (2007).

[139] V. Y. Davydov, V. V. Emtsev, I. N. Goncharuk, A. N. Smirnov, V. D. Petrikov, V. V. Mamutin, V. A. Vekshin, S. V. Ivanov, M. B. Smirnov, and T. Inushima, Applied Physics Letters **75,** pp. 3297-3299 (1999).

[140] M. Alevli, G. Durkaya, R. Atalay, R. Kirste, A. Weerasekara, A. G. U. Perera, A. Hoffmann, and N. Dietz, Journal of Vacuum Science & Technology A **in press** (2008).

[141] T. Araki, S. Ueta, K. Mizuo, T. Yamaguchi, Y. Saito, and Y. Nanishi, Phys. stat. sol. (c) **0** (2003).

[142] T. Koizumi, J. Wada, T. Araki, H. Naoi, and Y. Nanishi, Journal of Crystal Growth **275, 1-2,**e1073-e1077 (2005).

[143] T. V. Shubina, phys. stat. sol. (a) **202,** 377–382 (2005).

[144] V. A. Tyagai, A. M. Evstigneev, A. N. Krasiko, A. F. Andreeva, and V. Y. Malakhov, Sov. Phys. Semicond. **11,** 1257 (1977).

[145] J. S. Thakur, G. W. Auner, D. B. Haddad, R. Naik, and V. M. Naik, J. Appl. Phys. **95,** 4795 (2004).

[146] T. Inushima, T. Shiraishi, and V. Y. Davydov, **110,** 491 (1990).

[147] J. Wu and W. Walukiewicz, Superlattices and Microstructures **34,** 63-75 (2003).

[148] A. Yamamoto, T. Tanaka, K. Koide, and A. Hashimoto, Phys. stat. sol. (b) **194,** 510-514 (2002).

[149] F. Demangeot, C. Pinquier, J. Frandon, M. Gaio, O. Briot, B. Maleyre, S. Ruffenach, and B. Gil, Phys. Rev. B **71,** pp.104305-11 (2005).

[150] T. B. Wei, R. F. Duan, J. X. Wang, J. M. Li, Z. Q. Huo, P. Ma, Z. Liu, and Y. P. Zeng, J. Phys. D: Appl. Phys **40,** 2881-2885 (2007).

[151] J. S. Thakur, D. Haddad, V. M. Naik, R. Naik, G. W. Auner, H. Lu, and W. J. Schaff, Physical Review B **71** (2005).

[152] J. S. Thakur, Y. V. Danylyuk, D. Haddad, V. M. Naik, R. Naik, and G. W. Auner, Phys. Rev. B **76,** 035309 (2007).

[153] N. D. Mermin, Phys. Rev. B **1,** 2362 (1970).

[154] J. Linhard and K. Dan, Vidensk. Selsk. Mat. Fys. Medd. **28,** 881 (1954).

[155] J. Arvanitidis, D. Christofilos, G. A. Kourouklis, A. Delimitis, M. Katsikini, P. Komninou, S. Ves, E. Dimakis, and A. Georgakilas, Journal of Applied Physics **100,** 113516-5 (2006).

[156] H. Aynaou, V. R. Velasco, A. Nougaoui, E. H. El Boudouti, D. Bria, and B. Djafari-Rouhani, Surface Science **590,** 224-242 (2005).

[157] K. Xu, W. Tereshima, T. Hata, N. Hashimoto, M. Yoshitani, B. Cao, Y. Ishitani, and A. Yoshikawa, Phys. stat. sol. (c) **0,** 2814-2817 (2003).

[158] M. Losurdo, G. Bruno, T.-H. Kim, S. Choi, and A. Brown, Applied Physics Letters **88,** 121928-3 (2006).

[159] A. Aleksov, R. Collazo, S. Mita, R. Schlesser, and Z. Sitar, Appl. Phys. Lett. **89,** 052117 (2006).

[160] U. Fano, Phys. Rev. **124,** 1866 - 1878 (1961).